**Brisid Isufi**

Mestre em Engenharia Civil

# Seismic behaviour of flat slabs with punching shear reinforcement

Dissertação para obtenção do Grau de Doutor em

**Engenharia Civil**

| | |
|---|---|
| Orientador: | António Manuel Pinho Ramos, Professor Auxiliar, FCT/UNL |
| Co-orientador: | Válter José da Guia Lúcio, Professor Associado, FCT/UNL |

Júri

| | |
|---|---|
| Presidente: | Prof. Doutor João Jorge Ribeiro Soares Gonçalves Araújo |
| Arguentes: | Prof. Doutor Maurizio Orlando |
| | Prof. Doutor Rui Pedro César Marreiros |
| Vogais: | Prof[a]. Doutora Ildi Cismasiu |
| | Prof. Doutor António Manuel Pinho Ramos |
| | Doutor Manuel José Andrade Loureiro Pipa |
| | Prof[a]. Doutora Ana Rita Faria Conceição de Sousa Gião |

FACULDADE DE CIÊNCIAS E TECNOLOGIA
UNIVERSIDADE NOVA DE LISBOA

**Dezembro, 2018**

**Seismic behaviour of flat slabs with punching shear reinforcement**



Este documento foi gerado utilizando o processador (pdf)LaTeX, com base no template "novathesis" [1] desenvolvido no Dep. Informática da FCT-NOVA [2].
[1] https://github.com/joaomlourenco/novathesis [2] http://www.di.fct.unl.pt

*To my family.*

# Acknowledgements

I would like to start by expressing my sincere gratitude to my supervisor, Prof. António Pinho Ramos, for his expert advice, encouragement and close collaboration in every stage of my studies. His guidance was insightful and decisive in solving the many problems that arose. I am also thankful to my co-supervisor, Prof. Válter Lúcio, whose support for me stretched far beyond his academic duties. He was my first contact with Universidade NOVA de Lisboa and remained highly involved throughout the entire duration of my studies in academic and other issues. It was an honour and privilege for me to be guided by these two inspirational professors. I would like to extend my gratitude to all the members of the jury for their time and dedication, and for the valuable comments and suggestions.

During most of my time as a PhD student at DEC/FCT/UNL, I benefited from a scholarship under the Grant Agreement 2014-0848/001-001-Erasmus Mundus Action 2-Partnerships. This dissertation would not have been possible without this scholarship. The managerial support offered by the University of Warsaw, Poland, in the framework of the scholarship is greatly appreciated. I am grateful to the professors that supported my applications during the years 2014–2015, especially to Prof. Adriana Miri from École Spéciale des Travaux Publics, France and Prof. Niko Pojani from the Polytechnic University of Tirana, Albania.

I am thankful for the collaboration and the support I received by the technical and administrative staff of two companies in which the specimens were prepared: Secil Prebetão, SA and CONCREMAT, SA.

During my PhD studies, I was offered support by many professors, PhD students and Master students, for which I am grateful. In particular, I would like to thank André Almeida (PhD student) for his precious support during and after the experimental campaign. Master students Miguel Ornelas, Rui Santos, Florian Veliaj and Ricardo Faria are greatly appreciated for their help during the tests. I appreciate the help of Prof. Ildi Cismasiu, who devoted a lot of her time to discussing and reviewing the nonlinear analyses performed throughout this study and provided much appreciated thoughtful insight on several occasions. Professor Rui Marreiros is greatly appreciated for his contributions in practical matters during the experimental campaign and insightful discussions on several topics related to my research. Eng. Vitor Silva and technicians José Gaspar and Jorge

Silverio are appreciated for providing a lot of help and a cheerful environment in the laboratory.

The support offered during the experimental work by Nuno D. Gouveia, Hugo Fernandes and Micael Inácio when they were PhD students is also appreciated. I would like to thank the Master students André Saraiva and Rafael Serra for their help with the translation of the Abstract in Portuguese. Special thanks go to Maria Luz V. Sousa, Gracinda Caetano and Carla Figueiredo for their help throughout the years in administrative issues. Professors Carla Marchão and Ana Rita Gião are appreciated for their general support during my stay in Portugal.

Universidade NOVA de Lisboa offered me the opportunity to benefit from an international environment, which I highly appreciate. I was given the chance to meet and collaborate with PhD students Massimo Lapi from University of Florence and Andri Setiawan from Imperial College London, which turned out to be very helpful during the experimental campaign, cooperative during the analysis of the results and good friends after all.

I am thankful to my professors and colleagues from Polytechnic University of Tirana. Among others, Prof. Niko Pojani, Prof. Markel Baballëku, Prof. Luan Myrtaj, Prof. Arian Lako, Prof. Hektor Cullufi, Prof. Fisnik Kadiu and my friend Besjan Mulkurti played an important role in my formation as an engineer and offered moral support throughout these years.

I wish to express my most sincere gratitude to my parents, my sister and my grandmother for genuinely understanding me in times when they would have appreciated my presence. I dedicate this dissertation to them for their contribution and sacrifices in my formation as an individual.

Last but not least, I am sincerely thankful to my fiancée Helisa Muhaj. She was my closest companion throughout the entire duration of my doctoral studies. I am grateful for her love, encouragement and presence by my side, without which I can't imagine overcoming the challenges I faced throughout these years.

# Abstract

Flat slabs have found widespread use in buildings over the last decades. They owe their popularity to several advantages, including construction cost and speed, as well as convenience in architectural design. Traditionally designed as gravity load carrying systems, flat slabs are found even in earthquake prone areas. When subjected to horizontal drifts, flat slab–column connections are susceptible to brittle punching shear failure, which results in a sudden drop of the load carrying capacity. Especially in Europe, the designers are faced with difficulties arising from the lack of a full coverage by the codes.

Past experimental research has shown that the drift capacity of flat slabs can be significantly enhanced when punching shear reinforcement is used. This dissertation provides insight on the factors that influence the deformation capacity and the role of the enhancement of this capacity in the seismic behaviour of buildings with flat slabs. An experimental campaign containing five reinforced concrete flat slab specimens (four of which reinforced with headed shear studs) tested under constant gravity loads and reversed horizontal cyclic displacements constitutes the core of the dissertation. It is shown that the ultimate drifts are described reasonably well if the following factors are taken into account simultaneously: the gravity load, the punching shear resistance, flexural strength and the extent of shear reinforcement.

Although the main focus is on secondary seismic flat slabs (that do not take part in the earthquake resisting system), a contribution is made towards better understanding the behaviour and limitations of flat slabs as primary seismic elements, which are intended to be included in the new generation of Eurocodes. The role of punching shear reinforcement in the global behaviour of such buildings is studied through a series of nonlinear analyses, which show that properly designed punching shear reinforcement can enhance both safety and robustness. It is shown that the inherent high flexibility of slab–column connections remains a limitation for primary flat slabs, even when shear reinforcement is provided.

**Keywords:** flat slab, punching, seismic behaviour, cyclic loading, studs

# Resumo

Nas últimas décadas tem sido frequente o uso de lajes fungiformes em novos edifícios. Esta popularidade advém de várias vantagens apresentadas por este sistema estrutural, incluindo o relativamente baixo custo e rapidez de construção, bem como a conveniência no projeto de arquitetura. Apesar de serem normalmente dimensionadas para a resistência a cargas verticais, são soluções também utilizadas em áreas em que existe risco sísmico. Quando submetidas a deslocamentos horizontais, as ligações laje–pilar são suscetíveis a punçoamento, resultando numa queda imediata da capacidade resistente. Especialmente na Europa, os engenheiros enfrentam dificuldades decorrentes da falta de regras nos códigos para o dimensionamento deste tipo de estruturas sujeito a ações sísmicas.

Ensaios experimentais anteriores mostraram que a capacidade de deslocamento de lajes fungiformes pode ser significativamente aumentada quando é utilizada armadura específica de punçoamento. Esta dissertação apresenta uma análise sobre os fatores que influenciam a capacidade de deformação, e a sua influência no comportamento de edifícios com lajes fungiformes sujeitos a cargas sísmicas. Uma campanha experimental contendo cinco lajes fungiformes de betão armado (quatro das quais reforçadas com *studs*), ensaiadas sob cargas verticais constantes e deslocamentos cíclicos horizontais invertidos, formam o núcleo da dissertação. É demonstrado que os deslocamentos relativos são descritos razoavelmente bem se os seguintes fatores forem considerados simultaneamente: carga vertical, resistência ao punçoamento, resistência à flexão e extensão da zona com armadura específica de punçoamento.

Embora o foco principal seja em lajes fungiformes que não participam no sistema sismo-resistente, uma contribuição é dada para melhor compreender o comportamento e as limitações das lajes usadas como elementos sísmicos primários, com a intenção de ser incluidas na nova geração de Eurocódigos. A influência da armadura específica de punçoamento no comportamento global de tais edifícios é estudada através de uma série de análises não-lineares, que mostram que esta armadura, desde que adequadamente projetada, pode melhorar tanto a segurança como a robustez. É mostrado que a alta flexibilidade inerente das ligações laje–pilar, continua a ser uma limitação para a utilização de lajes fungiformes como elementos primários, mesmo contendo armadura específica de punçoamento.

**Palavras-chave:** laje fungiforme, punçoamento, comportamento sísmico, cargas cíclicas, *studs*

# Contents

# List of Figures

# List of Tables

# Notations

**Latin upper case letters**

| | |
|---|---|
| $A_s$ | area of reinforcement. |
| $A_{sw}$ | area of one perimeter of shear reinforcement. |
| $A_{sw,min}$ | minimum shear reinforcement. |
| $A_{sw,min,1leg}$ | minimum area of a single leg of shear reinforcement. |
| $C$ | torsional constant. |
| $E$ | area under a force–displacement curve, energy. |
| $EA$ | axial rigidity. |
| $E_c$ | modulus of elasticity of concrete. |
| $E_{cm}$ | mean modulus of elasticity of concrete. |
| $E_d$ | area enclosed by the hysteresis loop. |
| $EI$ | flexural rigidity. |
| $E_s$ | modulus of elasticity of steel; elastic strain energy. |
| $G_f$ | fracture energy. |
| $H_e$ | height of the equivalent SDOF system. |
| $J_c$ | a property of the assumed control section analogous to the polar moment of inertia in ACI 318 calculations. |
| $K$ | stiffness. |
| $K_c$ | stiffness of the column. |
| $K_e$ | elastic stiffness; effective stiffness of the SDOF system. |
| $K_{ec}$ | stiffness of the equivalent column. |
| $K_{exp}$ | stiffness calculated from a bilinear approximation of the experimental force–displacement curve. |

| | |
|---|---|
| $K_{sc}$ | secant stiffness. |
| $K_t$ | stiffness of the torsional member in the Equivalent Frame Method. |
| $L$ | span length. |
| $M$ | bending moment; mass. |
| $M^-$ | hogging, negative, moment. |
| $M^+$ | sagging, positive, moment. |
| $M_{Ed}$ | design unbalanced moment. |
| $M_{pr}$ | probable flexural strength expressed as a bending moment, in accordance with ACI 318. |
| $M_R$ | bending moment resistance. |
| $M_{rad}$ | radial moment. |
| $M_{tan}$ | tangential moment. |
| $M_{unb}$ | unbalanced moment. |
| $M_{unb,max}$ | maximum unbalanced moment. |
| $M_{y,unb}$ | yielding unbalanced moment. |
| $P$ | probability. |
| $P_{max}$ | maximum horizontal force. |
| $Sa(T_1)$ | spectral acceleration at the fundamental period of vibration. |
| $S_{De}(T)$ | elastic spectral displacement at period $T$. |
| $S_e(T)$ | elastic spectral acceleration at period $T$. |
| $T$ | period of vibrations. |
| $V_0$ | concentric punching shear resistance (zero unbalanced moment) for a specimen without shear reinforcement. |
| $V_{0,col}$ | concentric punching shear resistance (zero unbalanced moment) at the face of the column for a specimen with shear reinforcement. |
| $V_{0,out}$ | concentric punching shear resistance (zero unbalanced moment) outside the shear reinforced zone. |
| $V_{0c,s}$ | concentric punching shear resistance (zero unbalanced moment) at a control perimeter at a distance $2d$ away from the face of the column for a specimen with shear reinforcement. |
| $V_c$ | punching shear resistance provided by concrete alone in ACI 318 calculations (force). |

| | |
|---|---|
| $V$; $V_{Ed}$ | design shear force. |
| $V_{flex}$ | applied gravity load in the slab–column connection for which the specimen fails in flexure. |
| $V_g$ | applied gravity load in the slab–column connection. |
| $V_n$ | nominal punching shear resistance in ACI 318 calculations. |
| $V_{Rd}$ | design resisting shear force. |
| $V_{Rd,int}$ | shear resistance after punching, for the purpose of designing integrity reinforcement. |
| $V_{Rd,max}$ | maximum punching shear resistance controlled by concrete crushing. |
| $V_{TS}$ | shear force at mid–span, induced by the test setup. |
| $W_i$ | factor related to the distribution of shear along the basic control perimeter. |

**Latin lower case letters**

| | |
|---|---|
| $a_{gR}$ | reference ground acceleration. |
| $b_0$ | effective control perimeter in *fib* Model Code 2010 and control section for punching shear calculation in ACI 318. |
| $b_{eff}$ | effective beam width. |
| $b_{int}$ | control perimeter activated by the integrity reinforcement after punching. |
| $b_u$ | diameter of a circle with the same surface as the region inside the basic control perimeter in *fib* Model Code 2010. |
| $c$ | column cross section dimension. |
| $c_c$ | depth of the compression zone. |
| $d$ | average effective depth of the longitudinal reinforcement. |
| $d_g$ | maximum aggregate diameter. |
| $d_{g0}$ | reference aggregate diameter. |
| $d_r$ | drift ratio. |
| $d_{r,max}$ | maximum drift attained before failure. |
| $d_{r,Pmax}$ | drift ratio at maximum horizontal force. |
| $d_{r,u}$ | ultimate drift ratio. |
| $d_{r,y}$ | yielding drift ratio. |

| | |
|---|---|
| $d_{res}$ | effective depth for the purpose of designing integrity reinforcement in *fib* Model Code 2010. |
| $d_v$ | shear-resisting effective depth of the slab, taking also into account the support penetration. |
| $e_u$ | eccentricity of the resultant shear force. |
| $f_{bd}$ | design bond strength. |
| $f_c$ | concrete compressive cylinder strength. |
| $f_{c,cube}$ | concrete compressive cube strength. |
| $f_{ck}$ | characteristic compressive cylinder strength of concrete. |
| $f_{ct}$ | tensile strength of concrete. |
| $f_{ct,sp}$ | tensile splitting strength of concrete. |
| $f_y$ | yield stress of reinforcement. |
| $f_{yd}$ | design yield stress of reinforcement. |
| $f_{yk}$ | characteristic yield stress of reinforcement. |
| $f_{yw}$ | yield stress of shear reinforcement. |
| $f_{ywd}$ | design yield stress of shear reinforcement. |
| $f_{ywd,ef}$ | effective design strength of shear reinforcement. |
| $f_u$ | ultimate tensile stress of reinforcement. |
| $h$ | thickness of the slab. |
| $k$ | factor that takes into account size effects in Eurocode 2 calculations. |
| $k_{dg}$ | factor accounting for maximum aggregate size. |
| $k_e$ | coefficient accounting for eccentricity of loading. |
| $k_{sys}$ | factor that accounts for the performance of punching shear reinforcement in *fib* Model Code 2010 calculations. |
| $k_\psi$ | factor related to slab rotation in *fib* Model Code 2010. |
| $l_{ch}$ | characteristic length, related to the modulus of elasticity of concrete and fracture energy. |
| $m$ | bending moment per unit width. |
| $m_e$ | mass of the equivalent SDOF system. |
| $m_i$ | mass at storey $i$. |
| $m_{Rd}$ | design resisting bending moment per unit width. |
| $m_{sd}$ | design acting bending moment per unit width. |

| | |
|---|---|
| $r_0$ | radius of the critical shear crack. |
| $r_c$ | radius of a circular column. |
| $r_q$ | radius of the application point of the vertical force. |
| $r_s$ | radius of the zero-moment line, radius of a circular slab. |
| $r_y$ | radius of the yielded zone. |
| $s$; $s_r$ | spacing of shear reinforcement perimeters; radial spacing. |
| $s_t$ | spacing of shear reinforcement legs in the tangential direction. |
| $u_i$ | control perimeter $i$ in Eurocode 2 calculations. |
| $u_{out}$ | outer punching perimeter based on Eurocode 2, but enclosed (without reduction). |
| $u_{out,ef}$ | effective outer punching perimeter in accordance with Eurocode 2. |
| $v_c$ | punching shear resistance provided by concrete alone in ACI 318 calculations (stress). |
| $v_{Ed}$ | design shear stress. |
| $v_{min}$ | minimum value of the punching shear resistance in Eurocode 2 calculations. |
| $v_{Rd,c}$ | punching shear resistance provided by concrete in Eurocode 2 calculations. |
| $v_{Rd,cs}$ | punching shear resistance provided by concrete and the shear reinforcement in Eurocode 2 calculations. |
| $v_u$ | punching shear stress in ACI 318 calculations. |
| $w$ | width of the specimen. |

**Greek letters**

| | |
|---|---|
| $\alpha$ | angle that shear reinforcement forms to the plane of the structural member; coefficient used in the Effective Beam Width method. |
| $\alpha_s$ | factor depending on the type of slab–column connection (interior or exterior) in ACI 318 calculations. |
| $\alpha_{ult}$ | angle of integrity bars to the plane of the slab. |
| $\beta$ | factor that takes into account an uneven distribution of shear stresses under eccentric loading conditions in Eurocode 2 calculations; ratio of the sides of the column in ACI 318 calculations; dispersion of the fragility function. |

| | |
|---|---|
| $\beta_r$ | ratio of the span length in the direction of horizontal loading to the span length in the transversal direction. |
| $\gamma_c$ | partial safety factor for concrete. |
| $\gamma_f$ | portion of unbalanced moment transferred by flexure. |
| $\gamma_v$ | portion of unbalanced moment transferred by eccentricity of shear. |
| $\Delta_d$ | design displacement. |
| $\Delta_i$ | displacement at storey $i$. |
| $\Delta_p$ | acceptable plastic displacement, based on performance requirements. |
| $\Delta_r$ | residual horizontal displacement. |
| $\Delta_u$ | ultimate displacement. |
| $\Delta_y$ | yield displacement. |
| $\delta_{e,col}$ | elastic deformation of the column. |
| $\epsilon_{cu,c}$ | confined concrete ultimate strain. |
| $\epsilon_{cu1}$ | concrete ultimate strain. |
| $\epsilon_y$ | strain at yielding. |
| $\zeta$ | proposed unitless factor, taking into account GSR, GFR and the extent of punching shear reinforcement in the ultimate drift capacity. |
| $\Phi$ | reinforcing bar diameter; standard Normal cumulative distribution function. |
| $\Phi_w$ | diameter of the shear reinforcement legs. |
| $\phi_i$ | angle of sector $i$ of a slab–column connection to the bending axis. |
| $\eta$ | damping correction factor. |
| $\theta$ | median of the fragility function. |
| $\theta_y$ | yield drift of the frame. |
| $\lambda$ | modification factor to take into account the reduced mechanical properties of lightweight concrete. |
| $\mu$ | displacement ductility. |
| $\xi_{eq}$ | equivalent viscous damping coefficient. |
| $\rho$; $\rho_l$ | geometric mean of reinforcement ratios in each direction. |
| $\rho_s$ | ratio of the volume of hoops to the volume of confined concrete in a reinforced concrete column. |
| $\sigma_{swd}$ | stress in the shear reinforcement. |

| | |
|---|---|
| $\chi$ | curvature. |
| $\chi_1$ | curvature at the beginning of the stabilized cracked regime. |
| $\chi_{cr}$ | curvature at cracking. |
| $\chi_{TS}$ | curvature due to tension stiffening. |
| $\chi_y$ | curvature at yielding. |
| $\psi$ | slab rotation outside the critical shear crack. |
| $\psi(\phi)$ | rotation of the slab sector at angle $\phi$ to the bending axis. |
| $\psi_{max}$ | maximum slab rotation outside the critical shear crack. |
| $\psi_{min}$ | minimum slab rotation outside the critical shear crack. |

**Acronyms**

| | |
|---|---|
| **ADRS** | Acceleration–Displacement Response Spectrum. |
| **CFRP** | Carbon fibre-reinforced polymer. |
| **CSCT** | Critical Shear Crack Theory. |
| **DBD** | Displacement Based Design. |
| **DDBD** | Direct Displacement Based Design. |
| **DEC/FCT/UNL** | Departamento de Engenharia Civil, Faculdade de Ciências e Tecnologia, Universidade Nova de Lisboa. |
| **DLS** | Damage Limitation State. |
| **DS** | Damage State. |
| **FEA** | Finite Element Analysis. |
| **FSDS** | Flat Slab Damage State (DS specific for flat slabs). |
| **GFR** | Gravity Flexure Ratio. |
| **GSR** | Gravity Shear Ratio. |
| **IDA** | Incremental Dynamic Analysis. |
| **IM** | Intensity Measure. |
| **LA** | Level of Approximation. |
| **LS** | Limit State. |
| **MSA** | Multiple Stripes Analysis. |
| **NCS** | No-collapse state. |
| **NDP** | Nationally Determined Parameter. |

| | |
|---|---|
| **PBSD** | Performance Based Seismic Design. |
| **RDI** | Residual Deformation Index. |
| **SDOF** | Single Degree of Freedom. |
| **THA** | Time History Analysis. |
| **TST** | Tangential Strain Theory. |
| **UDL** | Uniformly Distributed Load. |

# Chapter 1

# Introduction

## 1.1 Background and motivation

Flat slabs are reinforced concrete slabs directly supported by columns, without beams. They are widely used in buildings, including in actively seismic regions (Figure 1.1), because they have several advantages compared to other systems. The lack of beams leads to freedom in the interior architectural design of the building. For instance, partition walls can be located anywhere, without running through the problem of having visible beams in the ceiling. Plumbing, electrical, heating, ventilation, and air conditioning installations can run freely through the ceiling and can be covered easily. In terms of construction, flat slabs are advantageous because of the simple formwork and simple reinforcement layout. Therefore, their construction is generally less labour intensive.

(a) (b)

Figure 1.1: Examples of buildings with flat slabs in earthquake prone zones in Portugal (photos courtesy of Válter Lúcio)

Buildings with flat slabs can have a reduced overall height compared to buildings with conventional beams if the same floor to ceiling free height is to be kept. Although this is an advantage in seismic loading conditions, it can be overshadowed by the disadvantages. The main disadvantage of flat slabs is their susceptibility to punching shear failure

(Figure 1.2) when subjected to a combination of gravity loads and unbalanced moments arising from the lateral deformation of the building. This type of failure is brittle and usually impossible to be noticed in advance. Once such a failure occurs, the adjacent slab–column connections are subjected to increased loads and can fail in punching as well. If a portion of the slab is left without sufficient supports, it can fall over the slab of the lower level and cause punching failures to be distributed throughout the entire building, leading to an eventual global or partial progressive collapse. A recent example of a global collapse of a building with flat slabs is shown in Figure 1.3.

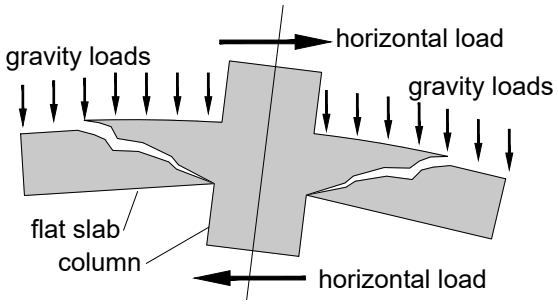


Figure 1.2: Illustration of a punching shear failure under combined gravity and horizontal loading

Figure 1.3: Collapse of a building with flat slabs in Mexico City during the 2017 Puebla-Morelos earthquake. Photo before (left) and after (right) the earthquake. (Images collected by Galvis et al. 2017 from Google Street View and media reports)

Another disadvantage of the flat slabs is their high flexibility towards horizontal actions. Because of the high flexibility, the contribution of flat slabs in the resistance towards seismic actions is low and the deformation demand on vertical elements (columns and walls) is high. Furthermore, flat slab–column connections are characterized by low energy dissipation capacity due to the typically strong pinching effect in the force–displacement hysteretic relationship. The fundamental vibration period of flat slab buildings (buildings in which the flat slabs are part of the primary earthquake resisting system) is generally

larger compared to that of buildings with moment resisting frames or shear walls. Although the high period may lead to lower seismic forces (depending on the period range and the ground motion characteristics), it makes it difficult for the building to fulfil the serviceability or damage limitation criteria as a result of the increased deformations.

For the reasons stated above, and because the behaviour of flat slabs under horizontal actions is still not completely understood, seismic design codes are cautious regarding the use of flat slabs in seismic regions. For instance, Eurocode 8 (EC8, CEN 2004d) does not fully cover buildings with flat slab frames. For buildings in which the flat slabs are accompanied by another lateral force resisting system, EC8 requires the flat slabs to be designed to carry the gravity load when subjected to deformations induced by the primary seismic elements.

To enhance the shear strength and deformation capacity of flat slabs, several punching shear reinforcement systems have been developed and tested throughout the last decades. Headed shear studs are among the most practical and efficient solutions. Their efficiency in the enhancement of the punching shear strength has been verified by numerous concentric monotonic loading tests. However, the available reversed horizontal cyclic loading tests are not exhaustive, mainly due to the considerable differences between the specimens in terms of the amount and extend of shear reinforcement, testing conditions, geometry and loading. A test setup has been developed recently at Departamento de Engenharia Civil, Faculdade de Ciências e Tecnologia, Universidade Nova de Lisboa (DEC/FCT/UNL) to test flat slabs under reversed horizontal cyclic loading with realistic boundary conditions that simulate slab continuity in the direction of the application of horizontal drifts. The test setup has been used in the past to test flat slabs without shear reinforcement, with various quantities of stirrups, fibre-reinforced concrete and high strength concrete.

The procedure normally employed for structural design nowadays is "force based". The structural designer estimates forces acting on the structure and analyses the internal action effects (forces, moments and the corresponding stresses). If the acting stresses are smaller than the corresponding resistances, considering also partial factors of safety, the design is considered satisfactory. After reaching a satisfactory design in terms of forces, deformations are checked against pre-established limits based on serviceability requirements. This force based methodology is used also for the seismic design of structures. The earthquake is commonly represented by lateral loads acting on the structure. This is a convenient procedure, because it is rather simple and allows the direct combination of seismic action with gravity loads (Fardis 2018). However, the determination of these lateral forces is based on a number of simplifications. Usually a force–reduction factor (a behaviour factor in European practice) is employed to relate the elastic forces to the inelastic ones. Such a factor is usually based on simplifying assumptions for typical structures. Furthermore, it has been observed that damage can be expressed more conveniently in terms of deformations. Especially in non–structural elements such as partition

walls and claddings, the inter–storey drifts imposed by the primary seismic elements are closely related to the damage suffered by these elements. The current version of Eurocode 8 (CEN 2004d) requires the limitation of deformations in buildings for damage limitation purposes. In flat slab–column connections, using drifts to guide the design is also convenient, as demonstrated by the North American practice (ACI 2014).

## 1.2 Objectives

The main objectives of this dissertation are listed below:

- Addition of new experimental results to the current database of reversed horizontal cyclic loading tests of flat slabs with shear reinforcement;
- Expansion of the number of types of shear reinforcement and punching shear enhancement techniques tested using the test setup that has already been developed at DEC/FCT/UNL;
- Assessment of the influence of various factors in the drift capacity of flat slab–column connections with and without shear reinforcement;
- Study of the benefits and limitations of shear reinforcement in the global seismic behaviour of flat slab frames in the framework of Performance Based Engineering;
- Provision of recommendations for the seismic design of buildings with flat slabs.

## 1.3 Methodology

To meet the objectives described in Section 1.2, a combination of experimental and numerical work is performed and described in this dissertation.

An experimental campaign consisting of five flat slab specimens, four of which reinforced with shear studs, is described and analysed in detail. The specimens were subjected to constant gravity loads and reversed horizontal cyclic displacements. The studs were arranged in a cruciform layout to avoid interference with the longitudinal reinforcement. The shear studs were placed in three perimeters around the column in one of the shear-reinforced specimens and in five perimeters in the other specimens. All specimens except one of them had approximately the same Gravity Shear Ratio (GSR) defined as the ratio between the gravity load applied during the test and the concentric punching shear resistance not considering the shear reinforcement. One specimen had an increased GSR. One of the specimens had no shear reinforcement and served as a control specimen. One of the shear-reinforced specimens was tested in a two-phase loading protocol to study the post-earthquake behaviour of flat slabs. This experimental campaign will contribute to increase the number of experimentally tested flat slabs with shear studs available in the

literature. In the meantime, it is a continuation of the work already started at DEC/FCT/UNL for other punching shear enhancement techniques. As a result, it will provide the grounds for a direct comparison of the efficiency of shear studs with other types of punching shear enhancement methods.

To assess the influence of various factors in the drift capacity of flat slab–column connections with and without shear reinforcement, a database of tests from the literature under reversed horizontal cyclic loading was compiled. To this end, a literature review was performed. The newly tested specimens with studs were added to the database and analysed in conjunction.

Numerical analyses were performed to assess the benefits and limitations of shear reinforcement in the global seismic behaviour of flat slab frames. The experimental results of the cyclic loading campaign were used to calibrate numerical models of the slab–column connections. Based on the specifics of the test setup used in the experimental campaign, numerical models of entire flat slab frames were developed. These frames are representatives of the prototype building upon which the experimental campaign was based. Seismic fragility functions that express the probability of reaching or exceeding certain damage states for a given earthquake intensity measure were derived based on a series of nonlinear dynamic time history analyses. These fragility functions are developed and discussed in the framework of Performance Based Engineering.

Conclusions and recommendations are derived after a synthesis of all the work described in this dissertation.

## 1.4 Organisation of the dissertation

The dissertation is organized in seven chapters. The first chapter is the present one. In the second chapter, the State-of-the-Art in the behaviour of flat slabs under lateral loads is presented. The chapter starts with a review of the most common types of shear reinforcement systems used to enhance the punching shear strength of flat slabs. The advantages and disadvantages of each type are discussed. Experimental campaigns on specimens with and without shear reinforcement are described. The compiled database of tests under constant gravity loads and reversed horizontal cyclic loading is presented. The distribution of characteristics (such as concrete strength, dimensions, reinforcement, etc.) of each specimen in the database is described, thus providing a view on the gaps in literature. The chapter summarizes also the code provisions for non-seismic and seismic design of flat slabs. Since EC8 (CEN 2004d) provides only limited guidance on the seismic design of flat slabs, reference is made to North American design codes, where more extended provisions can be found. The chapter closes with a review of analytical approaches developed in the past for analysis and design of flat slabs under horizontal actions. Analysis methods, including recently developed finite element modelling techniques, are described.

The third chapter provides a thorough description of the experimental campaign. The chapter starts with the conceptual design of the specimens, followed by a description of them. Details on the production of the shear studs in particular and the specimens in general are given. The test setup, instrumentation and the loading protocol are described in detail. Several tests were performed to determine the mechanical characteristics of the materials used for the production of the specimens. These tests are described and the obtained results are presented. The chapter concludes with a thorough description of each of the reversed horizontal cyclic loading tests, starting from gravity loading, observations throughout the test (cracking and significant events) and a description of failure for each specimen.

The fourth chapter contains the analysis of experimental results. First, the load–deformation hysteretic plots are presented and discussed. Then, the chapter continues with the determination of several parameters that enable a thorough analysis of the results, such as equivalent viscous damping, displacement ductility, residual deformations, stiffness, etc. Measurements, such as deflections and strains, are presented and analysed. Based on the experimental results, a discussion is made on the post-earthquake behaviour of flat slabs that suffer significant damage but resist large imposed drifts without a punching shear failure. The chapter continues with a comparison of the experimental results with analytical models applicable for horizontal loading conditions. In the final sections, a direct comparison is made with selected specimens from the literature. First, the results are compared with an experimental campaign (Brown 2003) performed using comparable specimens in terms of shear reinforcement and size, but under a very different test setup. In the last section, the experimental results are compared with results obtained at DEC/FCT/UNL in the past experimental campaigns using the same test setup.

In the fifth chapter, the ultimate drift ratios in slab–column connections are studied. Results from the literature and results from the experimental campaign are analysed for specimens without shear reinforcement and specimens with shear studs. Based on the test setup conditions of each specimen, a measure of the flexural and punching strength of each specimen is determined and its influence in the ultimate drift capacity is studied. For specimens with shear reinforcement, the role of the extent of shear reinforcement is also analysed. Design implications are discussed. A design example is provided.

The sixth chapter presents the analyses performed for the purpose of studying the role of punching shear reinforcement in the global behaviour of flat slab frames. The chapter starts with an introduction to the concepts used in the chapter, followed by a description of the modelling technique adopted for the slab–column connections. The model calibration with the experiments is described. The chapter goes on with the description of the considered frame models. Pushover analyses are performed on the frame models to assess the global behaviour in deterministic terms. To extend the analysis in probabilistic terms and to put it in the framework of Performance Based Engineering, a seismic fragility analysis is presented. In the following sections, uncertainties other

than those related to the ground motion characteristics are added and the analyses are described.

The final chapter contains the conclusions and perspectives for future work. The dissertation has three appendices. The first appendix contains the compiled database of reversed horizontal cyclic loading tests from the literature, with and without shear reinforcement. The second appendix contains complete readings from the strain gauges installed in the longitudinal bars and in the shear reinforcement. These readings are given as a function of time and horizontal drift rather than the condensed points (at peak drifts) presented in the main text of the dissertation. In the last appendix, details about the ground motion records used for the time history analyses of flat slab frames are provided.

# Chapter 2

# State of the art

Concepts from literature and previous experimental campaigns relevant to this dissertation are reviewed in this chapter. A description of the most common types of shear reinforcement systems used in flat slab–column connections is provided in the beginning of the chapter. Headed shear studs, which are used in the experimental campaign (Chapter 3), are discussed in more detail.

The chapter continues with a review of code requirements for punching shear design in non-seismic design situations. Reference is made to three design codes: the Eurocode 2 (EC2, CEN 2004c), *fib* Model Code 2010 (MC2010, *fib* 2013) and ACI 318 (ACI 2014). A review of published experimental work performed by various authors to date is made in the following section. The test setups and loading conditions in various experimental campaigns are described. Specimens with and without shear reinforcement are reviewed. The main findings from the literature, relevant to this dissertation, are summarized. Specimens with headed shear studs are distinguished from the set of specimens with shear reinforcement and the differences between them are discussed. A short discussion is made on exterior slab–column connections and tests on continuous slabs and large-scale buildings.

A review of seismic design requirements from codes and findings from the literature follows. Aspects such as minimum shear reinforcement, extent and layout of shear reinforcement are discussed. The concept of robustness, diaphragmatic behaviour at storey level and the effects of dynamic loading are briefly reviewed. The chapter continues with a review of analytical approaches for the estimation of the unbalanced moment and the deformation capacity of flat slab–column connections.

The chapter is concluded with a review of the analysis methods for flat slabs under horizontal actions. Commonly adopted approaches such as the Equivalent Frame Method and the Effective Beam Width Method are complemented by new finite element modelling techniques proposed by various authors.

## 2.1 Overview of shear reinforcement systems

### 2.1.1 Stirrups

Stirrups (Figure 2.1) are one of the most common types of shear reinforcement since they can be easily produced on-site with normal reinforcement bars, with the same technique and equipment used for the longitudinal reinforcement.

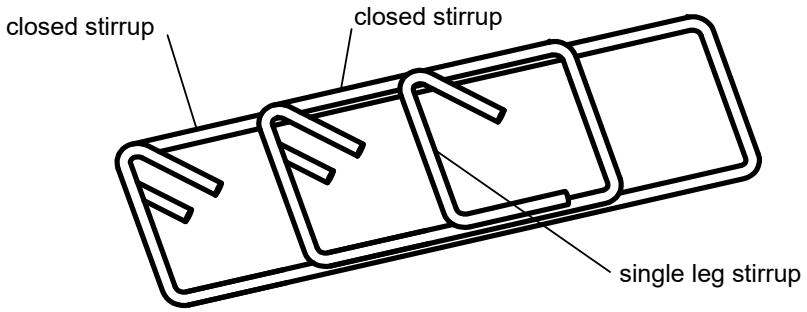


Figure 2.1: Illustration of stirrups shear reinforcement

The following deficiencies of stirrups are acknowledged:

- Loss of tension due to imperfect support on longitudinal reinforcement bars and due to rounding at corners (Figure 2.2). This phenomenon is described in guide ACI 421.1R-99 (ACI 1999).
- Difficulty of production and positioning on site for slabs with small thickness and dense reinforcement. When multiple layers of closed stirrups are to be placed at a small spacing, pouring and vibration of concrete becomes difficult.
- If thickness of the slab is to be kept the same, the effective depth of the slab is reduced compared to a slab without shear reinforcement, because the stirrups surround the main tension steel. Therefore, the durability requirements are guided by the cover of the stirrups instead of that of the flexural reinforcement. This also applies to several other types of shear reinforcement.

Numerous monotonic concentric punching shear tests of specimens reinforced with stirrups have been reported in the literature (for example, in Seible et al. 1980; Vollum et al. 2010; Lips et al. 2012; Hegger et al. 2017). The configuration of stirrups was different for the specimens in the aforementioned publications. These tests have shown that, when compared to specimens without shear reinforcement, the strength of the flat slabs with stirrups is significantly increased.

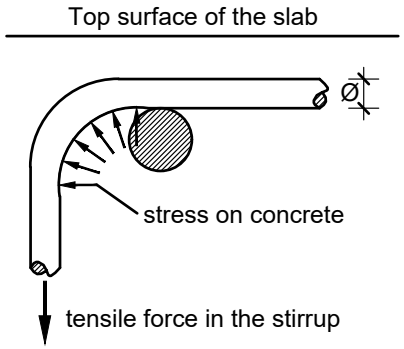


Figure 2.2: Loss of tension in stirrups (figure based on ACI 421.1R-99)

A limited number of reversed horizontal cyclic loading tests of specimens with stirrups is found in the literature. Among the earliest experimental campaigns were those conducted at the University of Washington, reported in Hawkins et al. 1974; Hanna et al. 1975; Symonds et al. 1976; Akiyama and Hawkins 1984 and those reported in Islam and Park 1976. More recent campaigns include Robertson 1990; Robertson et al. 2002; Park et al. 2012 and tests at DEC/FCT/UNL (Almeida et al. 2018).

These tests have shown that, when compared to specimens without shear reinforcement, the drift capacity of the flat slabs with stirrups is significantly increased. However, when compared to other shear reinforcement systems (such as with studs in Park et al. 2012), the stirrups do not always offer the greatest enhancement of the drift capacity.

### 2.1.2 Headed shear studs

Headed shear studs are bars (usually round) with integral widened heads that serve for anchorage (Figure 2.3). The heads can be welded or forged. Headed studs have many applications in reinforced concrete structures, from beams with thin webs, to shear walls, corbels, precast beams, etc., as summarized in Ghali and Youakim 2005. They are especially practical and effective in the enhancement of punching shear strength of flat slabs and footings. Sometimes the studs are connected with a thin strip to form a stud rail (Figure 2.4) that facilitates installation.

Shear studs have been shown to be very effective for both the enhancement of punching shear strength and the post-elastic behaviour of the slab–column connections. Their enhanced behaviour compared to other types of shear reinforcement is commonly attributed to the good anchorage conditions at both ends of the stud. The usage of shear studs in buildings is further encouraged by their advantage in construction speed. They are often used in practice as proprietary products which are ready to be placed on site after the slab longitudinal reinforcement has been fixed. Numerous commercial products exist. Various producers have designed different configurations of the connecting metal

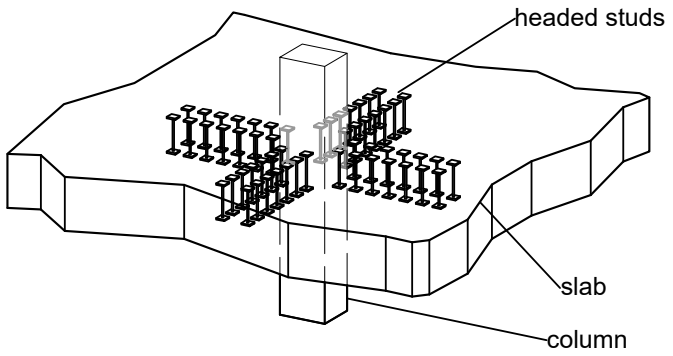


Figure 2.3: Visualisation of headed stud reinforcement

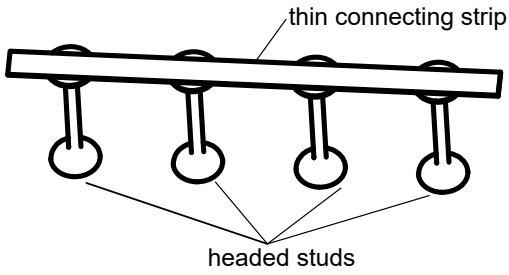


Figure 2.4: Illustration of a typical prefabricated stud rail

strip for stud rails, with the following (not exhaustive) purposes:

- ease of installation (the prefabricated unit rests on the flexural reinforcement or is made stable in fabrication, therefore the installation is straightforward);
- minimization of the influence on concrete cover (the connecting strip is usually thin and — in some products — transverse strips may be attached in order to support the prefabricated unit on the bars with larger concrete cover);
- better anchorage;
- flexibility to change spacing and layout of the studs on-site (in some products, the spacing of the studs can be adjusted by sliding the studs in the thin connecting strip).

Anchorage conditions of shear studs are better than those for stirrups, because the effect of tension loss that was mentioned in Section 2.1.1 is not relevant for correctly designed headed studs (Figure 2.5). Supporting experimental evidence is summarized in Ghali and Youakim 2005. The diameter of the head should be at least 3Φ according to

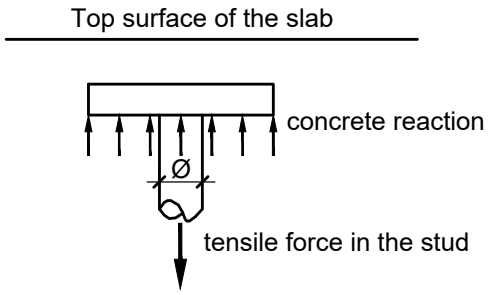


Figure 2.5: Anchorage conditions of shear studs

MC2010 (*fib* 2013) and $\sqrt{10}\Phi$ according to ACI 318 (ACI 2014) in order for the stud to develop its yield stress.

MC2010 (*fib* 2013) and ACI 318-14 (ACI 2014) recognize the superior properties of the shear studs compared to stirrups and they provide recommendations that generally lead to a higher calculated punching shear strength when studs are used. For instance, ACI 318-14 imposes limits on the punching shear stress $v_u$ and the punching shear resistance provided by concrete alone, $v_c$. For control sections within the shear-reinforced zone, these limits are set higher for flat slabs with shear studs. The maximum stress $v_c$ can be 3/2 times higher in slabs with shear studs compared to slabs with stirrups. The limiting stress $v_u$ is 4/3 times higher in slabs with shear studs.

MC2010 (*fib* 2013) considers the effectiveness of shear studs by recommending an increased value of the factor $k_{sys}$ that "accounts for performance of punching shear reinforcing systems to control shear cracking and to suitably confine compression struts at the soffit of the slab" (*fib* 2013). The factor $k_{sys}$ directly influences the calculation of the maximum punching shear resistance limited by crushing of the concrete struts. For studs in which the dimension of the head is at least 3 times the diameter of the stud and when certain spacing requirements are fulfilled, the value of $k_{sys}$ can be taken equal to 2.8. For stirrups, the value of $k_{sys}$ is lower. It can be taken equal to 2.4 when good anchorage conditions are provided and $k_{sys} = 2$ when no data is available.

EC2 does not give specific provisions for studs, but it recognizes the possibility of using proprietary products. In this case, it recommends that the shear strength be "determined by testing in accordance with the relevant European Technical Approval" (CEN 2004c).

The effectiveness of studs in the enhancement of punching shear strength has been confirmed by numerous experimental investigations (Seible et al. 1980; Voet et al. 1982; Mokhtar et al. 1985; Lips et al. 2012; Ferreira et al. 2014; Dam et al. 2017; Hegger et al. 2017 and others). The available experimental data suggest that studs are also effective in the enhancement of the drift capacity of flat slab–column connections. The behaviour of reinforced concrete flat slab specimens with shear studs under reversed horizontal cyclic

loading is discussed in Section 2.3 and Chapter 5.

### 2.1.3 Bent–up bars

Bent-up bars (Figure 2.6) over the column may be used as punching shear reinforcement. Geometric restrictions limit the efficiency of bent top flexural reinforcement serving as punching shear reinforcement in the same time. For instance, bent-up bars should be no further than $0.25d$ from the edge of the column to be counted as shear reinforcement according to EC2 (CEN 2004c). Furthermore, only the vertical component of the tensile force in the inclined bar is to be considered for the calculation of shear resistance according to the major design codes (CEN 2004c; *fib* 2013; ACI 2014).

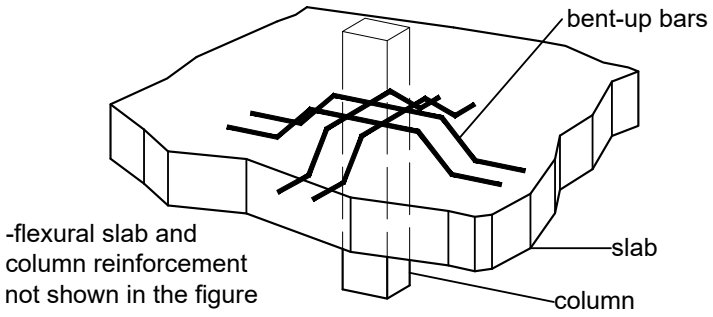


Figure 2.6: Bent-up bars as punching shear reinforcement

Regarding the drift capacity of flat slabs with bent–up bars, a few experimental campaigns are found in the literature. Islam and Park 1976 reported that bent–up bars increased the strength of flat slab–column connections but not their drift capacity. Robertson and Johnson 2006 showed that top flexural reinforcement passing through the column, bent and properly anchored to the bottom of the slab may be also used as a measure to prevent progressive collapse of the structure.

### 2.1.4 Shearheads

Structural steel profiles can be embedded into the slab–column connection as shown in Figure 2.7 to enhance the punching shear strength. This type of shear reinforcement is referred to as "shearhead". Various configurations are possible depending on the dimensions of the column and slab as well as the required strength. Multiple parallel profiles, edge and corner configurations can be used. EC2 (CEN 2004c) does not give specific provisions for this type of punching shear enhancement method. MC2010 (*fib* 2013) and ACI 318-14 (ACI 2014) do consider the usage of shearheads and provide recommendations for their design and detailing.

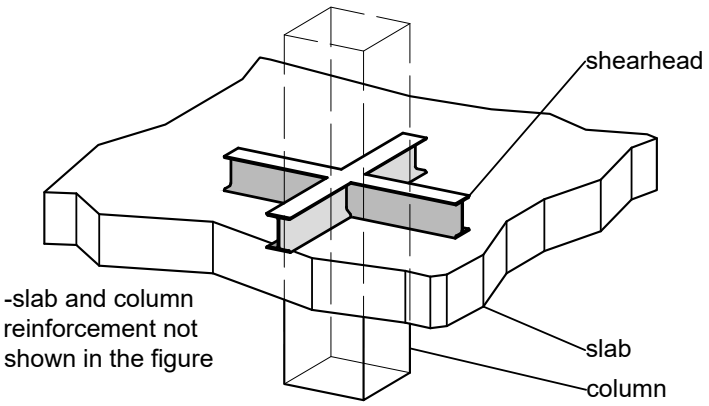


Figure 2.7: Visualisation of shearhead reinforcement

Shearheads may be especially suitable for structures in which the columns are made of structural steel, because the construction details of the shearhead–steel column connection can be very practical. According to guide ACI 421.2R (ACI 2010), shearheads are not often used in reinforced concrete structures, although the experimental evidence shows that they can enhance the punching shear strength (Corley and Hawkins 1968; Islam and Park 1976).

### 2.1.5 Other products

Some less common shear reinforcement systems are described in the following paragraphs. Other means of enhancing the punching shear strength of flat slabs under horizontal actions, such as drop panels or high strength concrete and fibre reinforced concrete, are outside the scope of this dissertation.

#### 2.1.5.1 Thin–plate stirrups

Thin–plate stirrups, also known as shearbands, consist of a thin strip of metal folded as shown in Figure 2.8. The product can be installed over the top flexural steel and its effect on the concrete cover is small, due to the small thickness of the metal strip. For better anchorage, the product has holes in its entire length. The system and the first tests performed on it are described in Pilakoutas and Li 2003, according to which the system improves ductility of the flat slab and increases the punching shear strength. Two more specimens are reported in Kang and Wallace 2008. A critical view on this system is given in Birkle and Gayed 2006.

#### 2.1.5.2 Lattice shear reinforcement

Park et al. 2007 presented a system for punching shear reinforcement of flat slabs in the form of a prefabricated lattice (Figure 2.9). The idea of the authors is to make use of the

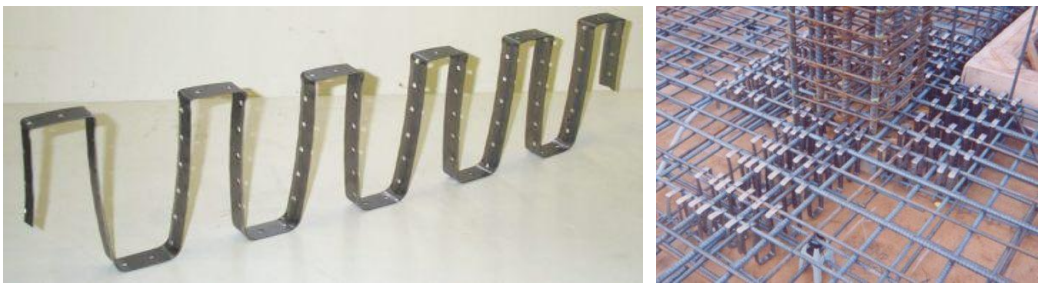

Figure 2.8: Thin–plate stirrup reinforcement (University of Sheffield 2016)

inclined bars as shear reinforcement and to benefit from the truss system of the lattice as a whole in case of local failures.

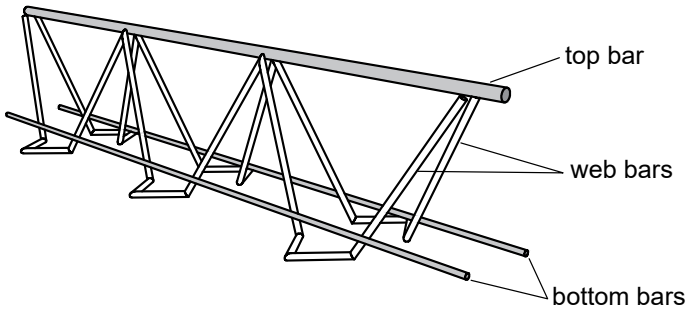


Figure 2.9: Lattice reinforcement (after Park et al. 2012)

Direct punching shear tests of the system are presented in Park et al. 2007 and cyclic loading tests are described in Park et al. 2012. In both cases, the authors argued that lattice shear reinforcement had considerable benefits in terms of seismic behaviour of the slab–column connection when compared to other shear reinforcement systems tested in the same experimental campaign. A similar shear reinforcement system was used in Eom et al. 2017 to test slab specimens under eccentric loads.

#### 2.1.5.3 Steel I-profiles

Gomes and Regan 1999b tested a series of 12 slab specimens with thickness 200 mm under concentric monotonic loading. The specimens were reinforced with short standard I-profiles, the flanges of which served as an anchoring head when the web is tensioned, in similarity with studs. The shear reinforcement is described in Figure 2.10.

Gomes and Regan 1999b found that the system worked reasonably well as punching shear reinforcement. No horizontal cyclic loading test was found with this type of shear reinforcement.

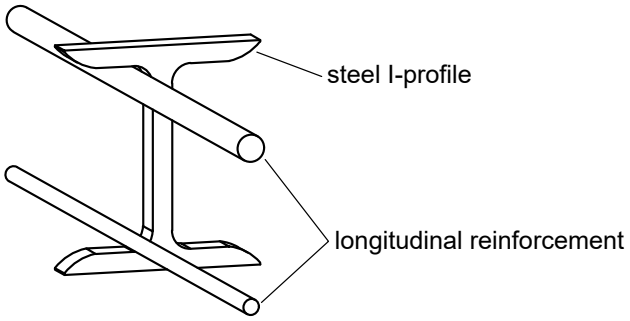


Figure 2.10: Short I-profiles as punching shear reinforcement (after Gomes and Regan 1999a; Gomes and Regan 1999b)

## 2.2 Punching shear design in building codes

### 2.2.1 Eurocode 2

The verification model for punching shear according to EC2 (CEN 2004c) is shown in Figure 2.11 (based on Figure 6.12 of EN 1992-1-1, CEN 2004c). According to this model, a basic control section is defined at a distance $2d$ from the face of the loaded area, where $d$ is the average effective depth of the longitudinal reinforcement. The distance $2d$ of the control perimeter has been chosen to make the shear resistance more uniform for different column sizes and to make the formulation for punching similar to that for one–way shear (European Concrete Platform ASBL 2008). The basic control perimeter is constructed such that its length is minimal (i.e. by rounding the corners, as shown in Figure 2.12a). For corner or edge loaded areas, the provisions of EC2 for the basic control parameter are described in Figure 2.12b. Provisions are also given in the code for the reduction of the control perimeter when openings are present.

The design expression for non-prestressed slabs without shear reinforcement has been derived using a reliability–based approach utilizing results from 112 experimental tests on flat slabs without shear reinforcement, with concrete strengths from 14 MPa to 120 MPa, effective slab depths from 100 mm to 275 mm, longitudinal reinforcement ratios 0.4% to 2.5% and ratio of the column diameter to the effective depth of the slab from 1.2 to 2.5 (European Concrete Platform ASBL 2008). The design punching shear resistance, including also prestressed slabs, is given as:

$$v_{Rd,c} = C_{Rd,c} k (100 \rho_l f_{ck})^{1/3} + k_1 \sigma_{c,p} \geq (v_{min} + k_1 \sigma_{c,p}) \tag{2.1}$$

where:

- $C_{Rd,c} = 0.18/\gamma_c$ and $\gamma_c$ is the partial safety factor for concrete;
- $k = 1 + \sqrt{200/d} \leq 2$ takes into account the size effects;

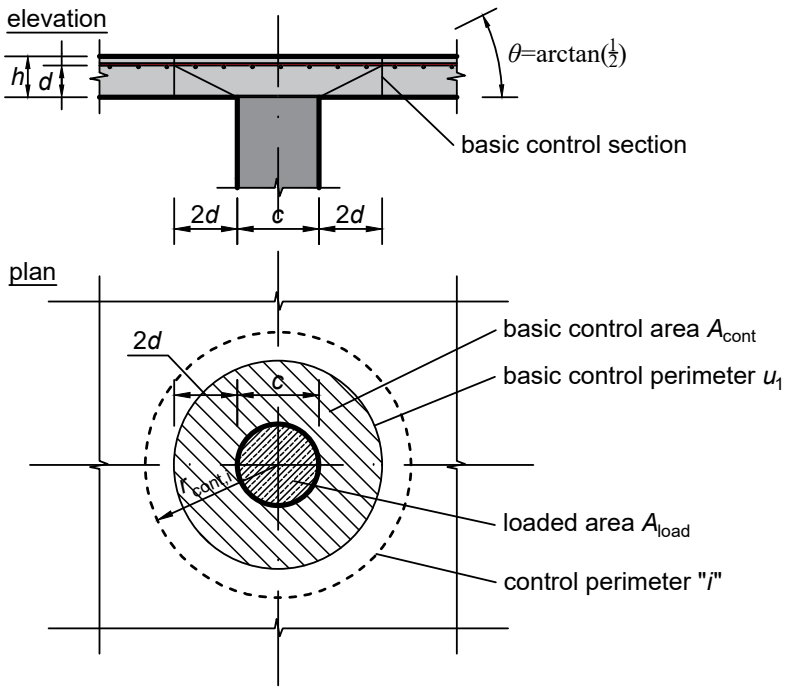


Figure 2.11: Verification model for punching shear according to EC2 (based on Figure 6.12 of EN 1992-1-1)

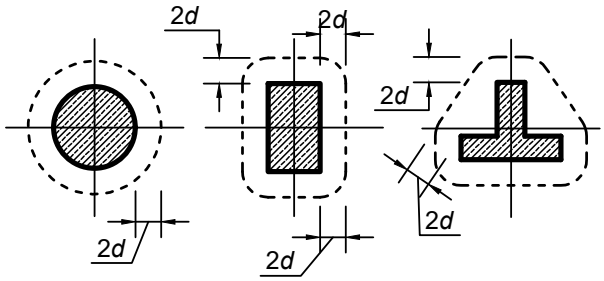


(a) Examples of basic control perimeters

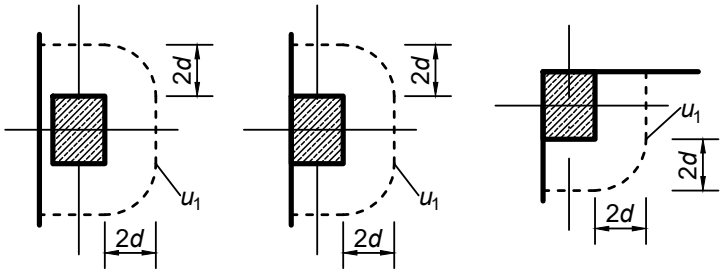


(b) Examples of the basic control perimeter in case of corner or edge loaded areas

Figure 2.12: Rules for the basic control perimeter according to EC2

- $\rho_l$ is the geometric mean of reinforcement ratios in each direction, but not larger than 0.02;
- $k_1$ is a coefficient for prestressed slabs, with recommended value equal to 0.1;
- $\sigma_{c,p}$ represents the arithmetic mean of normal concrete stresses in the control section in each direction;
- $v_{min}$ is an empirical minimum shear resistance, $v_{min} = 0.035k^{3/2}f_{ck}^{1/2}$.

The punching shear resisting stress considering the contribution of both concrete and shear reinforcement, $v_{Rd,cs}$, is:

$$v_{Rd,cs} = 0.75v_{Rd,c} + 1.5\frac{d}{s_r}A_{sw}f_{ywd,ef}\frac{\sin\alpha}{u_1 d} \tag{2.2}$$

where

- $A_{sw}$ is the area of one perimeter of shear reinforcement;
- $s_r$ is the spacing of shear reinforcement perimeters;
- $u_1$ is the control perimeter;
- $\alpha$ is the angle that shear reinforcement forms to the plane of the structural member and
- $f_{ywd,ef}$ is the effective design strength of shear reinforcement, as follows:

$$f_{ywd,ef} = 250 + 0.25d \leq f_{ywd} \text{ (in MPa)} \tag{2.3}$$

As pointed out in European Concrete Platform ASBL 2008, the reduction of $v_{Rd,c}$ in Equation 2.2 reflects the fact that direct summation of contributions from concrete and from shear reinforcement is not safe. Wider cracks are expected in shear-reinforced slabs and the ability of concrete to transfer shear is reduced with opening of the cracks (Muttoni and Ruiz 2008; Ruiz and Muttoni 2009). The limitation of the effective stress in the shear reinforcement (Equation 2.3) aims to limit the crack width in design.

The design acting shear stress at the basic control perimeter is calculated as follows:

$$v_{Ed} = \beta\frac{V_{Ed}}{u_1 d} \tag{2.4}$$

where $V_{Ed}$ is the design shear force in the control perimeter and $\beta$ is a factor that takes into account an uneven distribution of shear stresses under eccentric loading conditions (Figure 2.13). The value of $\beta$ is:

$$\beta = 1 + k\frac{M_{Ed}}{V_{Ed}}\frac{u_1}{W_1} \tag{2.5}$$

where $M_{Ed}$ and $V_{Ed}$ are the acting unbalanced moment and shear force, respectively. $W_1$ for the basic control perimeter and $W_i$ in general, is a factor related to the distribution of shear along the basic control perimeter and is calculated by the integral $W_i = \int_0^{u_i} |e| dl$ (see notations in Figure 2.13). The factor $k$ depends on the ratio of the sides of the column.

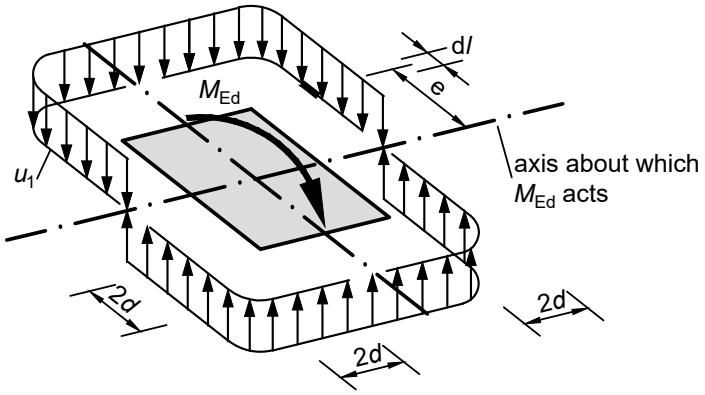


Figure 2.13: Simplified uneven shear distribution in a slab–column connection (according to EC2)

When $v_{Ed} > v_{Rd,c}$, shear reinforcement should be provided, based on Equation 2.2. Stresses should also be checked at a control perimeter located at the face of the column and at an outer perimeter, located outside the shear-reinforced zone. The latter check governs the extent of shear reinforcement.

### 2.2.2 ACI 318

In ACI 318-14 (ACI 2014), the control section[1] is denoted by $b_0$ and is located at a distance $d/2$ from each point in the perimeter of the loaded area. For rectangular loaded areas (or columns) a simplified shape of the control section with four straight lines is permitted (Figure 2.14).

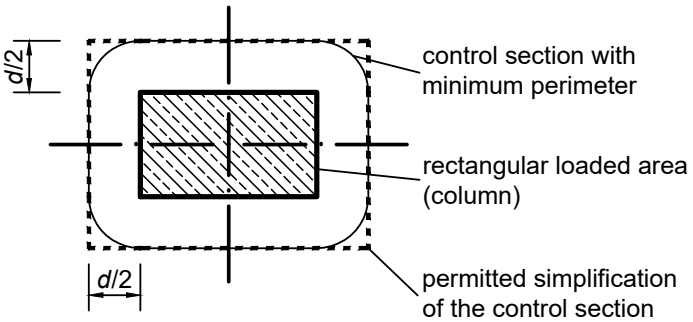


Figure 2.14: Control section for rectangular loaded areas in ACI 318

[1] In ACI 318-14, the adopted term is "critical section".

For non-prestressed slabs without shear reinforcement, the shear resistance $V_c$ (in terms of force) is calculated as the minimum of the three expressions below:

$$V_c = \min \begin{cases} 0.17\,(1+2/\beta)\,\lambda\sqrt{f_c}\,b_0 d \\ 0.083\,(\alpha_s d/b_0+2)\,\lambda\sqrt{f_c}\,b_0 d \quad \text{(in SI units)} \\ 0.33\lambda\sqrt{f_c}\,b_0 d \end{cases} \tag{2.6}$$

where:

- $\lambda$ is a modification factor to take into account the reduced mechanical properties of lightweight concrete (for normal-weight concrete, $\lambda = 1$);
- $\beta$ is the ratio of the sides of the column;
- $\alpha_s$ is a factor equal to 40 for interior columns, 30 for edge columns and 20 for corner columns.

To consider moment transfer in the calculations, the design shear stress is calculated in a similar manner as in the EC2 calculations presented earlier, but with a linear distribution of stresses along the control section. The acting shear stress under a combination of shear force $V_{Ed}$ and an unbalanced moment $M_{Ed}$ is:

$$v_{Ed} = \frac{V_{Ed}}{A_c} + \frac{\gamma_v M_{Ed}\left(\frac{c_2+d}{2}\right)}{J_c} \tag{2.7}$$

The first term in Equation 2.7 represents the contribution of force $V_{Ed}$ uniformly distributed over an area $A_c$ to the shear stress. The second term represents the contribution of the design unbalanced moment $M_{Ed}$ to the shear stress, by assuming a linear distribution of stresses. The dimension of the control section perpendicular to the direction of the horizontal force is $(c_2 + d)/2$. $J_c$ is a property of the assumed control section analogous to the polar moment of inertia. The factor $\gamma_v$ is used to determine the unbalanced moment transferred by eccentricity of shear at slab–column connections. It is related to the factor $\gamma_f$ representing the fraction of $M_{Ed}$ that is transferred by flexure as follows:

$$\gamma_v = 1 - \gamma_f \tag{2.8}$$

The factor $\gamma_f$ itself is defined as:

$$\gamma_f = \frac{1}{1+\frac{2}{3}\sqrt{\frac{b_1}{b_2}}} \tag{2.9}$$

where $b_1 = c_1 + d$ and $b_2 = c_2 + d$, with $c_1$ and $c_2$ being the column dimensions.

When the design resistance is smaller than the design action effects, shear reinforcement can be provided to increase the punching shear resistance. In this case, the nominal

shear strength $V_n$ is:

$$V_n = V_c + V_s \leq 0.50\sqrt{f_c}b_0 d \tag{2.10}$$

where $V_c$ is the portion of shear strength provided by concrete, as described earlier but limited to a value of $0.17\lambda\sqrt{f_c}b_0 d$ for stirrups and $0.25\lambda\sqrt{f_c}b_0 d$ for studs. $V_s$ is the nominal shear strength provided by shear reinforcement, as follows:

$$V_s = \frac{A_{sw} f_{yw} d}{s} \tag{2.11}$$

where:

- $A_{sw}$ is the cross-sectional area of all legs of reinforcement on one peripheral line with the same shape as the column section;
- $f_{yw}$ is the yield stress of shear reinforcement;
- $s$ is the spacing of perimeters of shear reinforcement.

Equation 2.10 is valid for stirrups and for shear stud reinforcement with spacing of perimeters not greater than $3d/4$. If spacing of the perimeters of studs is limited to $d/2$, it is permitted to use the following equation instead of Equation 2.10:

$$V_n = V_c + V_s \leq 0.66\sqrt{f_c}b_0 d \tag{2.12}$$

In case of moment transfer, the shear resistance (based on the value of $V_n$, the control perimeter and the relevant code partial factors) should be compared to the acting shear stress calculated in Equation 2.7.

### 2.2.3 *fib* Model Code 2010

The *fib* Model Code 2010 (MC2010, *fib* 2013) contains provisions for punching shear design. In distinction from Eurocode and ACI codes, MC2010 deals with punching in a more mechanically based approach by including the following key concepts:

- Critical Shear Crack Theory (CSCT);.
- Level of Approximation (LA) approach.

Some details related to CSCT and LA approach are given in the following paragraphs.

#### 2.2.3.1 Critical Shear Crack Theory

CSCT was first presented by Muttoni and Schwartz 1991, where it was shown that – for structural elements without shear reinforcement – "a critical shear crack" propagating through the strut that carries the shear force to the column is responsible for the reduction of failure load and that the punching resistance is a function of slab's rotation outside the critical shear crack. The theory was developed based on earlier work by Kinnunen and Nylander 1960. In Muttoni 2008, the theory was completed by adding a failure criterion and a code–like formulation for the punching shear design of flat slabs.

An example of application of CSCT is given in Figure 2.15. According to the theory, punching failure occurs at the intersection of the load–rotation curve with the failure criterion. The load–rotation curve is constructed using a finite element analysis or analytically for simple cases. The analytical solution for axisymmetric slabs is obtained by dividing the slab into sector elements extended from the critical shear crack (located at a radius $r_0 = r_c + d$, where $r_c$ is the radius of the column, assumed circular) to a radius equal to the radius of the hogging moment region of the slab. It is assumed that the slab rotation, $\psi$, is constant outside the critical shear crack. Inside the radius $r_0$, the radial and tangential moments are assumed constant and the radial curvature is assumed equal to the tangential curvature. Internal forces are then calculated assuming a quadrilinear moment–curvature relationship and the equilibrium conditions of the sector elements are used to calculate the shear force, $V$, for a given slab rotation, $\psi$ (Muttoni 2008).

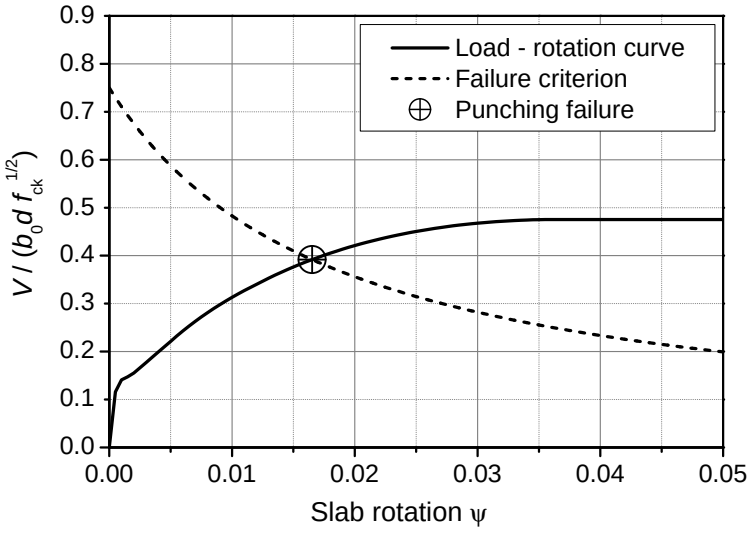


Figure 2.15: Example of the application of CSCT for $d = 118$ mm, $\rho = 0.96\%$, span length 3.84 m, square column with side 250 mm, $f_c = 40$ MPa, $f_y = 500$ MPa and maximum aggregate size 16 mm

Based on a semi-empirical formulation, assuming crack width proportional to the slab rotation ($\psi$) and effective depth ($d$) as well as taking into account the roughness of the

crack, the failure criterion is expressed as follows (Muttoni 2008):

$$\frac{V}{b_0 d\sqrt{f_c}} = \frac{3/4}{1 + 15\frac{\psi d}{d_{g0}+d_g}} \tag{2.13}$$

where $b_0$ is the control perimeter, taken at a distance $d/2$ from the face of the column; $d_g$ is the maximum aggregate size and $d_{g0} = 16$ mm is a reference aggregate size.

Ruiz and Muttoni 2009 extended the application of CSCT to the design of flat slabs with shear reinforcement. In this case, the load–rotation relationship is the same as in slabs without shear reinforcement, because it is only depended on the flexural characteristics of the slab. For slabs with shear reinforcement, failure can occur through the shear reinforcement, outside the shear-reinforced zone or near the face of the column due to crushing of concrete (Figure 2.16). The resistance for each of these three failure modes is determined at the intersection of the load–rotation curve with the corresponding failure criteria.

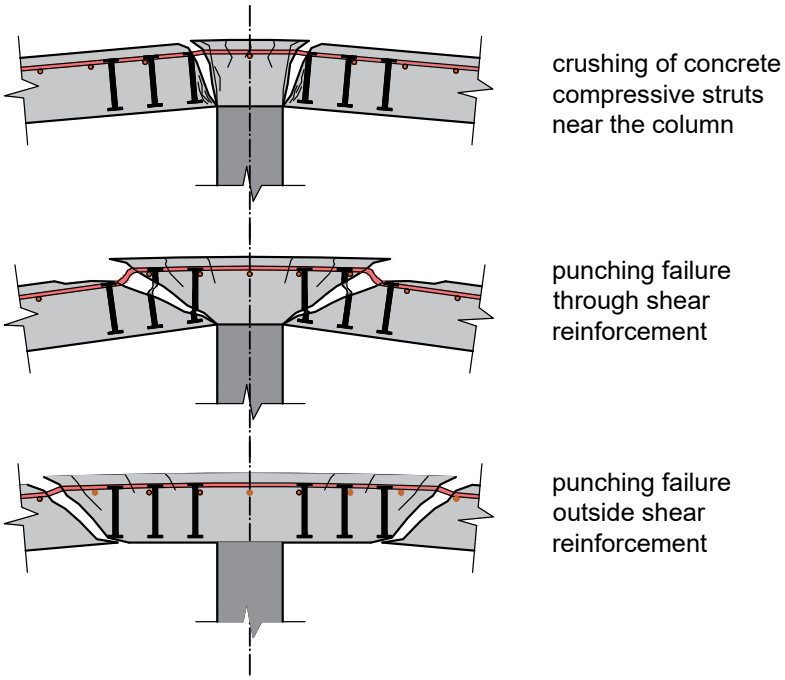


Figure 2.16: Possible punching failure modes for shear-reinforced flat slabs

The criterion for failure within the shear-reinforced zone is based on a simple mechanical model, which takes into account the stress in each shear reinforcement leg and bonding conditions. In contrast to other major design codes (CEN 2004c; ACI 2014), the contribution of shear reinforcement is not considered constant. In Figure 2.17, it is represented by the light grey area, and it changes with $\psi$.

The failure criterion for punching outside the shear reinforcement is calculated as in case of slabs without shear reinforcement, but with an adapted perimeter (taken at a

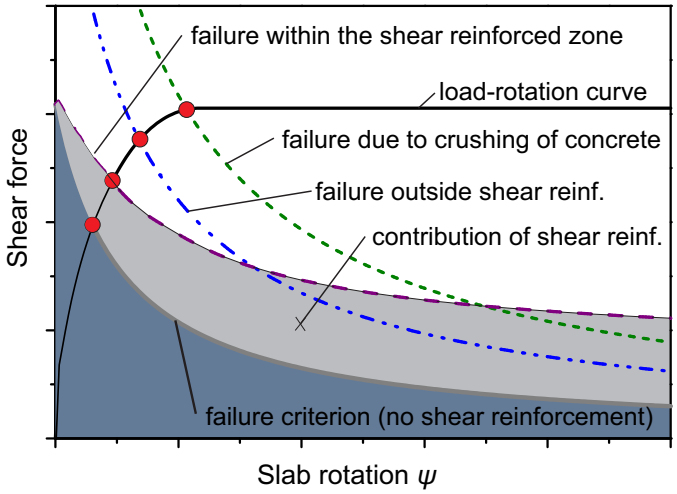


Figure 2.17: Application of CSCT in shear-reinforced flat slabs

distance $d/2$ from the outermost shear reinforcement units) and with a reduced effective depth to account for the geometry of the crack outside the shear-reinforced zone due to pullout of shear reinforcement as a block. Equations for the failure due to crushing of concrete near the column are also provided in Ruiz and Muttoni 2009.

In the following paragraphs, CSCT is described in its code–form, contained in MC2010 (*fib* 2013). First, the Levels of Approximation approach is described and then the design equations are provided.

#### 2.2.3.2 Level of Approximation approach

Model Code MC2010 (*fib* 2013) proposes several levels of approximation (LA) to deal with the higher degree of complexity in some design equations compared to the Eurocodes and the ACI codes and to meet the design requirements for different stages (for example, preliminary design, ordinary design, assessment and design of special structures, etc.). For punching shear design, four levels of approximation are proposed.

The complexity of calculations is increased from a lower level of approximation to a higher one. However, one can make use of a considerable amount of values calculated in lower levels as the calculations continue through higher levels. The basic formulas in different levels do not undergo significant changes in terms of complexity, but the estimation of parameters becomes more accurate and complex. The most important parameter is the slab rotation $\psi$. The calculations are supposed to result in a resistance getting closer to the actual one in each increased level.

Level I of Approximation (LA-I) can be used to obtain an initial estimate of the punching shear resistance. Calculations can be carried out with very little knowledge about the element being designed (for instance, it is not required to know the amount of flexural

reinforcement). The results are expected to be overly conservative. Such verifications may be considered suitable for structural elements in which punching resistance is not critical in design, as well as for the conceptual preliminary design phase.

Level II of Approximation (LA-II) offers a higher degree of accuracy in the calculation of the slab rotation, $\psi$, by considering the flexural capacity of the slab. In this level, one can determine whether punching shear reinforcement is necessary and whether such reinforcement is possible in the first place (i.e., whether re-dimensioning the slab is necessary). These verifications may be suitable for the preliminary design of structural elements in which punching shear may be critical.

A more precise design can be achieved in LA-III, in which slab rotations are calculated following an elastic analysis of the slab, where bending moments at support and the zero-moments line is obtained. This LA is deemed suitable for the detailed design of most structural elements.

MC2010 allows an even more accurate estimation of the slab rotation by means of a nonlinear structural analysis (LA-IV). This requires extensive knowledge about the actual behaviour of materials (concrete and steel) and significant computational power. Usage of LA-IV can be appropriate for important new structures or for assessing existing ones.

#### 2.2.3.3 Design for punching according to MC2010

The control section is assumed to be located at a distance $d/2$ from the loaded area and with a minimum perimeter (i.e. with rounded corners in case of rectangular loaded areas). A summary of the design steps for each LA is given below. In this paragraph, the structural element (for example, slab or footing) is assumed to lie on the Y-Z plane (thus the notations $y$ and $z$ below).

**Level I of Approximation** For LA-I, the rotations of the slab are assumed to be linearly proportional to the radius of the line of zero moments (line of contra-flexure), which in turn can be treated as being located at 22% of the span length (in each direction):

$$\psi_{y(z)} = 1.5 \frac{r_{s,y(z)} f_{yd}}{d E_s} \tag{2.14}$$

where $r_{s,y} = 0.22 L_y$; $r_{s,z} = 0.22 L_z$; $L_y$ and $L_z$ are the span lengths in $y$ and $z$-direction respectively; $f_{yd}$ is the design yield stress of tension reinforcement; $d$ is the average effective depth of the two main directions and $E_s$ is the modulus of elasticity of steel.

The governing rotation (the largest) of the two directions is then denoted simply by $\psi$, and calculations are carried on with it. Coefficients $k_\psi$ and $k_{dg}$ (accounting for the concrete aggregate size) are:

$$k_\psi = \frac{1}{1.5 + 0.9 \psi d k_{dg}} \leq 0.6 \tag{2.15}$$

and

$$k_{dg} = \frac{32}{16 + d_g} \geq 0.75 \tag{2.16}$$

where $d_g$ is the maximum aggregate diameter.

Shear strength of a slab without shear reinforcement is then calculated as:

$$V_{Rd,c} = k_\psi \frac{\sqrt{f_{ck}}}{\gamma_c} b_0 d_v \tag{2.17}$$

The value $d_v$ in Equation 2.17 is the shear-resisting effective depth of the slab, taking also into account the support penetration where relevant (see MC2010, *fib* 2013). The partial safety factor for concrete is $\gamma_c$. The effective control perimeter, $b_0$, is calculated as follows:

$$b_0 = k_e \left(2b_{c,y} + 2b_{c,y} + d_v \pi\right) \tag{2.18}$$

where $k_e$ is a coefficient accounting for eccentricity of loading, that for LA-I can be taken 0.9 for an internal column, 0.7 for an edge column and 0.65 for a corner column. Column cross section dimensions are $b_{c,y}$ and $b_{c,z}$ (assuming a rectangular column).

**Level II of Approximation** For LA-II, the design unbalanced moment $M_{Ed}$ needs to be known. The design shear force $V_{Ed}$ is equal to the column reaction force minus the applied load within the control perimeter. The control perimeter is calculated as described in LA-I. However, the coefficient $k_e$ that accounts for eccentricity of loading is:

$$k_e = \frac{1}{1 + e_u / b_u} \tag{2.19}$$

where $e_u$ is the eccentricity of the resultant shear force and

$$b_u = \sqrt{\frac{4A_c}{\pi}} \tag{2.20}$$

is the diameter of a circle with the same surface as the region inside the basic control perimeter.

The rotation $\psi$ is then calculated as:

$$\psi_{y(z)} = 1.5 \frac{r_{s,y(z)} f_{yd}}{d E_s} \left(\frac{m_{sd,y(z)}}{m_{Rd}}\right)^{1.5} \tag{2.21}$$

where $m_{Rd}$ is the design resisting flexural moment per unit width and $m_{sd,y(z)}$ is the acting bending moment per unit slab width in $y$-direction ($z$-direction). With the governing rotation $\psi$, the factor $k_\psi$ can be calculated using Equation 2.15. Shear strength of a flat slab without shear reinforcement is then calculated using Equation 2.17.

**Level III of Approximation** Equations for LA-III are similar to those of LA-II, with the exception of factor "1.2" replacing the factor "1.5" of Equation 2.21 in the calculation of rotations:

$$\psi_{y(z)} = 1.2 \frac{r_{s,y(z)} f_{yd}}{d E_s} \left( \frac{m_{sd,y(z)}}{m_{Rd}} \right)^{1.5} \tag{2.22}$$

This reduction is due to the elevated accuracy in the estimation of $m_{sd}$ and the radius $r_s$, which are now calculated via an elastic linear analysis. As in LA-II, the factor $k_\psi$ can be calculated using Equation 2.15. Shear strength of a flat slab without shear reinforcement is again calculated using Equation 2.17.

**Level IV of Approximation** In LA-IV, the slab rotation $\psi$ can be calculated using a suitable nonlinear model that takes into consideration cracking, nonlinear behaviour of materials and other possible relevant effects. The rest of the calculations is the same as in LA-III.

**Design of shear reinforcement** If shear reinforcement is required, the first step is to calculate the maximum punching shear force $V_{Rd,max}$ (Equation 2.23) that the slab can resist before crushing of concrete struts occurs. If the acting shear force is larger than $V_{Rd,max}$, then it is not possible to apply shear reinforcement, and other measures are required (for example, increase of the slab thickness or concrete strength).

$$V_{Rd,max} = k_{sys} V_{Rd,c} \leq \frac{\sqrt{f_{ck}}}{\gamma_c} b_0 d_v \tag{2.23}$$

The factor $k_{sys}$ takes into account the effectiveness of the selected type of shear reinforcement (refer to Section 2.1.2 for values). The resistance of the slab is considered to be the result of summation of the contributions of concrete and shear reinforcement:

$$V_{Rd} = V_{Rd,c} + V_{Rd,s} \tag{2.24}$$

with:

$$V_{Rd,s} = \sum A_{sw} k_e \sigma_{swd} \tag{2.25}$$

where "$\sum A_{sw}$ *is the sum of the cross-sectional area of all shear reinforcement suitably anchored, or developed, and intersected by the potential failure surface (conical surface with angle 45°) within the zone bounded by* $0.35 d_v$ *and* $d_v$ *from the edge of the supported area*" (*fib* 2013). For shear reinforcement at angle 90° in relation to the plan of the slab, the stresses in shear reinforcement can be calculated as:

$$\sigma_{swd} = \frac{E_s \psi}{6} \left( 1 + \frac{f_{bd}}{f_{ywd}} \frac{d}{\Phi_w} \right) \leq f_{ywd} \tag{2.26}$$

where $f_{bd}$ is the bond strength, $f_{ywd}$ is the design yield stress of shear reinforcement and $\Phi_w$ is the diameter of the shear reinforcement legs. The required area of shear reinforcement is then calculated based on Equation 2.24. Finally, the extent of shear reinforcement is governed by the stresses in the outer perimeter.

## 2.3 Review of experimental work on flat slab–column connections under horizontal cyclic loading

Since the second half of the twentieth century, a considerable research effort has been devoted to understanding the behaviour of flat slab–column connections subjected to reversed horizontal cyclic displacements. The experimental campaigns found in the literature on specimens without shear reinforcement and with various types of punching shear reinforcement are reviewed in this section.

### 2.3.1 Test setups for isolated specimens

The specimens reported in literature have been tested under a variety of boundary and loading conditions. The majority of tests are reported on isolated, interior slab–column assemblies consisting of a flat slab and a reinforced concrete or steel column. The dimensions and support conditions are such that, in the majority of cases, the negative bending moment region for gravity loading of the flat slab in the prototype building is modelled. In fewer cases, the region from mid-span to mid-span is represented by the specimen.

The main types of test setups found in literature are described in Figure 2.18. In the setup of Figure 2.18a, the column is pinned at the bottom end, the slab is simply supported at both ends and free to move horizontally while the horizontal load is applied at the top column end. The gravity load is applied either through a jack installed at the bottom end of the column, or directly on the slab specimen. In the first case, the slab is subjected to negative bending moments only. In case the gravity load is applied on the slab, positive bending moments are present. This setup was used in numerous experimental campaigns (Morrison et al. 1983; Zee and Moehle 1984; Pan and Moehle 1989; Wey and Durrani 1992; Robertson et al. 2002; Stark et al. 2005; Tan and Teng 2005; Robertson and Johnson 2006; Kang and Wallace 2008; Tian et al. 2008). A modified version of this test setup was used by Ali and Alexander 2002, in which the edges of the slab were restrained by means of frames attached to the slab in two directions (Figure 2.18e).

The test setup shown in Figure 2.18b was used especially in the early experimental campaigns (Hawkins et al. 1974; Hanna et al. 1975; Islam and Park 1976; Symonds et al. 1976). In this case, cyclic displacements are applied at the slab ends while both column ends are pinned. This way, the specimen represents the region from mid-span to mid-span considering a prototype building subjected to horizontal actions. A recent case of applying the cyclic load reversals at the slab edges, although with substantial differences,

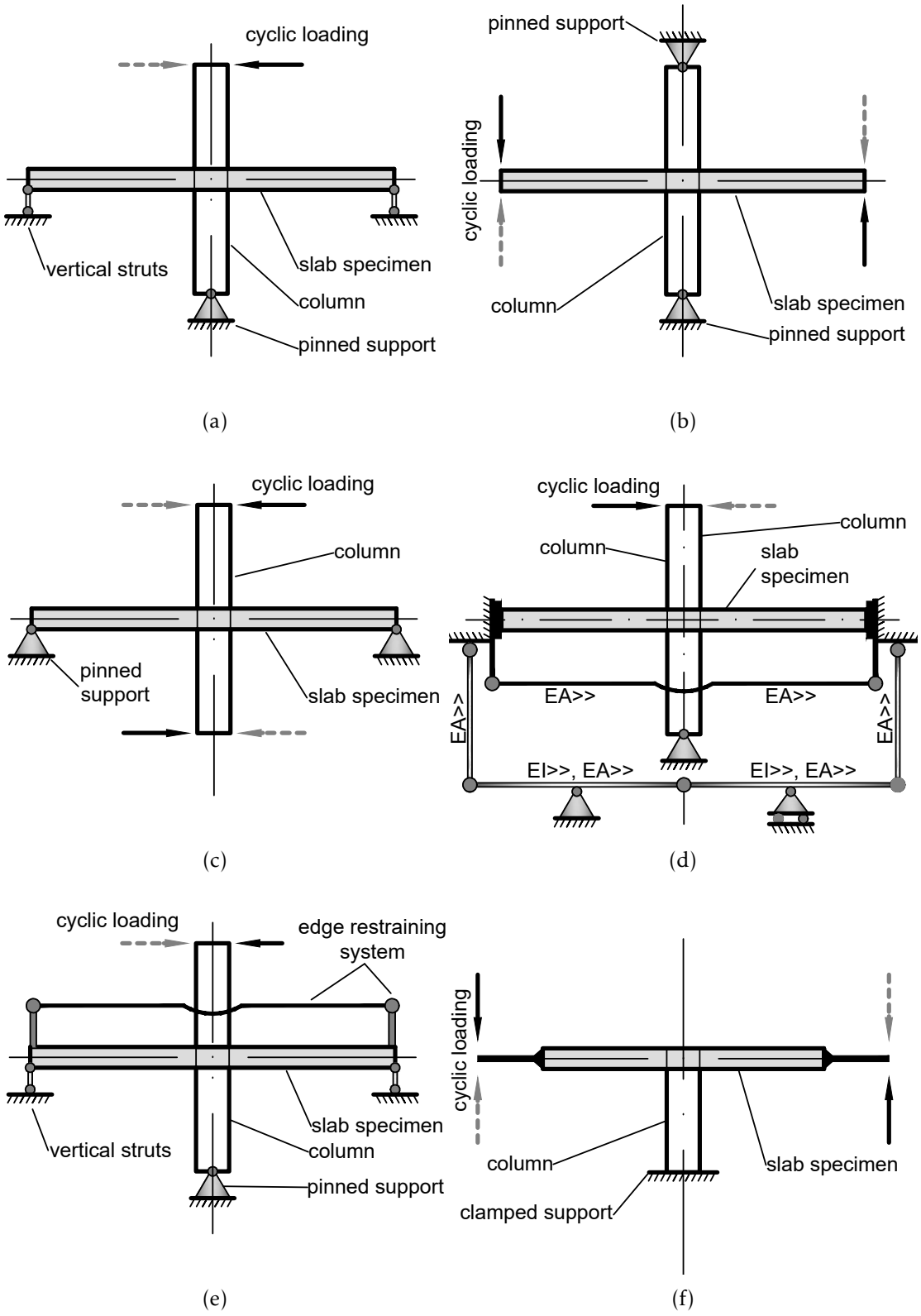


Figure 2.18: Test setups used in reversed cyclic loading tests

is reported in Drakatos et al. 2016, where the slab was square with dimensions approximately equal to the extent of negative bending moments under gravity loading. The lever arm of the force was extended via steel profiles rigidly connected to the slab edges in order to have the application of vertical cyclic loads at a distance equal to the midspan of the slab in the prototype building (Figure 2.18f). The column was fully restrained at the bottom end.

Figure 2.18c represents the setups for specimens of Cao 1993; Marzouk et al. 2001; Brown 2003 and Emam et al. 1997. Though similar in concept to the setup of Figure 2.18e, this setup has pinned supports at slab ends and horizontal loads applied at column ends. Specimens of Farhey et al. 1993 were tested under similar conditions but with application of cyclic loading only at one end of the column.

The test setup developed at the Department of Civil Engineering, Faculty of Science and Technology, Universidade NOVA de Lisboa (DEC/FCT/UNL) is schematically shown in Figure 2.18d. It is described in detail in Chapter 3, but it is given here for comparison with the test setups from other experimental campaigns. The slab specimens tested in this setup have both negative and positive bending moment regions. In the direction of loading, the length of the specimen is equal to the span length of the flat slab and the borders represent the mid-span region in the prototype building. The deflections and rotations at the borders are constrained to equal values via a system of struts and a see–saw–like mechanism attached to the reinforced concrete flat slab specimen. This test setup has been used in several experimental campaigns in the past, for specimens without shear reinforcement (Almeida et al. 2016), with high strength concrete (Inácio 2016), with steel fibre reinforced concrete (Gouveia et al. 2018) and stirrup shear reinforcement (Almeida et al. 2018). An earlier and less complex version of this test setup, enabling similar boundary conditions, was reported in Soares 1993, where two specimens without shear reinforcement were tested under monotonically increasing horizontal displacements and another specimen was tested under concentric monotonic vertical loads.

### 2.3.2 Arrangement of supports and gravity loading

The test setups used for reversed horizontal cyclic loading tests of flat slab specimens have also differences between them in terms of the number of supports, arrangement of supports, etc. For instance, specimens of Emam et al. 1997; Marzouk et al. 2001 are supported along the entire outer perimeter of the slab (Figure 2.19a), via either a line (continuous) support or multiple point supports distributed along the edges. Specimens of Hawkins et al. 1974; Islam and Park 1976; Symonds et al. 1976; Morrison et al. 1983; Zee and Moehle 1984; Wey and Durrani 1992; Cao 1993; Farhey et al. 1993; Robertson et al. 2002; Brown 2003; Stark et al. 2005; Robertson and Johnson 2006; Kang and Wallace 2008 have line supports or multiple point supports for the slab in one direction only (Figure 2.19b). In specimens of Pan and Moehle 1989; Pan and Moehle 1992; Tan

and Teng 2005 there are struts located at the corners of the slab (Figure 2.19c) and at midpoints of the edges. In specimens of Tian et al. 2008 the struts are arranged along the edges but corners are free to move (Figure 2.19d). A similar arrangement was adopted by Drakatos et al. 2016.

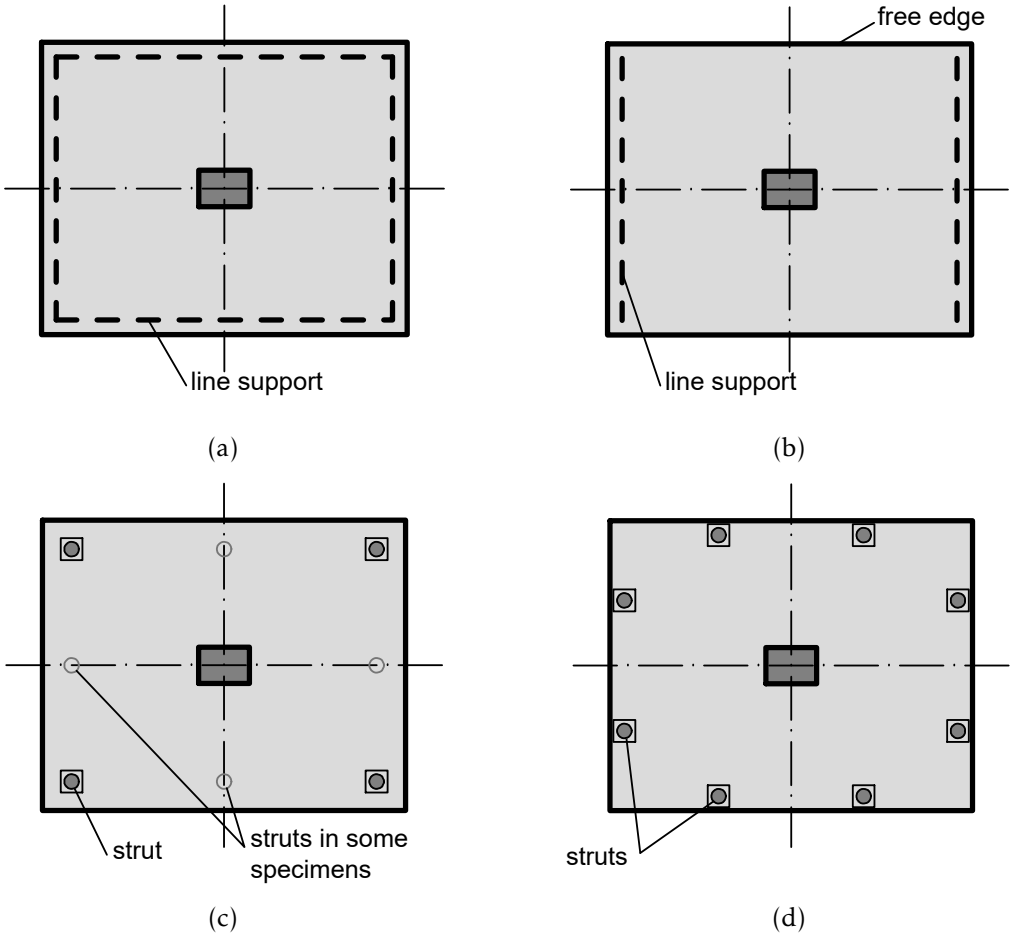


Figure 2.19: Different arrangements of supports

The gravity load is usually applied in one of the manners described below, although specifics exist from specimen to specimen:

- Force directly applied to the column (Figure 2.20a). In this case, an actuator is located at the support of the column and the shear force is directly transmitted to the slab–column connection. This approach is adopted, for example, in Cao 1993; Brown 2003.

- Gravity load distributed over the specimen as an uniformly distributed load (UDL) or several concentrated loads spread over the specimen (Figure 2.20b). UDL is applied for example in the specimens of Pan and Moehle 1992, where lead blocks were laid over the top surface of the slab specimen. Concentrated loads spread over

the specimen are adopted, for example, in the specimens tested at DEC/FCT/UNL (Almeida et al. 2016; Inácio 2016; Gouveia et al. 2018).

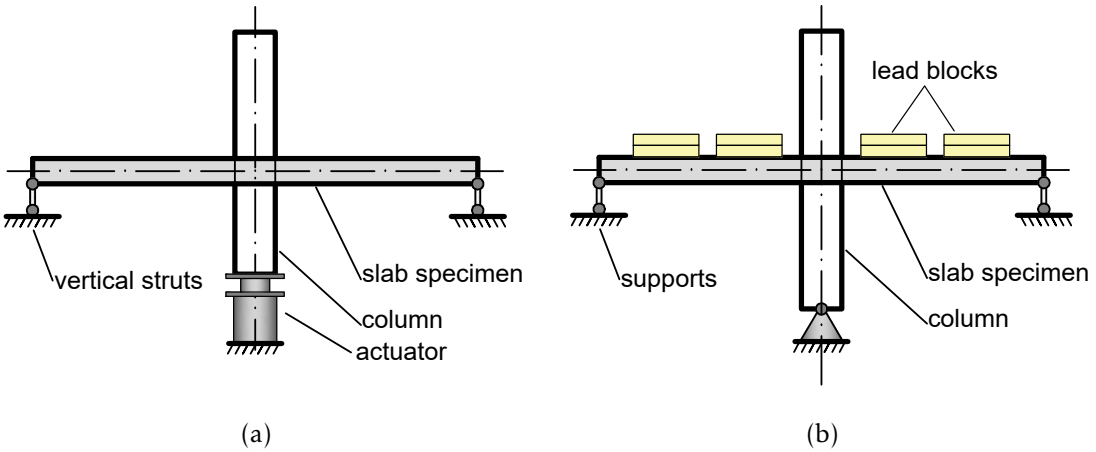


Figure 2.20: Examples of application of the gravity load

The gravity load is usually kept constant throughout the application of the drift cycles. Depending on the test setup, some variation of the gravity load throughout the test may occur. This is the case, for example, when vertical struts are used in the borders of the specimen and there is redistribution of forces in the slab due to cracking.

### 2.3.3 Application of horizontal drifts

The load protocol in the majority of experimental campaigns found in the literature consists in the application of unidirectional reversed cycles until failure of the specimen (Figure 2.21a). Cycle repetitions are often applied to observe the deterioration of the specimen under repeated loading, as shown in Figure 2.21b. Few specimens have been tested in two phases. For example, Robertson et al. 2002 and Robertson and Johnson 2006 tested specimens under reversed cycles, until a certain drift, followed by positive–only drifts (Figure 2.21c).

Tian et al. 2008 applied monotonically increasing gravity loads until failure of the specimen that had been previously subjected to reversed lateral drifts. In few cases (for example Morrison et al. 1983), the specimen was tested under cyclic loading until a relatively high drift and then the unbalanced moment was increased monotonically until failure of the specimen.

Bidirectional loading has been reported in few experimental campaigns (Pan and Moehle 1992; Tan and Teng 2005; Cheng et al. 2010; Matzke et al. 2015). To achieve cyclic loading in two directions, a loading sequence as described in Figure 2.22 is usually adopted.

The experiments show that bidirectional loading has a detrimental effect on the drift capacity of flat slab–column connections. Pan and Moehle 1992 compared the behaviour

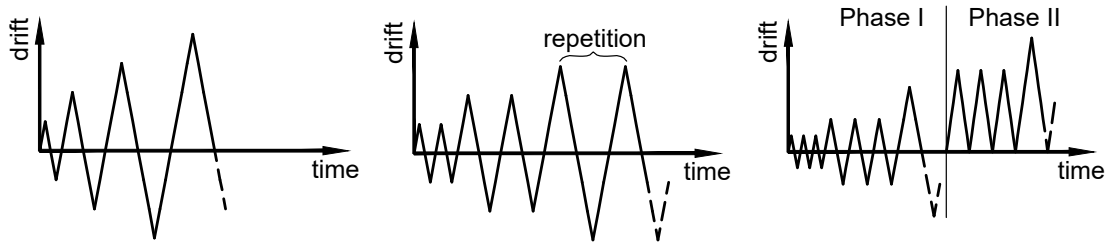


(a) Without cycle repetition (b) With cycle repetition (c) Robertson and Johnson 2006

Figure 2.21: Examples of horizontal loading protocols

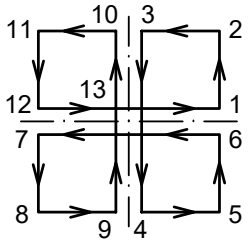


Figure 2.22: Typical loading sequence for bidirectional loading

of four specimens without shear reinforcement, under unidirectional and bidirectional loading, for two levels of the gravity load. They showed that, for both gravity load levels, the application of drifts in two direction reduced both strength and deformation capacity compared to similar specimens tested under drifts imposed only in one direction.

Tan and Teng 2005; Cheng et al. 2010; Matzke et al. 2015 reported bidirectional loading tests on specimens with shear reinforcement. In Cheng et al. 2010, specimens with studs and fibre-reinforced concrete were tested, but the effects of bidirectional loading cannot be studied because a reference specimen tested under unidirectional drifts is not provided. In Matzke et al. 2015, four slab specimens were presented. All of the specimens had studs shear reinforcement. Although the experimental campaign did not contain a specimen tested under unidirectional drifts for direct comparison, it was shown that the drift ratios obtained were considerably lower than those obtained in other experimental campaigns for comparable gravity loads (relative to the punching shear resistance) and shear studs reinforcement.

Tan and Teng 2005 reported five slab specimens, two of which were reinforced with headed shear studs, and three of which were tested under bidirectional loading following a path similar to the typical path shown in Figure 2.22. They demonstrated the detrimental effect of bidirectional loading by directly comparing similar specimens with and without shear reinforcement horizontally loaded in one and two directions respectively. It was shown however, that the drift capacity of shear-reinforced specimens was significantly enhanced, even when bidirectional loading is applied.

In summary, the limited number of experimental tests indicates that bidirectional loading reduces the drift capacity of specimens with and without shear reinforcement.

### 2.3.4 Database of isolated interior specimens

A database of isolated interior flat slab specimens found in the literature was compiled. The database contains specimens with and without shear reinforcement, tested under a combination of constant (or almost constant) gravity loads and horizontal cyclic displacements. The purpose of this section is to provide an overview of the previous tests and to study the range of properties (concrete strength, slab depth, reinforcement ratio, etc.) used in the previous experimental campaigns. A subset of the database, containing specimens that meet certain criteria, is used in Chapter 5 to study the ultimate drift capacity of flat slabs with and without shear studs.

#### 2.3.4.1 Specimens without shear reinforcement

A summary of the distinctions between specimens without shear reinforcement from the same experimental campaign is given in Table 2.1. The first column in this table contains the publication reference. The names of the specimens without shear reinforcement described in the publication are given in the second column. The last column summarizes the differences between the specimens.

Table 2.1: Experimental campaigns containing specimens without shear reinforcement

| Publication | Specimens | Distinction between specimens |
|---|---|---|
| Hawkins et al. 1974 | S1, S2, S3, S4 | Reinforcement ratio |
| Islam and Park 1976 | 3C | - |
| Symonds et al. 1976 | S6, S7 | Reinforcement ratio |
| Morrison et al. 1983 | S1, S2, S3, S4, S5 | Reinforcement ratio, gravity loading |
| Zee and Moehle 1984 | INT | - |
| Robertson 1990 | 8I | - |
| Pan and Moehle 1992 | AP1, AP2, AP3, AP4 | Gravity loading, unidirectional vs. bidirectional drifts |
| Farhey et al. 1993 | 1, 2, 3, 4 | Gravity loading; column dimensions, loading history |
| Wey and Durrani 1992 | SC0, SC6, SC4, SC2 | Drop panels |
| Cao 1993 | CD-1, CD-5, CD-8 | Gravity loading |

| | | |
|---|---|---|
| Emam et al. 1997 | H.H.H.C.0.5, H.H.H.C.1.0, N.H.H.C.0.5, N.H.H.C.1.0 | Type of concrete: high vs. normal strength, reinforcement ratio |
| Marzouk et al. 2001 | HSLW0.5C, HSLW1.0C, NSLW0.5C, NSLW1.0C, NSNW.05C, NSNW1.0C | Type of concrete: high vs. normal strength, lightweight vs. normal weight, reinforcement ratio |
| Ali and Alexander 2002 | SP-A, SP-B | Debonded longitudinal reinforcement in specimen SP-A |
| Robertson et al. 2002 | 1C | - |
| Brown 2003 | SJB-7 | - |
| Stark et al. 2005 | C-02, C-63 | Reinforcement |
| Tan and Teng 2005 | YL-L1, YL-H2, YL-L2 | Gravity loading, unidirectional vs. bidirectional loading |
| Robertson and Johnson 2006 | ND1C, ND4LL, ND5XL, ND6HR, ND7LR, ND8BU | Continuity of reinforcement, gravity load, reinforcement, presence of bent-up bars |
| Kang and Wallace 2008 | C0 | - |
| Tian et al. 2008 | L0.5, LG0.5, LG1.0 | Loading conditions and slab reinforcement |
| Park et al. 2012 | RC-A, RC-B | Concrete strength |
| Drakatos et al. 2016 | PD8, PD6, PD2, PD13, PD11 | Reinforcement ratio, gravity loading, loading history |
| Almeida et al. 2016 | C-30, C-40, C-50 | Gravity loading |

Detailed information about each specimen in contained in Appendix A. The main characteristics of the specimens in the database are analysed and processed, resulting in the histograms presented in Figure 2.23. These histograms show the range of characteristics such as concrete strength (Figure 2.23a), reinforcement yield stress (Figure 2.23b), slab thickness (Figure 2.23c), longitudinal reinforcement ratio (Figure 2.23d), specimen size (Figure 2.23e) and column size (Figure 2.23f).

Figure 2.23a shows clearly that the majority of tests were performed with concrete strength in the interval 30–40 MPa. The reinforcement yield stresses (Figure 2.23b) are

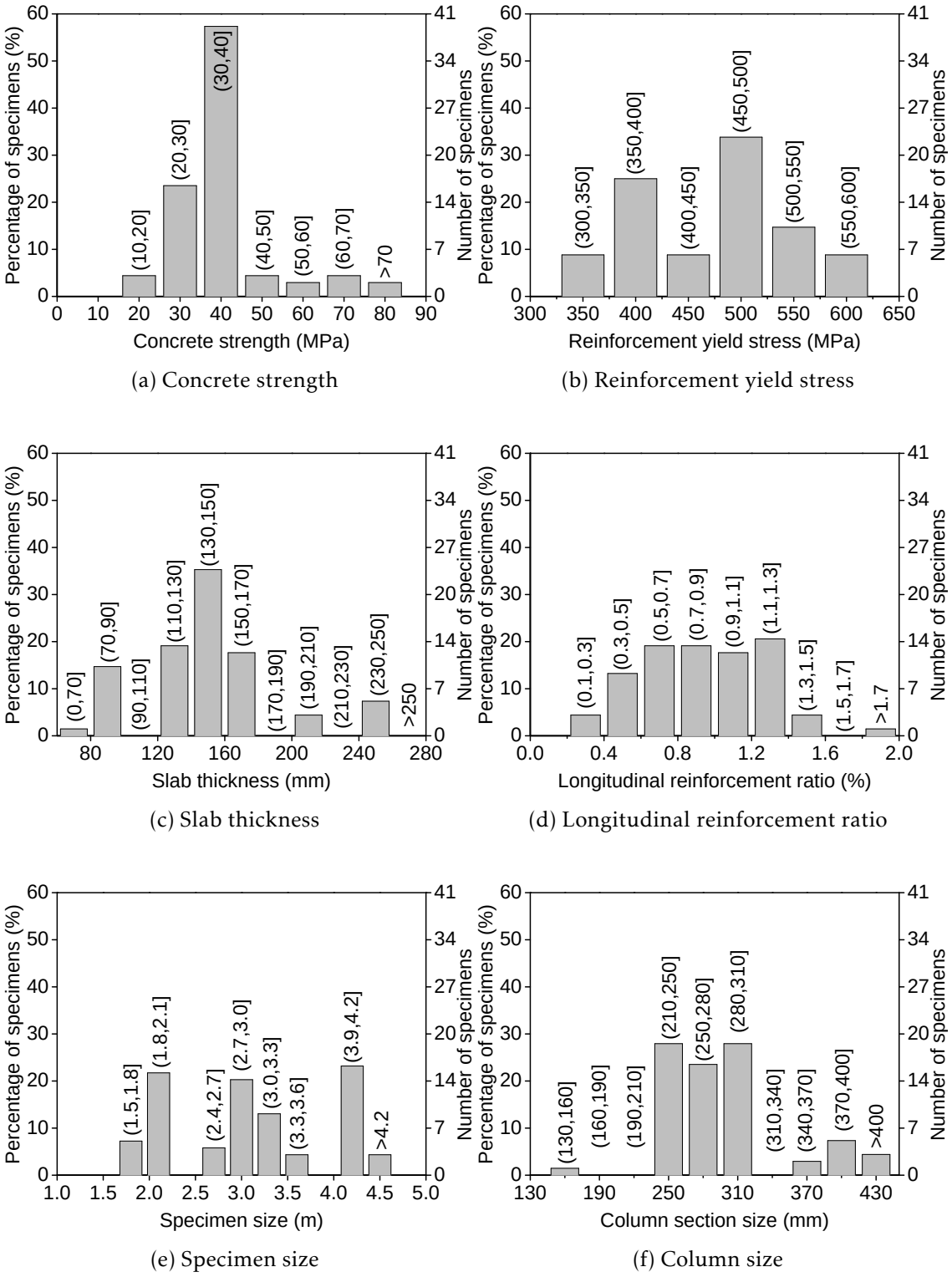


(a) Concrete strength

(b) Reinforcement yield stress

(c) Slab thickness

(d) Longitudinal reinforcement ratio

(e) Specimen size

(f) Column size

Figure 2.23: Range of characteristics of specimens without shear reinforcement

distributed over values commonly adopted in practice (350 MPa to 600 MPa). It is interesting to observe the range of slab thicknesses of the slab specimens. Figure 2.23c demonstrates that values are concentrated around the thickness 150 mm. Less than 12% of the specimens have a thickness larger than 200 mm. The longitudinal reinforcement ratios are distributed almost uniformly among the specimens in the range from 0.4% to 1.6% (Figure 2.23d). The specimen size and the column cross section dimensions also vary from one specimen to another (Figure 2.23e, Figure 2.23f). It should be noted, however, that the specimen size is not a direct measure of the span length of the flat slab being simulated, because it depends on the test setup configuration. Another observation is that the majority of the column cross sections in the database are square. Only the specimens of Farhey et al. 1993 and Tan and Teng 2005 had rectangular columns. In case of rectangular columns, the largest dimension is used to construct the histogram of Figure 2.23f.

#### 2.3.4.2 Specimens with shear reinforcement

Many of the specimens described in this paragraph have been part of test campaigns that include specimens without shear reinforcement. Therefore, main characteristics of the specimens are similar to those previously described in Section 2.3.4.1. A list of the specimens with shear reinforcement that were found in the literature is given in Table 2.2, where the publication is given in the first column, the specimen name given by the author is given in the second column and the distinctions between the specimens of the same author are briefly described in the third column.

Table 2.2: Experimental campaigns containing specimens with shear reinforcement

| Publication | Specimens | Distinction between specimens |
|---|---|---|
| Hawkins et al. 1974 | SS-1, SS-2 | Flexural reinforcement, diameter and extent of shear reinforcement |
| Hanna et al. 1975 | SS-3, SS-4, SS-5 | Flexural reinforcement, diameter and extent of shear reinforcement |
| Islam and Park 1976 | 6CS, 7CS, 8CS | Area of shear reinforcement per perimeter |
| Symonds et al. 1976 | SS-6, SS-7 | Flexural reinforcement, diameter and extent of shear reinforcement |
| Cao 1993 | CD-3, CD-4, CD-6, CD-7 | Area of shear reinforcement per perimeter, spacing of perimeters, gravity loading |
| Robertson et al. 2002 | 2CS, 3SL, 4HS | Type of shear reinforcement, area of shear reinforcement per perimeter |

| | | |
|---|---|---|
| Brown 2003 | SJB-1, SJB-2, SJB-3, SJB-4, SJB-5, SJB-8, SJB-9 | Flexural reinforcement, orientation of the column, number of perimeters of shear reinforcement |
| Tan and Teng 2005 | YL-H2V, YL-H1V | Unidirectional or bidirectional loading |
| Broms 2007 | 18c, 18d | Flexural reinforcement |
| Kang and Wallace 2008 | PS2.5, PS3.5, HS2.5 | Type of shear reinforcement, area of shear reinforcement per perimeter, spacing and extent of shear reinforcement |
| Cheng et al. 2010 | SB3 | - |
| Park et al. 2012 | LR-A1, LR-A2, SR-A, SB-A, ST-A, LR-B1, LR-B2, SR-B, SB-B, ST-B | Type of shear reinforcement and concrete strength |
| Matzke et al. 2015 | B1, B2, B3, B4 | Shear reinforcement layout |

Detailed information about each specimen in contained in Appendix A. Similarly to the case of specimens without shear reinforcement, the characteristics of the specimens are analysed and processed, resulting in the histograms of Figure 2.24. These histograms show the range of concrete strength (Figure 2.24a), reinforcement yield stress (Figure 2.24b), slab thickness (Figure 2.24c), longitudinal reinforcement ratio (Figure 2.24d) and column size (Figure 2.24f). The range of specimen sizes is similar to that in specimens without shear reinforcement (not shown in the figure).

From Figure 2.24 it is noticed that the concrete strengths are concentrated around 40 MPa and tests with low and high concrete strength are scarce. The distribution of steel yield stresses is comparable with that observed in specimens without shear reinforcement. Observing Figure 2.24c, it is noticed that there are no slabs thicker than 190 mm in tests under reversed horizontal cyclic loading in the compiled database. The range of longitudinal reinforcement ratios and column sizes is similar to that of specimens without shear reinforcement (Figure 2.23).

The type of shear reinforcement used is analysed in Figure 2.24e. The following abbreviations are used in the figure: ST - stirrups, SL - single leg stirrups, SSR - shear studs, THP - thin plate stirrups and LT - lattice type reinforcement. It is noticed that more than 50% of the available tests in the database are performed on specimens with studs as shear reinforcement. However, the differences between the specimens with studs are considerable (see Table 2.3). The differences consist mainly in the test setup used, the

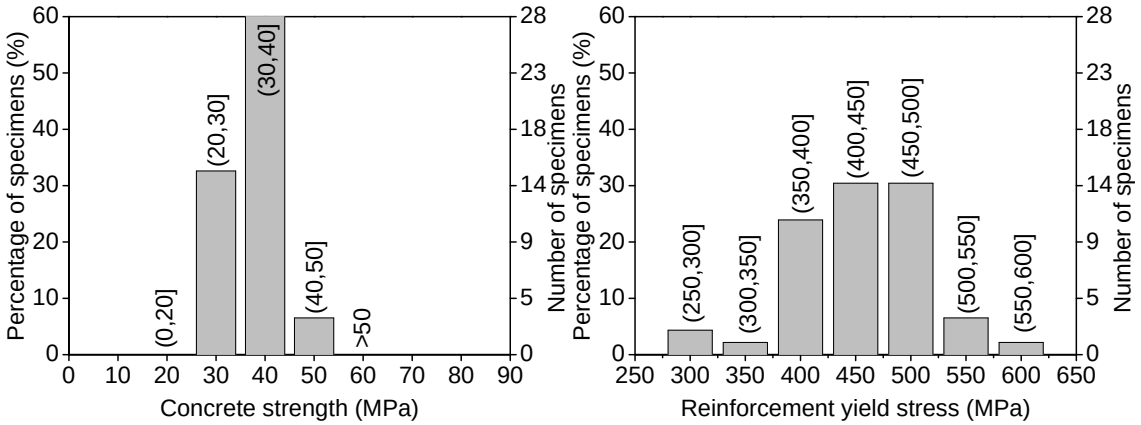


(a) Concrete strength




(b) Reinforcement yield stress

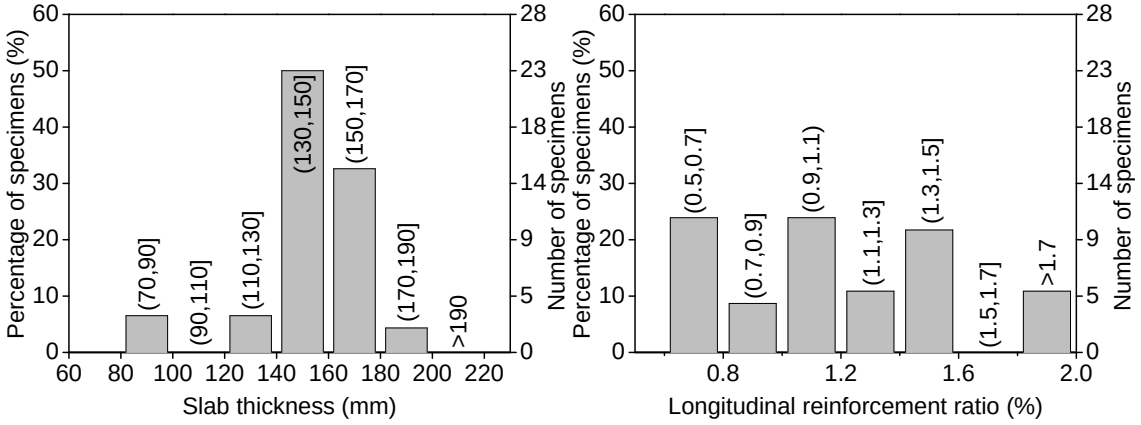


(c) Slab thickness




(d) Longitudinal reinforcement ratio

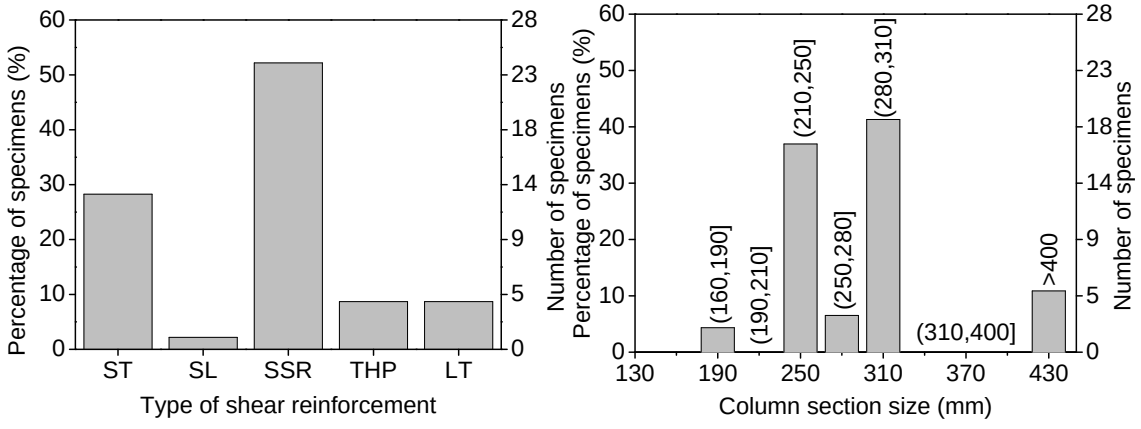


(e) Type of shear reinforcement




(f) Column size

Figure 2.24: Range of characteristics of specimens with shear reinforcement

diameter of studs, radial and tangential spacing, extent of shear reinforcement and the amount of shear reinforcement per perimeter ($A_{sw}$). Considering also the fact that the total number of specimens is relatively small, these differences between the specimens justify more experimental work.

Table 2.3: Shear reinforcement in specimens with studs under cyclic loading

| Publication | Specimen | $A_{sw}$ (mm$^2$) | Spacing (mm) | No. of rows | Specifics |
|---|---|---|---|---|---|
| Cao 1993 | CD-3 | 774 | 90 | 6 | |
| | CD-4 | 774 | 90 | 6 | |
| | CD-6 | var. | 45; 90 | 5 + 3 | |
| | CD-7 | 774 | 90 | 6 | |
| Robertson et al. 2002 | 4HS | 567 | 65 | 11 | |
| Brown 2003 | SJB-1 | 567 | 65 | 4 | |
| | SJB-2 | 567 | 65 | 4 | |
| | SJB-3 | 567 | 65 | 7 | |
| | SJB-4 | 567 | 65 | 7 | |
| | SJB-5 | 567 | 65 | 7 | |
| | SJB-8 | 567 | 65 | 7 | Column rotated 45° |
| | SJB-9 | 567 | 65 | 7 | Column rotated 45° |
| Tan and Teng 2005 | YL-H2V | 785 | 90 | 7 | Column aspect ratio 5 |
| | YL-H1V | 785 | 90 | 7 | Column aspect ratio 5 |
| Broms 2007 | 18c | 1232 | 75; 100 | 9 | |
| | 18d | 1232 | 75; 100 | 9 | |
| Kang and Wallace 2008 | HS2.5 | 142 | 63 | 4 | |
| Cheng et al. 2010 | SB3 | 570 | 89 | 6 | Bidirectional loading |
| Park et al. 2012 | SR-A | 628 | 52 | 7 | |
| | SR-B | 628 | 52 | 7 | |
| Matzke et al. 2015 | B1 | 855 | 60 | 9 | Bidirectional loading |
| | B2 | 855 | 89 | 8 | Bidirectional loading |
| | B3 | 855 | 60 | 11 | Bidirectional loading |
| | B4 | 1425 | 60; 86 | 11 | Bidirectional loading |

### 2.3.5 Corner and edge slab–column connections

The most common approach of experimentally studying the behaviour of exterior slab–column connections is through multi–panel specimens and full scale building tests, which

are discussed in Section 2.3.7. However, a brief review of tests on such connections is made in this paragraph.

Few reversed horizontal cyclic loading tests are found in the literature for edge slab–column connections, without shear reinforcement (Zee and Moehle 1984; Robertson 1990) and with shear reinforcement (Megally and Ghali 2000b). The test setups used in the aforementioned publications on isolated specimens are schematically shown in Figure 2.25. These test setups are basically adapted versions of the test setups commonly used for interior slab–column connections (Section 2.3.1). No cyclic loading test on isolated corner connections was found.

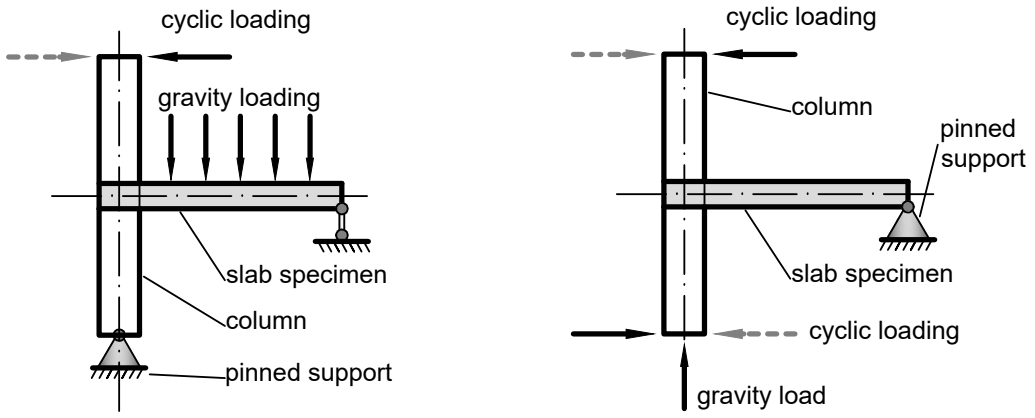


(a) Zee and Moehle 1984; Robertson 1990 (b) Megally and Ghali 2000b

Figure 2.25: Test setups used for isolated exterior connections

The experimental campaign of Megally and Ghali 2000b is of particular interest because it contains specimens with and without shear reinforcement. Megally and Ghali 2000b tested five isolated specimens, four of which were reinforced with shear studs. One specimen had no shear reinforcement and served as a reference. The shear-reinforced specimens differed by the spacing of the studs and the gravity load. It was shown that studs can be efficient in the enhancement of drift capacity of slab–column connections even in exterior configurations. Ultimate drifts as high as around 6.0% were reached by the specimens with studs. As also observed in the experimental campaigns on internal specimens, the gravity load played a detrimental role in the ultimate drift capacity of the connections.

### 2.3.6 Brief summary of the main conclusions from tests in literature on isolated specimens

Some important findings and conclusions drawn by the authors of the experimental works on specimens without shear reinforcement are:

- The increase of longitudinal reinforcement ratio results in an increase in the capacity of the connection to resist lateral drifts (Emam et al. 1997; Marzouk et al. 2001; Robertson and Johnson 2006; Tian et al. 2008);
- Cyclic loading induces damage that reduces connection stiffness more than monotonic loading (Tian et al. 2008; Almeida et al. 2016);
- According to Robertson and Johnson 2006, continuity of bottom reinforcement is not relevant for the pre-punching behaviour of the flat slabs. However, it is very important to have continuous bottom reinforcement to prevent progressive collapse after punching shear failure (Pan and Moehle 1992; Robertson and Johnson 2006);
- The increase of gravity loading reduces the connection drift capacity under lateral cyclic loading (Pan and Moehle 1989; Pan and Moehle 1992; Robertson and Johnson 2006);
- According to Marzouk et al. 2001, the usage of high strength lightweight concrete results in higher energy dissipation during cyclic loading;
- Bidirectional lateral loading reduces the slab–column connection's deformation capacity (Pan and Moehle 1989; Pan and Moehle 1992).

Regarding specimens with shear reinforcement:

- Energy dissipation and ductility of specimens with shear reinforcement is generally higher than that of specimens unreinforced for shear. Connections with shear reinforcement exhibit a more adequate seismic behaviour (Hawkins et al. 1974; Islam and Park 1976; Symonds et al. 1976; Robertson et al. 2002; Kang and Wallace 2008; Park et al. 2012);
- Amount, extend and spacing of shear reinforcement are critical factors in the shear resistance of a slab (Hawkins et al. 1974; Hanna et al. 1975);
- Headed studs used as shear reinforcement are especially effective in increasing both strength and ductility of a slab–column connection (Cao 1993; Robertson et al. 2002; Brown 2003; Tan and Teng 2005; Kang and Wallace 2008);
- As in specimens without shear reinforcement, biaxial loading has a detrimental effect in strength and ductility of the connection (Tan and Teng 2005).

### 2.3.7 Multi–panel specimens and large-scale building tests

#### 2.3.7.1 Continuous or multi–panel slab specimens

Some examples of cyclic loading tests based on continuous or multi-panel slabs can also be found in the literature, although they are scarcer. Robertson 1990 studied the adequacy

of procedures of that time and code specifications and recommendations for flat slab–column connections for seismic regions. Nine specimens were tested varying the gravity shear ratio, slab shear reinforcement, slab overhang and the presence or not of a stiff edge beam. The multi–panel specimens of Robertson 1990 were sub-assemblies as the one shown in Figure 2.26a. Robertson and Durrani 1993 and Durrani et al. 1995 tested two–bay slabs with geometry and test setup similar to Robertson 1990. Specimens without shear reinforcement were tested and it was shown that interior connections are more likely to fail compared to exterior connections under horizontal actions.

Rha et al. 2014 tested 5 two by two bay specimens without shear reinforcement (Figure 2.26b) with varying longitudinal reinforcement ratios. Two of the specimens were tested under gravity loads only, whereas two others were tested under a combination of gravity loads and monotonically increasing horizontal displacements. Another specimen was tested under reversed horizontal cyclic loading and constant gravity loads. Progressive punching failures occurred under horizontal loads, but redistribution of loads was observed, and the structure was able to sustain the imposed actions until a global near collapse state (Rha et al. 2014). Comparing the results of monotonic horizontal loading tests to the reversed horizontal cyclic test, the authors observed a strength and stiffness reduction in case of cyclic loading. The first punching failure occurred in an interior slab–column connection, supporting the previously discussed observation made in Durrani et al. 1995.

Hwang and Moehle 2000b tested a larger specimen, with nine panels, under vertical and horizontal cyclic loading to assess the flat slab behaviour and bending moment distribution (Figure 2.26c). The specimen had no shear reinforcement. The configuration and size of the specimen offers the opportunity to study multiple slab–column connections under different conditions: interior, edge and corner locations and varying gravity shear forces in the connection. Rectangular and square column cross sections were used. Interior slab–column connections failed first, and punching failures progressed almost immediately to several connections (Hwang and Moehle 2000b). Interestingly, punching shear failures were not detected in three of the corner connections. A specimen with similar geometry but under monotonic horizontal loading was reported earlier in Lúcio 1991. The 105 mm thick slab was a waffle slab supported on square columns regularly spaced at nearly 1.8 m in both directions. In the specimen of Lúcio 1991, the main focus was on the vertical and lateral stiffness of the system and response was dominated by flexure, although punching failures were detected in two interior connections and an edge connection.

The geometrical characteristics of the multi–panel and continuous slab specimens under horizontal cyclic loading are summarized in Table 2.4.

Kang and Wallace 2005 tested two reinforced concrete frames under uniaxial shaking (on a shaketable). The frames had two storeys and they were on a scale approximately

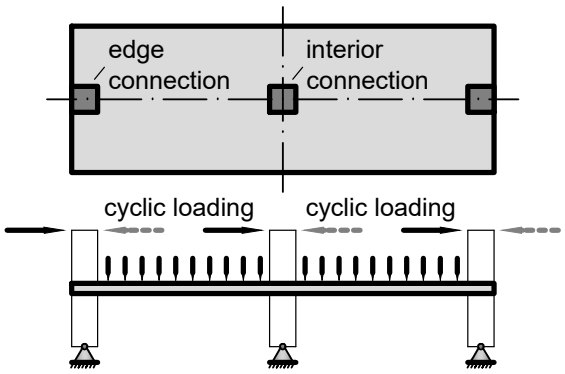


(a) Robertson 1990; Robertson and Durrani 1993; Durrani et al. 1995

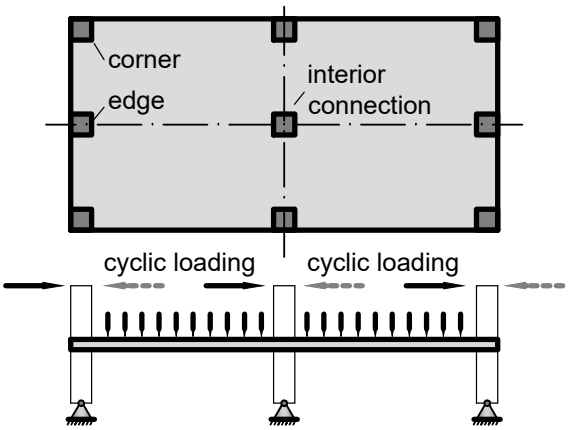


(b) Rha et al. 2014

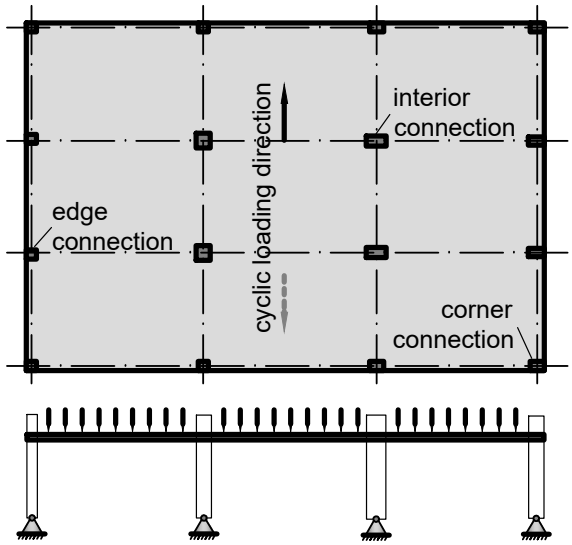


(c) Hwang and Moehle 2000b

Figure 2.26: Geometry of continuous and multi–panel slab specimens (not to scale)

Table 2.4: Main geometrical properties of multi–panel slabs under cyclic loading

| Publication | Test ID | Effective depth (mm) | Span lengths (mm) |
|---|---|---|---|
| Robertson 1990 | 1, 2C, 3SE, 5SO, 6LL, 7L | 89.8 | 2895.6 |
| Robertson and Durrani 1993 | A, B, C | 96.8 | 2895.6 |
| Durrani et al. 1995 | DNY_1, DNY_2, DNY_3, DNY_4 | 96.8 | 2895.6 |
| Hwang and Moehle 2000b | - | 70.0 | 2743.2 × 1828.8 |
| Rha et al. 2014 | LC-S2 | 70.0 | 2750.0 × 1650.0 |

equal to 1/3. One of the frames was post-tensioned. Slab–column connections in both frames were reinforced with shear studs. The frame had two spans in the direction of shaking and one span with cantilevers on both sides in the perpendicular direction (Figure 2.27). The cantilevers were introduced to simulate interior connection conditions.

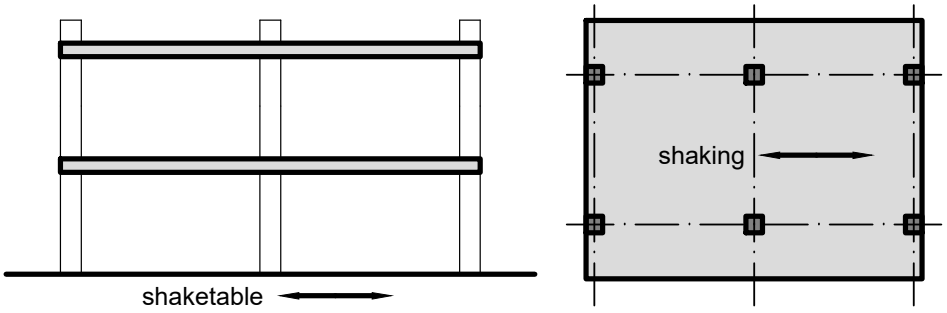


Figure 2.27: Shaketable test presented in Kang and Wallace 2005 (not to scale)

Comparing the two frames, damage was more pronounced in the frame without post-tensioning. Damage at punching failure was very limited compared to tests under quasi-static conditions. The connection in which punching failure occurred first is not reported.

For the purposes of this dissertation, it is important to emphasise two observations from the aforementioned experimental campaigns:

- When integrity reinforcement is used, redistribution of forces occurs after a punching shear failure in continuous flat slabs, and the structure can continue to sustain the gravity loads.
- For the described tests, interior slab–column connections were more prone to punching shear failure under horizontal actions than the exterior connections. This is likely due to the higher gravity shear force and unbalanced moment, that makes these connections critical even though the perimeter that resists punching shear is smaller in exterior connections.

#### 2.3.7.2 Large-scale tests

Large-scale tests of flat slab buildings are scarce. In this section, the tests reported in Zaharia et al. 2006 and Fick et al. 2017 are discussed (Figure 2.28). These were performed under pseudo-dynamic and reversed cyclic loading conditions respectively. To the author's knowledge, no shaketable test (purely dynamic) has been performed on flat slab buildings with a scale larger than that of Kang and Wallace 2005 (see Section 2.3.7.1).

Zaharia et al. 2006 reported two tests performed on a three storey waffle flat slab building at the European Laboratory for Structural Assessment (ELSA). Their aim was

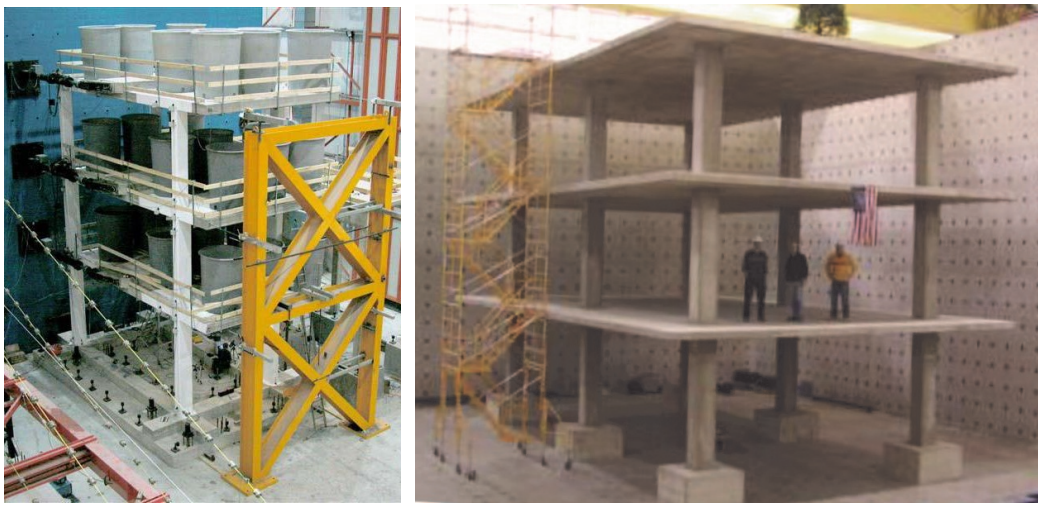

(a) Zaharia et al. 2006 (b) Fick et al. 2017

Figure 2.28: Photographs from large-scale experimental campaigns

to study the general behaviour of flat slab structures under seismic actions, with focus on slab–column connections (edge, corner and interior), as well as column orientation and cross section dimensions. The test specimen was a three storey single bay building with slab cantilevers of 1.5 m and 1.25 m over two perpendicular edges. The outer planar dimensions were 8.5 m by 5.2 m. Four rectangular columns of cross section 0.3 × 0.5 m were built for the two lower storeys and a reduction of the cross section to 0.3 × 0.4 m was applied to the top storey. The slab thickness was 0.295 m for the entire structure. The waffle slab was reinforced with 8 mm diameter steel stirrups. Concentrated longitudinal reinforcement was used for the "beam regions" connecting the columns.

Lateral loading was applied at storey height via two actuators in each level fixed at the reaction wall of the laboratory with increasing levels of intensity. A photograph of the specimen and the test setup is shown in Figure 2.28a. The test showed that slab–column connections and column bases suffered the most damage. Interior connections (which were all shear-reinforced) failed mainly in flexure, but shear cracks were present.

Fick et al. 2017 reported a three-storey flat slab building tested under reversed lateral loads. The specimen was a three storey two by one bay building with approximately 1.5 m long cantilevers along all edges. The outer planar dimensions were 15.25 m by 9.15 m. Interaxial distance between adjacent columns was 6.1 m. The columns had constant square cross section 457.2 mm × 457.2 mm. The slab was solid (without voids) with a thickness of 180 mm for the entire structure. The effective depth of the slab was 152 mm. Reinforcement of the slab was non-uniform, with concentration of reinforcement at column strips. The slab was not shear-reinforced. A photograph of the specimen and the test setup is shown in Figure 2.28b.

Gravity loads were applied via water containers in each floor. Lateral loading was

applied via two actuators in each storey level fixed at the reaction wall of the laboratory. Throughout the test, a linear variation of lateral loads in height was assumed, with zero lateral loads at foundation level. Loading was unidirectional, in the direction with two bays.

The first punching failure occurred at nearly 3.3% storey drift ratio at a connection one level below the roof level, in an interior connection (at the middle column in the direction with two spans). Although there were only six columns, the edge connections were treated as interior connections due to the presence of slab cantilevers.

## 2.4 Requirements for seismic design of flat slabs

### 2.4.1 Punching shear design

Eurocode 8 (CEN 2004d) does not fully cover concrete buildings in which the primary lateral force resisting system contains flat slabs. Usually, shear walls or moment resisting frames provide lateral resistance in buildings with flat slabs, thus turning the flat slabs into "secondary seismic elements". Nonetheless, the flat slabs must be able to carry the gravity load under seismic displacements induced by the primary seismic elements. However, EC8 does not provide further guidance regarding the fulfilment of this requirement. The current version of the *fib* Model Code, MC2010 (*fib* 2013), also lacks specific guidance for the design of flat slabs in seismic situation.

The design equations for punching shear in Eurocode 2 (CEN 2004c) require the knowledge of the shear stress acting on the control perimeter, i.e., they are "force–based". Under a strong earthquake, the primary lateral load resisting system is expected to behave inelastically. The determination of stresses in the slab–column connection in these circumstances is difficult and associated with uncertainties. Besides force–based formulations, North American code ACI 318-14 (ACI 2014) and standard CSA A23.3-04 (CSA 2004) suggest a workaround for this problem by giving "deformation–based" criteria for the design of flat slabs under horizontal actions. Both documents acknowledge that, based on experimental observations on slab–column connections under lateral loading, the Gravity Shear Ratio (GSR) – defined as the ratio between the applied gravity load $V_g$ and the concentric punching shear resistance $V_0$ – is correlated with the ultimate drift. The criteria of the North American codes are depicted in Figure 2.29, the lines in which determine two regions: one where shear reinforcement is required (above the graph) and another where shear reinforcement is not required (below the graph).

The criterion of ACI 318-14 (ACI 2014), after the work of Moehle 1996; Megally and Ghali 2000a, can be expressed as:

$$d_r = 0.035 - \frac{GSR}{20} \tag{2.27}$$

where GSR and $d_r$ are expressed as decimal numbers, with a lower bound of 0.005 for

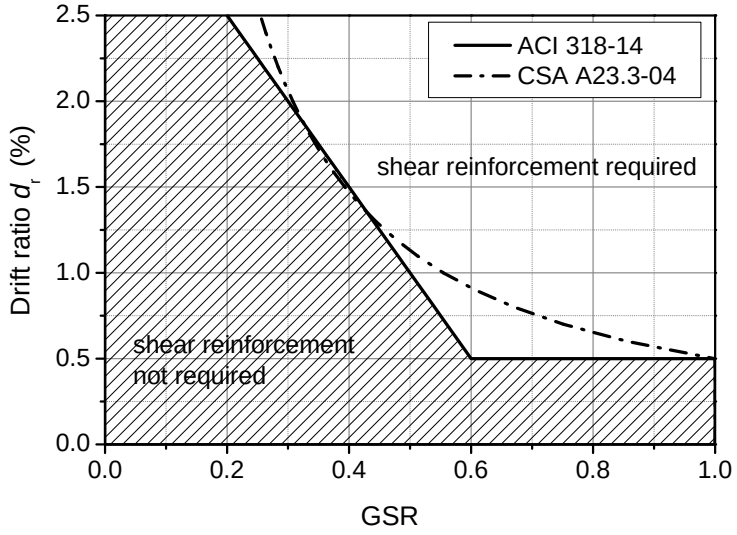


Figure 2.29: Deformation based criteria for the design of flat slabs under seismic actions

$d_r$. Based on CSA A23.3-04 (CSA 2004) (see also Dilger et al. 2005 for a summary of provisions):

$$GSR = \left(\frac{0.005}{d_r}\right)^{0.85} \leq 1 \tag{2.28}$$

with $d_r \leq 0.025$.

This format is very suitable for the design of flat slabs as secondary seismic elements, because it does not require any knowledge about the earthquake induced stresses. Given appropriate choices are made for the stiffness of the elements, this design format can also be adopted for frames that are part of the primary seismic load resisting system (Dilger et al. 2005).

Similarly, Hueste and Wight 1999 proposed a relationship between GSR and the ultimate drift ratio based on the available experimental results at that time. The relationship proposed by Hueste and Wight 1999 yields slightly larger drifts compared to the ACI 318-14 (ACI 2014) criterion. Based on the same concept, Hueste et al. 2007 proposed Performance-Based Seismic Design (PBSD) recommendations for slab–column connections. Ramos et al. 2017 analysed the main differences between three major design codes and proposed similar criteria applicable for GSR calculated in accordance with EC2 (CEN 2004c) and MC2010 (*fib* 2013).

### 2.4.2 Minimum shear reinforcement

Once shear reinforcement is required, EC2 (CEN 2004c), ACI 318-14 (ACI 2014) and MC2010 (*fib* 2013) require the provision of a minimum area of shear reinforcement.

A minimum area of reinforcement is imposed indirectly in EC2 (CEN 2004c) because

the shear strength provided by concrete ($v_{Rd,c}$) is reduced to 75% in the formula for the strength when shear reinforcement is provided (Equation 2.2). When the shear stress caused by the acting forces and moments reaches the shear resistance of the concrete section, i.e. for $v_{Ed} = v_{Rd,c}$:

$$A_{sw,min,EC2} = 0.25 v_{Rd,c} \frac{s_r u_1}{1.5 f_{ywd,eff}} \tag{2.29}$$

The minimum area of a single leg of shear reinforcement $A_{sw,min,1leg}$ is governed by the following equation in EC2:

$$A_{sw,min,1leg} \frac{1.5 \sin\alpha + \cos\alpha}{s_r s_t} \geq 0.08 \frac{\sqrt{f_{ck}}}{f_{yk}} \tag{2.30}$$

where $s_r$ and $s_t$ are the spacings of shear reinforcement legs in radial and tangential direction respectively.

In MC2010 (*fib* 2013), the minimum area of shear reinforcement is:

$$A_{sw,min,MC} = \frac{0.5 V_d}{k_e f_{ywd}} \tag{2.31}$$

According to MC2010 (*fib* 2013), the purpose of providing this minimum amount of shear reinforcement is to ensure sufficient deformation capacity.

None of the above-mentioned codes requires a minimum area of shear reinforcement unless it is shown by calculations that the punching shear strength of the structural element is insufficient.

Rizk and Marzouk 2013 proposed minimum shear reinforcement for thick plates and flat slabs. Based on compressive field theory, they recommend a minimum shear reinforcement ratio $\rho_{z,min}$, as follows:

$$\rho_{z,min} = 1.44 \frac{f_{ct}}{f_y} \sin^2\theta \left(\frac{l_{ch}}{h}\right)^{0.33} \tag{2.32}$$

where $f_{ct}$ is the tensile strength of concrete, $f_y$ is the yield stress of the reinforcement, $\theta$ is the angle of the compression field in relation to the plan of the slab, $h$ is the thickness of the slab and $l_{ch}$ is the characteristic length. The latter is a material property that relates the modulus of elasticity of concrete $E_c$, the fracture energy, $G_f$ and the tensile strength, $f_{ct}$, as follows (Rizk and Marzouk 2013):

$$l_{ch} = \frac{E_c G_f}{f_{ct}^2} \tag{2.33}$$

To enforce failures inside the shear-reinforced zone, Rizk and Marzouk 2013 propose limiting the "shear reinforcement index", $k$, defined as the ratio between the force in the shear reinforcement intersected by the punching failure cone and the concentric punching

shear resistance without shear reinforcement. They observed that all specimens in their database failed inside the shear-reinforced zone for $k < 0.55$. Earlier, Vaz et al. 2009 had proposed a shear reinforcement index between 0.5 and 0.7, based on a series of concentric monotonic tests on flat slab specimens reinforced with shear studs.

The method of Rizk and Marzouk 2013 is formulated considering only gravity loads and is checked only against concentric monotonic tests. Therefore, it is not validated for the seismic design of flat slabs. On the other hand, research has shown that even the introduction of a relatively small amount of shear reinforcement can make a significant improvement of the drift capacity of slab–column connections. For example, two flat slab specimens with shear reinforcement in the form of stirrups with a quantity approximately equal to the minimum required by MC2010 (*fib* 2013, Equation 2.31) were tested at DEC/FCT/UNL (Almeida et al. 2018) and ultimate drift ratios of 2.5% to 3.0% were attained. The difference between the two specimens was the extent of shear reinforcement (3 and 5 perimeters around the column). A similar specimen without shear reinforcement (specimen C-50 in Almeida et al. 2016) failed for only 1.0% drift, which demonstrates that the drift capacity enhancement was significant even though the amount of shear reinforcement was low.

In guide ACI 421.2R (ACI 1999), which is a guide to seismic design of flat slabs, a minimum shear reinforcement is required for ductility reasons, such that the following inequality holds true:

$$v_s = \frac{A_{sw} f_{yw}}{b_0 s} \geq \frac{\sqrt{f_c}}{4} \tag{2.34}$$

where $A_{sw}$ is the area of shear reinforcement in one perimeter, $s$ is the spacing of perimeters of shear reinforcement, $b_0$ is the control perimeter in accordance with the ACI code (located at a distance $d/2$ from the face of the column) and $f_{yw}$ is the yield stress of shear reinforcement. The minimum reinforcement provided by Equation 2.34 is to be placed when shear reinforcement is required by calculation or when GSR exceeds the value for which the drift capacity equals the design drift.

### 2.4.3 Layout of shear reinforcement

The layout and extent of shear reinforcement are important aspects to be considered in the design of flat slabs. EC2 requires a reduction of the outermost perimeter in which shear stresses should be checked to determine the extent of shear reinforcement, as described in Figure 2.30. The perimeter reduction applies when the distance between the vertical legs of the shear reinforcement in the outer perimeter is larger than 2 times the effective depth $d$ of the slab. The value $k$ in the figure is a Nationally Determined Parameter (NDP) in the Eurocodes, with a recommended value of 1.5.

In MC2010 (*fib* 2013), a reduction of the outer perimeter is required when the distance between vertical legs of the punching shear reinforcement exceeds $3d_v$ (three times the shear-resisting effective depth). The ACI code (ACI 2014) does not require such a reduction of the perimeter for cruciform layout of shear reinforcement and this layout is popular because it is practical.

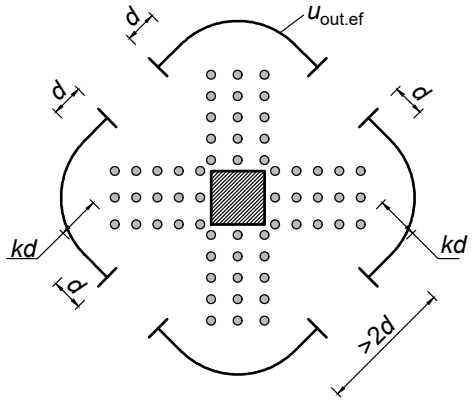


Figure 2.30: The outermost perimeter according to EC2

The influence of the layout was recently studied by Dam and Wight 2016; Dam et al. 2017, which tested specimens with shear studs under concentric loading. They showed that in cases where slab flexural yielding is expected to occur prior to punching, the radial layout of studs can result in a higher punching shear strength. Furthermore, they showed that depending on the longitudinal reinforcement ratio, a radial layout can lead to an enhanced ductility of the connection, since it favours the formation of flexural mechanisms. As pointed out in Dam and Wight 2016, there is a small number of specimens tested with the radial layout, and the available results are divided into a) radial and cruciform layouts being equally effective and b) the radial layout exhibiting superior behaviour.

### 2.4.4 Extent of shear reinforcement

The EC2 provision described in Figure 2.30 imposes a practical limitation on the extent of shear reinforcement. Once the outer perimeter reaches its maximum length, adding more layers of shear reinforcement results in no increase of the punching shear strength outside the shear-reinforced zone (when calculated in accordance with EC2, CEN 2004c). The experimental campaign presented in Vollum et al. 2010 indicates that such an approach can be over–conservative for concentric loading. Furthermore, there is some experimental evidence that the drift capacity of slabs with studs is increased with the extent of shear reinforcement. For instance, specimens SJB-2 and SJB-4 in Brown 2003 were similar, but the studs in SJB-4 were extended more than in SJB-2 (Figure 2.31). In both specimens, the outer perimeter determined in accordance with EC2 (CEN 2004c) was the same, but the drift capacity of specimen SJB-4 resulted higher (Figure 2.32).

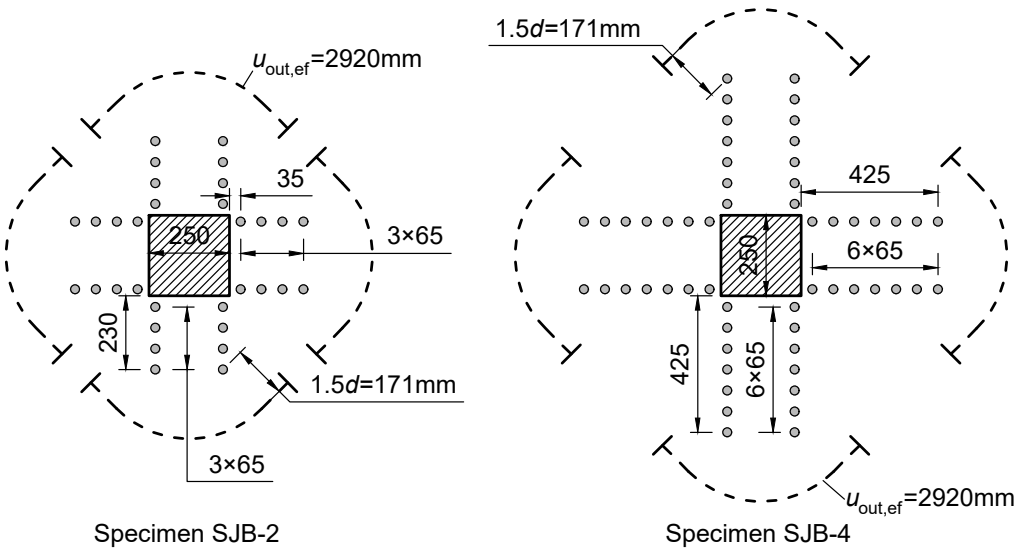


Figure 2.31: The outermost perimeter of specimens SJB-2 and SJB-4 in Brown 2003

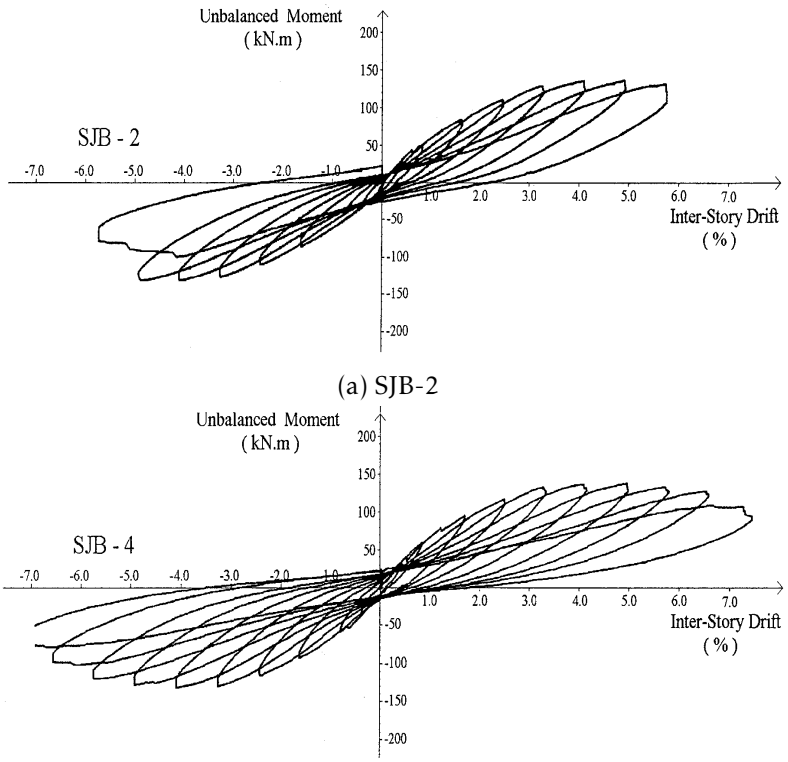


Figure 2.32: Unbalanced moment–drift relationships for specimens SJB-2 and SJB-4 (image from Brown 2003)

In ACI 318 (ACI 2014), when shear reinforcement is required, it is recommended to extend at least $4h$ from the face of the column. In guide ACI 421-2 (ACI 2010), which deals with the seismic design of punching shear reinforcement in flat slabs, the extent of shear reinforcement is required to surpass $3.5d$. For flat slabs, no specific seismic detailing requirements are provided in the current version of the European code for seismic design, EC8 (CEN 2004d).

### 2.4.5 Robustness

Flat slabs are prone to progressive collapse if necessary measures are not taken. The occurrence of a punching failure in a slab–column connection can lead to the punching failure of adjacent connections or of connections in lower storeys, due to the increased gravity load and the associated dynamic effects that occur when a flat slab panel falls when left without sufficient supports. Such failures have proven catastrophic in several cases in the past, for both seismic situations (Mitchell et al. 1995) and non–seismic situations (Wood 1997; Park 2012). The robustness requirement is a principle commonly adopted by modern design codes. The Eurocodes (CEN 2002), for example, require the buildings to be designed so that they are not damaged disproportionally to the corresponding cause. Progressive collapse clearly violates the requirement for robustness.

At column supports, flat slabs generally do not require bottom reinforcement for flexure strength. However, bottom reinforcement has been shown to be an appropriate measure for preventing progressive collapse (eventually, progressive collapse in a structure) in case of a punching shear failure (Pan and Moehle 1992; Robertson and Durrani 1993; Durrani et al. 1995; Hwang and Moehle 2000b; Robertson and Johnson 2006; Rha et al. 2014).

The major design codes require bottom reinforcement passing through the column, commonly referred to as *integrity reinforcement*. EC2 (CEN 2004c) and ACI 318-14 (ACI 2014), for instance, require that at least two bars in each direction pass through the column. In MC2010 (*fib* 2013), integrity reinforcement is required in cases where the slab has no shear reinforcement or when it does not possess sufficient deformation capacity. The approach according to which the required integrity reinforcement is calculated in MC2010 is based on the calculation of the shear resistance "after punching" $V_{Rd,int}$ as follows:

$$V_{Rd,int} = \sum A_s f_{yd} \left(\frac{f_t}{f_y}\right)_k \sin\alpha_{ult} \leq \frac{0.5\sqrt{f_{ck}}}{\gamma_c} d_{res} b_{int} \tag{2.35}$$

In Equation 2.35, $A_s$ and $f_{yd}$ refer to the cross section area and design yield stress of integrity bars respectively, $(f_t/f_y)_k$ refers to the ductility of the bars as defined in MC2010; $\alpha_{ult}$ refers to the angle of integrity bars to the plane of the member (slab, footing, etc.) at punching failure (this angle is given in MC2010 in a tabulated form as a function of the

shape of the bar and its ductility class). The value of $d_{res}$ is shown in Figure 2.33 along with requirements for geometry and quantity of bars. In Equation 2.35, $b_{int}$ is the "*control perimeter activated by the integrity reinforcement after punching*" (*fib* 2013).

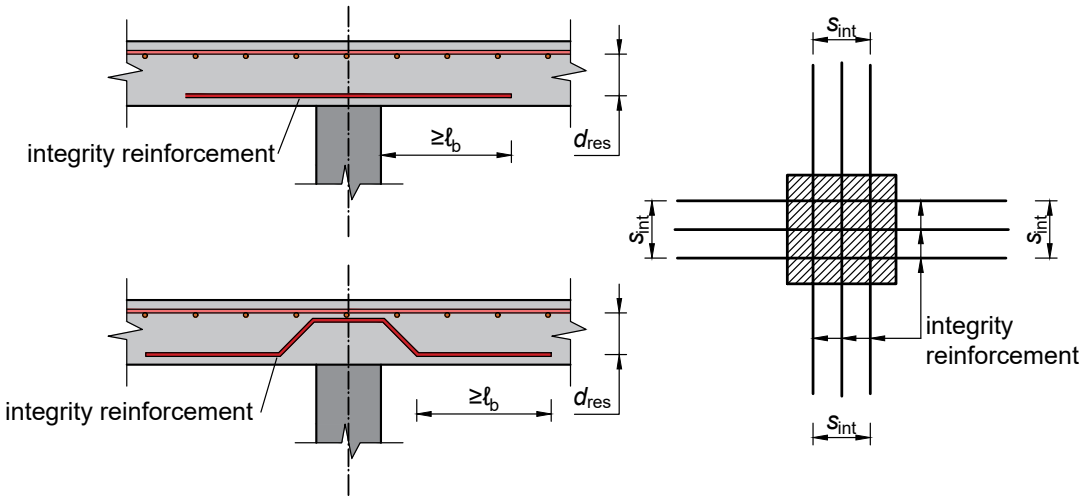


Figure 2.33: Rules for integrity reinforcement in MC2010

Mitchell and Cook 1984 studied the post-punching strength of flat slabs, based on numerical models and experimental results from literature. Post-punching behaviour of flat slab–column connections was experimentally investigated by Melo and Regan 1998, which tested a series of flat slab specimens with straight bottom bars used as integrity reinforcement and confirmed their efficiency. Ruiz et al. 2013 tested twenty slabs with various integrity reinforcement layouts and configurations and showed that bent-up bars are among the most efficient solutions. Ramos and Lúcio 2008 and Faria et al. 2012 showed that prestressing is effective in enhancing the post-punching strength of flat slabs and an effective mean of preventing progressive collapse.

The aforementioned investigations were focused on the residual strength of slab–column connections after punching failure. However, extending the research to the robustness of flat slab 2D or 3D frames is not straightforward. A column removal scenario in a flat slab building was experimentally simulated by Qian and Li 2016 under quasi–static conditions, offering important insight on the progressive collapse phenomena. Kokot et al. 2012 used a previously tested full scale flat slab building to perform a controlled demolition of an interior column, in order to investigate the subsequent collapse. The structure was able to withstand quasi–static removal of a column, but accompanying finite element analyses revealed that the situation could have been different under dynamic loading conditions.

Numerical simulations of progressive collapse of buildings have been made possible lately, due to recent advancements in numerical methods such as the Applied Element Method (for example, Attia et al. 2017) and computing capacity.

### 2.4.6 Diaphragmatic behaviour

Diaphragmatic behaviour at storey level is an important principle in modern seismic design codes. The slabs must have adequate stiffness in their plan to transmit the lateral inertia forces to the vertical elements in a uniform manner (proportional to the stiffness of each element). A slab that fails to provide adequate stiffness in its plan might cause certain vertical elements to become overstressed due to stress concentration and non-proportional distribution of lateral loading as well as significant deviation from predictions of the structural analysis.

Eurocode 8 (CEN 2004d) requires a minimum thickness of 70 mm for the concrete solid slabs and bidirectional reinforcement in order for them to be considered as a diaphragm. It should be noted that the provision for thickness is easily met in practice for most of the flat slabs, in which the thickness is usually guided by punching shear resistance and deflections. The provision for bidirectional reinforcement is also met in flat slabs because of their structural behaviour as "two-way slabs".

Einpaul et al. 2015 studied the effect of the compressive membrane action around interior slab–column connections. It was shown that such an action, combined with moment redistribution in continuous flat slabs, leads to an increase of the punching shear strength that is neglected in the current design codes.

## 2.5 Effects of dynamic loading

For practical reasons, the common approach to experimentally investigating the drift capacity of flat slabs is to test them under reversed, cyclic, quasi–static, horizontal loading. However, seismic loading is of a fundamentally different nature, because it is primarily dynamic. The load abruptly changes its magnitude and direction over short periods of time. It is well established that concrete strength and steel yield stress are increased for high rates of loading (Bischoff and Perry 1991; Fu et al. 1991; Grote et al. 2001). In flat slabs, if the failure mode is not altered due to the increase of material strengths, the enhancement of material properties generally means that the punching shear strength is also increased. Furthermore, quasi-static tests have the advantage of an increased control over the input and output data, which are easier to process. Nonetheless, it is important to consider the differences between static and dynamic loading when studying the behaviour of flat slabs under seismic conditions.

Ghali et al. 1976 reported the experimental investigation on six slab–column connections without shear reinforcement, three of which were tested under dynamic loads. The comparison of dynamic tests with static tests on similar specimens resulted in higher ultimate unbalanced moments and energy dissipation in case of dynamic loading.

As previously discussed in Section 2.3.7, full scale shaketable tests offer a good opportunity to study the behaviour of structures under dynamic loading. As already discussed

in Section 2.3.7.1, Kang and Wallace 2005 reported shaketable tests of two reinforced concrete frames, one of which had a post-tensioned slab. Both specimens were reinforced with headed studs. Compared to a previously performed quasi-static test, the authors observed that the specimens were less damaged in case of dynamic loading, although the failure mode (punching failure) was not altered.

## 2.6 Review of analytical approaches for the estimation of unbalanced moment and deformation capacity

### 2.6.1 Unbalanced moment

For design purposes, Megally and Ghali 2000a proposed a procedure for the determination of the unbalanced moment in slab–column connections that are not part of the lateral load resisting system. They proposed using simple frame models with support conditions similar to the common test setups for horizontal loading of slab–column connections, and analysing them under imposed drifts to determine the unbalanced moment. More specifically, a model similar to the test setup of Figure 2.18a was proposed for interior connections, but with frame elements (beams and columns) instead of plate or shell elements. For exterior connections, a frame model similar to Figure 2.25a was proposed. In both cases, the joint region should be modelled using rigid elements. For design, conservative estimates of the stiffness of the elements should be used.

According to Megally and Ghali 2000a, the unbalanced moment $M_{unb}$ determined as described above does not need to be taken greater than an empirical upper limit, as follows:

$$M_{unb} \leq \frac{M_{pr}}{\alpha_m} \tag{2.36}$$

where $M_{pr}$ is the sum of probable[2] flexural strengths (expressed as bending moments) of the two opposite sides of the control section (determined in accordance with ACI 318) and $\alpha_m$ is a factor that the authors proposed based on finite element analyses. For interior connections:

$$\alpha_m = 0.85 - \gamma_v - \frac{\beta_r}{20} \tag{2.37}$$

where $\gamma_v$ is described in Section 2.2.2 (Equation 2.8) and $\beta_r$ is the ratio of the span length in the direction of horizontal loading to the span length in the transversal direction.

Brown 2003; Brown and Dilger 2004 proposed to determine the unbalanced moment, $M_{unb}$, based on a modified yield line approach, resulting in the following relatively simple formula:

$$M_{unb} = 2\pi c_y \sqrt{m_y m_x} + 2c_x m_x - \frac{3c_y V_g}{4} \tag{2.38}$$

[2]The probable flexural strength is defined in ACI 318-14 (ACI 2014) as the flexural strength determined assuming a tensile stress in the longitudinal bars of at least $1.25f_y$ and a strength reduction factor equal to 1.

where $c_x$ and $c_y$ are the dimensions of the column ($x$ is the direction perpendicular to the direction of horizontal loads), $m_x$ and $m_y$ are the unit negative bending moment resistances in the direction of loading and perpendicular to it and $V_g$ is the applied gravity shear force. According to Brown and Dilger 2004, a suitable yield line pattern is that shown in Figure 2.34, which contrary to common yield line patterns that include sagging (positive) moment yield lines, contains only hogging (negative) yield lines. Brown and Dilger 2004 showed that the energy associated with this pattern is lower than the energy in case of patterns that include sagging yield lines. Furthermore, positive yield lines are not observed in laboratory tests (Brown and Dilger 2004). This yield line approach is not intended for use in extreme loading conditions (very high shear force with low unbalanced moment and vice versa).

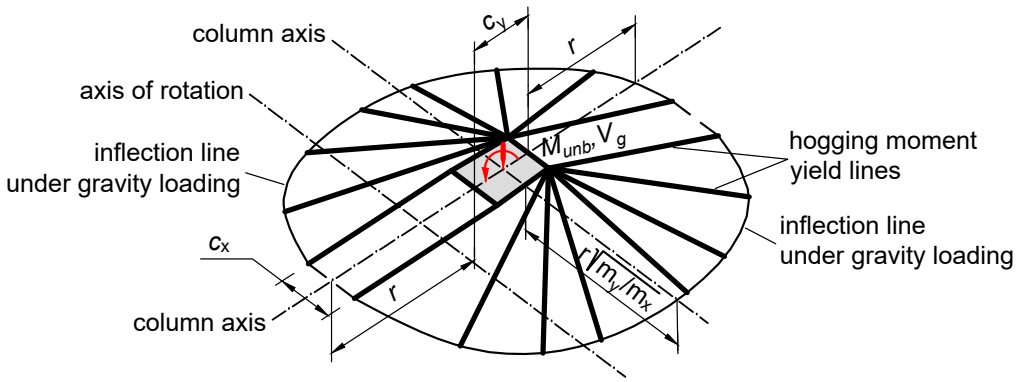


Figure 2.34: Yield line pattern according to Brown 2003; Brown and Dilger 2004

The purpose of these approaches is to design the connections so that they can resist the prescribed unbalanced moments without punching failure. As a result, the slab–column connections "yield" before punching and a ductile behaviour is ensured. On the other hand, the deformation capacity of the connections is also important in seismic design, because it governs the global structural safety under severe earthquakes. Mechanical models proposed by Broms 2009 and Drakatos et al. 2018 (discussed in the following sections) aim to determine both the deformation capacity and the unbalanced moment capacity. To date, none of these approaches have gained popularity outside the research community.

### 2.6.2 Mechanical model proposed by Broms

In 2009, Broms 2009 proposed a "design method for imposed rotations", applicable to interior slab–column connections without shear reinforcement subjected to a combination of gravity load and unbalanced moment. The model was based on the assumption that concentric punching shear failure occurs when the concrete compressive strain in the tangential direction near the column reaches a critical value and that the same critical strain is responsible for punching failure in case of eccentric loading. The model was

recently elaborated into the Tangential Strain Theory (TST) (Broms 2016). According to this model, the shear force is transmitted to the column by inclined compression struts that result in compression of the slab within the column region, leading to the formation of a crack on the soffit of the slab near the column that eventually leads to punching failure.

Although the purpose of the model for imposed rotations is to estimate the ultimate rotation of the flat slab at failure, the corresponding unbalanced moment can also be estimated. It is not possible, however, to construct the entire unbalanced moment–rotation relationship using the model of Broms 2009.

### 2.6.3 Mechanical model based on Critical Shear Crack Theory

Recently, Drakatos et al. 2018 presented a mechanical model for "drift–induced punching" of flat slabs without shear reinforcement. The model is based on the Critical Shear Crack Theory (CSCT, Section 2.2.3.1), with several modifications to account for seismic loading conditions. The authors propose an analytical approach to derive the unbalanced moment–rotation relationship, and consequently unbalanced moment–drift relationship. The slab region inside the radius $r_s = 0.22L$ (where $L$ is the span length) is divided into sector elements bounded by the shear crack and the zero-moments line. It is assumed that the rotation of each sector element varies following a sinusoidal law (Equation 2.39) that has a maximum rotation, $\psi_{max}$, for an angle of the sector equal to $\phi = \pi/2$ with regard to the axis about which the unbalanced moment acts. The minimum rotation, $\psi_{min}$, is assumed to occur for $\phi = 3\pi/2$.

$$\psi(\phi) = \frac{\psi_{max} + \psi_{min}}{2} + \frac{\psi_{max} - \psi_{min}}{2} sin(\phi) \tag{2.39}$$

The radius of the critical shear crack is assumed to be a function of the eccentricity of loading. The equilibrium of sector elements is then used to derive the moment–rotation relationship through an iterative procedure. Based on the mechanical model, the total shear force $V_k$ acting on the slab–column connection at load step $k$ can be calculated as:

$$V_k = \sum_{i=1}^{n} \frac{1}{r_q - r_c} \left\{ M_{rad}(\phi_i, r_0) - M_{rad}(\phi_i, r_s) + \left[ M_{tan}\left(\phi_i + \frac{\Delta\phi}{2}\right) + M_{tan}\left(\phi_i - \frac{\Delta\phi}{2}\right) \right] sin\left(\frac{\Delta\phi}{2}\right) \right\} \tag{2.40}$$

The symbols in Equation 2.40 are explained in Figure 2.35, where a slab sector $i$ at angle $\phi_i$ to the bending axis is shown. The slab is divided into $n$ sector elements. The model (Drakatos et al. 2018) assumes no shear transfer between the sectors and no torsional moment at the faces of the sector, therefore the corresponding forces and moments are not shown in the figure.

To estimate the total slab rotation, the deformation of the slab outside the radius $0.22L$ is taken into account by adopting an effective beam width approach. Finally, drifts are

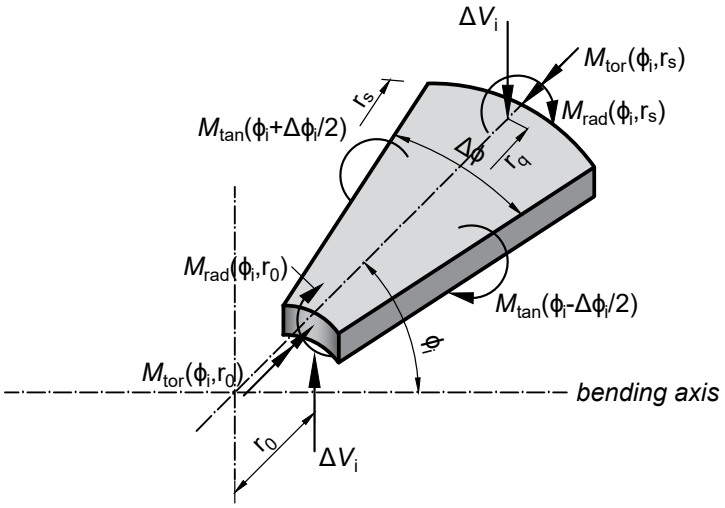


Figure 2.35: Equilibrium of a sector element based on the mechanical model of Drakatos et al. 2018

obtained by adding the slab rotation with the contribution of the column.

Similarly to CSCT, punching shear failure is assumed to occur at the intersection of the load–deformation curve with a failure criterion. Drakatos et al. 2018 proposed two failure criteria, both based on the failure criteria of CSCT, for monotonic loading and cyclic loading conditions.

## 2.7 Analysis methods for flat slabs under horizontal actions

Structural analysis of buildings with flat slabs is not as straight-forward as that of conventional buildings with slabs supported on beams. Flat slabs are "two–way" structural elements, for which the determination of action effects usually involves simplifications and the development of representative models that are computationally efficient. For linear elastic analysis, the Finite Element Method (FEM) has become popular given the present development state of computers. Nonlinear analysis based on FEM, especially for relatively complex structures (which are common nowadays), still remains cumbersome and impractical for design purposes. A review of the main analysis and modelling approaches for linear and nonlinear analysis is given in this section.

### 2.7.1 Equivalent Frame Method

In the early seventies of the twentieth century, the Equivalent Frame Method was introduced in the ACI design code of that time, as described in Corley and Jirsa 1970, based on previous work presented in Corley et al. 1961. Although the method is old, it is described here because it is still relevant today, as it remains part of ACI 318 (ACI 2014).

The method requires the building to be divided into a series of frames, as described

in Figure 2.36. An equivalent frame consists of the following parts, also described in Figure 2.37:

- *Slab–beam strip* (grey area of the slab in Figure 2.36, including any beams if present). According to ACI 318, the moment of inertia of the portion inside the joint region (from the centre to the face of the column) should be divided by $(1 - c_2/l_2)^2$, where $c_2$ is the column's dimension perpendicular to the plane of the frame and $l_2$ is the span length transverse to the direction of the span for which moments are being determined (ACI 2014). Outside the joint region, the gross section can be used;

- *Vertical supporting elements* (columns). Outside the joint region, ACI 318 allows the use of gross section characteristics of the column. The section is assumed rigid within the joint region. When slab–beams are analysed separately for gravity loads, the concept of an equivalent column should be used for horizontal loading;

- *Torsional elements* that ensure moment transfer between the columns and the slabs. In case of flat slabs (i.e., without a beam framing into the column), the torsional member's width is equal to the width of the column (Figure 2.37). Assuming a triangular shape of the distribution of twisting moments, based on the work of Corley and Jirsa 1970, the approximate stiffness of the torsional element is given as:

$$K_t = \sum \frac{9E_{cs}C}{l_2\left(1 - \frac{c_2}{l_2}\right)^3} \tag{2.41}$$

  where $E_{cs}$ is the modulus of elasticity of slab concrete and $C$ is the torsional constant.

For practical modelling purposes, the columns and the torsional elements constitute an "equivalent column" element. The stiffness of this element can be determined by considering the column and the torsional member as two springs in a series:

$$\frac{1}{K_{ec}} = \frac{1}{K_c} + \frac{1}{K_t} \tag{2.42}$$

where $K_{ec}$ is the stiffness of the equivalent column, $K_c$ is the stiffness of the column and $K_t$ is given in Equation 2.41.

The Equivalent Frame Method presented in ACI 318 (ACI 2014) was largely based on gravity loading assumptions. Recognizing this drawback, Park et al. 2009 proposed a modified Equivalent Frame Method suitable for horizontal loading. In this modified approach, the torsional member was attached to the slab element, resulting in "equivalent slab elements" instead of "equivalent columns". Kim et al. 2014 proposed an "Unified Equivalent Frame Method" suitable for both vertical (gravity) and horizontal loading. This approach takes into account the influence of gravity loading on the lateral stiffness by modifying the stiffness of the torsional member as a function of the gravity load on

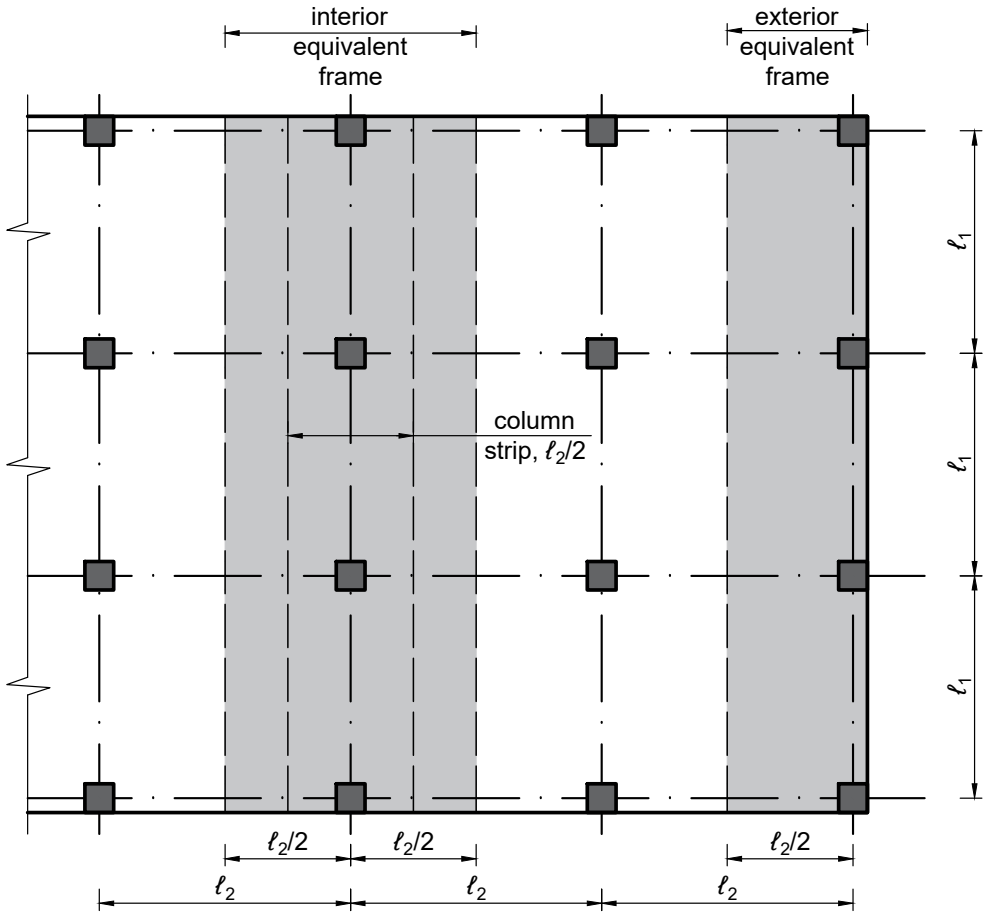


Figure 2.36: Dividing the structure into equivalent frames according to ACI 318 (ACI 2014)

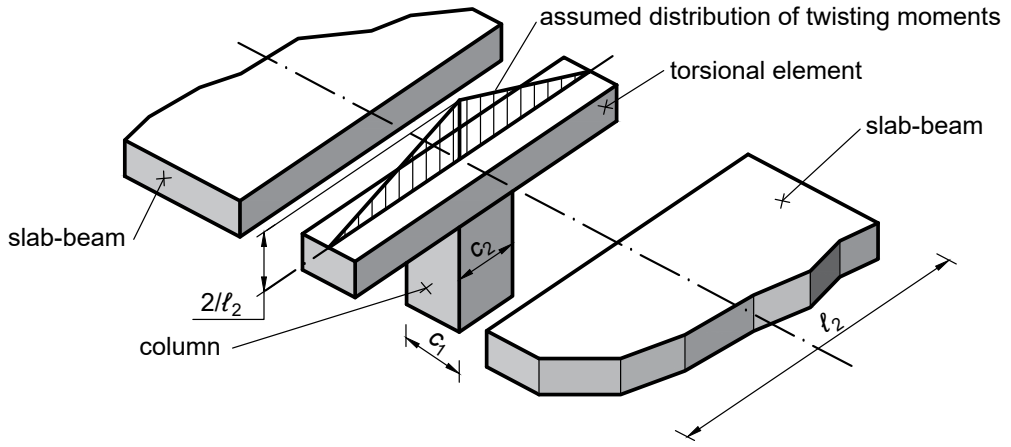


Figure 2.37: Parts of an equivalent frame

the slab. The model has both "equivalent columns"and "equivalent slabs". To the author's knowledge, these approaches have not gained significant popularity outside the research community.

In EC2 (CEN 2004c), it is permitted to analyse flat slab frames for vertical and horizontal loading using the Equivalent Frame Method. However, there are no torsional members in the approach presented in EC2, and hence, no equivalent columns. Instead, gross section characteristics are used. The full width of the slab is used for vertical loading, whereas 40% of the slab width is adopted for horizontal loading. The total bending moments calculated using this approach are then distributed across the width of the slab in column strips and middle strips.

### 2.7.2 Effective Beam Width Method

The Effective Beam Width Method consists in defining the width of a beam element that adequately represents the behaviour of the flat slab. If an unbalanced moment acts in the slab–column connection, the slab rotation varies along the slab width. The rotation is maximum close to the column and it becomes smaller with distance (Figure 2.38). The equivalence with a beam is determined by choosing an appropriate effective width, such that the stiffness of the beam with width $\alpha l_2$ is equal to the stiffness of the slab with width $l_2$. Referring to Figure 2.38, the equivalence to a beam can be achieved by equating the areas under the two rotation diagrams (Vanderbilt and Corley 1983).

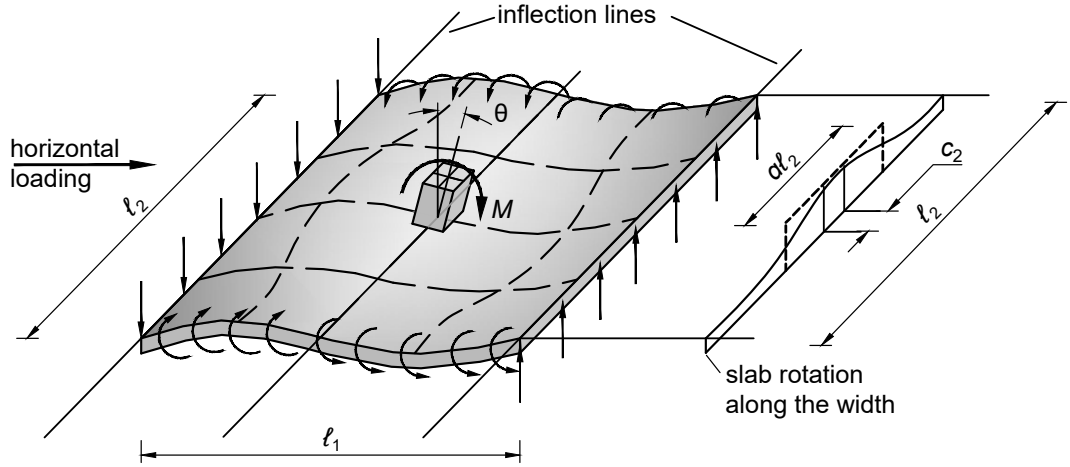


Figure 2.38: Slab–column connection under lateral loading and distribution of slab rotations along the column centreline (Vanderbilt and Corley 1983)

An analytical solution of the effective beam width based on elastic plate theory is described in Pecknold 1975. Tabulated values of the effective width coefficients $\alpha$ were given in Allen and Darvall 1977 for varying ratios $c_1/l_1$, $c_2/l_2$ and $l_1/l_2$.

For design purposes, it is convenient to have simpler solutions. Lúcio 1991 proposed

the following simple formula for the effective beam width, $b_{eff}$:

$$b_{eff} = 4.17c_1 + \frac{l_1}{4} \tag{2.43}$$

Later, Hwang and Moehle 2000a proposed the following formula:

$$b_{eff} = 2c_1 + \frac{l_1}{3} \tag{2.44}$$

for interior slab–column connections, and

$$b_{eff} = c_1 + \frac{l_1}{6} \tag{2.45}$$

for exterior connections.

## 2.8 Modelling for nonlinear analysis

Nonlinear methods of analysis are not usually suitable for the design of new reinforced concrete structures, because they require complete knowledge of the reinforcement design beforehand. However, they can be used in the assessment of existing structures and in the verification of design for new ones.

Modelling of flat slabs for nonlinear structural analysis remains challenging to date. Successful examples of detailed models consisting of solid finite elements exist (Mamede et al. 2013; Genikomsou and Polak 2015). However, such models require a high level of expertise, detailed information on the material behaviour and excessive computational power that renders them impractical for large models (such as a reinforced concrete frame).

Nonlinear layered shells are often preferred over solid elements due to simplicity and the reduced effort in modelling and analysis. In this approach, the slab is divided into a stack of layers in the thickness direction. Each layer can have a constitutive material model to account for material nonlinearity of concrete and steel. The reinforcement is smeared into layers with a uniform thickness that is calculated based on the area of longitudinal bars. From this, it is obvious that effects of individual bars (bond–slip, dowel effect, etc.) cannot be directly modelled by the element. Although Finite Element Analysis of shells has undergone significant advances in the last decades, using nonlinear layered shells to accurately model the full behaviour of reinforced concrete flat slabs still remains challenging in practice. In general, these types of shells can be used to model the bending behaviour of the flat slabs. However, they cannot account for punching failures, which may occur before reaching the flexural capacity of the slab. Layered shell formulations able to model punching shear failure have been proposed by Polak 1998 and, more recently, Wang and Teng 2008.

Models consisting of shell elements combined with linear elements and springs are proposed by Choi and Kim 2015 for nonlinear static analysis and by Liu et al. 2015 for

progressive collapse analysis. A "grid model" is proposed by Coronelli 2010 to model the flat slab with a grid of beam elements. Tian et al. 2009 proposed a force-based model to predict the strength of flat slabs under horizontal loading. The model consists of rotational springs to resist torsion and the slab modelled as a wide beam to resist flexure and shear. This model is suitable for pushover analysis of flat slab frames.

The first model that directly incorporates punching failures into the structural analysis was presented in Hueste and Wight 1999 and implemented in the nonlinear program DRAIN-2DM (Tang and Goel 1998). The element checks for punching failures based on a failure criterion determined as a function of the experimentally observed relationship between the Gravity Shear Ratio (GSR) and the ultimate drift ratio.

Kang et al. 2009 proposed a model that involves zero length column strip slab flexural hinges, a connection spring and rigid end zones inside the joint region (Figure 2.39). The connection spring is assigned a rigid-plastic behaviour and a limit-state model that triggers degradation once the conditions are met for a punching failure. Such conditions are set in terms of stresses in the control punching shear perimeter and inter-storey drift ratios. OpenSees (McKenna et al. 2009) is a suitable platform for this type of modelling because it already contains a limit state model (developed originally for shear critical columns in Elwood and Moehle 2003; Elwood 2004). The slab springs are used to model flexural plastic hinges in the slab that are calibrated so that the following failure modes can be captured by the model:

- punching failure prior to slab reinforcement yielding (stress–induced punching failure, when the acting stress calculated as per design code exceeds the punching shear resistance before yielding of the slab reinforcement, Figure 2.40-a);
- yielding of slab reinforcement followed by a punching failure (stress–induced punching failure, when the acting stress calculated as per design code exceeds the punching shear resistance after yielding of the slab reinforcement, Figure 2.40-b);
- punching failure after flexural yielding of the entire slab (column strip) for a certain inter-storey drift ratio (drift–induced punching failure, when the ultimate drift for the corresponding Gravity Shear Ratio is reached, Figure 2.40-c).

The model was verified against shake table tests (Kang et al. 2009) and showed promising results.

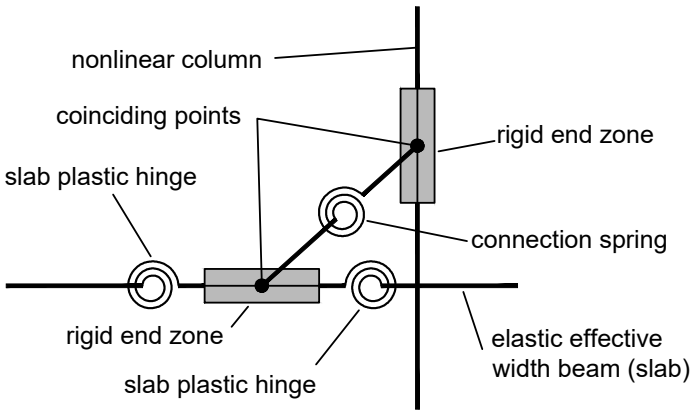


Figure 2.39: Flat slab–column connection model proposed by Kang et al. 2009

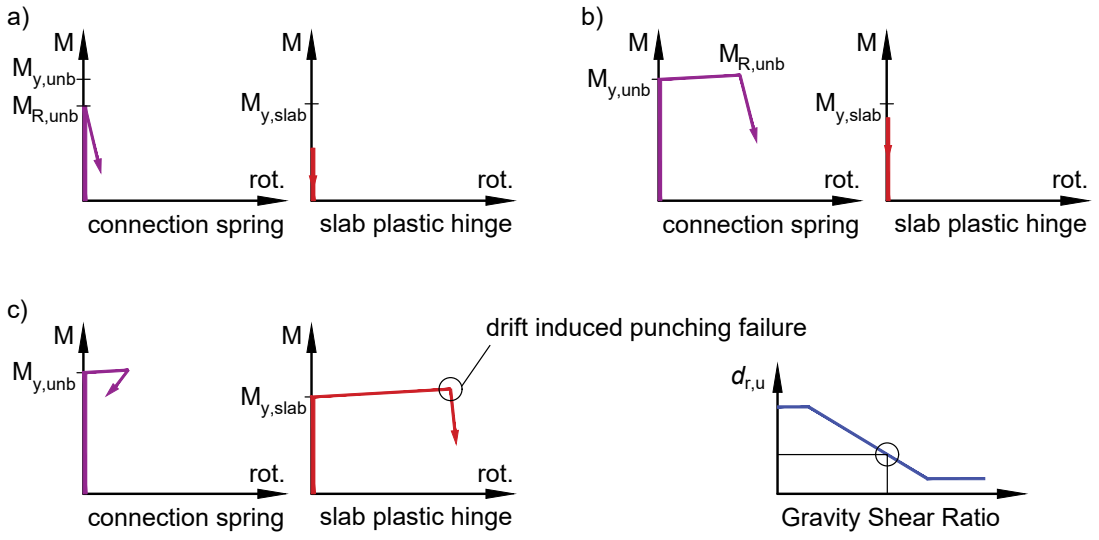


Figure 2.40: Failure modes captured by the model of Kang et al. 2009

# Chapter 3

# Experimental campaign

Horizontal cyclic loading tests of five flat slab specimens are described in this chapter. The specimens are named C-Ref, C-SSR3, C-SSR5a, C-SSR5b and C-SSR5c. C-Ref is the reference specimen and does not contain any shear reinforcement. Shear stud reinforcement is used in the other four specimens. The names of the specimens describe the type of loading (C – cyclic), type of shear reinforcement (SSR – shear stud reinforcement) followed by the number of perimeters of studs. Specimens with the same number of perimeters of studs are distinguished by small Latin letters at the end of the name. A condensed version of this chapter including the main findings from the experimental campaign was published in Isufi et al. 2018b.

## 3.1 Conceptual design of the specimens

The reference specimen (C-Ref) corresponds to an interior slab–column assembly in a prototype building with flat slabs. The prototype building has approximately square slab panels (almost equal spans in both directions, around 6 m) and is dimensioned with cross sections that are typical for low to mid–rise buildings designed for gravity loads. The prototype building is subjected to relatively high quasi–permanent gravity loads (typical, for example, for industrial buildings, shopping or storage areas, etc.). The specimens with shear reinforcement correspond to variants of the prototype building in which shear reinforcement is added to the slab–column connections to enhance their deformation capacity, although the strength of the slab without shear reinforcement is sufficient for the fundamental combination of actions for non–seismic design.

Figure 3.1 summarizes the conceptual design of the specimens for gravity loading based on CSCT (see Section 2.2.3.1). To construct the load–rotation relationship and the failure criteria, a slab with radius 845 mm (nearly 22% of the span, considering a 2/3 scale for the specimens in relation to the prototype building), thickness 150 mm and effective depth 118 mm supported on a square column with side dimension equal to 250 mm was considered. The material characteristics are assumed to be as follows: $f_c$ = 40 MPa,

$f_y$ = 500 MPa, $f_{yw}$ = 400 MPa, $d_g$ = 16 mm. The tensile strength and the modulus of elasticity of concrete are taken based on EC2 (CEN 2004c) for a compressive strength $f_c$. A quadrilinear moment–curvature relationship is adopted. The top longitudinal reinforcement ratio is taken $\rho_l \approx 1\%$. Shear reinforcement consisting of 12 studs per perimeter made of deformed steel bars with diameter 8 mm is considered. A cruciform layout of the studs is assumed. The distance of the first perimeter of studs from the face of the column is taken equal to 40 mm and the radial spacing of the studs is kept constant at 70 mm.

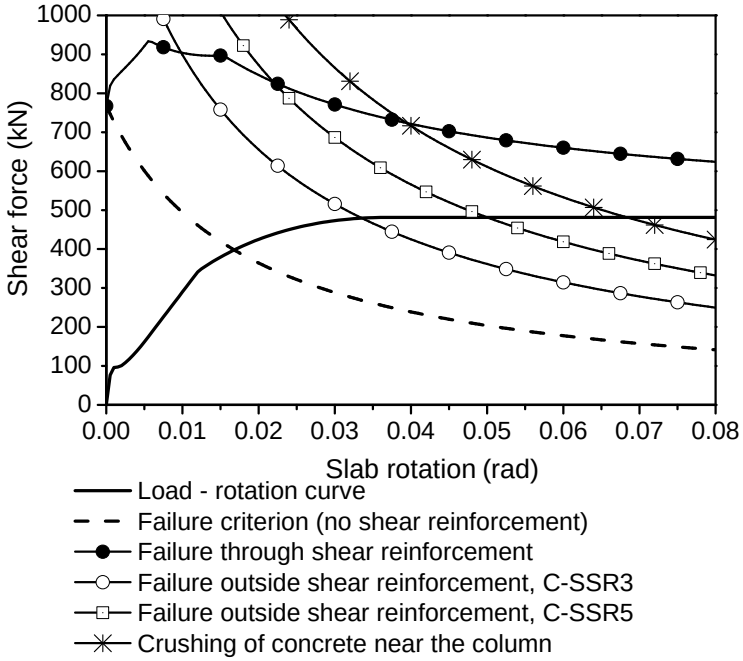


Figure 3.1: Design of the specimens for gravity loading based on CSCT

In the experimental campaign, the specimens were tested under constant gravity load and reversed horizontal loading. The load was lower than the punching failure load (even if no shear reinforcement is provided), as it is expected in a seismic situation. Therefore, Figure 3.1 cannot be used to predict the behaviour of the specimens under horizontal cyclic loading. Nonetheless, it gives some important insight on the relationship between the resistances against various failure modes under gravity loading. The format of CSCT is suitable for this purpose. Figure 3.1 shows that, with the provided shear reinforcement, failure within the shear-reinforced zone is not governing the design of the shear reinforced specimens. Also, the figure shows that the governing failure mode for the specimens with studs is failure outside the shear-reinforced zone. The introduction of headed studs as shear reinforcement leads to an expected increase of concentric punching shear strength by about 20% in this particular case. Another important observation is that, for the current conditions, the theory does not predict a significantly higher strength for C-SSR5(a, b and c) specimens compared to C-SSR3, since the predicted strength is conditioned by the slab's flexural capacity. It does, however, predict a higher deformation

capacity of the specimens with more perimeters of shear reinforcement.

## 3.2 Description of the specimens

### 3.2.1 General description

The specimens represent a 2/3 scale representation of the column and the area bounded by the mid-span lines in the longitudinal direction of the specimen and by lines parallel to the longitudinal direction located at a distance equal to 22% of the span length in the transversal direction in the prototype building. The specimens have overall dimensions 4.15 m × 1.85 m, thickness equal to 150 mm and a 2.0 m steel column (1.0 m above and below the slab) with a rigid square base plate with side dimensions equal to 250 mm. A summary of the main characteristics of each specimen, with focus on the distinctions between them, is contained in Table 3.1.

Table 3.1: Brief description of the characteristics of each specimen

| Specimen | Perimeters of studs | Distinctive features |
|---|---|---|
| C-Ref | none | Reference specimen with no shear reinforcement. |
| C-SSR3 | 3 | Three perimeters of studs. |
| C-SSR5a | 5 | Lower absolute value of the applied gravity load but a Gravity Shear Ratio (Section 3.9) comparable to that of the other specimens except C-SSR5c. |
| C-SSR5b | 5 | Tested in two phases to observe the post-earthquake strength and stiffness of flat slab–column connections with shear studs. |
| C-SSR5c | 5 | Increased Gravity Shear Ratio (Section 3.9) compared to the other specimens. |

The studs are arranged in a cruciform layout to avoid interference with the longitudinal reinforcement. Based on the Eurocode 2 (CEN 2004c) geometrical requirement for reduction of the perimeter in which shear stresses should be checked to determine the extent of shear reinforcement when the cruciform layout is used, all specimens have the same outermost perimeter (discussed in more detail in Section 3.2.3).

The purpose is to study the effect of the gravity load and the extent of shear reinforced zone in the behaviour of slab–column connections with shear studs under combined gravity and horizontal actions. The characteristics and distinctive features of each specimen are discussed in more detail in the subsequent sections.

### 3.2.2 Longitudinal reinforcement

All five specimens had the same detailing of longitudinal reinforcement. The top reinforcement consisted of Φ12 mm bars spaced at 100 mm in the vicinity of the column and Φ12 mm and Φ10mm bars spaced at 200 mm outside the column region. Reinforcing bars parallel to the longest direction were placed on top of the bars in the shortest direction. The bottom reinforcement consisted of Φ10 mm bars with a uniform spacing of 100 mm. The nominal concrete cover for the top and bottom longitudinal bars was 20 mm. Detailing of the top and bottom bars is given in Figure 3.2 and 3.3. The longitudinal reinforcement and instrumentation used was similar to that of the slab specimens without shear reinforcement described in Almeida et al. 2016.

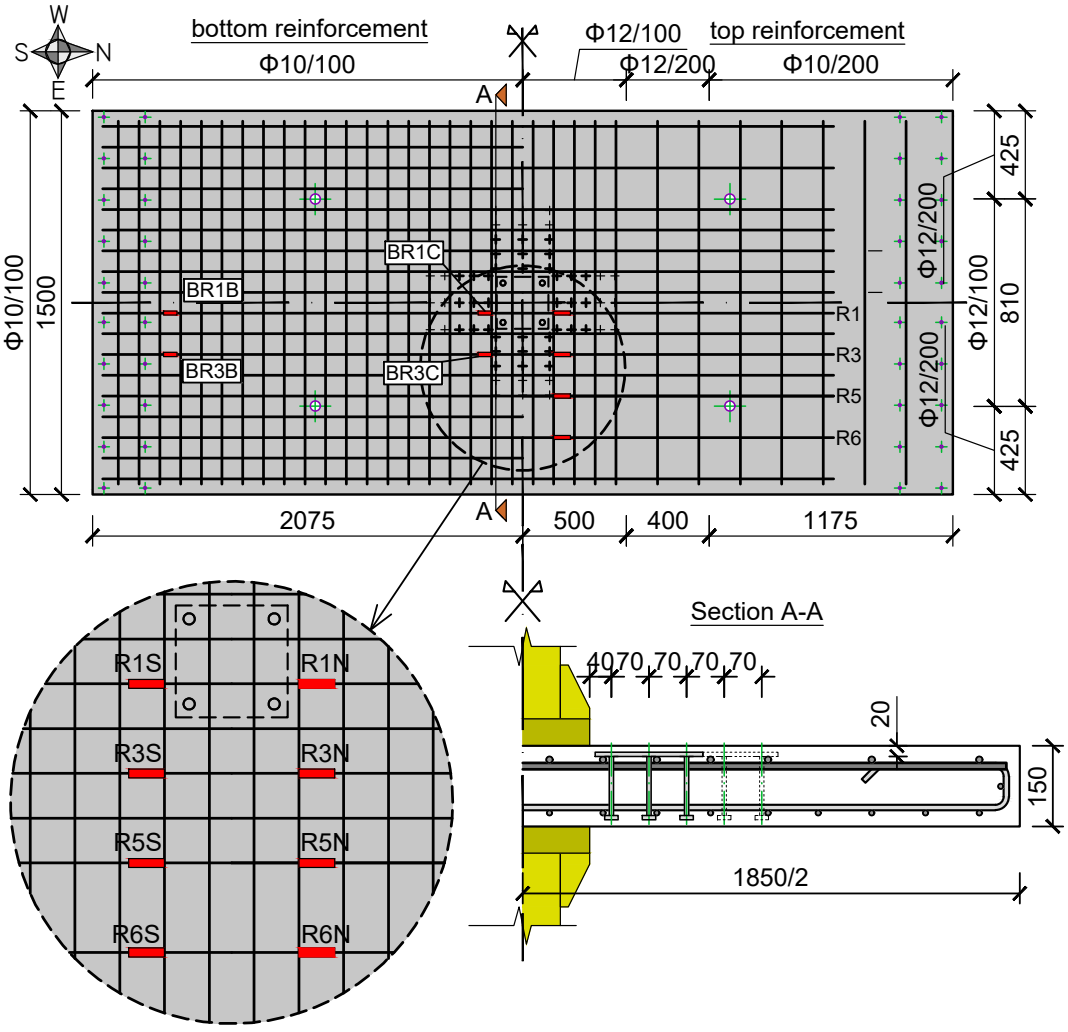


Figure 3.2: Reinforcement details and instrumentation (dimensions in millimetres)

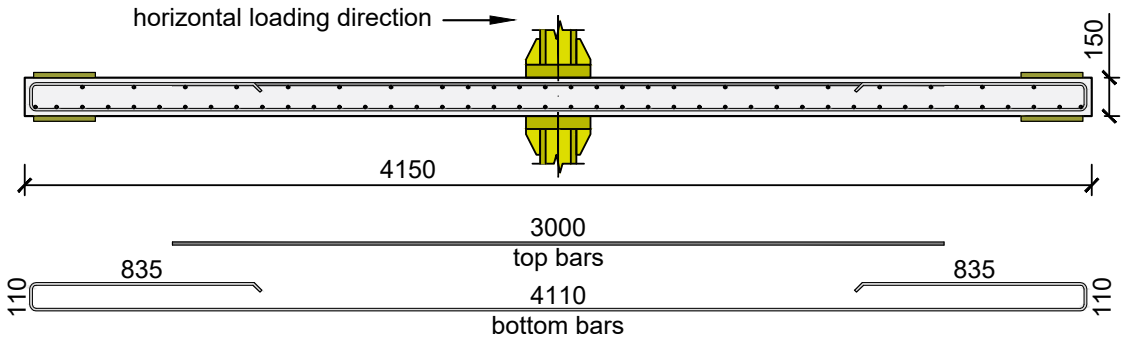


(a) Longitudinal direction

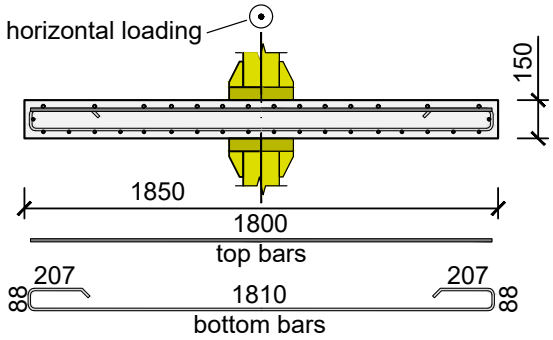


(b) Transversal direction

Figure 3.3: Detailing of longitudinal bars (dimensions in millimetres)

### 3.2.3 Shear reinforcement

For specimens with shear reinforcement, shear studs as depicted in Figure 3.4 were used. A deformed reinforcement bar was used for the shaft of the stud. A steel bar with rectangular cross section dimensions equal to $25 \times 8$ mm was used for the connecting strip and the lower stud heads. The connecting strip serves three purposes. Firstly, it serves as anchorage for the top of the stud. Secondly, it holds the studs at the specified distance. Finally, it is used as a support for the assembly of studs on top of the longitudinal bars. Details about the production of shear reinforcement are contained in Section 3.3.

The bottom rectangular bars were cut to create a square stud head with side dimension equal to 25 mm. The dimension of the head was chosen to have approximately three times the diameter of the studs, in accordance with the recommendations of *fib* Model Code 2010 (*fib* 2013) for anchorage that leads to development of the full yield capacity of the stud. The layout and instrumentation of the shear reinforcement is presented in Figure 3.5. In this figure, the outer punching perimeter $u_{out,ef}$ based on EC2 (CEN 2004c) is shown. EC2 proposes a reduction of the perimeter in which shear stresses should be checked to determine the extent of shear reinforcement when the cruciform layout is used. This perimeter is located at a distance $kd$ from the last perimeter of studs, with $k = 1.5$ as a recommended value in EC2. In Figure 3.5, it is shown that the outer perimeter is equal for all the specimens. The studs in specimen C-SSR3 are arranged such that no further

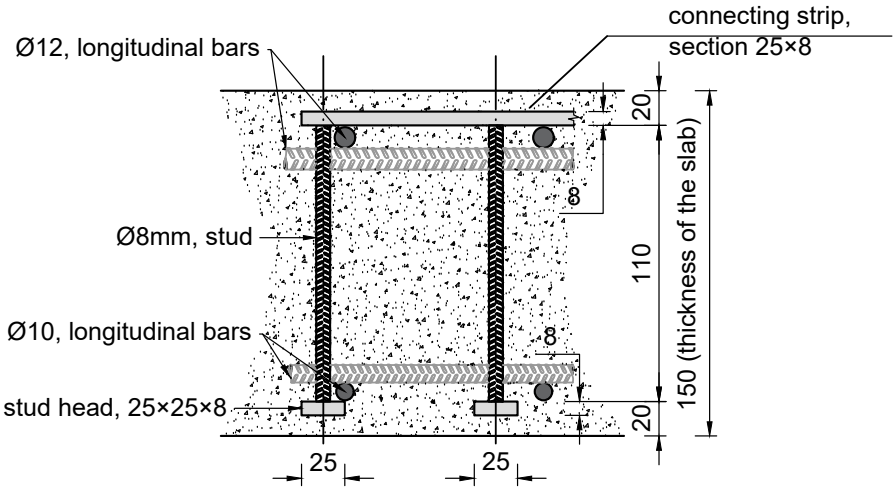


Figure 3.4: Detail of the studs

increase of $u_{out,ef}$ can be achieved by increasing the number of perimeters of studs. When calculated using the nominal effective depth of the slab, $u_{out,ef}$ is equal to 3211 mm. The distance of the first stud from the face of the column was 40 mm and the spacing of the perimeters of studs was uniform, equal to 70 mm.

The third perimeter of studs does not fulfil the EC2 (CEN 2004c) requirement for spacing of the vertical legs of shear reinforcement within the control section at a distance $2d$ from the face of the column, which should not exceed $1.5d$. In European Technical Approval documents for proprietary shear studs, it is common to override the aforementioned detailing requirement (for example, in ETA-13/0151 (EOTA 2013), the allowed distance of the studs is $1.7d$ inside the radius $1.125d$ and larger outside this radius). In the absence of more specific guidance in EC2 for this case, it is assumed that the same rules for the reduction of the outer perimeter as in case of studs outside the control section apply. The result is a reduction of the perimeter by nearly 5 mm (not noticeable in Figure 3.5).

## 3.3 Production and testing of the shear stud rails

The shear stud rails were made of the following parts (Figure 3.6):

- rectangular steel bars 25×8 (mm) with nominal strength class S275JR+AR according to EN 10025-1,-2 (CEN 2004a; CEN 2004b);
- reinforcing bars Φ8 mm, with nominal yield stress $f_{yk}$ = 400 MPa.

The rectangular steel bars were used for the anchorage zones. Square parts were cut for the bottom head of the stud. For the upper connecting strip, the rectangular bars were cut in accordance with the drawings (Figure 3.4). Reinforcing bars with diameter 8 mm

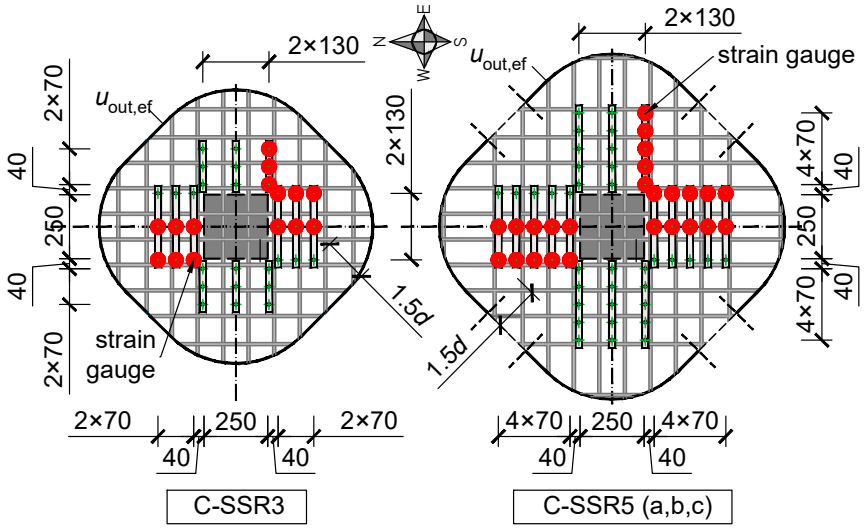


Figure 3.5: Layout and instrumentation of the studs

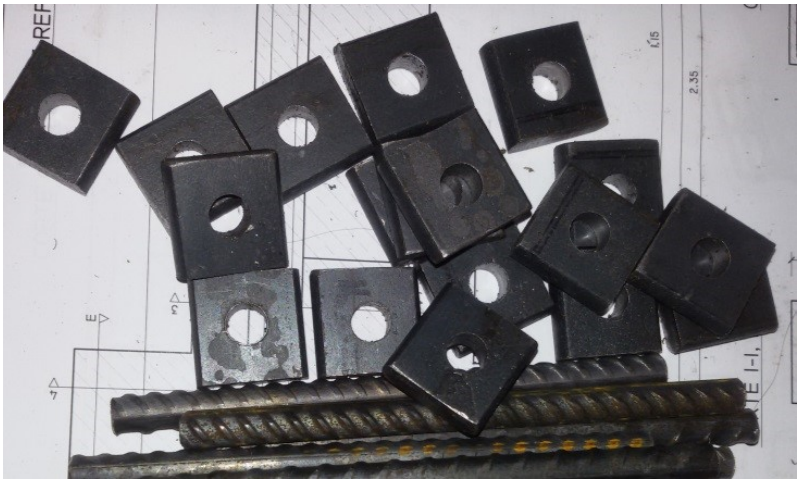

Figure 3.6: Steel parts before assemblage of the shear stud rails

were used for the shafts. The reinforcement bars were cut using an electrical machine with abrasive blades. The rectangular bars were cut using a band saw machine with higher precision compared to the abrasive blade machine. Holes were drilled using a drill press, with 9 mm drills (Figure 3.7a). The assemblage of parts was done through welding (Figure 3.7b). The entire production process was completed in the facilities available at DEC/FCT/UNL.

To determine the most suitable solution for the purposes of this study, the following alternatives were tried for the connection of the reinforcement bar to the rectangular bars:

- one–sided welding with enlarged hole (truncated cone shape), with base diameters 16 mm and 9 mm (Figure 3.8a);

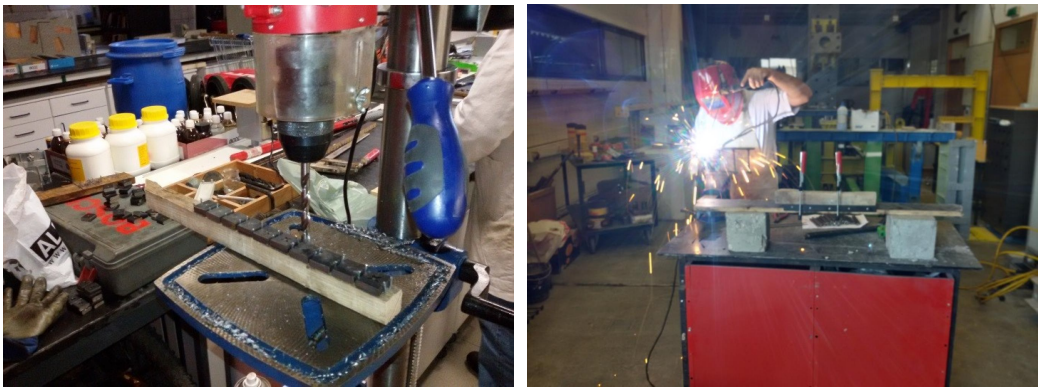

(a) Drilling (b) Welding

Figure 3.7: Preparation of shear studs

- two–sided welding with enlarged hole (Figure 3.8b);
- two–sided welding with 9 mm cylindrical hole (Figure 3.8c).

The purpose was to have a simple connection in which failure occurs when the reinforcement bar yields in tension. In all cases, the stud penetrated the holes. The reinforcement bar was cut 1–2 mm shorter to allow welding. Based on a tensile test (Figure 3.9, Figure 3.10), it was found that two–sided welding with cylindrical hole was the most appropriate technique for the aforementioned purpose. The solutions with two–sided welding were tested on the same stud (the upper connection was produced in accordance with Figure 3.8b and the lower connection was produced in accordance with Figure 3.8c). It was found that the weakest link was the reinforcement bar, i.e., the stud failed by yielding of the reinforcement bar. The behaviour of the stud was comparable with the behaviour observed in a reinforcement bar tested under similar conditions (Figure 3.9). On the other hand, the one–sided welding connection failed prior to developing the yielding stress of the bar (Figure 3.9, Figure 3.10b). The enlargement of the holes as depicted in Figure 3.8b can be beneficiary for two–sided welding to reduce the excess of welding material on the outer part of the stud and to provide additional strength to the connection. However, it was not further used in this study.

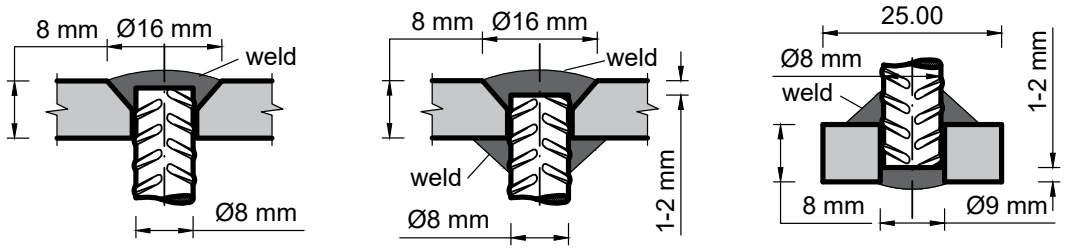


(a) One–sided (b) Two–sided, enlarged hole (c) Two–sided, cyl. hole

Figure 3.8: Welding of the reinforcing bars

The determination of the most suitable solution for industrialized production of the studs is outside the scope of this study. In that case, the thickness of the connecting strip would need to be reduced in order to preserve the necessary concrete cover for durability purposes. The reduction of thickness, however, could affect the strength of the welded connection. The thickness equal to 8 mm (i.e., cross section of the rectangular bar with height equal to 8 mm) in the present study is conservative in terms of bending strength of the head of the stud embedded in concrete and subjected to tension in the stud. An alternative option adopted by several commercial products is to provide a plastic connecting strip.

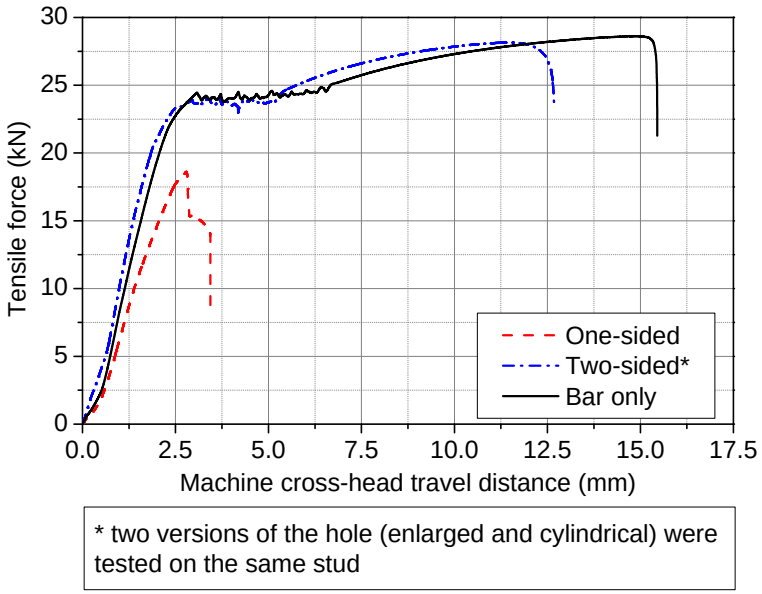


Figure 3.9: Tensile test results

(a) Tensile test (b) Failure of the one–sided connection

Figure 3.10: Test of the welding connection

Figure 3.11 shows the finished product. The complete set of studs for the specimen with three rows of studs, C-SSR3, is shown in Figure 3.11a. A stud rail belonging to a specimen with five rows of studs is shown in Figure 3.11b.

(a) Complete set of studs for C-SSR3

(b) A stud rail for specimens C-SSR5(a, b, c)

Figure 3.11: Studs, photos of the finished product

## 3.4 Preparation of the specimens

Specimens were prepared in two different precast concrete plants[1,2]. Photos of the moulds corresponding to different plants are shown in Figure 3.12.

Shear reinforcement was positioned after the longitudinal reinforcement was put in place. Photos of the installed shear studs are shown in Figure 3.13 for specimen C-SSR3 and a typical specimen with 5 perimeters of studs (C-SSR5a).

Before casting, the average effective depth of the top reinforcing bars in both directions was measured. The average values for each specimen are summarized in Table 3.2. The effective depths in the table are determined as the average value of 24 measurements near the column, 12 along each direction.

The specimens were cast on a vibrating platform (Figure 3.14a). Concrete was further

[1]Secil Prebetão, SA for specimens C-SSR3, C-SSR5a
[2]CONCREMAT, SA for specimens C-Ref, C-SSR5b, C-SSR5c

(a) C-SSR3, C-SSR5a

(b) C-Ref, C-SSR5b, C-SSR5c

Figure 3.12: Moulds used to cast the specimens

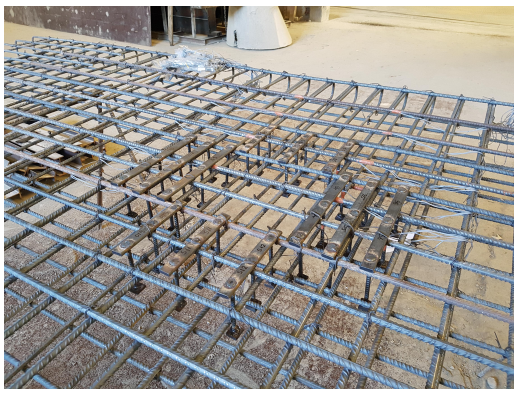

(a) Shear studs in C-SSR3

(b) Shear studs in C-SSR5a

Figure 3.13: Shear reinforcement positioned in place before casting

Table 3.2: Measured average effective depths

| Specimen | $d$ (mm) |
|---|---|
| C-Ref | 118.1 |
| C-SSR3 | 117.9 |
| C-SSR5a | 117.5 |
| C-SSR5b | 117.1 |
| C-SSR5c | 118.1 |

compacted with a hand–held concrete vibrator. Three 150 mm cubes and five 150 × 300 mm cylinders were cast for each concrete batch (Figure 3.14b). Each of the specimens was cast in two batches, therefore a total of six cubes and ten cylinders was prepared for each specimen.

(a) Casting of the specimen

(b) Casting of cubes and cylinders

Figure 3.14: Casting of the specimen and material samples

## 3.5 Test setup

The most common test setups found in the literature for horizontal cyclic loading of flat slab–column connections were described in Section 2.3.1. Such test setups have been commonly accepted and used as good and simple representatives of slab–column connections. However, they use simplified boundary conditions, such as borders that are free of bending moments and vertically fixed, which lead to a static position of the zero-moment line and inability to have bending moment redistribution (Ramos et al. 2017). To overcome these limitations, a new test setup has been developed at DEC/FCT/UNL.

This setup allows vertical displacements at the slab borders; equal magnitude of shear forces, bending moments and rotations at the slab edges; mobility of the line of inflection location along the longitudinal direction and the possibility of applying high vertical load ratios. The specimens tested in this test setup have both negative and positive bending moment regions and they represent the portion of the flat slab from mid–span to mid–span in the horizontal force direction. A photo of the test setup is shown in Figure 3.15. The elevation drawing of the test setup is given in Figure 3.16. The test setup is also described in Almeida et al. 2016.

A steel column with a square rigid base plate with side dimension equal to 250 mm is used. The column consists of two parts connected with each other through four pre-stressed threaded rods that pass through the concrete slab. The bottom end of the column is pinned to the laboratory strong floor. The top end of the column is attached to a mechanical actuator with a load cell through a pinned connection that is used to apply the reversed horizontal cyclic displacements. The actuator is attached to a reaction wall. The

Figure 3.15: Photo of the test setup

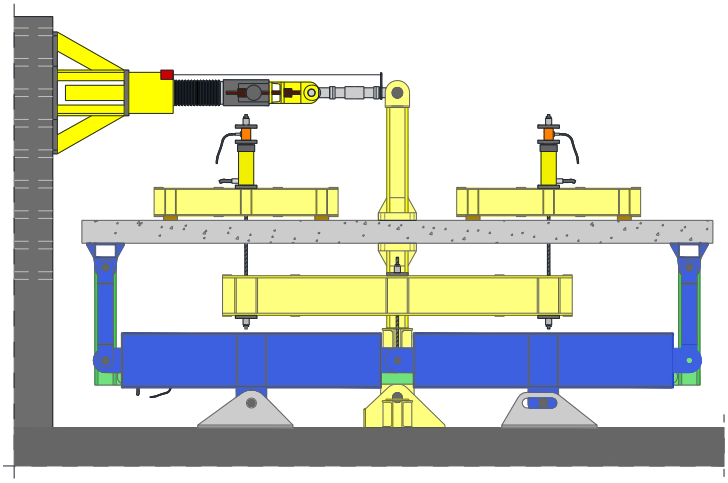

Figure 3.16: Elevation drawing of the test setup (Almeida et al. 2016)

two pinned ends of the column represent the inflection point, assumed to be located at mid–height of the storey in the prototype building. The overall length of the column is 2.0 m. As a result, the unbalanced moments are directly obtained by multiplying the horizontal load with the total length of the column. The horizontal drift ratios are obtained by dividing the horizontal displacements by 2.0 m. These drift ratios include the deformation of the steel column, which was designed to remain elastic.

Two sub–systems of steel profiles are used to achieve the features of the test setup, as shown in the idealized scheme of Figure 3.17. The outer steel profiles in Figure 3.15 (blue profiles in colour print) are represented in Figure 3.17 by the sub-assembly denoted as (1). This sub-assembly ensures equal displacements at the opposite slab borders. Under gravity loading and no horizontal displacement, this system is not loaded because it is a mechanism. When horizontal displacements are applied, the slab specimen tends to rotate as a rigid body but is effectively restrained by the sub–assembly (Figure 3.18a). As a result, shear forces are induced at the borders of the specimen (at the simulated mid–span). Equal deflections are ensured by the scheme.

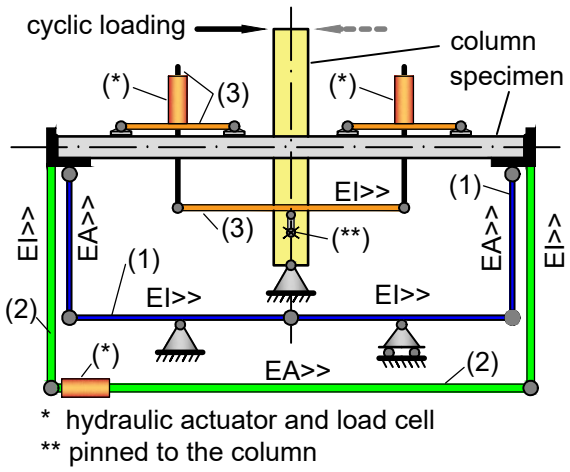


Figure 3.17: Schematic representation of the test setup

The sub-assembly denoted in Figure 3.17 as (2) ensures equal rotation at the opposite slab borders. In the photo of Figure 3.15, the steel profiles of this sub-assembly are the inner ones and are located underneath the specimen (green profiles in colour print). This sub-assembly is shown in action in Figure 3.18b. The system also works for the gravity loading phase, during which the rotations at the borders of the specimen are supposed to be zero. Steel profiles are rigidly connected to each border of the specimen and they are connected with each other via pinned struts equipped with a hydraulic jack and a load cell to monitor the positive bending moments at the borders of the specimen. During the application of the gravity load and during cyclic loading, the force in the struts is manually adjusted to account for cracking and deterioration of the slab's stiffness. The adjustment is made based on the measured rotations at the borders of the specimen, in order to ensure equal rotations at the opposite simulated mid–spans. The manual adjustment generally leads to an increase of the positive bending moments in the slab along the cyclic loading test.

The gravity (vertical) load is applied by four hydraulic jacks located above the slab (see Figure 3.19). In Figure 3.17, the sub–assembly that applies and maintains the gravity load is denoted as (3). Each hydraulic jack distributes its load via a spreader steel beam in two locations on top of the slab. In total, there are 8 vertical load distribution points, uniformly distributed on top of the slab (at 1.0 m distance from each other) as indicated in Figure 3.23. The vertical loading system is independent from the other sub–systems. A good control of the vertical load is maintained throughout the test, because the entire sub–system follows the movement and deformation of the slab specimen at all times.

## 3.6 Loading protocol

The specimens were tested under constant gravity loads and reversed horizontal cyclic displacements. After the application of the full gravity load, horizontal displacements

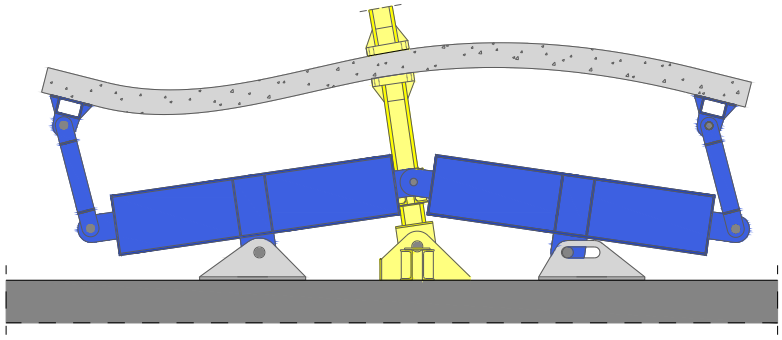

(a) Sub–assembly that ensures equal deflections and equal magnitude shear forces

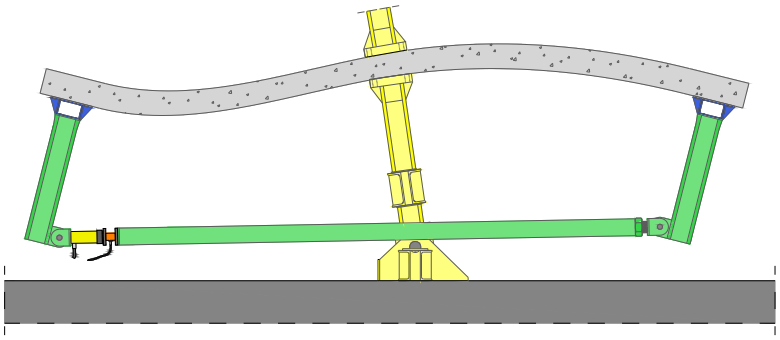

(b) Sub–assembly that ensures equal rotations

Figure 3.18: Sub–assemblies of steel profiles that ensure the proper boundary conditions in the test setup (Almeida et al. 2016)

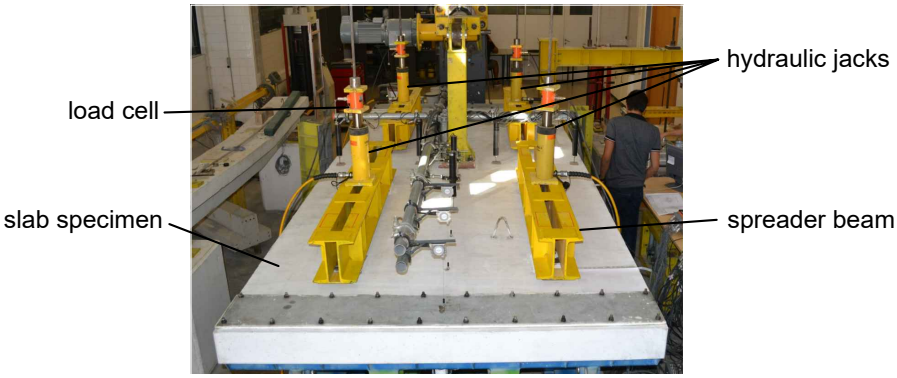


Figure 3.19: Gravity load application

were applied at the upper end of the column, following the protocol depicted in Figure 3.20. For drift ratios smaller than 4%, the cycles for each target drift were repeated three times, in order to observe the strength and stiffness deterioration during successive cycles. Two repetitions were performed for 4% drift ratio. For specimens that sustained higher drifts, only one cycle per target drift was completed. Target drifts in the protocol are increased in steps of 0.5% until failure of the specimen.

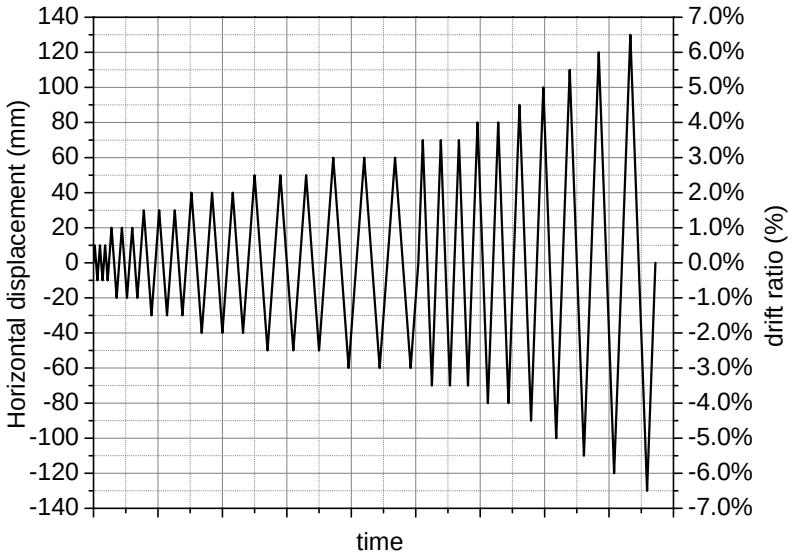


Figure 3.20: Horizontal displacements history for all specimens except C-SSR5b

For specimen C-SSR5b, a two–phase cyclic loading history was followed (Figure 3.21), resulting in the following overall loading phases:

- Phase I: Application of the full gravity load, reversed horizontal cyclic loading until a horizontal drift ratio of 3% (only half a cycle, for positive drifts only) and unloading of the gravity and horizontal loads;

- Phase II: Re-application of the gravity load with the same GSR and restart of the horizontal loading protocol from zero drifts to failure of the specimen.

This loading history for specimen C-SSR5b simulates a scenario in which the building experiences a major earthquake event (such that 3% drifts are imposed on the slab–column connection) but the connections successfully carry the gravity loads without punching failure. The specimen is reloaded to observe the strength and stiffness of the already cracked specimen and to observe the behaviour for drifts larger than those corresponding to the major seismic event.

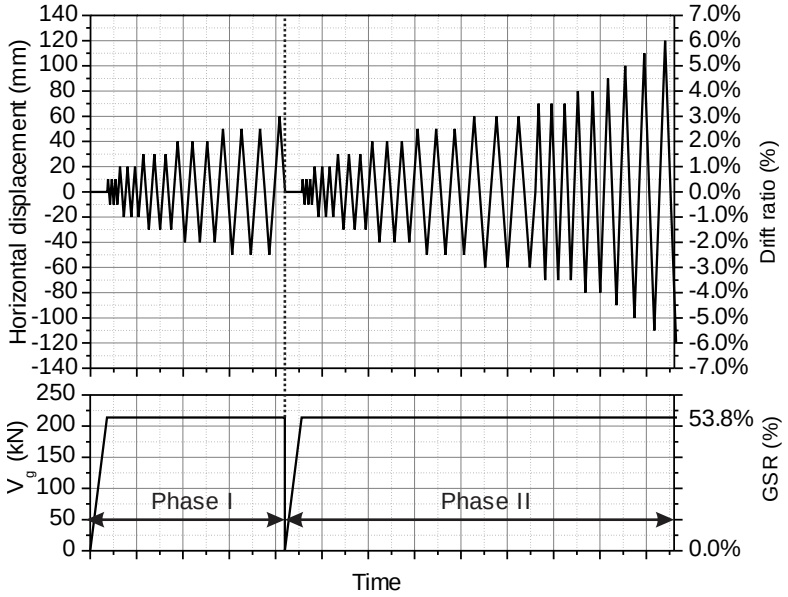


Figure 3.21: Horizontal displacements history for specimen C-SSR5b

## 3.7 Instrumentation

Strain gauges were installed in 15 studs of specimen C-SSR3 and in 25 studs of each of the specimens with five rows of studs, as indicated in Figure 3.5. Four bars of the top longitudinal reinforcement were also fitted with strain gauges in two symmetric locations near the column (Figure 3.2). Strain gauges were also installed in two bottom bars at locations close to the column and in the positive bending moment region (Figure 3.2). For the longitudinal bars, two strain gauges were installed in each monitored location (Figure 3.22a), on opposite sides of the bar. Due to the smaller diameter, a single strain gauge was installed in each monitored stud (Figure 3.22b). All the strain gauges were of type FLA-5-11-5L, by TML, with a gauge resistance of 120 Ω.

Fourteen displacement transducers (Figure 3.24a) were installed along the longitudinal axis of the slab and four others in the transversal direction to monitor the vertical deflections of the slab, in the locations indicated in Figure 3.23. Three types of displacement transducers were used, with measuring range of 50 mm (type CDP-50 by TML), 100 mm (type CDP-100 by TML) and 1270 mm (type SP3 by Measurement Specialities). The transducers with the smallest measuring range were positioned near the column (locations D6–D9 in Figure 3.23). The displacement transducers with the largest measuring range were installed in positions where maximum deflections are expected (D1–D3 and D12–D14 in Figure 3.23). Transducers with a 100 mm range were installed on all the other locations specified in Figure 3.23.

The applied gravity load was monitored throughout the test using four CLC-200KNA center-hole type compression load cells (by TML), one for each spreader beam, with maximum capacity of 200 kN (Figure 3.24b). The positive bending moments at the slab

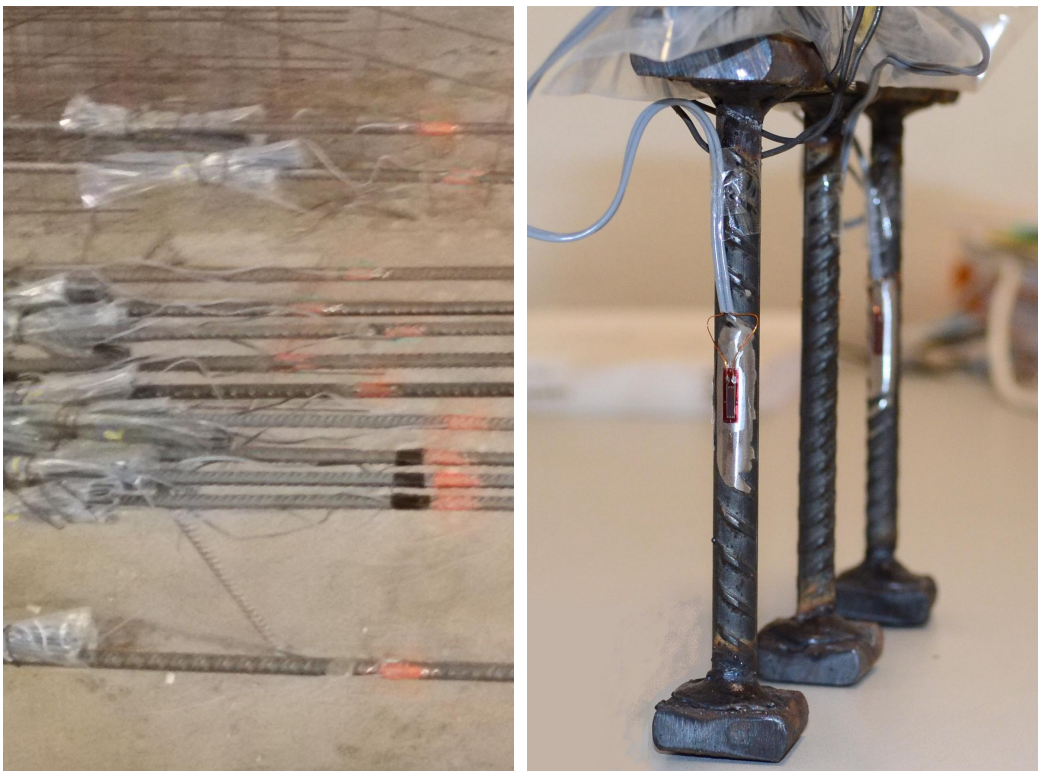

(a) Strain gauges in longitudinal bars (b) Strain gauges in a stud assembly

Figure 3.22: Strain gauges in longitudinal bars and studs

borders were also monitored by similar load cells located at the struts of the test setup (see Section 3.5 and Figure 3.24c). Inclinometers (type SST300, by Vigor Technology, with a measuring range ±30°) were used to monitor the rotations at the specimen borders and to indicate the necessity of slightly adjusting the force in the test setup strut elements in order to maintain equal rotations at the opposite borders. The actuator is equipped with a tension/compression load cell with capacity range of 500 kN and a displacement transducer with a measuring range of 500 mm to monitor the horizontal force and displacements during the application of horizontal drifts (Figure 3.24d).

## 3.8 Materials

### 3.8.1 Concrete

The mean value of the compressive strength of concrete cubes ($f_{c,cube}$) was determined as the average compressive strength of six cubes with side dimensions equal to 150 mm (Figure 3.25a). The tests were carried out on the same day as the respective slab. The cylinder compressive strength ($f_c$) was determined based on the compressive strength test of five cylinders with diameters of 150 mm and heights of 300 mm (Figure 3.25b). Prior to crushing, these five cylinders were used to determine the modulus of elasticity of concrete (Figure 3.25c). Five other cylinders were used to determine the tensile splitting

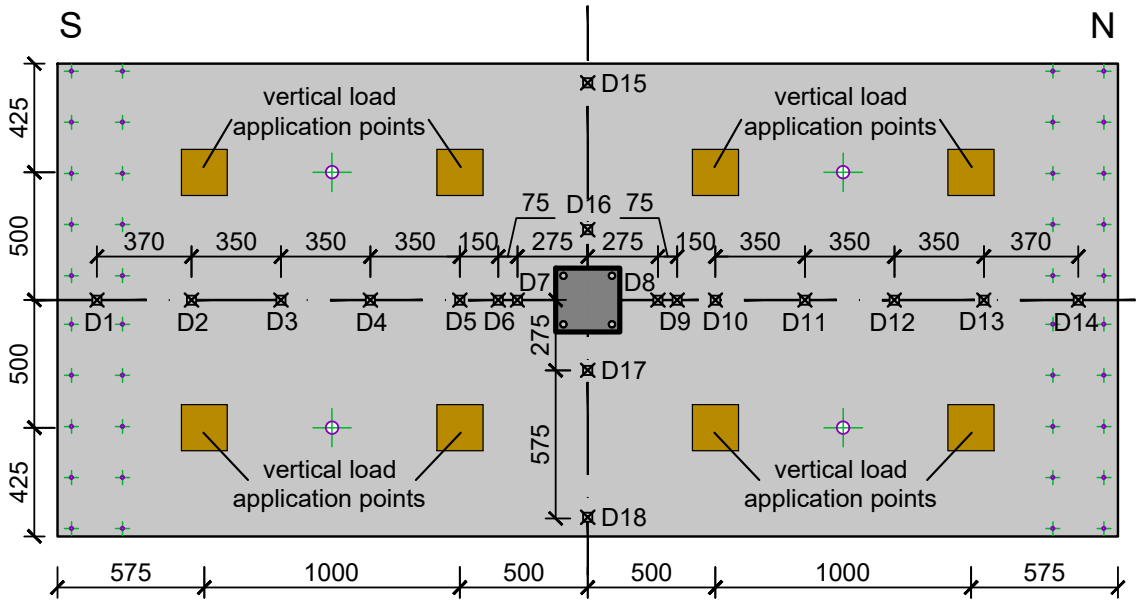


Figure 3.23: Displacement transducers and points of application of the vertical (gravity) loads

(a) Displacement transducers

(b) Hydraulic cylinder and load cell for gravity loading

(c) Hydraulic cylinders and load cells in the test setup struts

(d) Mechanical actuator and load cell

Figure 3.24: Photos of the instruments used to measure force and displacements

strength of concrete ($f_{ct,sp}$, Figure 3.25d). The tests were carried out in accordance with EN 12390-3 (CEN 2009a), EN 12390-6 (CEN 2009b) and EN 12390-13 (CEN 2013). The concrete properties determined from tests are summarized in Table 3.3.

(a) Cube compressive strength

(b) Cylinder compressive strength

(c) Modulus of elasticity

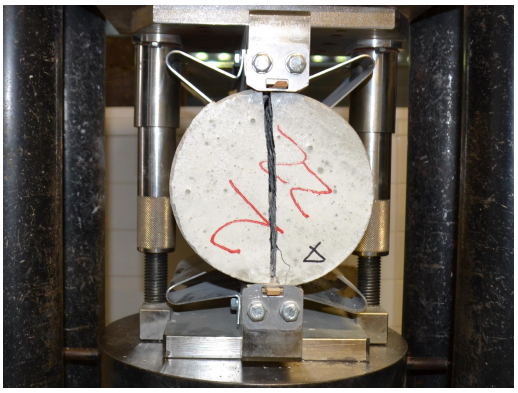

(d) Tensile splitting strength

Figure 3.25: Tests on concrete cubes and cylinders

Table 3.3: Average concrete properties determined from tests

| Specimen | age (days) | $f_c$ (MPa) | $f_{c,cube}$ (MPa) | $f_{ct,sp}$ (MPa) | $E_{cm}$ (GPa) |
|---|---|---|---|---|---|
| C-Ref | 150 | 62.3 | 66.1 | 4.4 | 41.4 |
| C-SSR3 | 63 | 41.2 | 44.2 | 3.2 | 35.2 |
| C-SSR5a | 76 | 27.0 | 28.6 | 2.3 | 30.9 |
| C-SSR5b | 44 | 57.6 | 58.3 | 4.1 | 38.8 |
| C-SSR5c | 146 | 69.9 | 70.0 | 4.2 | 39.6 |

### 3.8.2 Reinforcing steel

Three reinforcing bars from each batch were tested in tension (Figure 3.26) in accordance with ISO 15630-1 (ISO 2010). Table 3.4 summarizes the yield stress of the shear reinforcement ($f_{yw}$), as well as the yield stress of the longitudinal bars ($f_y$) and the corresponding yield strains ($\epsilon_y$). The ultimate tensile stress, $f_u$, is also given. For clarity and future reference, the properties are given for each specimen, although specimens C-SSR3 and

C-SSR5a were made of steel from the same supply and the three other specimens were made from another supply.

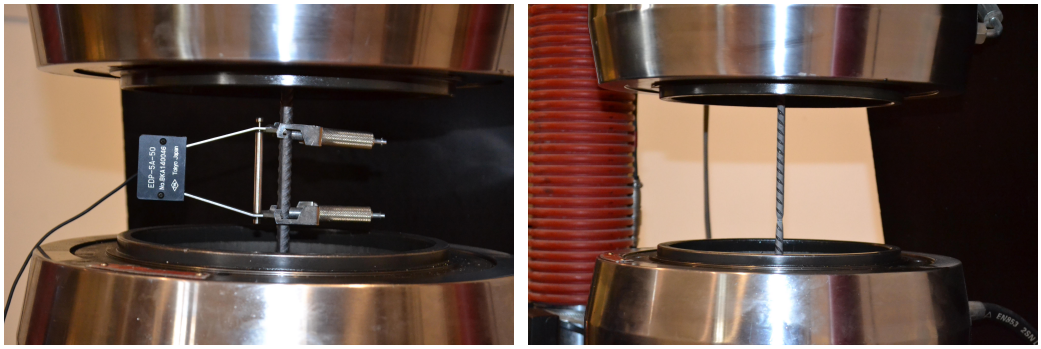

Figure 3.26: Tensile strength test of reinforcing bars

Table 3.4: Main steel reinforcement properties determined from tests

| Specimen | $f_y$ (MPa) | | $f_{yw}$ (MPa) | $f_u$ (MPa) | | | $\epsilon_y$ (%) | | |
|---|---|---|---|---|---|---|---|---|---|
| | Φ10 | Φ12 | Φ8 | Φ8 | Φ10 | Φ12 | Φ8 | Φ10 | Φ12 |
| C-Ref | 549.5 | 541.9 | - | - | 647.5 | 643.6 | - | 0.27 | 0.27 |
| C-SSR3 | 523.9 | 544.9 | 485.0 | 584.9 | 620.7 | 629.3 | 0.24 | 0.26 | 0.27 |
| C-SSR5a | 523.9 | 544.9 | 485.0 | 584.9 | 620.7 | 629.3 | 0.24 | 0.26 | 0.27 |
| C-SSR5b | 549.5 | 541.9 | 488.8 | 575.8 | 647.5 | 643.6 | 0.24 | 0.27 | 0.27 |
| C-SSR5c | 549.5 | 541.9 | 488.8 | 575.8 | 647.5 | 643.6 | 0.24 | 0.27 | 0.27 |

Continuous reading of the strains up to failure was not possible due to limitations of the testing equipment. The ultimate strains (at tensile failure of the reinforcing bars) were estimated approximately. For all the steel batches, the average ultimate strain exceeded 11%. Nonetheless, the force up to failure was recorded and it was used to determine $f_u$ in Table 3.4.

### 3.8.3 Aggregates

The maximum aggregate size is required in the formulation of the failure criterion based on CSCT (see Section 2.2.3.1). The aggregate size influences the roughness of the crack and, consequently, the amount of shear that can be transferred across the critical shear crack (Muttoni 2008).

For specimens C-SSR3 and C-SSR5a, the maximum aggregate size was provided by the company that produced the concrete. For these two specimens, the maximum aggregate size was 12 mm. For the other three specimens, a sample of the aggregates was taken and a sieve analysis was performed in accordance with NP EN 933-1 (CEN 2000). Figure 3.27a is a photo of the aggregates and Figure 3.27b shows the sieves and the sieve shaker. The test was repeated on three batches of aggregates and the results are plotted in Figure 3.27c. The maximum aggregate size resulted 12.5 mm. This was the smallest sieve opening for

which less than 10% of the mass was retained. The result was confirmed independently by the company that produced the concrete.

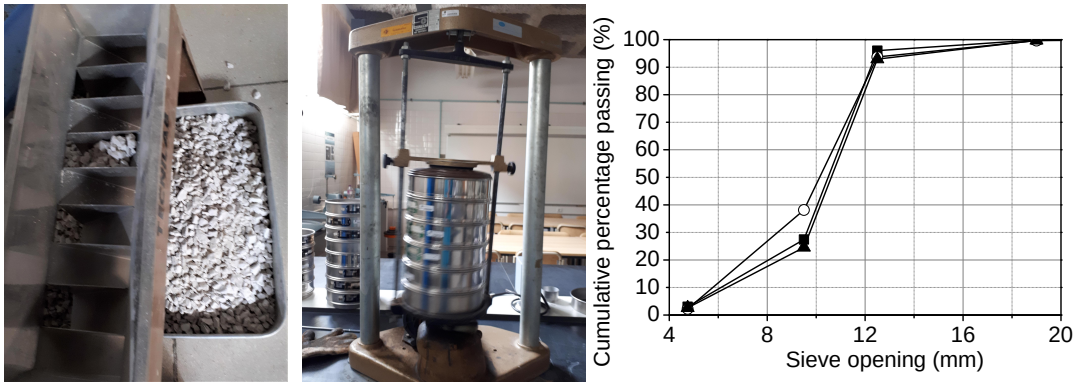


(a) Aggregates (b) Sieves and apparatus (c) Sieve analysis results

Figure 3.27: Sieve analysis of the aggregates for C-Ref, C-SSR5b, C-SSR5c

## 3.9 Gravity loading

The total gravity load applied in each specimen, $V_g$, (including self–weight and the weight of equipment) for each specimen is given in Table 3.5. This table contains also the shear resistance $V_0$ calculated in accordance with EC2 (CEN 2004c) with average values for material properties (Section 3.8) for concentric loading without the contribution of the shear reinforcement, as follows:

$$V_0 = 0.18k(100\rho_l f_c)^{1/3} ud \tag{3.1}$$

where $\rho_l$ is the longitudinal reinforcement ratio calculated as the geometric mean of reinforcement ratios in each direction (but limited to 0.02), $f_c$ is the concrete cylinder strength, taken equal to the average strength as determined by tests, $d$ is the effective depth of the top longitudinal reinforcement, calculated as the average value of the measured effective depths for each direction (Table 3.2), $u$ is the control perimeter, taken in accordance with EC2 at a distance $2d$ from the face of the column and $k = 1 + \sqrt{200/d} \leq 2$ is a factor accounting for size effect. For the range of effective depths for the specimens (Table 3.2), the calculated value of $k$ exceeds 2. Therefore, $k = 2$ is considered for all the specimens.

The values of the Gravity Shear Ratio (GSR) are given in Table 3.5. As discussed in Chapter 2, these values are obtained as the ratio $V_g/V_0$. All specimens had approximately the same GSR around 0.55 (55%), except for C-SSR5c in which a GSR approximately 0.10 higher was applied.

Table 3.5: Gravity load and GSR applied in each specimen

| Specimen | $V_0$ (kN) | $V_g$ (kN) | $GSR$ (%) |
|---|---|---|---|
| C-Ref | 412.8 | 224.8 | 54.5 |
| C-SSR3 | 358.7 | 196.4 | 54.7 |
| C-SSR5a | 310.3 | 169.2 | 54.5 |
| C-SSR5b | 397.9 | 213.9 | 53.8 |
| C-SSR5c | 429.0 | 275.0 | 64.1 |

The choice regarding the applied gravity load was based on a combination of detected voids in literature, previous experimental campaigns under similar conditions but with other types of shear reinforcement and limitations of the test setup. Tests reported in Almeida et al. 2018 showed that similar specimens, but with stirrups, were able to sustain relatively large drift ratios. Since it is impossible due to limitations of the test setup and because there is little practical interest in testing specimens that sustain drifts larger than 6%, relatively high values of GSR were adopted. On the other hand, it was found impractical to apply GSR higher than 65%, since it would result in significant yielding of the longitudinal reinforcement before even starting the reversed horizontal cycles.

## 3.10 Cyclic loading tests

### 3.10.1 C-Ref

The application of the gravity load was associated with the appearance of few flexural cracks in both negative (approximately 0.2 mm wide) and positive (about 0.1 mm wide) bending moment regions. Cracks developed further, and their width gradually increased during the application of horizontal drifts. New flexural cracks became visible at 0.5% drift ratio (Figure 3.28a) at distances further away from the column's face. Narrow radial cracks were visible, originating from the corners of the column.

At the first two 1.0% drift cycles, the cracks developed further, and their width gradually increased. By the end of the second cycle of 1.0% drifts, signs of the initiation of a punching failure were present. Relative shear displacement of concrete cover was observed at distances 100 mm to 200 mm from the faces of the column and the radial cracks were increased in number and width, reaching up to 0.3 mm wide at the sides of the specimen and wider closer to the column (Figure 3.28b). A brittle punching failure occurred in the third cycle at 1% drift ratio. Photos of the specimen at failure are shown in Figure 3.28c and Figure 3.28d. It is noticed that top reinforcement bars shattered the concrete cover around the column, which resulted in the production of rubble all over the affected area. The bottom part of the slab suffered very few visible damage (Figure 3.28d) outside the column's cross section as the column punched through the slab.

Saw-cut of specimen C-Ref (Figure 3.36) reveals a typical punching failure, with a

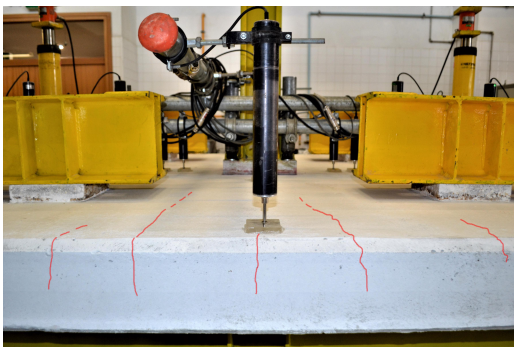

(a) 0.5% drifts

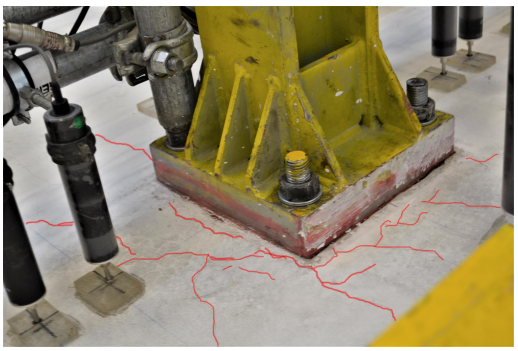

(b) 1.0% drifts

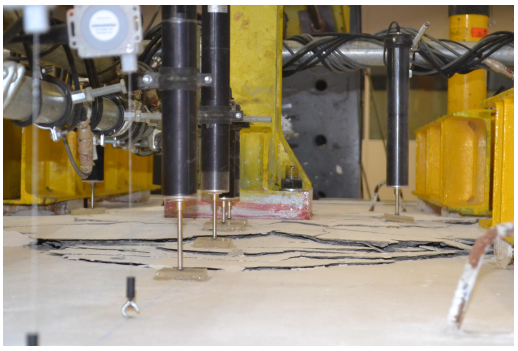

(c) Punching failure (top surface)

(d) Punching failure (bottom surface)

Figure 3.28: Photos during the cyclic loading test of specimen C-Ref

diagonal crack inclined at approximately 40°–45° from the horizontal and originating from the bottom face of the slab around the column. It was observed that the vertical relative displacement between the failure cone and the rest of the slab was larger than the relative displacement in the other specimens (see Figure 3.36). This is explained by the smaller failure cone compared to the other specimens, which engages fewer longitudinal bars.

### 3.10.2 C-SSR3

Flexural cracks were observed in the top face of the slab near the column after the application of the full gravity load (Figure 3.29a). Small radial cracks appeared in the top face of the slab at the column region for 0.5% drift ratio. The cracks continued to develop further for larger drifts. At 2.0% drift ratio, minor flexural cracks started to appear at positive bending moment regions, whereas the cracks on the top face were opened considerably. At 3% drift ratio, a tangential crack appeared at approximately 50–60 mm away from the column face and the connection reached its maximum unbalanced moment capacity (Figure 3.29b). At 3.5% drift, more radial cracks propagated; however, the hysteretic behaviour remained stable without significant strength degradation. Stable behaviour was also observed in the first cycle of 4.0% drift ratio, but a sudden punching failure

occurred during the second cycle (Figure 3.29c, Figure 3.29d), leading to an immediate reduction of the horizontal load. The top surface concrete cover was spalled in a relatively large diameter compared to the extent of shear reinforcement. The concrete cover in the bottom face of the slab was also spalled (Figure 3.29d), especially at the locations of the shear studs.

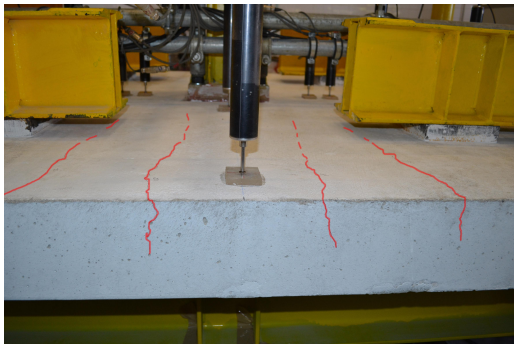

(a) After gravity loading

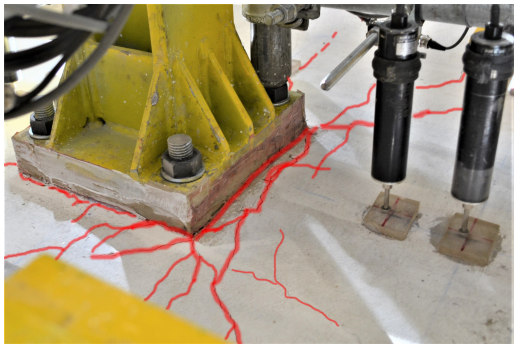

(b) 3.0% drifts

(c) Punching failure (top surface)

(d) Punching failure (bottom surface)

Figure 3.29: Photos during the cyclic loading test of specimen C-SSR3

The saw–cut of the specimen (Figure 3.36) reveals that punching occurred outside the shear reinforced zone. Spalling of concrete cover was observed in the lower part of the slab and the diagonal crack was initiated exactly at the lower part of the studs of the outer shear reinforcement perimeter. Above the top reinforcement, the angle to the horizontal was decreased and the failure region was extended up to a radius ranging approximately from 650 mm to 750 mm from the axis of the column, due to concrete cover spalling.

From the saw–cut it can also be observed that almost vertical bending cracks were developed near the column face. The area bounded by shear studs was not excessively cracked, and damage was more pronounced between the column region and the first stud and outside the third and last stud. A relatively outstretched and slightly non-symmetrical crack is observed from the saw-cut. The inclination of the crack from the horizon is 35° to 41°.

### 3.10.3 C-SSR5a

Flexural cracks were observed in the upper face of the slab near the column after the application of the full gravity load. Flexural cracks aligned transversally to the slab developed starting from 0.5% drift ratio and gradually increased throughout the test. Cracking was increased at a slow pace with the increase of horizontal drifts (Figure 3.30a, Figure 3.30b). Most of the damage was concentrated in vicinity of the column face. A crack parallel to the face of the column, located at a distance 30 to 50 mm from the column, developed in the early stages of cyclic loading but was opened considerable throughout the test. At large drifts (starting from around 4%), the crack opening on each side of the column became visibly distinct from the rest of the cracks, due to the large opening and the noticeable shear displacement of the concrete along the crack (Figure 3.31). The specimen reached a horizontal drift ratio of 6.0% with a gradual degradation of the horizontal load and without a visible punching failure (Figure 3.30c). The bottom face of the column, however, was excessively damaged (Figure 3.30d) and the distinct crack near the column on the top face continued to increase. The test ended after completing a full cycle at 6.0% drift.

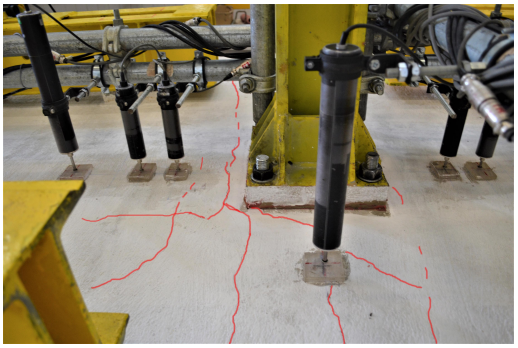

(a) 1.0% drifts

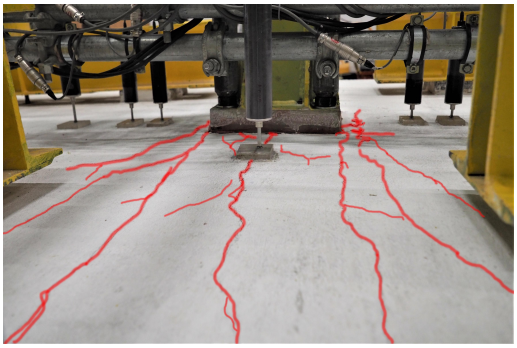

(b) 4.0% drifts

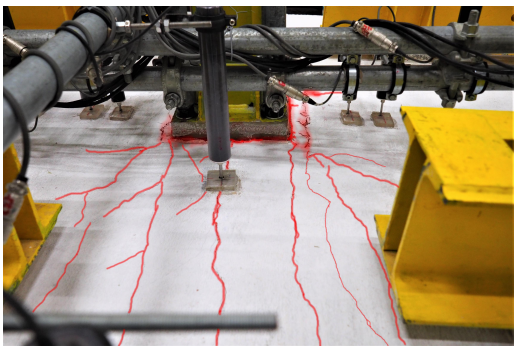

(c) 6.0% drifts (top surface)

(d) 6.0% drifts (bottom surface)

Figure 3.30: Photos during the cyclic loading test of specimen C-SSR5a

Signs of the initiation of a punching failure at the end of the test are visible in the saw-cut (Figure 3.36). However, as described above, a brittle punching failure did not

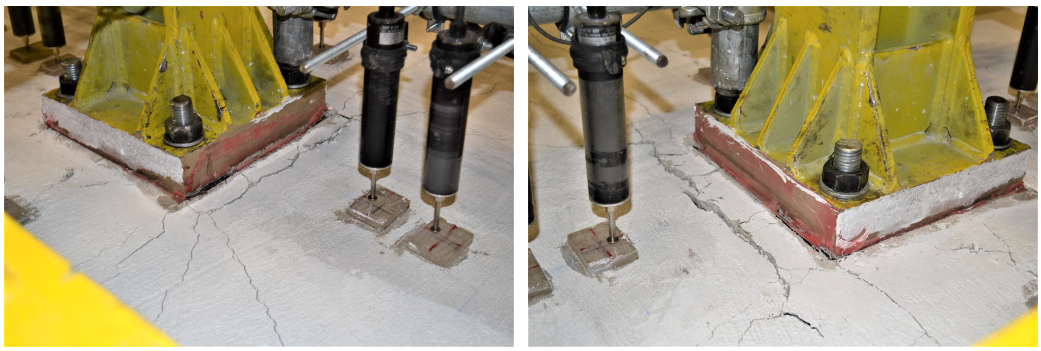

(a) North side, +6.0% drift (b) South side, -6.0% drift

Figure 3.31: Photos of the distinct crack near the column at specimen C-SSR5a

occur. Besides the cracks visible from the top face, interior cracks with various angles to the horizontal can be seen in the saw-cut. One of the cracks passed almost horizontally through the bottom concrete cover of the shear reinforcement. Another crack, smaller and barely visible, propagated from the bottom part of the first shear stud and stretched diagonally to the top surface, passing through the shear studs of the second perimeter up to near the top part of the studs of the third perimeter. Finally, two larger cracks found their way through the region bounded by the column and the first shear stud. One of the cracks was almost vertical, the other was at an angle of about 75°.

### 3.10.4 C-SSR5b

#### 3.10.4.1 Phase I

Small negative and positive bending moment cracks were observed during the application of the gravity load. For the first horizontal cycles, new cracks developed, and the openings of the existing cracks further increased. At 1.0% drift, there were three visible cracks on each side of the column on the top face and small radial cracks. Cracking continued to extend, starting from 1.5% drift (Figure 3.32a), where radial cracks became visible and the crack next to the face of the column opened considerably. After the completion of the first 3.0% drift (Figure 3.32c, 3.32d), the slab was cracked along the entire length (in positive and negative bending moment regions). Some concrete spalling was observed in the bottom face of the slab near the column but there were no signs indicating the initiation of a punching failure. This marked the end of the first phase.

#### 3.10.4.2 Phase II

No major developments were observed at up to 3.0% drifts when the loading protocol was restarted from zero in the second cyclic loading phase. Before restarting the horizontal loading protocol, cracking was already extensive (Figure 3.33a). The crack widths measured at the border of the specimen were 0.7 mm on the top face near the column region and relatively small at the positive bending moment region. Only few new cracks

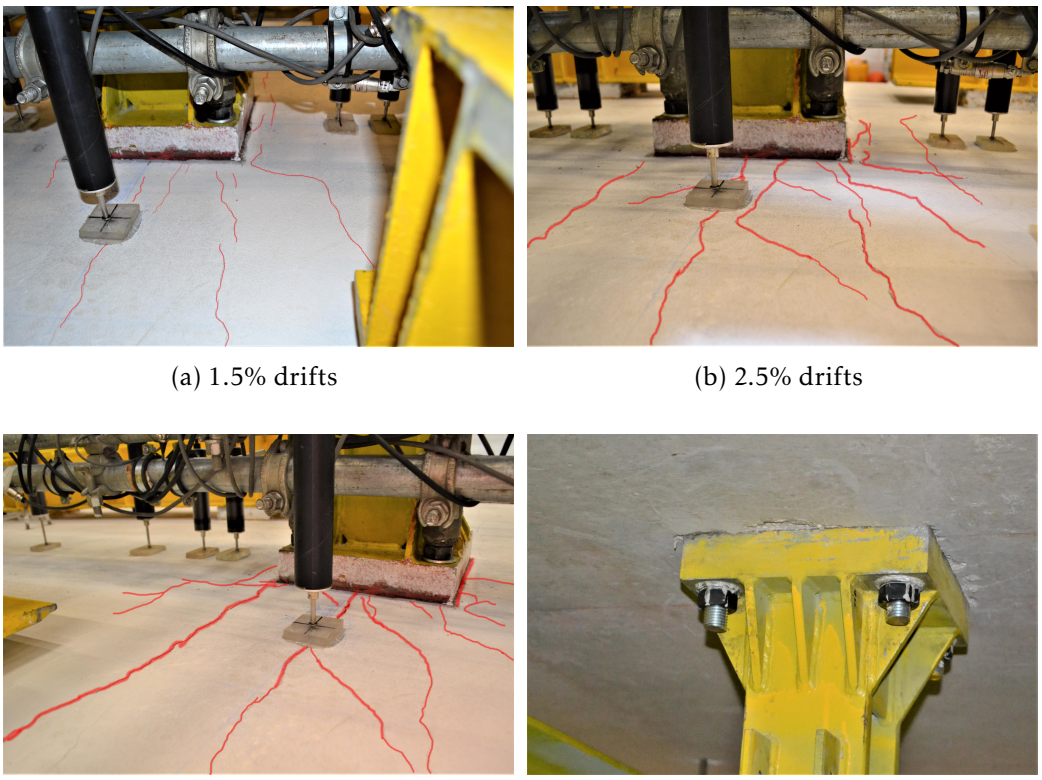

(a) 1.5% drifts

(b) 2.5% drifts

(c) 3.0% drifts (top surface)

(d) 3.0% drifts (bottom surface)

Figure 3.32: Photos during the first phase of cyclic loading test of specimen C-SSR5b

were observed and widening of existing cracks was gradual and slow up to 3.0% drifts. For instance, at around 1.5% drift ratio, the cracks of the negative and positive bending moment regions met (this was visible at the edges of the specimen). At 2.5%, the radial cracks developed considerably. When seen from the sides of the specimen, they reached the mid–thickness of the slab. Maximum crack openings became larger than 1.0 mm.

Once the specimen reached the drift at which the test was stopped in the previous phase (i.e., 3.0%), damage started to increase at a higher rate. At 3.0% the crack widths on the top face were around 1.4 mm, with a distinct wide crack about 120 mm from the face of the column on the west side, that reached an opening of 2.5 mm. Cracking continued to develop all over the specimen (Figure 3.33b). At 3.5% to 4.5%, the bottom part of the slab was severely damaged. A crack along the E–W direction (perpendicular to the direction of cyclic loading) became notably wide at drifts above 5.0% (Figure 3.33c, Figure 3.33d). The bottom part of the column punched through the slab a few millimetres and continued to punch progressively with the increase of the drifts, until a one-sided punching failure occurred on the north side of the specimen, outside the shear reinforced zone (Figure 3.33e, Figure 3.33f). The specimen had successfully sustained a complete 5.5% drift cycle but reached the 6.0% drift level only after it punched mid-way (at around 90 mm horizontal displacement).

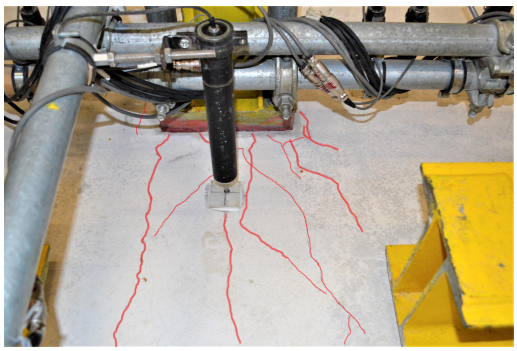

(a) Re-application of $V_g$

(b) 4.0% drifts

(c) 5.5% drift

(d) Crack opening at 5.5% drift

(e) Punching failure (top surface)

(f) Punching failure (bottom surface)

Figure 3.33: Photos during the second phase of cyclic loading test of specimen C-SSR5b

Specimen C-SSR5b was not forced to complete the full cycle after the one–sided punching failure, therefore a single sided failure can be observed in the saw–cut of Figure 3.36. However, this offers some insight regarding the situation just prior to punching failure. The saw–cut reveals that prior to the development of the inclined crack marking the punching failure, there were already significant cracks passing from the bottom part of the slab near the column to the first row of studs and other cracks with varying inclination and passing through the studs of the second and third row at angles from 80°to 20°. Generally symmetrical cracks were observed on the punched side, but with a slightly smaller width and length. The inclined failure crack was similar to that of the specimen C-SSR3, even though the extent of shear reinforcement was larger in specimen C-SSR5b. The crack was inclined at circa 25° from the horizontal.

### 3.10.5 C-SSR5c

The effects of the increased gravity load in C-SSR5c were visually detectable in comparison to the other specimens. At the end of the application of the full gravity load, flexural cracks in negative and positive bending moment regions were present, as well as radial cracks. The negative bending moment cracks were larger than the other types, reaching values up to 0.2 mm at the sides of the specimen and larger (but not measured) values near the column. The cracks were spaced at around 150 to 200 mm. Small new radial cracks started to develop at 0.5% drifts. At the sides of the specimen, the negative moment cracks reached two thirds of the height of the slab. At 1.0% drift, positive moment cracks extended up to about 500 mm from the northern and southern border. The width of the radial cracks reached 0.2 mm, whereas the width of the crack near the column's perimeter on the top face reached 0.6 mm. With increased drifts, cracks continued to develop in number and width (Figure 3.34a).

At 1.5% drift, visible damage appeared near the column perimeter at the bottom face. At 2.0%, cracks developed along the entire specimen, that is the negative and positive regions were all cracked. Negative moment cracks remained wider than the other types throughout the entire test. At 2.5%–3.0% drifts, the damage extended further (Figure 3.34b). The crack widths reached 1.6 mm and were further opened to 2.0 mm before failure. The upper and lower parts of the slab were severely damaged at 3.5%–4.0% drift (Figure 3.34c, Figure 3.34d) and signs of the initiation of a punching failure were present. After the successful completion of a 4.0% drift cycle, a one-sided punching failure occurred on the northern side when the specimen was reaching the positive 4.0% drift cycle. The specimen was then forced to complete the cycle and the punching failure developed on the other side as well when attempting to reach the -4.0% drift ratio (Figure 3.34e). Severe damage was observed underneath the slab (Figure 3.34f) with a tendency of alignment of the spalled area along the E–W direction in the transversal axis of the slab.

Due to the increased gravity load compared to the other specimens, the deflections of the slab were noticeable with the naked eye, even for small horizontal drifts. A photograph of the deformed specimen, at a horizontal drift ratio of 4.0% is given in Figure 3.35.

The saw cut of specimen C-SSR5c (Figure 3.36) revealed a relatively steep angle of the inclined crack, and a significant variation in the angle towards the horizontal along the thickness of the slab. In this specimen, the vertical cracks near the column face reached the bottom face of the slab. The crack pattern between the studs was similar to that observed in the other specimens, although the region between the second and the third row of studs was not affected by visible cracks. However, a crack that has started to propagate from the bottom head of the fourth stud and extended approximately 20 mm towards the top head of the fifth stud was present in this saw-cut. A similar crack was observed in specimen C-SSR5b, but not in the other specimen with 5 rows of studs.

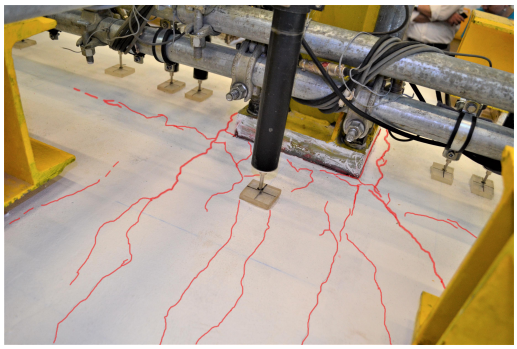

(a) 1.5% drifts

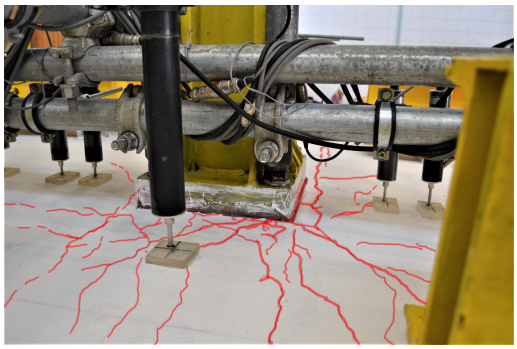

(b) 2.5% drifts

(c) 3.5% drifts (bottom face)

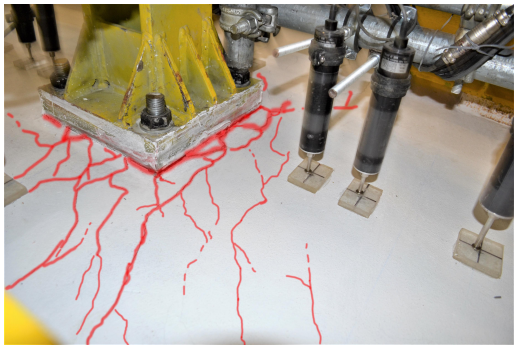

(d) 3.5% drifts (top face)

(e) Punching failure (top surface)

(f) Punching failure (bottom surface)

Figure 3.34: Photos during the cyclic loading test of specimen C-SSR5c

Figure 3.35: Visible deformation of the specimen C-SSR5c at 4.0% drift

An additional saw-cut in the transversal direction of specimen C-SSR5c was performed to get a clearer view about the type of failure for this specimen and the other specimens that failed outside the shear-reinforced zone. The transversal saw-cut (Figure 3.37) revealed that the failure mode was indeed a punching failure. It was found through the transversal section (E–W direction) that damage inside the slab thickness is more pronounced in this direction. This is explained by the large flexural moment acting on the section.

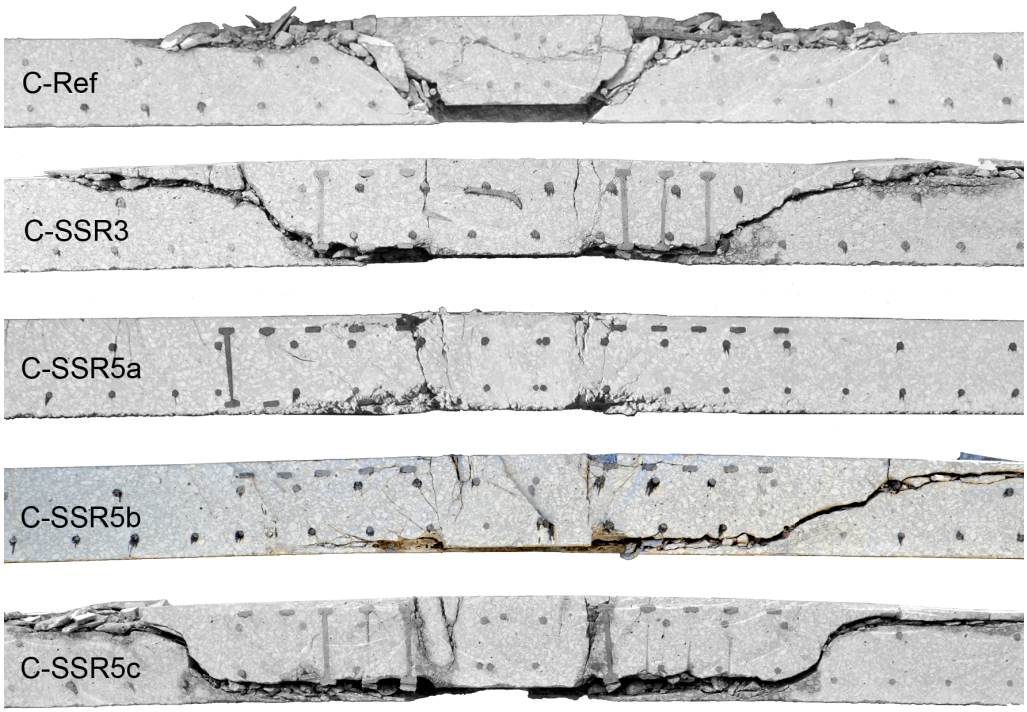


Figure 3.36: Saw–cuts in longitudinal direction (N–S)

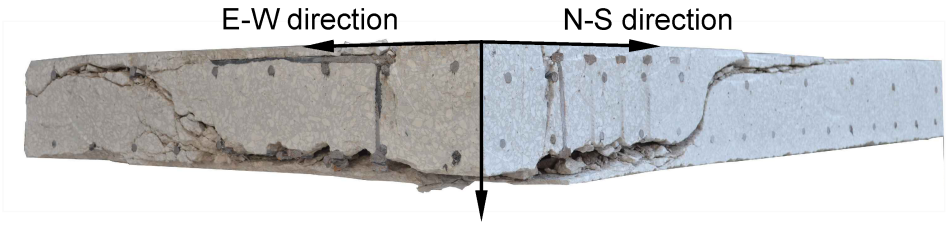


Figure 3.37: Two-directional saw-cut of specimen C-SSR5c (photographed at the corner of the cut specimen, distorted due to perspective)

# Chapter 4

# Analysis of experimental results

The results from the experimental campaign are analysed in this chapter. First, the load–deformation relationships are presented and discussed. Various factors are calculated based on the load–deformation data (equivalent viscous damping ratios, displacement ductility, residual deformation indices and the lateral stiffness). Based on the processing of the readings from the displacement transducers, the deflected shapes of the specimens in the longitudinal and transversal direction are also presented. The chapter continues with the presentation and analysis of the readings from the strain gauges installed in the flexural and shear reinforcement. A section is dedicated to the post–earthquake behaviour of flat slabs, based on a refined analysis of specimen C-SSR5b. Finally, the results of the experimental campaign are compared with code predictions, analytical models used to estimate the unbalanced moment and with other similar specimens from past experimental research.

## 4.1 Load–deformation responses

Hysteretic diagrams, showing the horizontal force–displacement (unbalanced moment–drift ratio) relationships, are given in Figures 4.1–4.5 and in Isufi et al. 2018b. Based on the geometry and conditions of the test setup, the unbalanced moment and the drift ratios are directly obtained by respectively multiplying the horizontal force and dividing the horizontal displacement by the total height of the column (2 m).

From the figures, it is noticed that the hysteresis diagrams were stable for all specimens. The specimen that did not fail in punching (C-SSR5a, Figure 4.3) suffered a gradual loss of horizontal load up to about 18.3% of the peak value. In the other specimens, the punching failure was associated with a sudden and significant (more than 20%) drop of the horizontal load.

To facilitate the comparison between the load–deformation responses, the envelope curves for positive displacements are given in Figure 4.6 for all tested specimens. All specimens, except C-Ref, reached an almost horizontal plateau in the load–deformation

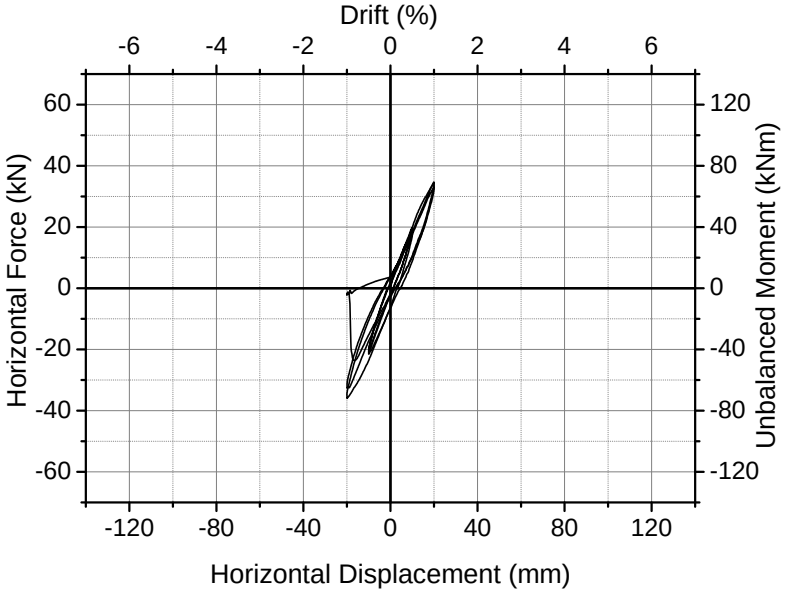


Figure 4.1: Hysteretic diagram of specimen C-Ref

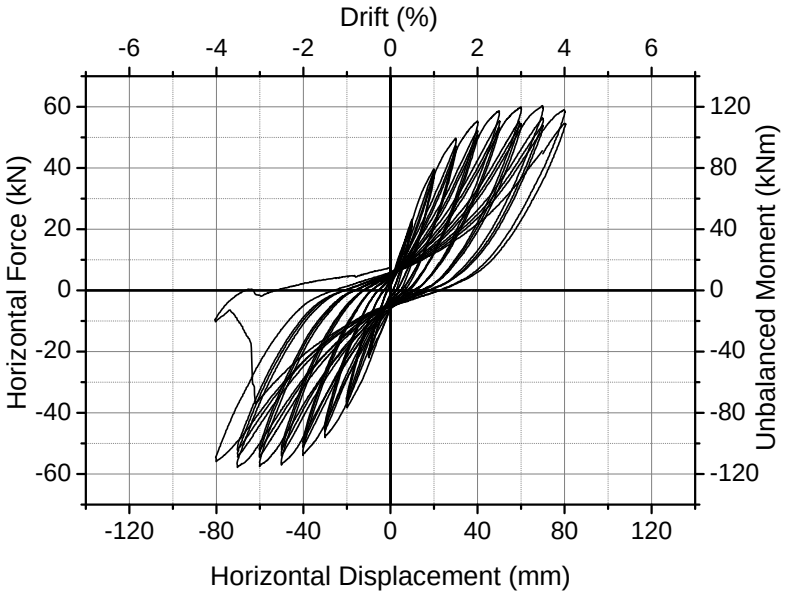


Figure 4.2: Hysteretic diagram of specimen C-SSR3

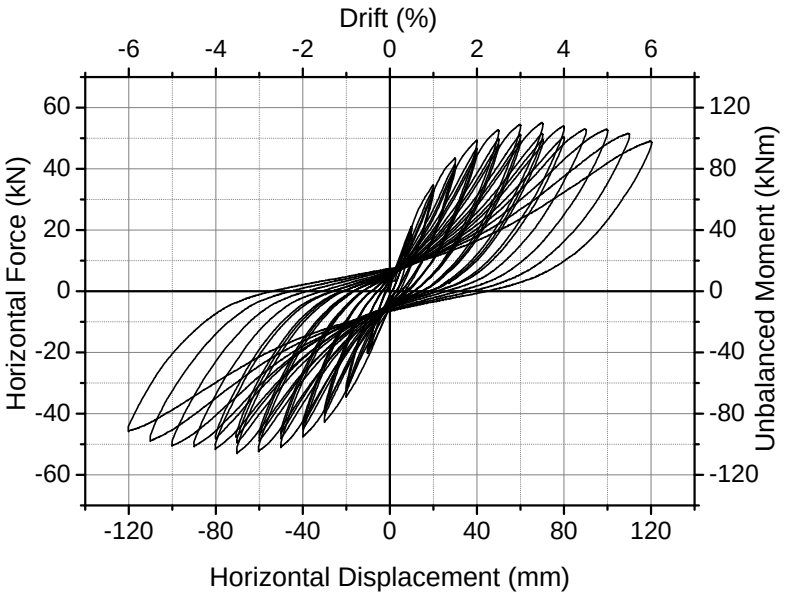


Figure 4.3: Hysteretic diagram of specimen C-SSR5a

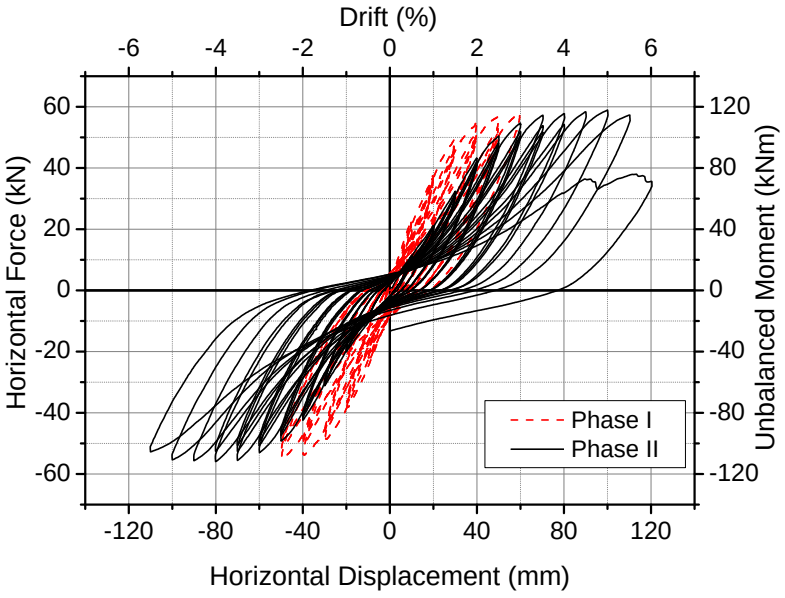


Figure 4.4: Hysteretic diagram of specimen C-SSR5b

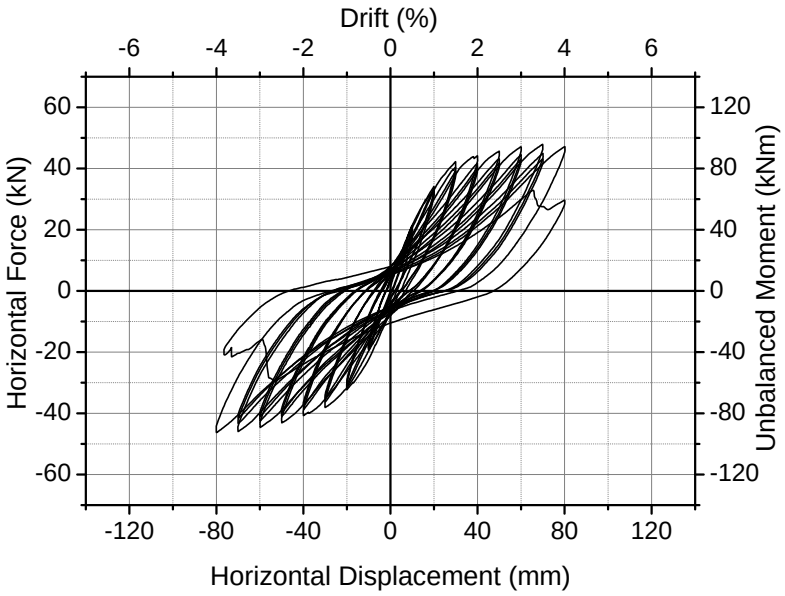


Figure 4.5: Hysteretic diagram of specimen C-SSR5c

response at around 3.0% drift ratio, with a maximum horizontal force at around 3.5% drift due to yielding of the top reinforcement. The applied gravity load influenced the maximum horizontal force. For instance, the envelope curve of specimen C-SSR5c is considerably lower than the other curves in Figure 4.6, due to the higher Gravity Shear Ratio applied to this specimen.

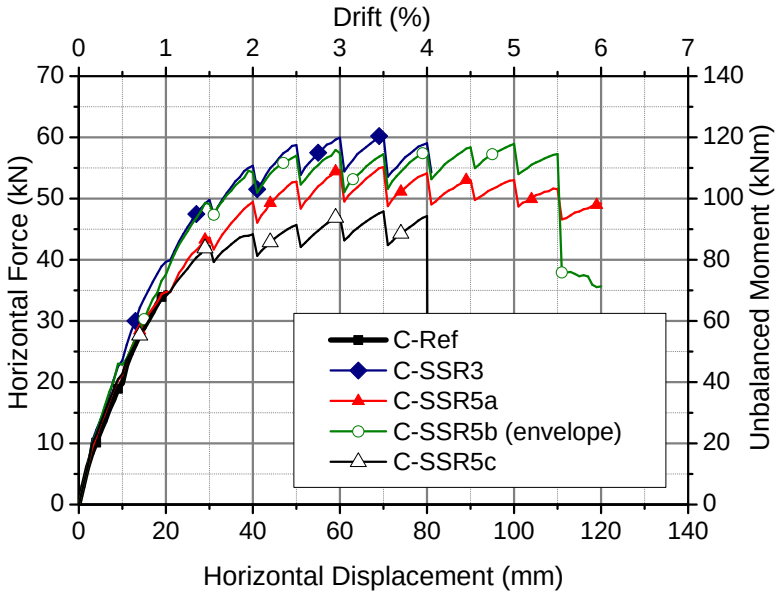


Figure 4.6: Envelope curves for positive horizontal displacements

A summary of the maximum horizontal force ($P_{max}$), the corresponding drifts ($d_{r,Pmax}$), maximum drifts attained before failure ($d_{r,u}$) and a description of failure for each specimen is contained in Table 4.1. It is noticed that the maximum horizontal force was

reached at drift ratio 3.5% for all specimens except C-Ref which failed at a lower drift and specimen C-SSR5b that followed a different loading history. For specimen C-SSR5b, the restart of the protocol after reaching 3.0% drift postponed the deformation for which the maximum horizontal force was attained, but it did not impair the ability of the specimen to reach a maximum force comparable to that of the other specimens.

Table 4.1: Force, drifts and failure modes

| Specimen | $P_{max}$ (kN) | $d_{r,Pmax}$ (%) | $d_{r,u}$ (%) | Description |
|---|---|---|---|---|
| C-Ref | 36.0 | 1.0 | 1.0 | Punching failure prior to full yielding of top reinforcement |
| C-SSR3 | 60.4 | 3.5 | 4.0 | Punching failure outside the shear-reinforced zone after yielding of top reinforcement |
| C-SSR5a | 55.2 | 3.5 | 6.0 | Gradual loss of horizontal force after flexural yielding of top reinforcement and signs of initiation of a punching failure between the face of the column and the first row of studs |
| C-SSR5b | 58.9 | 5 | 5.5 | Punching failure outside the shear-reinforced zone after yielding of top reinforcement |
| C-SSR5c | 47.9 | 3.5 | 4.0 | Punching failure outside the shear-reinforced zone after yielding of top reinforcement |

## 4.2 Equivalent viscous damping

To compare the energy dissipation capacity of the specimens and to observe the effect of repeated cyclic loading, an equivalent viscous damping coefficient $\xi_{eq}$ was calculated for each complete cycle. The procedure outlined in Hose and Seible 1999 was followed, according to which:

$$\xi_{eq} = \frac{1}{4\pi}\left(\frac{E_{d1}}{E_{s1}} + \frac{E_{d2}}{E_{s2}}\right) \tag{4.1}$$

where $E_{d1}$ and $E_{d2}$ are the areas within the hysteresis curve for positive and negative displacements, whereas $E_{s1}$ and $E_{s2}$ are the elastic strain energies for positive and negative displacements respectively, as described in Figure 4.7.

The coefficients $\xi_{eq}$ are plotted in Figure 4.8a for complete cycles (i.e., excluding the cycle in which failure occurred) as a function of the drift ratio for all specimens except C-SSR5b. For the two test phases of specimen C-SSR5b, the results are shown separately in Figure 4.8b for clarity. To increase readability, the values are shown in the figure slightly scattered around the fixed drift levels of the loading history. The size of the markers in Figure 4.8 represents the cycle: the first cycle has the largest marker.

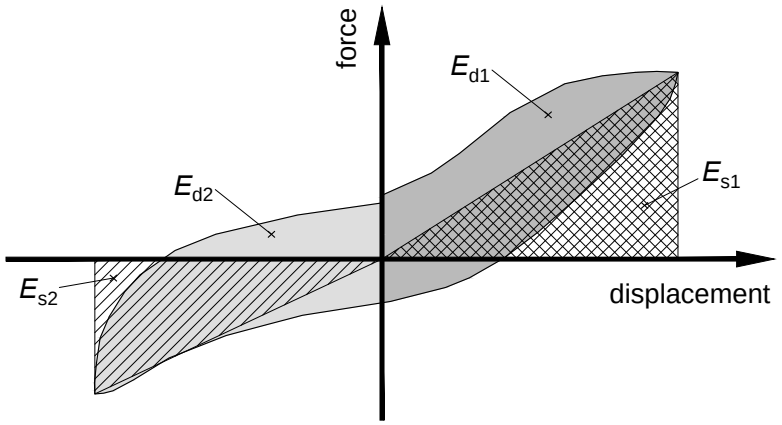


Figure 4.7: Definition of quantities needed for the calculation of the equivalent viscous damping coefficient $\xi_{eq}$

Figure 4.8 shows that specimen C-SSR5c had the highest values of $\xi_{eq}$. It should be noted that this specimen had higher gravity loads than the other specimens, leading to significant nonlinearity even for low horizontal drift ratios. Repetition of the cycles at a previously experienced drift ratio leads to a decrease of $\xi_{eq}$, due to stiffness deterioration. For the first cycles in each drift level, damping appears to have a minimum value at around 2.0–2.5% drift ratio, which corresponds to the last phases of loading before approaching a horizontal plateau in the global unbalanced moment–drift relationship. After that point, the values tend to increase, except for specimen C-SSR5c. Figure 4.8 also shows that the first cycles up to 1.0% drift have a higher equivalent viscous damping coefficient due to the significant damage in the specimen and, therefore, the low elastic strain energy (Equation 4.1).

## 4.3 Displacement ductility and Residual Deformation Index

The Residual Deformation Index (RDI) is a parameter that is often used as an estimator of damage in structural elements subjected to earthquake loading. RDI is obtained as the ratio between the residual horizontal displacement $\Delta_r$ and the ideal yield displacement $\Delta_y$ (Hose and Seible 1999). Herein, the RDI is calculated for positive displacements only, and the ideal yield displacement $\Delta_y$ is calculated from the backbone curve, idealized into an elasto–plastic relationship with the same area under the curve, following a procedure similar to that described in EC8 (CEN 2004d, Annex B, for pushover analysis of structures). The ideal yield displacement $\Delta_y$ is therefore:

$$\Delta_y = 2\left(\Delta_{Pmax} - \frac{E}{P_{max}}\right) \tag{4.2}$$

where $\Delta_{Pmax}$ is the horizontal displacement for maximum horizontal force $P_{max}$ and $E$ is the total area under the curve up to $P_{max}$ (Figure 4.9a). For all the specimens, the

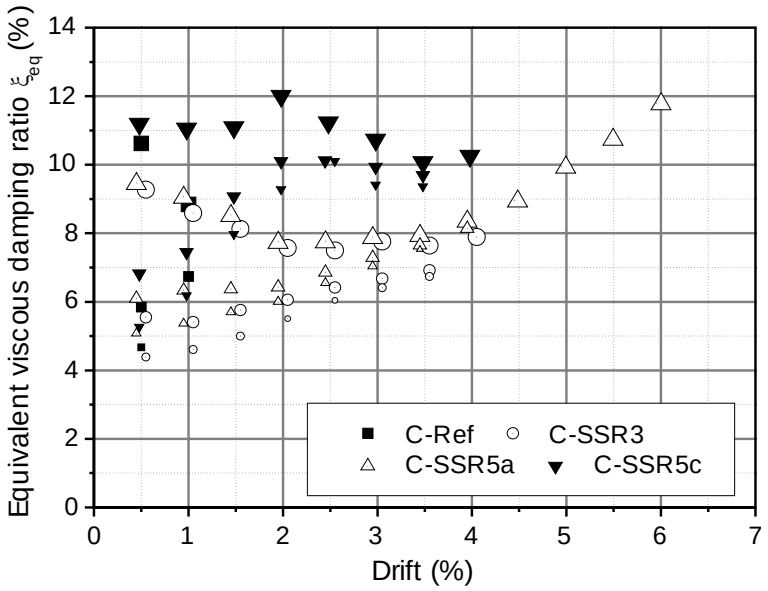


(a) Specimens C-Ref, CSSR3, C-SSR5a and C-SSR5c

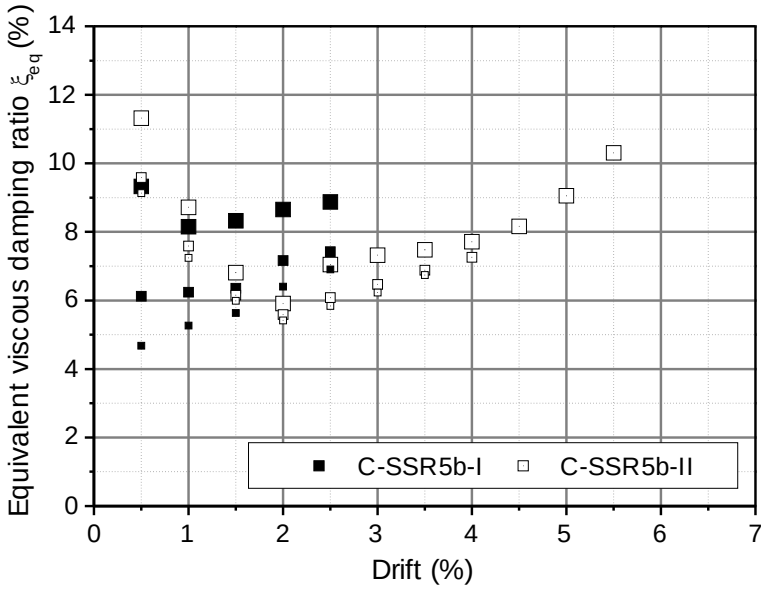


(b) Specimen C-SSR5b (-I First phase, -II Second phase)

Figure 4.8: Equivalent viscous damping coefficient (largest marker represents the first cycle)

idealized curves are shown in Figure 4.9b. For specimen C-SSR5b, the idealized curve is calculated considering the first phase of cyclic loading, based on similarity with the other specimens and to avoid potential misinterpretations due to the presence of a hardening branch in the second phase. The displacement ductility, calculated as $\mu = \Delta_u/\Delta_y$ is also given in Figure 4.9b. The ultimate displacement, $\Delta_u$ is determined as the maximum horizontal displacement experienced before failure. The most ductile specimens were those with 5 perimeters of studs and GSR around 55% (i.e., specimens C-SSR5a and C-SSR5b). The displacement ductility for the two other shear-reinforced specimens was 2.3 and 2.5. Comparing with specimen C-Ref, it is noticed that the introduction of shear reinforcement changed the behaviour of the flat slab from brittle to ductile.

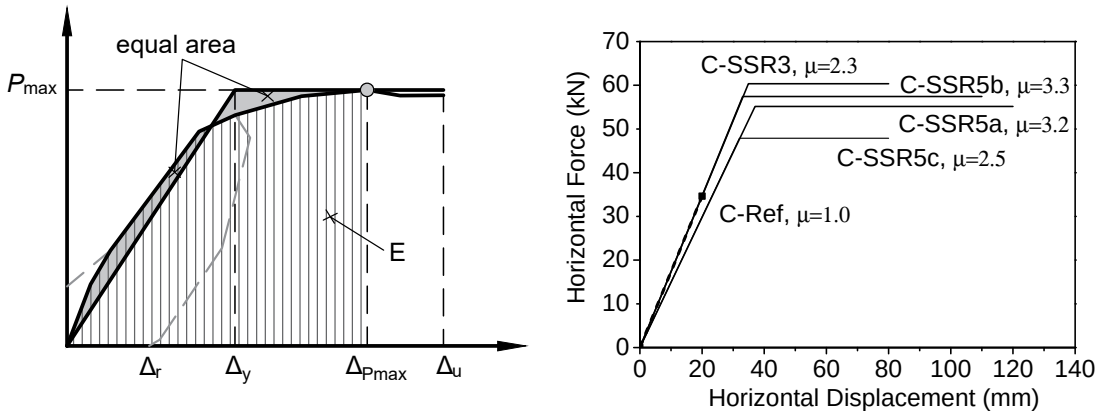


(a) Notations

(b) Elasto–perfectly plastic curves

Figure 4.9: Idealization into elasto–perfectly plastic curves

RDI is calculated for each positive half-cycle and the results are plotted in Figure 4.10 for all specimens with shear reinforcement. For C-Ref, global yielding was not reached and the determination of $\Delta_y$ is therefore not possible. It is noticed that the indices were comparable for all specimens up to around 2% drifts. For larger drifts, the indices start to disperse and the differences between the specimens become more noticeable. Specimen with high GSR (C-SSR5c) suffers significant damage and the values of RDI are rapidly increased after 2% drift.

For specimen C-SSR5b, the figure shows that for the drift ratios imposed in Phase I, the residual horizontal displacements are not significantly increased when the loading protocol is repeated (i.e., in Phase II). For larger drifts, the RDI values for specimen C-SSR5b are above the values corresponding to the other specimens, except C-SSR5c. For all the specimens, it is noticed that the residual horizontal displacements are not significantly influenced by the repetitions of drift excursions within the same loading phase. This can be confirmed also by looking at the load–displacement curves (Figures 4.1–4.5), where it is noticed that the hysteresis loops of the same target drift intersect the x-axis at almost the same displacement values.

In the last cycle (at failure), the RDI values are rapidly increased due to the increase in the residual horizontal displacement after punching failure (for specimens that failed in punching). The evolution of RDI values presented in Figure 4.10 correlates well with the visually assessed damage during the tests.

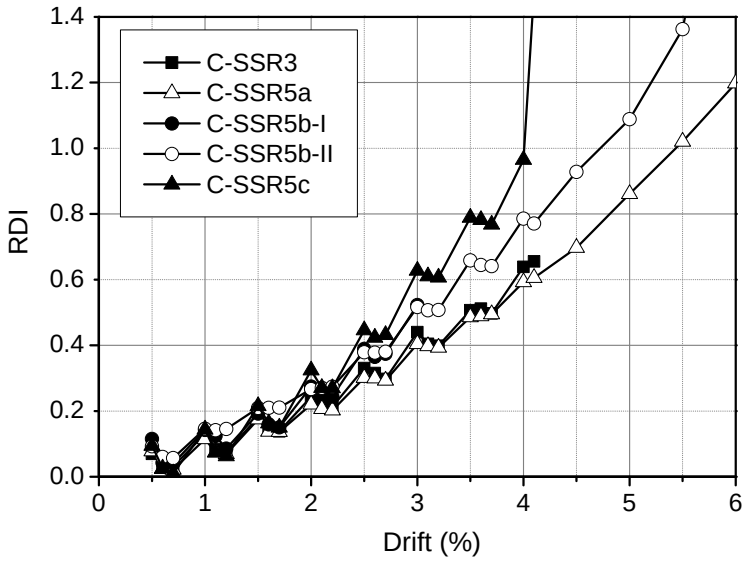


Figure 4.10: Residual deformation indices for positive half–cycles in specimens with shear reinforcement

## 4.4 Deflections

### 4.4.1 Longitudinal direction

Slab deflections at the first cycles for each drift level in the horizontal loading history are shown in Figures 4.11–4.15 for the longitudinal direction (N–S), based on the measurements obtained from the displacement transducers. The figures show that the deflections of the slab increase with the growth of the horizontal drifts due to stiffness degradation caused by the cyclic unbalanced moments, even though the gravity load is kept constant. The figures also show that the test setup worked as intended, thus imposing equal deflections at slab borders (i.e. at the simulated mid-spans).

As expected, the deflections at the beginning of the reversed cycles are proportional to the gravity load acting on the slab. The figures reveal that the gravity load also significantly influences the increase of deflections during cyclic loading. For example, the deflections in specimen C-SSR5a (Figure 4.13) at 6.0% drift are comparable to deflections in specimen C-SSR3 (Figure 4.12) at around 4.0% drift or to deflections in specimen C-SSR5b (Figure 4.14) at around 3.0% drift. The three specimens had almost the same GSR but significantly different values of the applied gravity load $V_g$ (Table 3.5) due to the differences in concrete strength. As a result, the initial bending moments due to gravity

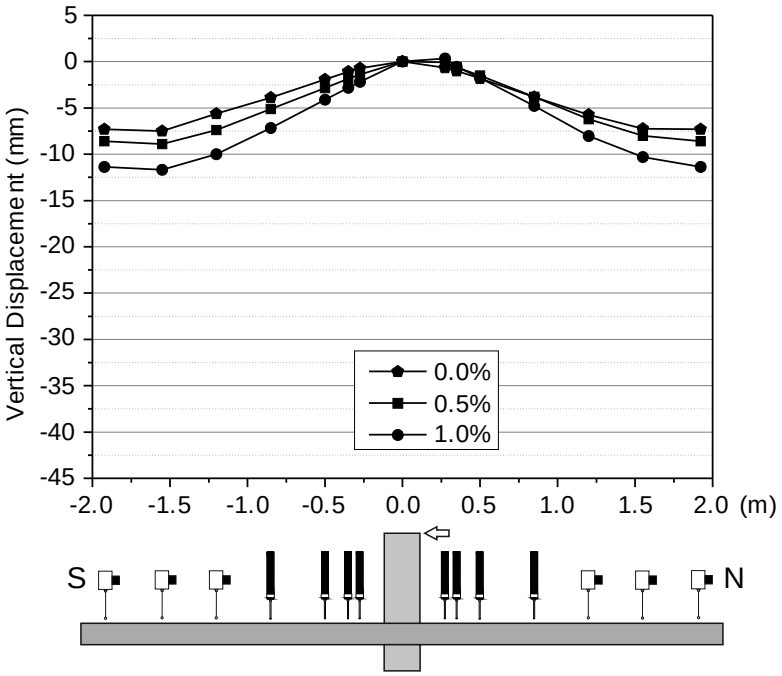


Figure 4.11: Deflections at first cycle of each drift level for C-Ref

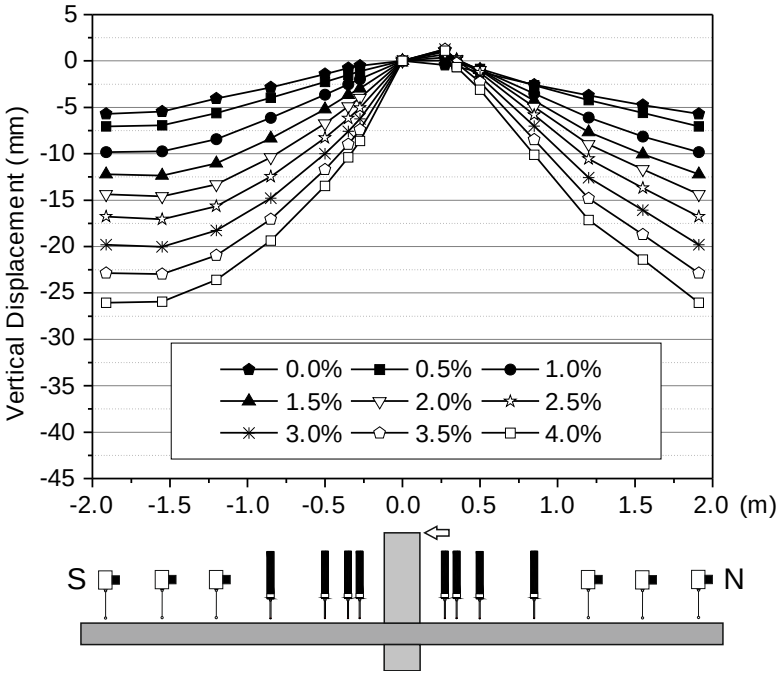


Figure 4.12: Deflections at first cycle of each drift level for C-SSR3

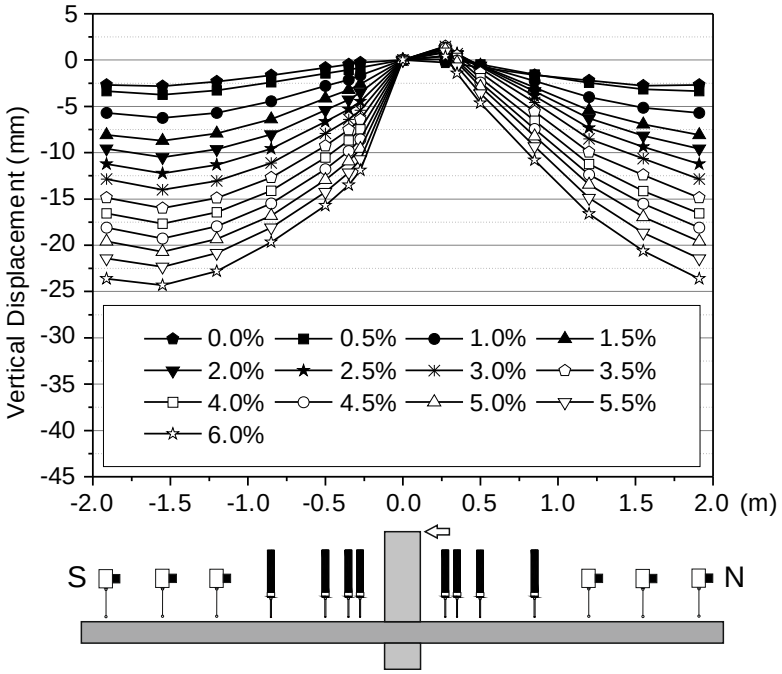


Figure 4.13: Deflections at first cycle of each drift level for C-SSR5a

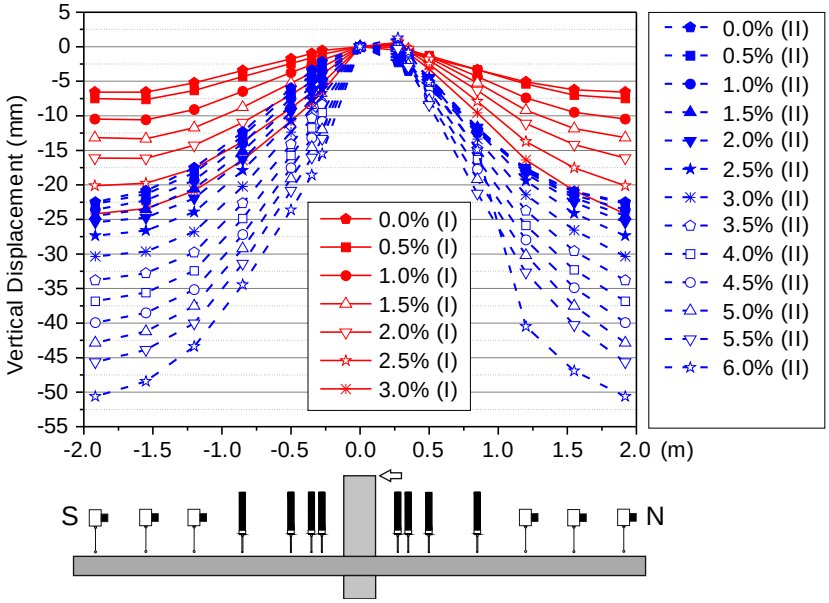


Figure 4.14: Deflections at first cycle of each drift level for the two phases of cyclic loading of C-SSR5b

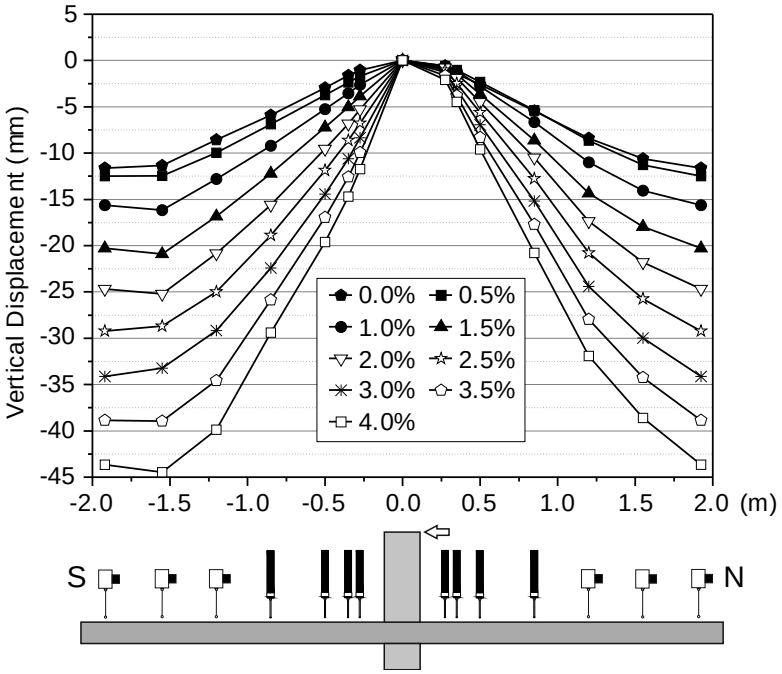


Figure 4.15: Deflections at first cycle of each drift level for C-SSR5c

loads are also different and the deflections are therefore different, being both higher for higher gravity loads. This means that GSR alone cannot properly describe the degradation of the slab under reversed cyclic loading, because it does not consider the fact that the bending moments in the slab can vary considerably for a fixed value of GSR depending on the concrete strength, since the slab's flexural capacity is less sensitive to changes on concrete strength than the punching capacity. This is further discussed in Chapter 5.

The deflections for the two phases of loading of the specimen C-SSR5b are shown in the same plot in Figure 4.14, in which it can be noticed that in the second phase the registered vertical deformations are higher when comparing similar stages, because after the first testing phase the slab was already heavily cracked. Starting from 3.0% drifts, the deflections were considerably large when compared to the other specimens with similar GSR.

The deflection plots also indicate that the specimens have both negative and positive bending moment regions in the longitudinal direction. Furthermore, the inflection point is not fixed throughout the test. This is clearly shown in Figures 4.16–4.20, in which the location of the inflection points is shown as a function of time. To obtain these figures, the data from Figures 4.11–4.15 were fit into polynomial functions. Different polynomials were used for the two halves of the specimen with respect to the column. The inflection points were then determined at locations where the second derivative of the polynomial is equal to zero.

At the end of the gravity loading phase, the inflection lines were located around

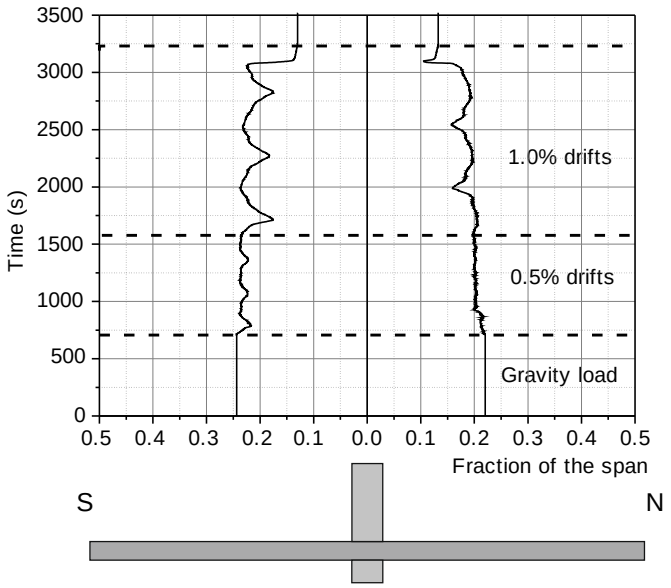


Figure 4.16: Location of the inflection point throughout the test of specimen C-Ref

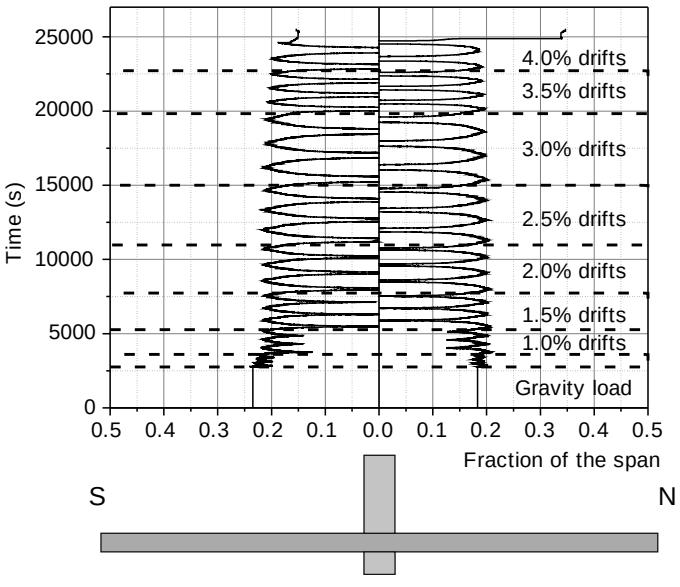


Figure 4.17: Location of the inflection point throughout the test of specimen C-SSR3

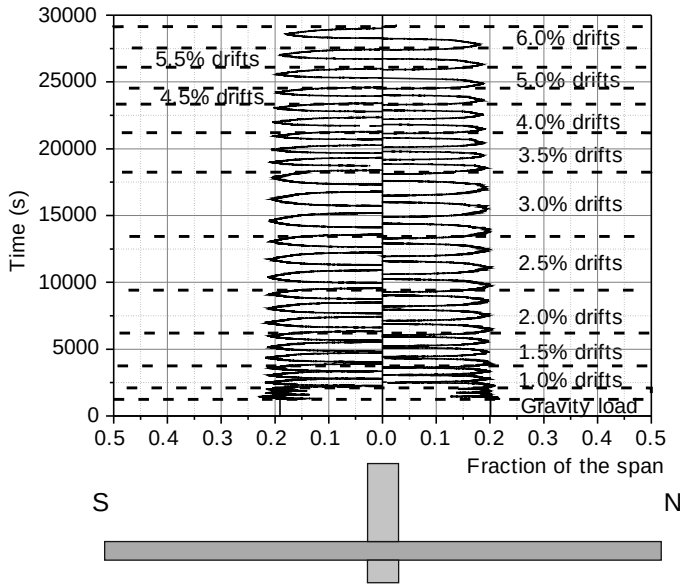


Figure 4.18: Location of the inflection point throughout the test of specimen C-SSR5a

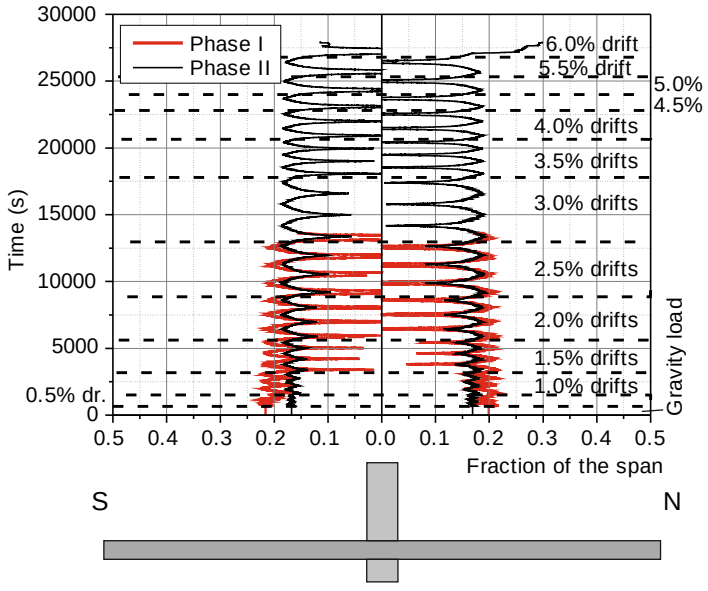


Figure 4.19: Location of the inflection point throughout the test of specimen C-SSR5b

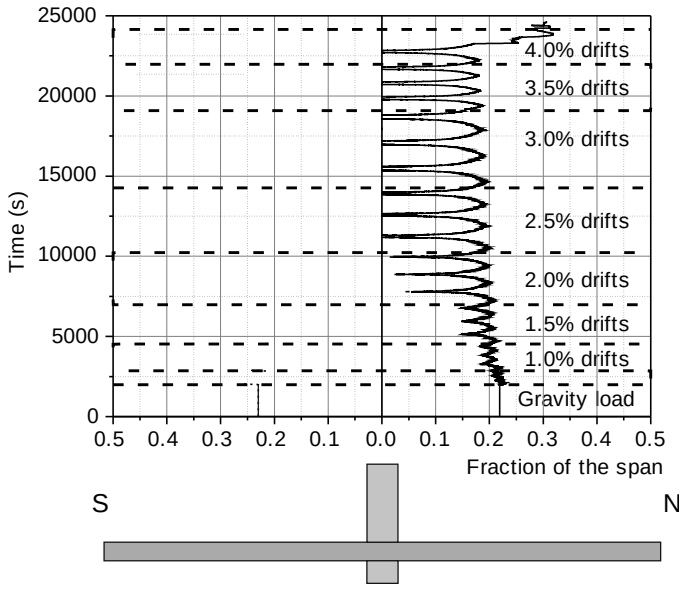


Figure 4.20: Location of the inflection point throughout the test of specimen C-SSR5c

the theoretical value: 22% of the span (Figures 4.16–4.20). During the reversed cyclic loading phase, the location of the inflection line shifted back and forth, with generally higher ranges for higher drifts. From the figures it can be noticed that the inflection line reaches the column for specimens that experience large drifts (i.e., all specimens except C-Ref). This means that there are positive bending moments near the column, and that the moments due to the horizontal actions have become larger than those from gravity loading. Also, the figures show that the maximum distance reached within a cycle between the column and the inflection line is gradually reduced with the increase of the horizontal drifts.

In Figure 4.19, the position of the inflection line is shown for both phases of the test of specimen C-SSR5b by adapting the time axis so that the horizontal drifts for both phases match. The figure shows that at the beginning of the second phase, the inflection line was closer to the column compared to the beginning of the first cyclic loading phase. For specimen C-SSR5c, the inflection line position is plotted only for the northern side in Figure 4.20, because it was not possible to obtain continuous values due to a technical issue that resulted in noise in the readings from the displacement transducer D2 (see Figure 3.23).

### 4.4.2 Transversal direction and iso-deflection curves

In the transversal direction (E–W), the deflections were measured through four displacement transducers aligned with the axis of the column (Figure 3.23). Deflections at the first cycles for each drift level in the horizontal loading history are shown in Figure 4.21. The same conclusions (as discussed in the previous section) can be drawn by looking at the

graphs: deflections increase with the horizontal drifts, deflections right before starting the reversed cycles are proportional to the gravity load (as an absolute value). Repeated loading at specimen C-SSR5b caused an detrimental effect in terms of deflections.

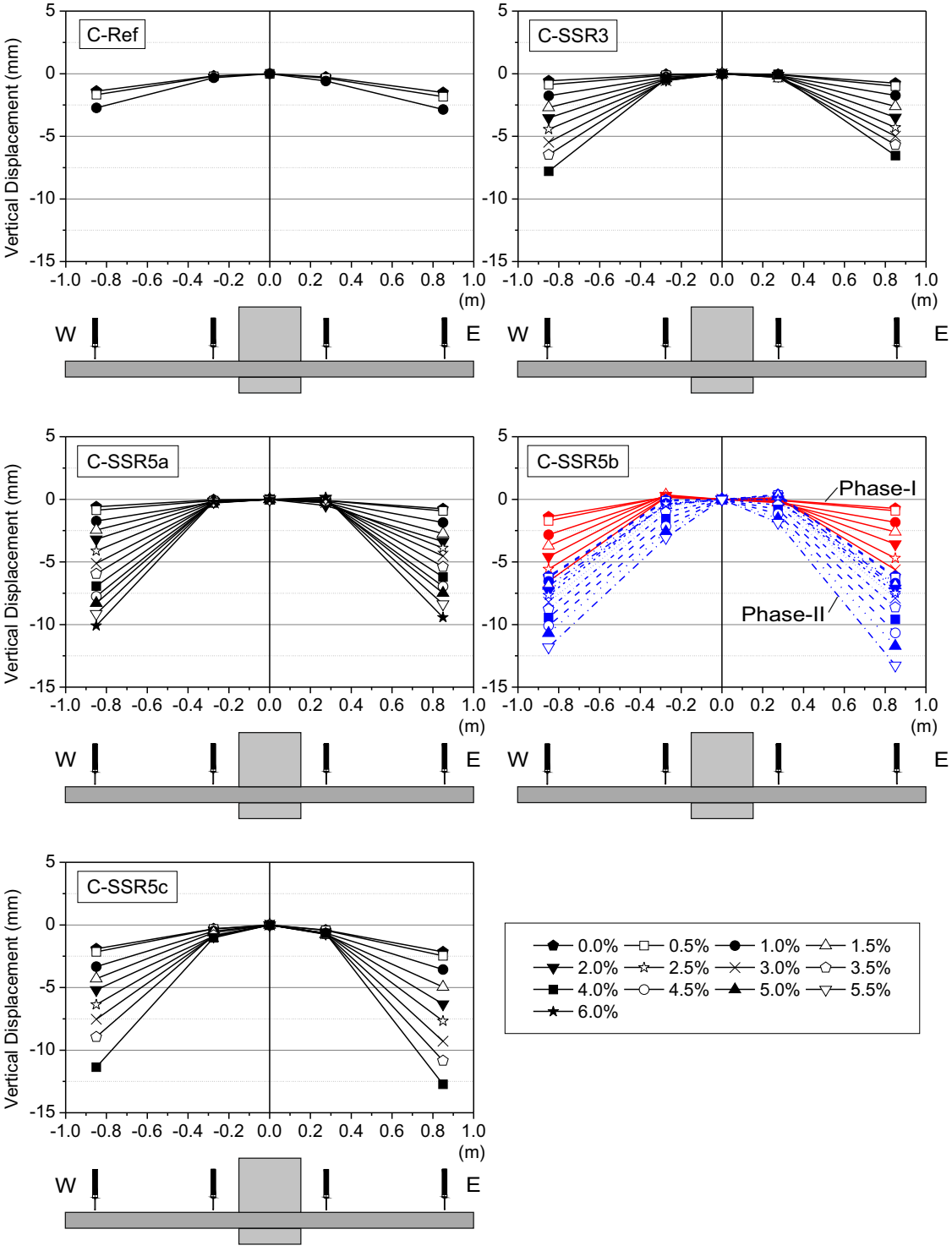


Figure 4.21: Deflections in the transversal direction

Figure 4.21 also shows that the slab specimen worked as a two–way slab, with deflections in both principal directions. To further investigate the deformed shape of the specimens under vertical and horizontal loads, the deflections of specimen C-SSR5c are studied in more detail. This specimen is chosen due to the large deformations in comparison with the other specimens, and this facilitates the graphical representation. However, the deformations were similar in shape across specimens and the same conclusions can be drawn for all of them. Iso-deflection lines are shown in Figure 4.22 for C-SSR5c. These lines are constructed using the measurements from the displacement transducers and by fitting a curve to the measurements. Although readings were available only along the central axes of the slab, the deflections with the same value are joined with a closed convex curve.

A finite element model confirmed the shape of the iso-deflection curves. The model is described in detail in Section 4.11.3, referring to another specimen (C-SSR3, therefore the values are expected to be different but the shape is expected to be maintained). Figure 4.22 demonstrates once again that deflections of the slab in both directions continually increased throughout the test. Furthermore, it shows that the increase of deflections was more pronounced in the direction of horizontal loading (i.e., along the N–S direction).

## 4.5 Lateral stiffness

### 4.5.1 Evolution of secant stiffness

The specimens are subjected to cycle repetitions within a loading phase. Specimen C-SSR5b is also subjected to an additional repetition, in Phase II (Figure 3.21). Stiffness degradation is studied herein by looking at the secant (effective) stiffness, $K_{sc}$, calculated based on Figure 4.23a as the average of the secant stiffness for positive ($K_{sc1}$) and negative ($K_{sc2}$) half-cycle for each cycle. It should be noted, however, that the force–deformation response was reasonably symmetric for all specimens and the difference between $K_{sc1}$ and $K_{sc2}$ was small. For the calculation of stiffness, the elastic deformation of the column ($\delta_{e,col}$) was taken out, as demonstrated in Figure 4.23b.

The secant stiffness as a function of the horizontal drifts and displacements is presented in Figure 4.24 for all the specimens. For clarity of the figure (to match with the loading history), the drifts and horizontal displacement values include the elastic deformation of the column, although stiffness was calculated assuming a rigid column. The markers represent the peak drift points in the loading history. The figure shows that the rate of degradation for all the specimens was similar. The first drifts are the most detrimental ones. Afterwards, the stiffness degradation is slower.

Repeated loading at the same drift level caused additional stiffness degradation. In Figure 4.24, such a degradation is represented by the "steps" visible at peak drift levels. In the specimen tested in two phases (C-SSR5b), it is noted that stiffness from the second

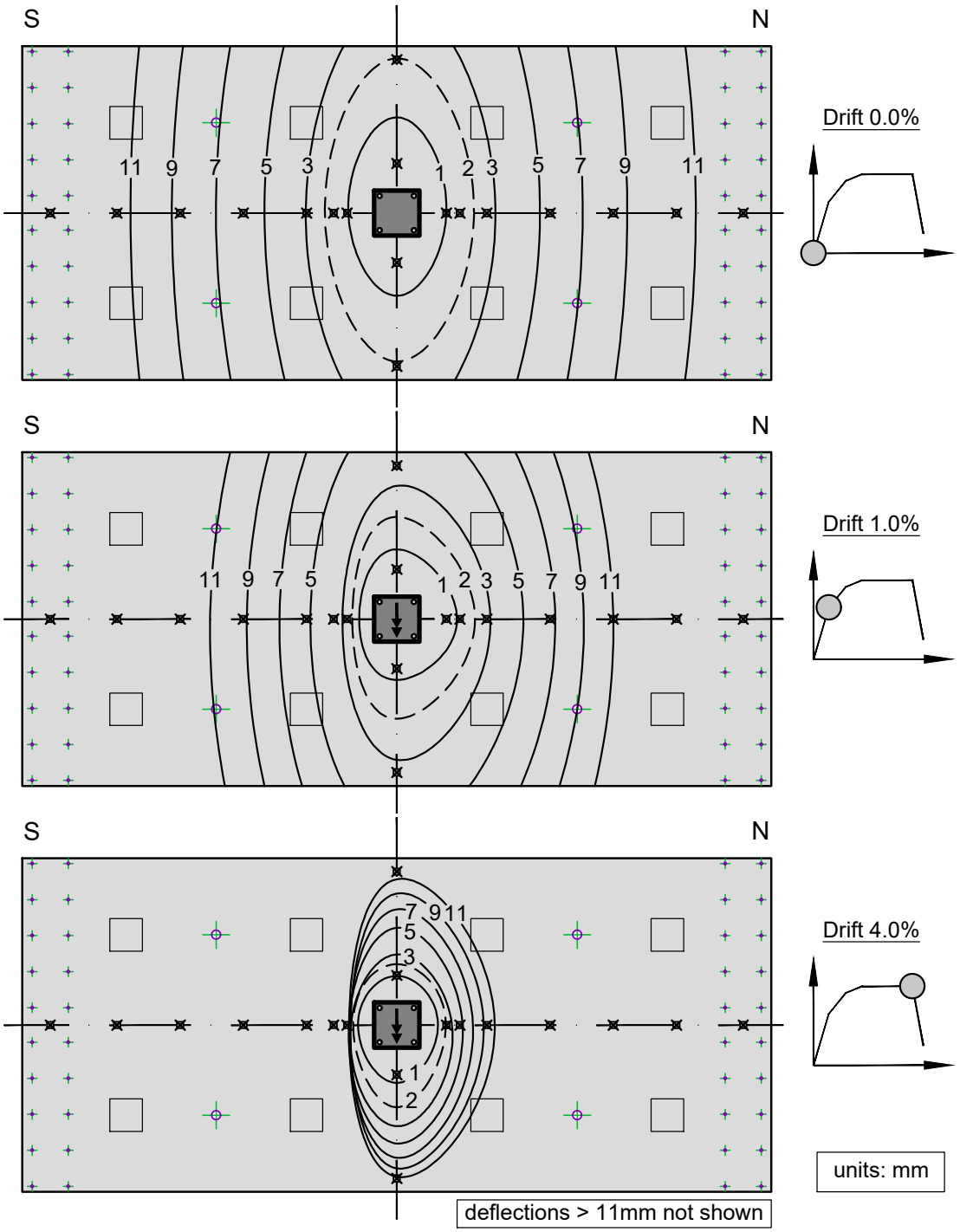


Figure 4.22: Iso-deflection curves for specimen C-SSR5c

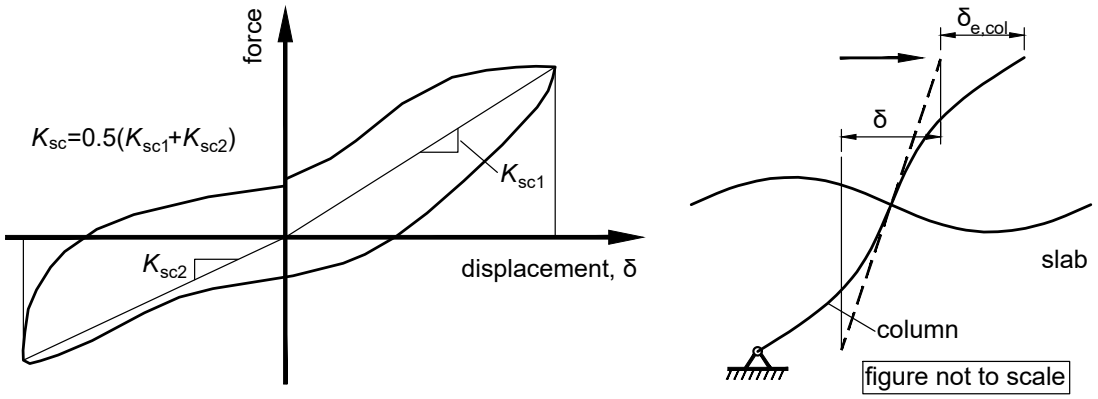


(a) Definition (b) Displacement $\delta$

Figure 4.23: Calculation of the secant stiffness

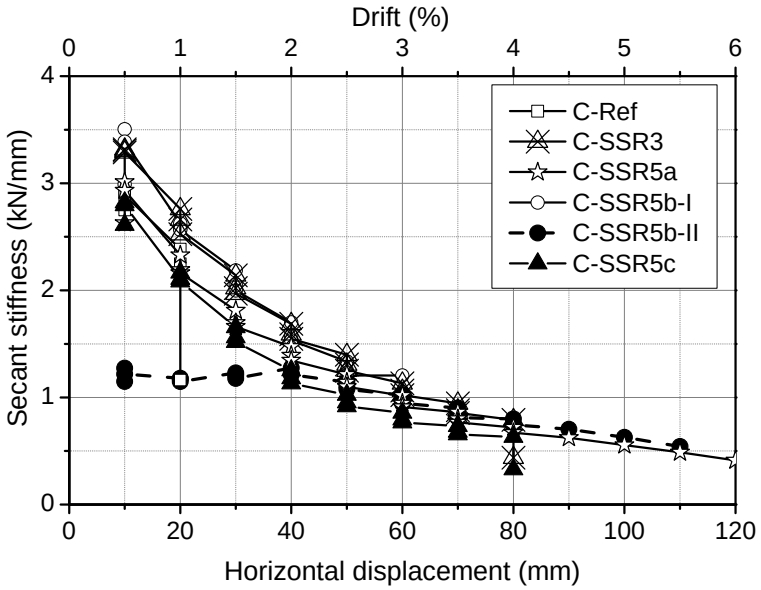


Figure 4.24: Secant stiffness as a function of horizontal displacement (and drift ratio)

phase approximates the curves corresponding to specimens tested in a single phase for drifts larger than 3.0%. A refined analysis of the stiffness degradation from Phase I to Phase II in this specimen is presented in Section 4.9.3.

### 4.5.2 Comparison with elastic stiffness

In design practice, linear methods of analysis are preferred over nonlinear ones due to their simplicity and decreased computational effort and time. Finite element modelling and analysis has especially gained popularity with the development of computers and the gradual acceptance in design codes. However, the structural behaviour under horizontal actions is rarely linear elastic. Especially for earthquake loading, the structures are expected to behave nonlinearly. The designer is therefore faced with the problem of choosing correct material and section properties to account for the nonlinear behaviour in a linear elastic analysis.

To study this issue, a linear elastic model of the specimens was built in the OpenSees platform (McKenna et al. 2009). The column is modelled as rigid. The slab–column joint region (250×250×150 mm) is constrained to behave as a rigid body. Boundary conditions are set in accordance with the conditions enforced by the test setup (Figure 3.17). This means that the finite element nodes in the mid-span lines are constrained to have the same vertical deflection and rotation in the direction of loading and the column is pinned to the ground on the bottom end. The slab is modelled with overall dimensions $3.84 \times 1.85$ m to account for the exact location of the subassemblies of the test setup (Figure 3.17). Shell elements with 4 nodes, based on the theory of Mixed Interpolation of Tensorial Components (MITC4 element, Dvorkin and Bathe 1984), were used. An elastic section was assigned to the shell elements, using the gross concrete section (depth 150 mm) and modulus of elasticity in accordance with Table 3.3. The model is shown in Figure 4.25.

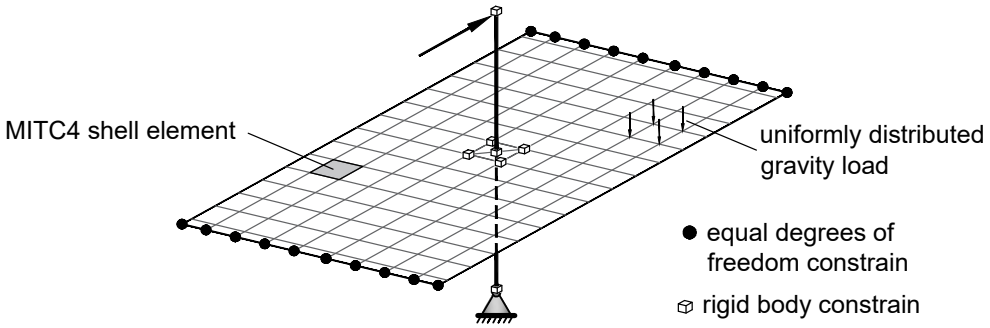


Figure 4.25: Linear elastic finite element model used to estimate elastic stiffness

After the application of the gravity load as an uniformly distributed load, monotonically increasing horizontal displacements were applied. For specimen C-SSR5b, the results of the linear analysis are presented in Figure 4.26 (curve "$1.00E_c$"), where the enveloping curve of the specimen's response in both phases is also shown (considering

a rigid column). As expected, the elastic model with gross cross section and uncracked material characteristics significantly overestimates the stiffness of the specimen. The specimen was already cracked due to gravity loading at the beginning of the horizontal loading. As a result, the stiffness overestimation starts from the very beginning of horizontal loading.

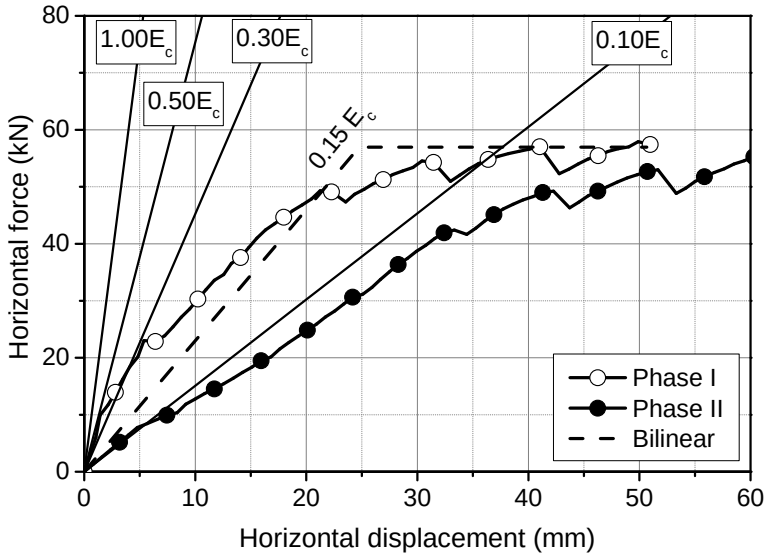


Figure 4.26: Comparison of specimen C-SSR5b with elastic finite element models (rigid column)

Results considering a reduction of the modulus of elasticity of concrete to 50%, 30% and 10% of the initial value are also plotted in Figure 4.26. The curve corresponding to $0.5E_c$ approximates reasonably well the initial stiffness of the specimen. However, the stiffness is rapidly decreased with the increase of horizontal displacements. The curve corresponding to $0.3E_c$ describes the initial stiffness more reasonably if the envelope curve is studied as a whole. The beginning of the second phase is described reasonably well by an elastic analysis in which the stiffness of the slab is reduced to 10% of the initial value. The stiffness of the approximated bilinear model is between the $0.1E_c$ and $0.3E_c$ curves. More precisely, the linear stiffness of the bilinear model is 15% of the elastic linear stiffness.

Similarly, the reduction of the cross sectional properties is estimated for the rest of the shear-reinforced specimens presented in this dissertation and the results are summarized in Table 4.2. In the table, the stiffness calculated from the bilinearisation of the backbone curve is denoted as $K_{exp}$ and the elastic stiffness is $K_e$.

It is noticed that the ratio $K_{exp}/K_e$ is the lowest in specimen C-SSR5c, which had the highest gravity load both in absolute terms ($V_g$) and relative terms (GSR).

Table 4.2: Reduction of cross sectional properties in the bilinear model

| Specimen | $K_{exp}$ (kN/mm) | $K_e$ (kN/mm) | $K_{exp}/K_e$ (%) |
|---|---|---|---|
| C-SSR3 | 2.4 | 13.8 | 17 |
| C-SSR5a | 1.8 | 12.1 | 15 |
| C-SSR5b | 2.3 | 15.2 | 15 |
| C-SSR5c | 1.8 | 15.5 | 12 |

### 4.5.3 Design implications

Design codes recommend a reduction of the stiffness of structural elements to consider cracking in linear analyses. The presented analysis indicates that the reduction of the section properties can be as low as 12% of the uncracked properties, when heavy gravity loads are applied. For the more normal cases of gravity loading (specimens other than C-SSR5c), the cracked section properties are reduced to 15–17%. These values are considerably lower than those recommended in the codes. For example, EC8 (CEN 2004d) recommends a reduction to 50% and ACI 318 (ACI 2014) recommends a reduction from 25% to 50% of the uncracked stiffness.

## 4.6 Seismic-induced moments

During the application of horizontal loads, $P$, the test setup reacts with the forces $V_{TS}$ at the borders of the specimen, as shown in Figure 4.27. These reaction forces restrain the specimen from performing a rigid body rotation under horizontal loads and they arise from the test setup sub–assembly that ensures equal deflections at the mid–spans of the flat slab specimen (Figure 3.17). The forces $V_{TS}$ can be calculated by equilibrium. Then, bending moments along the specimen can be estimated if the behaviour is assumed to be analogous to that of a "beam", as in the Effective Beam Width Method of analysis (Section 2.7.2, Pecknold 1975; Allen and Darvall 1977; Hwang and Moehle 2000a). In Figure 4.27, the sagging moments at the borders of the specimen are denoted by $M^+$. For simplicity, the self-weight of the slab and equipment is concentrated at the gravity load application points.

For each specimen, Figures 4.28–4.33 show the total bending moments at the first excursion at each peak drift level and at zero horizontal force (i.e., for gravity loading) along the test. The difference between these two bending moment diagrams produces the bending moment diagram of the specimen under horizontal loads and zero gravity loads. The positive bending moments applied at the end of the gravity loading phase through the test setup struts take into consideration the nonlinear behaviour of the specimen. As

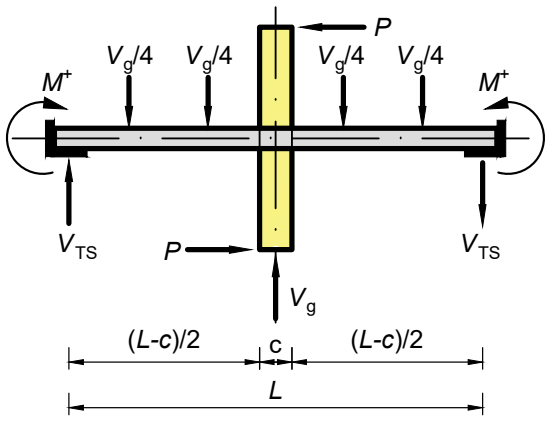


Figure 4.27: Free body diagram of a specimen under horizontal loads

a result, the bending moment diagrams corresponding to gravity loading in Figures 4.28–4.33 differ from the diagrams that would have been expected from a linear elastic analysis in terms of the relative magnitude of negative and positive bending moments.

As damage progresses, the sagging (positive) bending moments are increased due to bending moment redistribution. In all specimens except C-Ref (Figure 4.28) that failed prematurely and C-SSR5c (Figure 4.33) that had an increased GSR, it is noticed that sagging total bending moments are present at the face of the column for relatively small drifts (i.e., bending moment sign reversal occurred). This means that, in these cases, the seismic induced moment became larger than the moment from gravity loads. In C-SSR5c, moment sign reversal did occur for large drifts, but the positive bending moments at the face of the column were small (Figure 4.33).

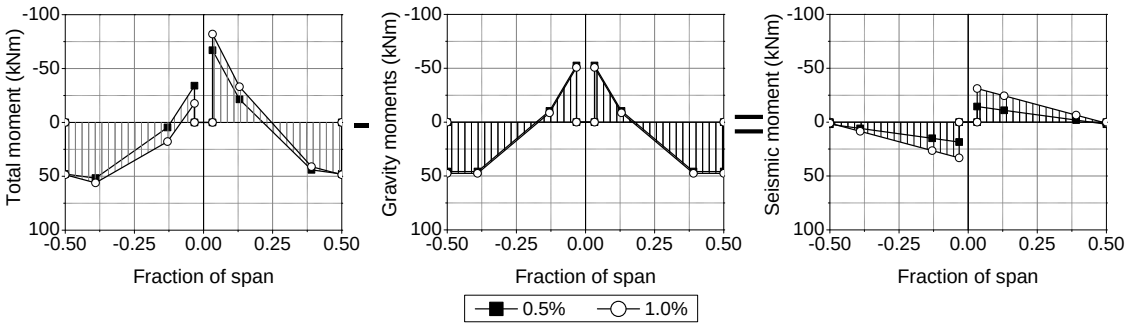


Figure 4.28: Total, gravity and seismic bending moments in specimen C-Ref

As expected, the shape of the seismically induced moment diagrams is triangular (Figures 4.28–4.33), with a value of zero near the simulated mid–span, at the borders of the specimen. Because of the symmetric nature of the bending moments due to gravity loading, the unbalanced moment calculated from the seismically induced moments is the same as the unbalanced moment calculated from the total bending moment diagram or

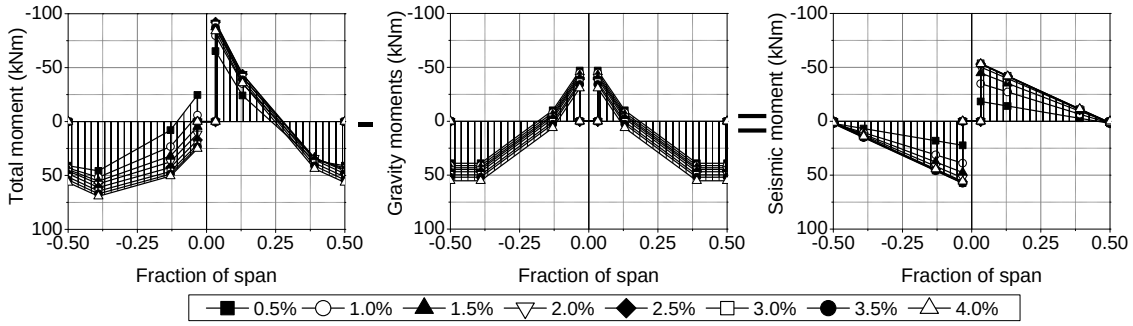


Figure 4.29: Total, gravity and seismic bending moments in specimen C-SSR3

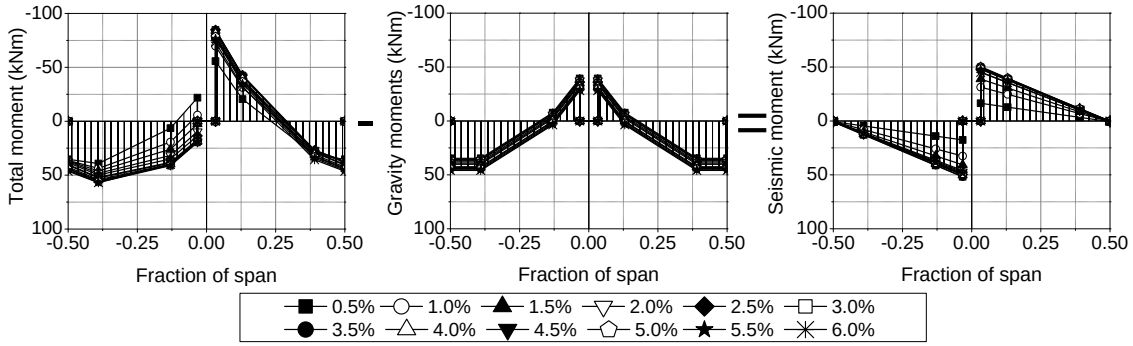


Figure 4.30: Total, gravity and seismic bending moments in specimen C-SSR5a

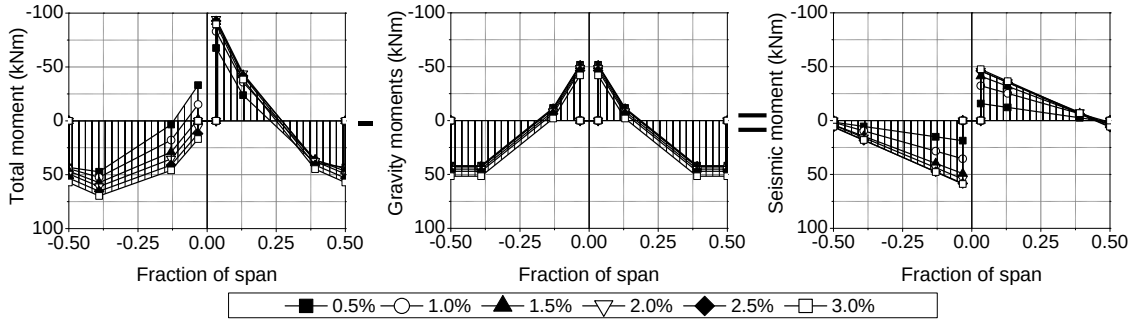


Figure 4.31: Total, gravity and seismic bending moments in specimen C-SSR5b, Phase I

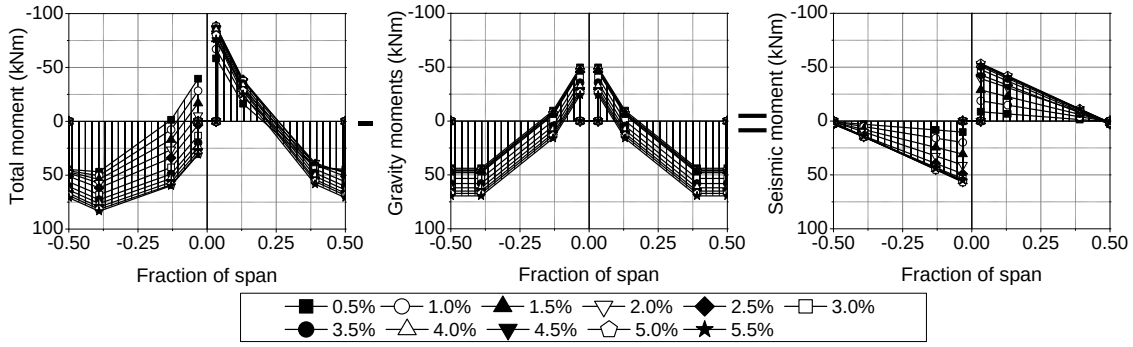


Figure 4.32: Total, gravity and seismic bending moments in specimen C-SSR5b, Phase II

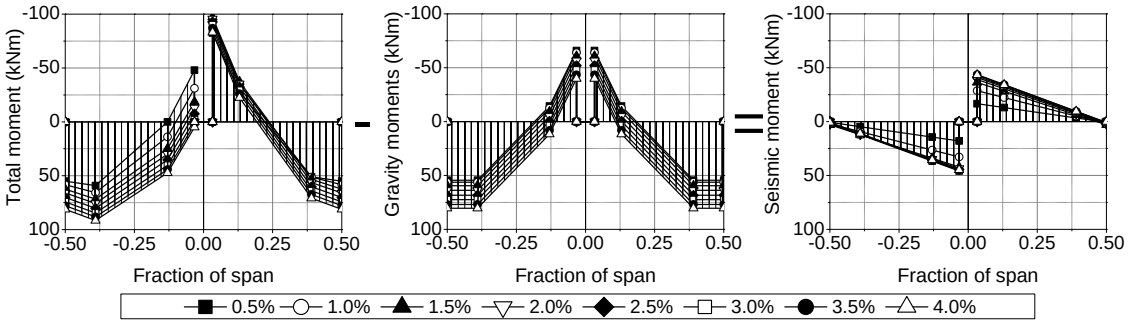


Figure 4.33: Total, gravity and seismic bending moments in specimen C-SSR5c

from the measured horizontal force.

## 4.7 Strains in the longitudinal reinforcement

Top reinforcement strains at peak points of the loading history are shown in Figure 4.34, for one loading direction. The direction is shown with an arrow near the column in each figure. For clarity in the figure, only the results for the first excursion to the denoted drift ratio are presented. During the tests, some strain gauges stopped reading correctly due to the heavily cracked specimen, especially after yielding of reinforcing bars. For this reason, some of the graphs lack certain data points. The yield strain considered is represented by a horizontal dashed line. Many strain gauges malfunctioned during the unloading phase at the end of Phase I for specimen C-SSR5b. Therefore, the results for that specimen are presented in Figures 4.34 only for Phase I. The strain gauge readings throughout the entire duration of the tests are contained in Annex B.

The top reinforcement strain graphs show that the first bars to reach yielding are those that pass through the column (R1 bars). The drift ratios for which these reinforcing bars yield is related to the magnitude of the gravity load. For instance, in specimen C-SSR5c with the highest gravity load, the strain at the end of the application of the full gravity load was very close to the yield strain (Figure 4.34). For specimens that sustained high drift ratios (i.e. for specimens with shear reinforcement), reinforcing bars further away from the column reached their yielding strain for higher drift ratios. In specimen C-Ref, reinforcing bars R1 and R3 yielded at 1.0% drift ratio and the bars R5 and R6 never yielded due to the premature punching failure. By 2.0% drift ratio, all the instrumented top reinforcement bars had yielded for all the specimens with shear reinforcement, except C-SSR5a, thus indicating that the ultimate hogging bending moment capacity of the entire section of the specimen was reached. The postponed yielding of the longitudinal bars in specimen C-SSR5a can be explained by the relatively low value of $V_g$ (Table 3.5).

For specimen C-SSR5b it was not possible to obtain useful readings from the strain

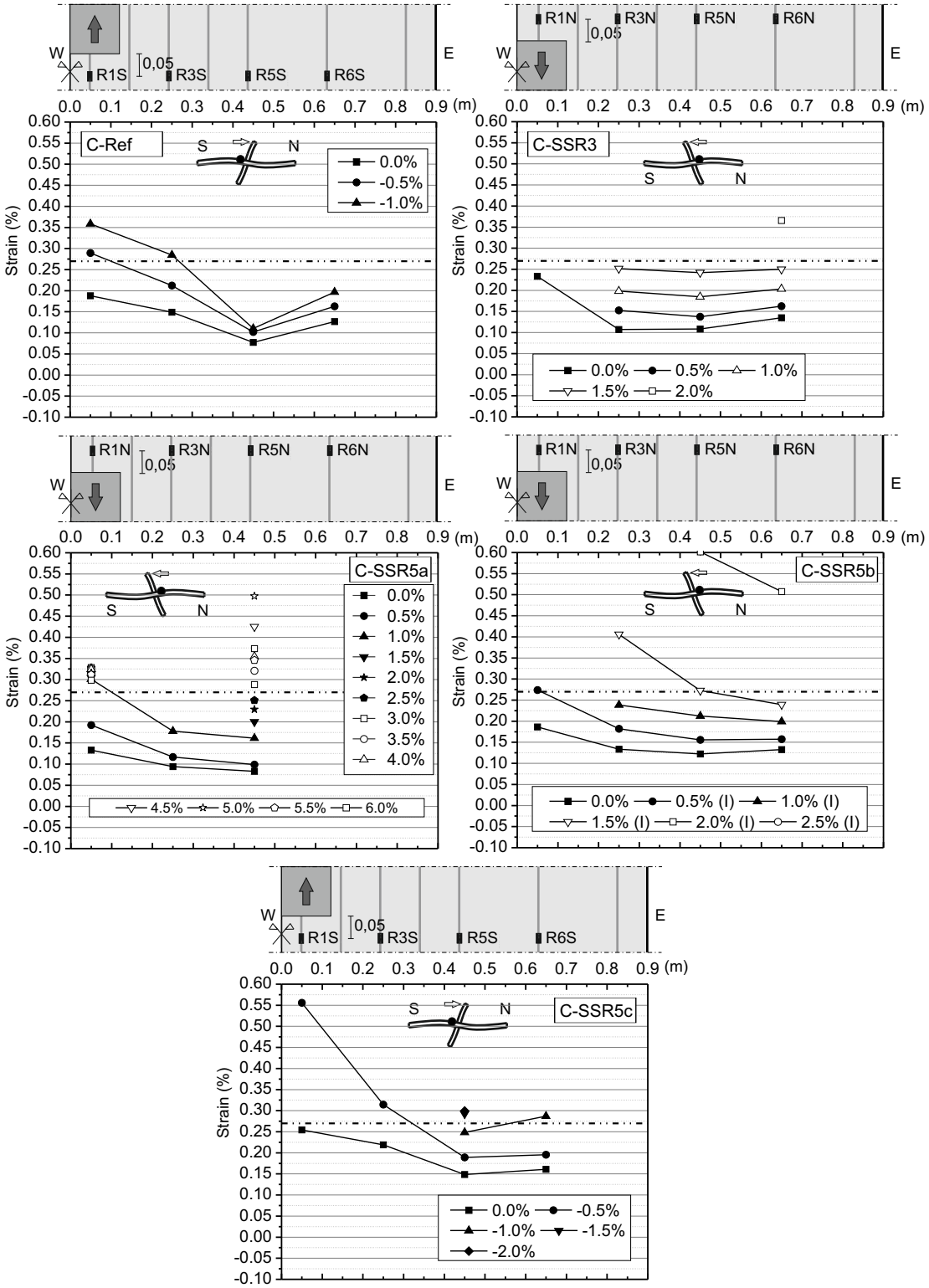


Figure 4.34: Top reinforcement strains at the first cycle of each drift level for all specimens

gauges during the second phase. Nevertheless, Figure 4.34 shows that all the instrumented bars yielded by the end of the first phase.

The maximum strains in the bottom reinforcement bars at peak drift levels are shown in Figures 4.35–4.39. The strain gauge locations for the bottom reinforcement are given in Figure 3.2. The notations used for the strain gauges near the column are BR1C and BR3C for the first and third bottom bar respectively. For the strain gauges near the borders of the specimen (i.e. near the simulated mid-span) the notations BR1B and BR3B respectively are used.

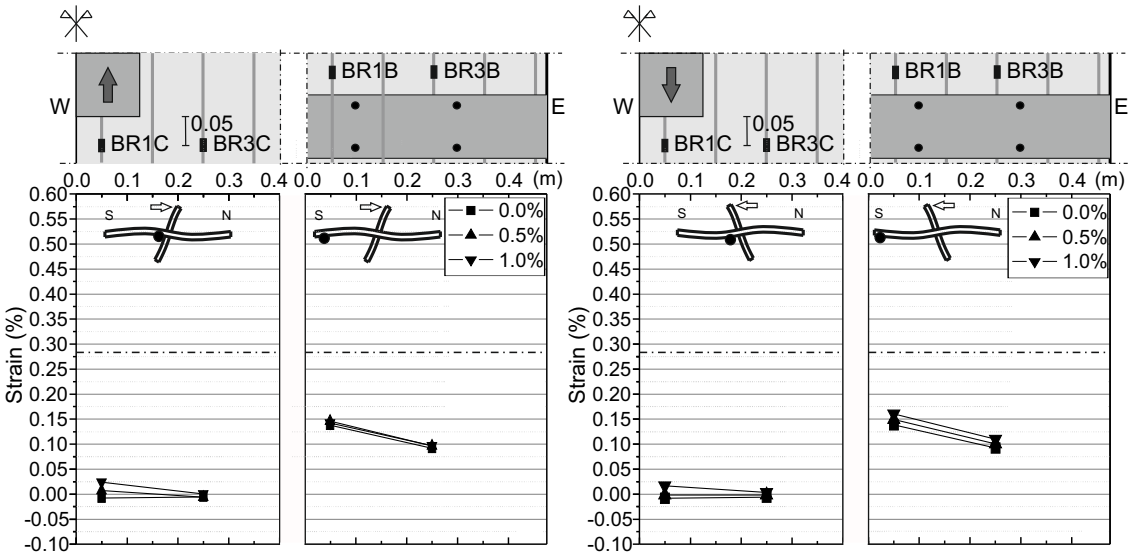


Figure 4.35: Bottom reinforcement strains at the first cycle of each drift level for specimen C-Ref

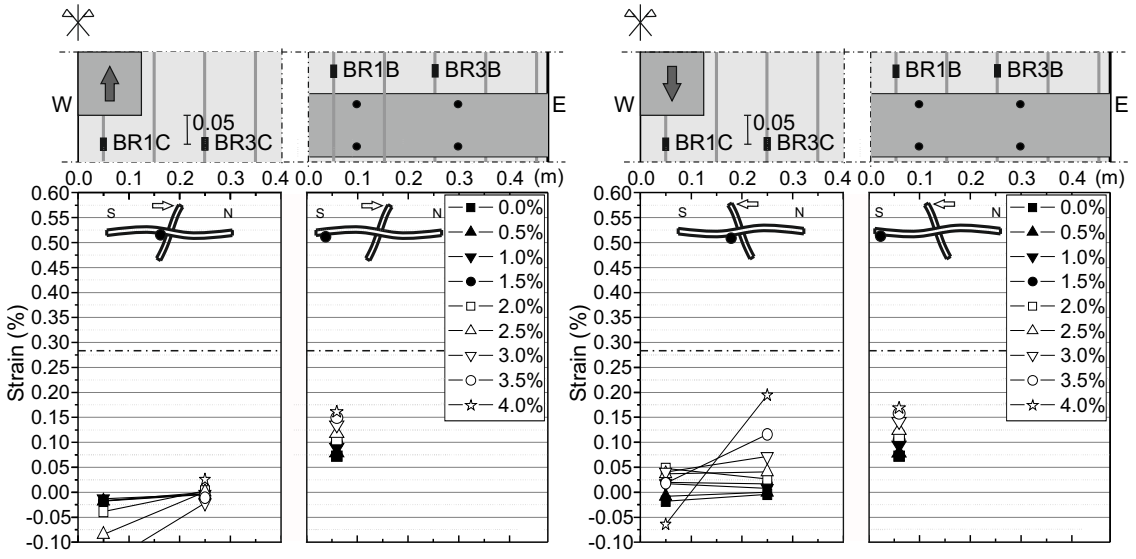


Figure 4.36: Bottom reinforcement strains at the first cycle of each drift level for specimen C-SSR3

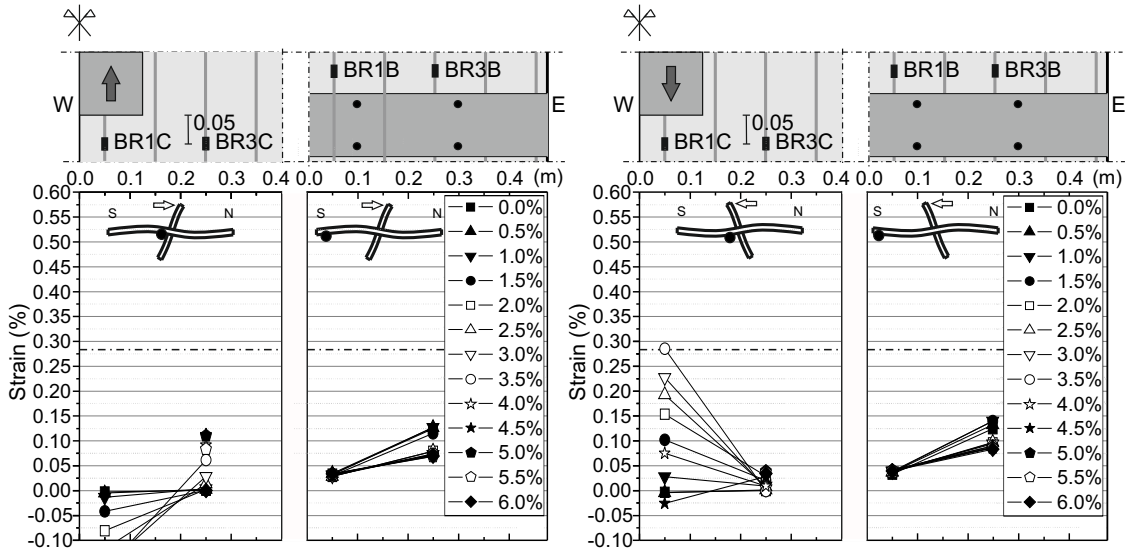


Figure 4.37: Bottom reinforcement strains at the first cycle of each drift level for specimen C-SSR5a

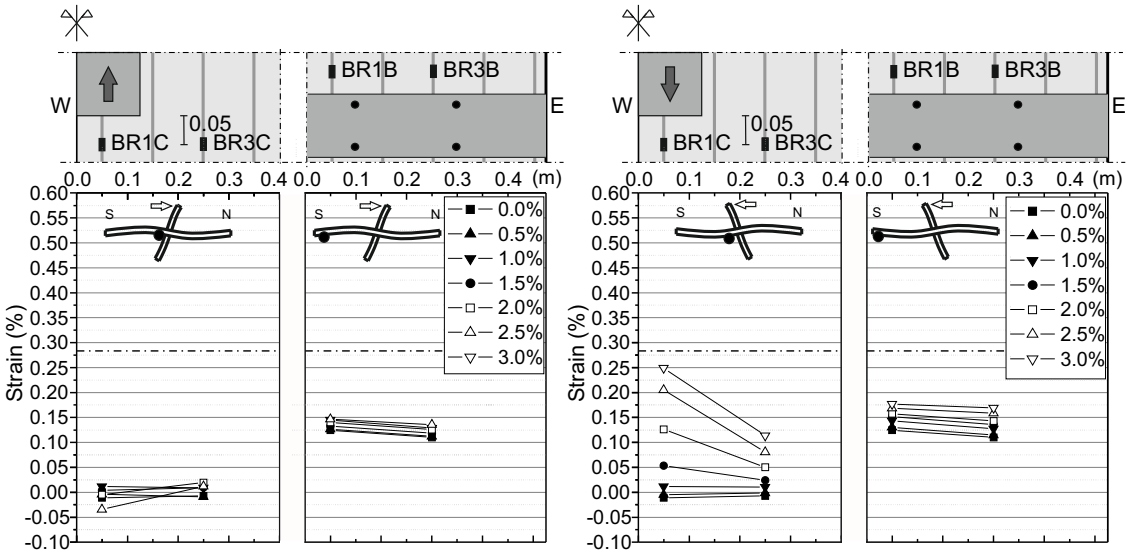


Figure 4.38: Bottom reinforcement strains at the first cycle of each drift level for specimen C-SSR5b, Phase I

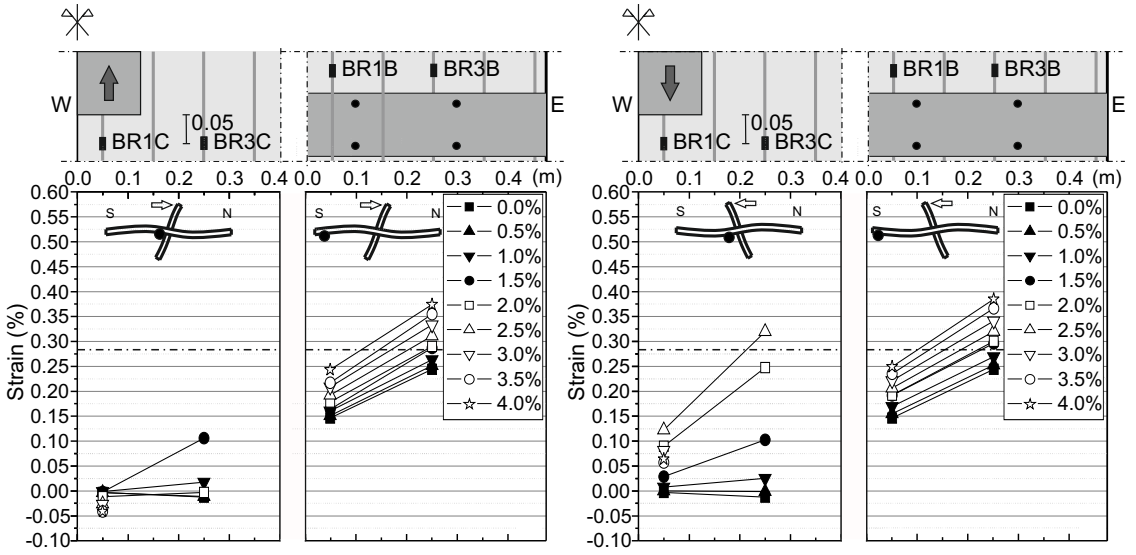


Figure 4.39: Bottom reinforcement strains at the first cycle of each drift level for specimen C-SSR5c

It is noticed that yielding of the bottom instrumented bars at the borders (i.e., the simulated mid-span) occurred only in specimen C-SSR5c. In this specimen, yielding at "mid-span" was extended to both instrumented reinforcing bars just prior to failure of the specimen (at 4.0% drift). On the other hand, bottom reinforcing bars near the column reached higher strains for smaller drifts compared to the bottom bars near the borders (mid-span). The complete strain gauge readings for the bottom bars are contained in Annex B.

## 4.8 Strains in punching shear reinforcement

For the specimens with shear reinforcement, the strains in the instrumented studs are shown in Figures 4.40–4.43. Strain gauges in studs in the second perimeter around the column detected the highest strains among the studs in the longitudinal (N–S) direction for all the specimens, regardless of the total number of perimeters of shear reinforcement (i.e. 3 or 5). Studs along the E–W direction (orthogonal direction to the horizontal loading) did not follow this pattern for specimens with 5 perimeters of studs. For specimens C-SSR5a and C-SSR5b (first phase of loading), it is observed that the studs in the fifth perimeter (the farthest away from the column) have very low strains detected by the strain gauges. Even for high drift ratios, the measured strains in these studs were less than 0.05%. The other specimen with five perimeters of studs (C-SSR5c) also had low strains in the studs of the fifth perimeter, but these strains were notably higher compared to the other two specimens. The evolution of strain gauge readings in shear reinforcement during the tests is given in Annex B.

Yielding of the studs was limited to a few studs and for relatively large drift ratios.

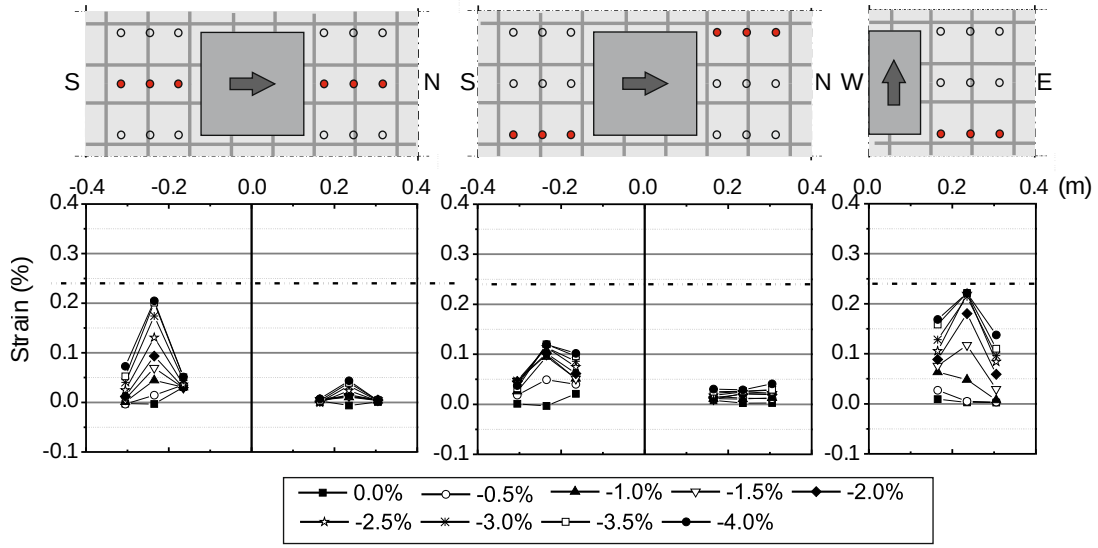


Figure 4.40: Strains in shear reinforcement, specimen C-SSR3

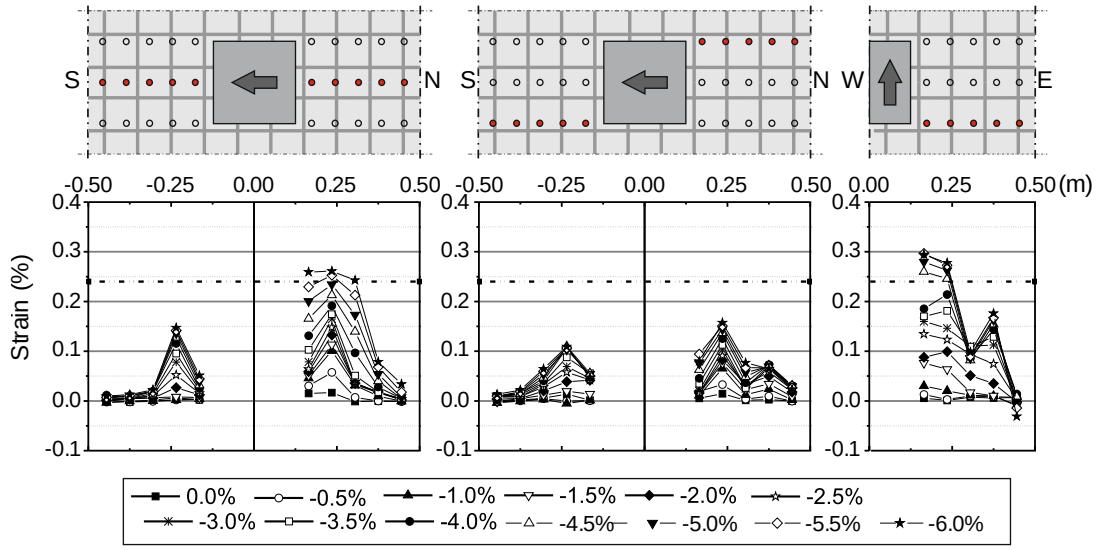


Figure 4.41: Strains in shear reinforcement, specimen C-SSR5a

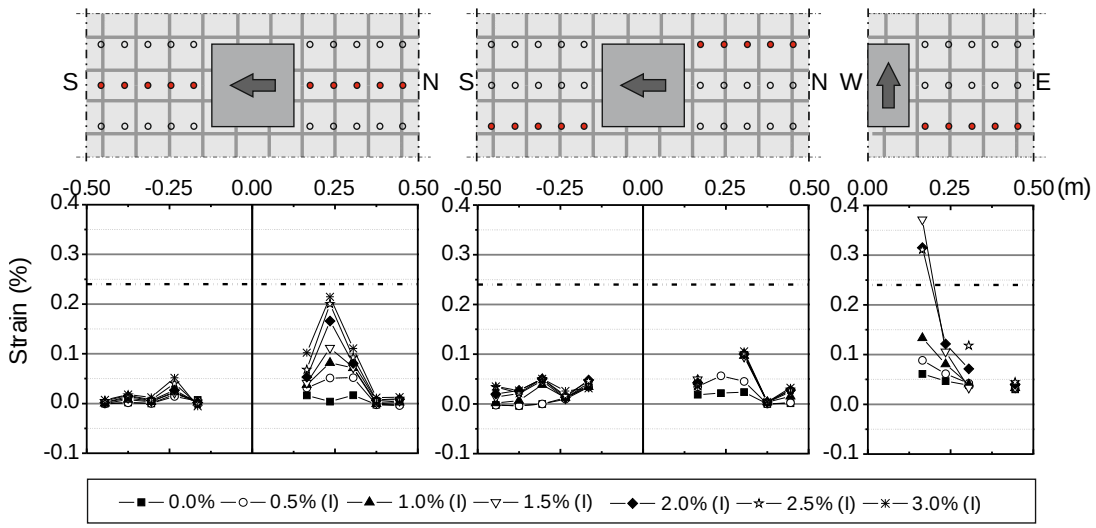


Figure 4.42: Strains in shear reinforcement, specimen C-SSR5b, Phase I

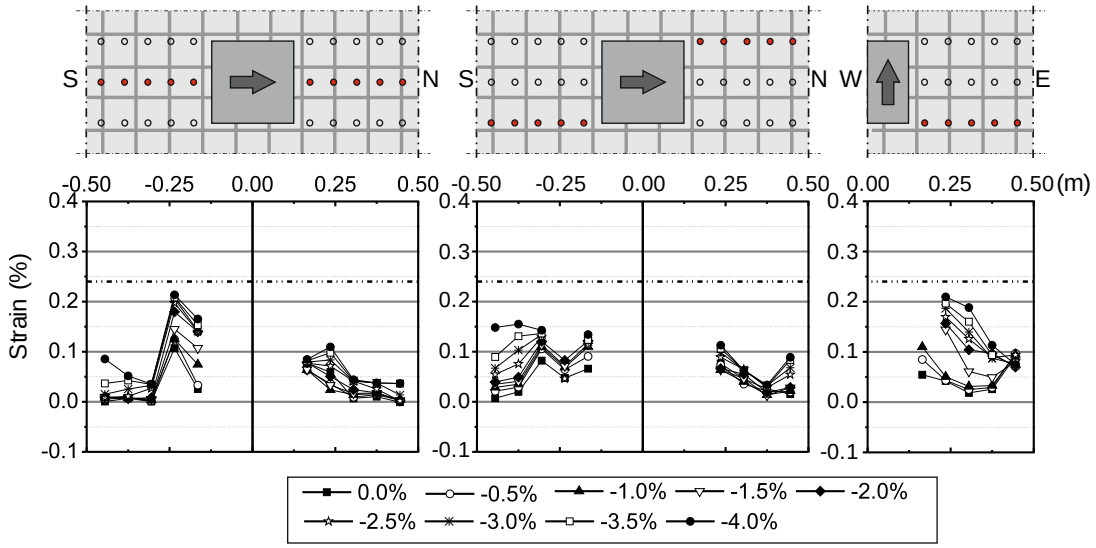


Figure 4.43: Strains in shear reinforcement, specimen C-SSR5c

In specimen C-SSR3, no stud yielding was detected. However, the studs in the second perimeter were very close to yielding in the last cycle (Figure 4.40). In specimen C-SSR5a, yielding started initially on the studs along the E–W (transversal) direction at around 4.5% drifts and was extended to the studs in the N–S (longitudinal) direction for drift ratio 5.5% (Figure 4.41). At the last cycle (6.0%), yielding had been reached by three consecutive studs in the N–S direction near the column along the centreline.

Similar to the strain gauges on the longitudinal reinforcement, many strain gauges on the shear studs malfunctioned during the unloading phase at the end of Phase I for specimen C-SSR5b. Therefore, the results presented in Figure 4.42 are only for Phase I. In that specimen, only the first stud along the E–W direction reached yielding. However, since the specimen reached very high drift ratios (5.5%) on Phase II, it is probable that yielding occurred in other studs as well, such as those in the second perimeter along the centreline in the N–S direction, which were already at strains larger than 0.2% at 3.0% horizontal drift ratio (Phase I).

Yielding was not detected by the readings of the strain gauges in specimen C-SSR5c (Figure 4.43). Due to the larger gravity load, the specimen reached a maximum drift ratio smaller than the other specimens with 5 stud layers. The same was observed in specimen C-SSR3, which failed at the same drift ratio (4.0%) without yielding of the shear studs.

## 4.9 Post-earthquake behaviour

### 4.9.1 Introduction

As previously mentioned, experimental results from the literature and from the experimental campaign presented herein agree that there is a considerable enhancement of the drift capacity of the connections with shear reinforcement compared to similar specimens without shear reinforcement. Considering the risk of progressive collapse and that the repair of punching failures is labour intensive and potentially infeasible, it is necessary to ensure that such failures do not occur under seismic loading.

Several studies and experimental campaigns focused on the post-punching behaviour of flat slabs are found (Mitchell and Cook 1984; Melo and Regan 1998; Ramos and Lúcio 2008; Faria et al. 2012; Ruiz et al. 2013; Habibi et al. 2014) (see also Section 2.4.5). These studies have led to a better understanding of the necessary measures that need to be taken to prevent progressive collapse of flat slab buildings when a punching failure occurs under seismic loading conditions.

Pan and Moehle 1992 reported the cyclic loading behaviour of a repaired specimen, which had previously failed in punching under a combination of constant vertical loads and reversed horizontal bidirectional displacements. Repair was performed using epoxy and grout. The stiffness and strength of the repaired specimen were almost halved compared to the first test (before repair). However, failure occurred for almost the same drift

ratio as in the first test.

Farhey et al. 1995 repaired four previously tested specimens using external steel plates and high-pressure epoxy and tested them under horizontal loads. It was possible to restore the stiffness of the specimens and even improve the strength as a result of the strengthening technique.

Widianto et al. 2010 tested a series of flat slab–column connections under a variety of conditions, including concentric punching after repairing specimens that had previously survived 1.25% horizontal drifts without punching and horizontal cyclic loading of a repaired specimen that had previously been loaded until 1.25% horizontal drift and subsequently punched by monotonically increasing the gravity loads. The repair techniques adopted in Widianto et al. 2010 included the installation of steel collars on the column under the slab, external carbon fibre-reinforced polymer (CFRP) stirrups and CFRP sheets on the top surface of the slab. The repaired specimen that was tested under horizontal cyclic loading exhibited a reduced loading stiffness but an enhancement of the deformation capacity as a result of repair and strengthening.

Koppitz et al. 2015 studied the effect of unloading and reloading of the gravity loads in a flat slab, prior to punching failure. They showed, however, that the effect of such a loading history in the punching shear resistance is small for most common cases. The simulated scenario can be relevant in case of slab strengthening, where the slab needs to be unloaded and propped in order to activate the added shear reinforcement system (Koppitz et al. 2015).

Three repaired slab specimens with shear reinforcement were tested under cyclic loading in Robertson and Johnson 2004. The specimens had previously been tested under horizontal cyclic displacements but had survived until 8% drift without a punching failure. The repair, consisting in a combination of epoxy and CFRP sheets, resulted very effective because it restored both strength and stiffness of the specimens.

Besides the aforementioned cases, it is also important to study the seismic behaviour of unrepaired flat slabs that survive considerable imposed drifts without punching failure. Based on the available experimental evidence, it is not clear whether flat slabs that survive large imposed drifts are adequate for the post-earthquake life of the structure in terms of residual strength and deformation capacity. To this end, the behaviour of specimen C-SSR5b is studied in more detail in this section. Although the experimental investigation of this specimen does not cover all the aspects of post-earthquake behaviour of flat slabs, attention is brought to several aspects that can be important both in the design of flat slabs and the assessment of existing buildings.

### 4.9.2 Response of the specimen

The different loading protocol did not significantly influence the enveloping load–deformation response. The maximum horizontal force (unbalanced moment) reached by specimen C-SSR5b is close to the values corresponding to the other specimens with shear reinforcement and with approximately the same GSR. The backbone curve constructed by joining the maximum horizontal forces at the first cycle in each drift ratio level of the loading protocol shows a smooth transition between the different phases of loading (Figure 4.44).

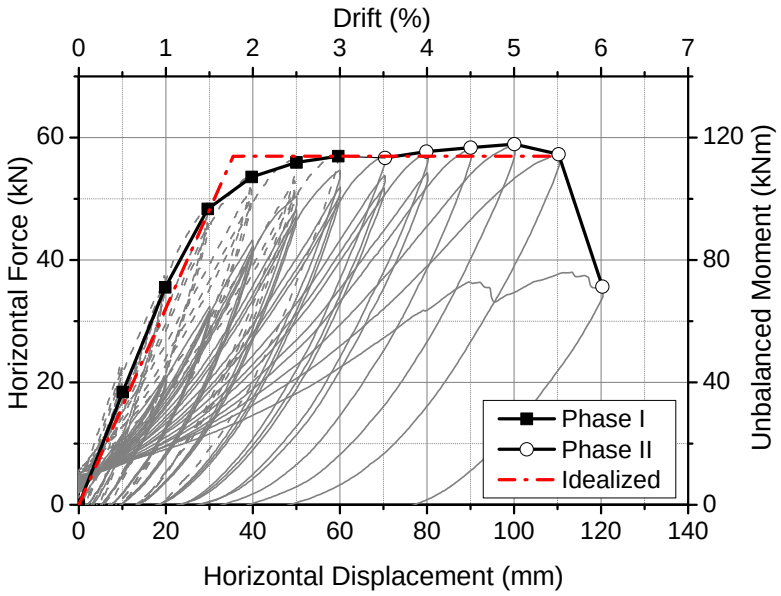


Figure 4.44: Transition between the two cyclic loading phases for specimen C-SSR5b, positive displacements

In Figure 4.45a, the gravity load $V_g$ is plotted as a function of the average increment of deflections at the borders of the specimen, $\Delta u$. The increment is measured as the difference between the actual value and the initial value at the beginning of the phase (i.e., self-weight, including test setup and equipment). Figure 4.45b shows the envelope curves for each horizontal cyclic loading phase. It is noticed that the vertical and the horizontal stiffness are both reduced in Phase II, due to the cracking already present in the beginning of that phase (from Phase I).

### 4.9.3 Effect of repeated loading on stiffness

The specimen is subjected to cycle repetitions within a loading phase and repetition of the same cycles in Phase II. Stiffness degradation for both types of cycle repetitions is studied by looking at the secant stiffness, $K_{sc}$, as described in Figure 4.23. The degradation of secant stiffness as a function of the dissipated energy is presented in Figure 4.46. The dissipated energy is calculated as the area enclosed by the hysteresis curve up to zero displacement point marking the completion of the respective cycle. The figure

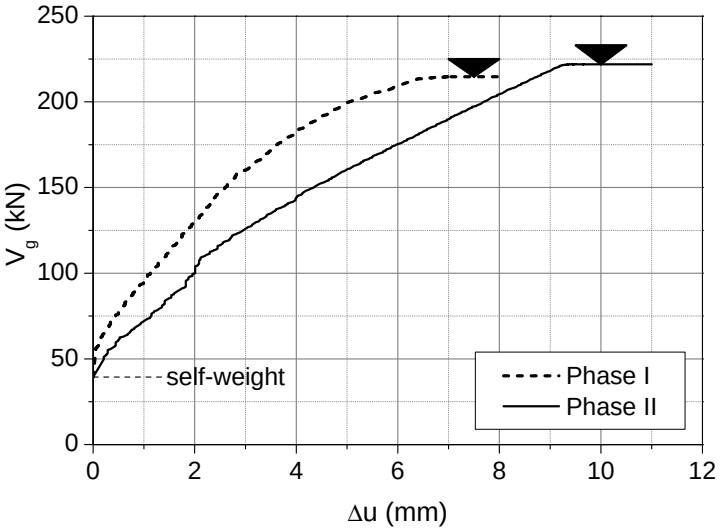


(a) Gravity loading

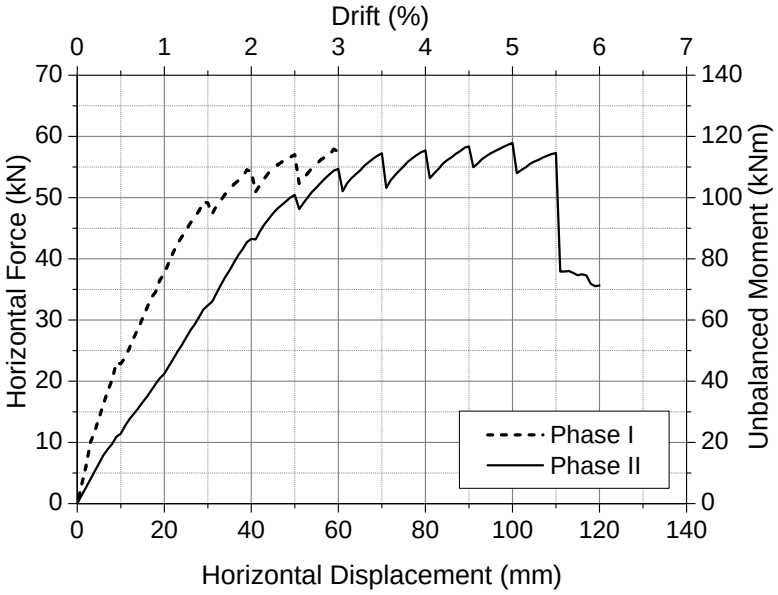


(b) Horizontal loading

Figure 4.45: Envelope force–deformation relationships

demonstrates that there is a rapid stiffness degradation during the first horizontal cycles. Afterwards, the slope of the graph decreases, following reasonably well (with $R^2 = 0.97$) the logarithmic law below:

$$K_{sc} = -0.507 \ln E_d + 5.96 \tag{4.3}$$

where $E_d$ is the dissipated energy in units "kNmm" and $K_{sc}$ is expressed in "kN/mm".

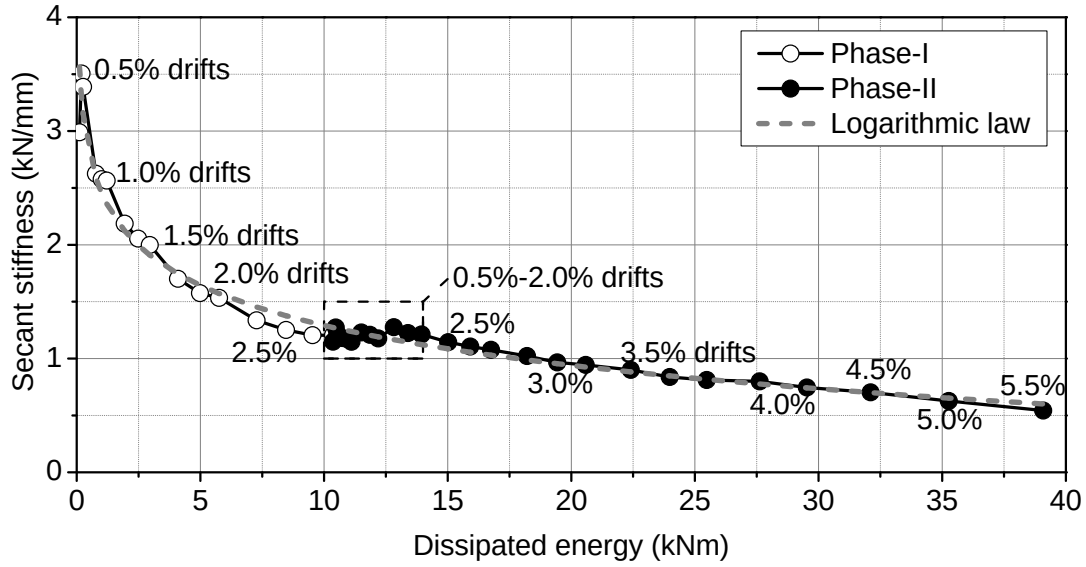


Figure 4.46: Secant stiffness as a function of dissipated energy

The stiffness was continuously reduced throughout the test, both during cycle repetitions within the same phase and from Phase I to Phase II. However, the stiffness degradation was slower after initial damage of the specimen. It is interesting to notice that there is a nearly horizontal plateau in the graph at the beginning of Phase II up to 2.0% drift ratios. In Figure 4.44, this roughly corresponds to the initial branch of the bilinear curve.

### 4.9.4 Residual deformations

In Section 4.3 it was shown that for the drift ratios imposed in Phase I, the residual horizontal displacements are not increased when the loading protocol is repeated (i.e., in Phase II). Also, the residual horizontal displacements are not significantly influenced by the repetitions of drift excursions within the same loading phase.

Besides avoiding punching failure, it is necessary to take into account horizontal residual displacements, energy dissipation and the stiffness against horizontal actions in buildings in which the contribution of the flat slabs in the earthquake resisting system is considered. On the other hand, in buildings where earthquake resistance relies on shear walls, moment resisting frames or braces, the avoidance of punching failures in slab–column connections and the limitation of required repair works are more relevant

aspects. However, the deflections of the slab can be important in terms of serviceability, regardless of the slabs being designated as primary or secondary seismic elements.

Specimen C-SSR5b was already deflected at the beginning of Phase II, due to the applied gravity loads in Phase I and the degradation during cyclic loading under constant gravity loads. As described in Figure 4.47, the residual deflections at the borders of the specimen (i.e., at the mid-span of the prototype structure) for zero horizontal displacement kept increasing throughout the test, unlike the residual horizontal displacements that remained almost unchanged from Phase I to Phase II (up to 3% drift). In the second phase, the increase of deflections was slow until 2% drifts, but then it continued to progress with a rate similar to that observed in Phase I.

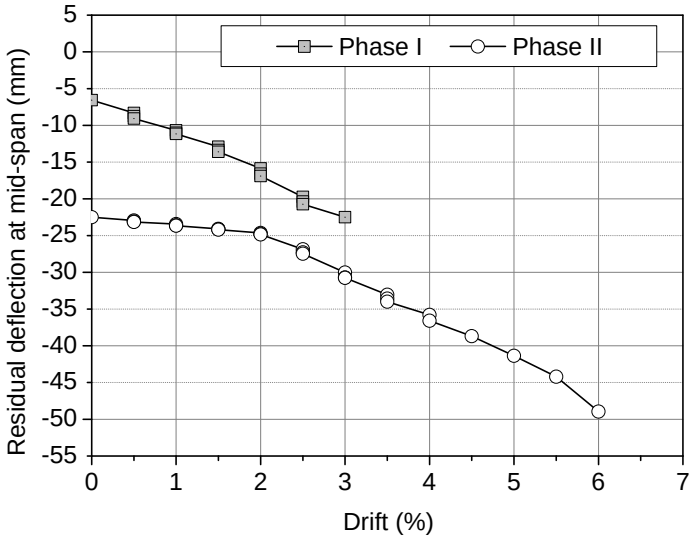


Figure 4.47: Evolution of residual deflections at the borders of the specimen for zero horizontal displacement at the end of different drift cycles

### 4.9.5 Concluding remarks

The reversed horizontal cyclic loading test of specimen C-SSR5b provided insight on the post-earthquake behaviour of flat slab–column connections. Although the specimen was loaded up to considerably high drift ratios in the first phase (3.0% drift), it was able to sustain further deformations in the second phase. The ultimate drift ratio of this specimen was comparable with that of the other specimens with similar characteristics. For flat slabs that are not part of the primary seismic resisting system, this is a desirable behaviour.

The second phase was characterized by a reduced loading stiffness and lower horizontal forces, which can be regarded as negative aspects of the post-earthquake behaviour for flat slabs that are primary seismic elements (for secondary seismic elements, these are

not very important as long as punching failure is avoided). Moreover, repeated horizontal loading caused significant degradation of the bending stiffness of the slab, resulting in a continuous increase of deflections throughout the entire test. This can be considered as a negative aspect for the serviceability of the flat slabs after earthquake loading, regardless of the designation of the flat slabs as primary or secondary seismic elements.

## 4.10 Comparison with code predictions

### 4.10.1 Eurocode 2

In the design of shear-reinforced flat slabs for punching in EC2 (CEN 2004c), it is required to check the shear resistance in at least three perimeters around the column, located:

- at the face of the column, $V_{0,col}$;
- at a distance $2d$ away from the face of the column, $V_{0c,s}$, and
- outside the shear-reinforced zone, $V_{0,out}$.

For the four specimens with shear reinforcement, the resistances in the three considered perimeters are calculated based on Equations 2.1–2.3. The results are summarized in Table 4.3, which shows that the outer perimeter is the most critical one for all specimens. Indeed, except for C-SSR5a, all specimens failed outside the shear-reinforced zone. However, there is no apparent relationship between $V_{0,out}$ and $d_{r,u}$. For example, C-SSR5a has the lowest resistance but sustained the highest drift ratio. It should be noted that $V_{0,out}$ in the table is calculated using the same value of $u_{out,ef}$ for all specimens (refer to Figure 3.5). However, the results of the present experimental campaign indicate that drift capacity can be enhanced by increasing the number of perimeters of studs beyond the number of perimeters for which EC2 (CEN 2004c) does not recommend further increase of $u_{out,ef}$.

Table 4.3: Concentric EC2 punching shear resistance considering the shear reinforcement

| Specimen | $V_g$ (kN) | $V_{0,col}$ (kN) | $V_{0c,s}$ (kN) | $V_{0,out}$ (kN) | $d_{r,u}$ (%) |
|---|---|---|---|---|---|
| C-SSR3 | 196.4 | 1217.1 | 695.1 | 464.5 | 4.0 |
| C-SSR5a | 169.2 | 849.0 | 657.1 | 402.5 | 6.0 |
| C-SSR5b | 213.9 | 1557.3 | 721.1 | 517.0 | 5.5 |
| C-SSR5c | 275.0 | 1784.1 | 748.5 | 554.6 | 4.0 |

In EC2 (CEN 2004c), the maximum value of $\beta$ (from Equation 2.4) for which punching failure outside the shear-reinforced zone does not occur can be calculated as:

$$\beta = \frac{v_{Rd,c} u_{out,ef} d}{V_g} \tag{4.4}$$

The corresponding resisting unbalanced moment (from Equation 2.5), for a "force–based" design, is:

$$M_{R,unb} = \frac{V_g W_{out}(\beta - 1)}{k \cdot u_{out,ef}} \tag{4.5}$$

where $k = 0.6$ for square column and $W_{out}$ is calculated as follows (CEN 2004c):

$$W_{out} = \int_0^{u_{out,ef}} |e| \, dl \tag{4.6}$$

where $dl$ is the length increment along the outer perimeter and $e$ is the distance of $dl$ from the bending axis, as shown in Figure 4.48. Dimensions in the figure correspond to specimens with 5 perimeters of studs (C-SSR5 series). For the specimen C-SSR3, the segments had the same shape but they were closer together. As a result, the value of $W_{out}$ depends on the number of perimeters of studs around the column, although $u_{out,ef}$ is the same for all the specimens.

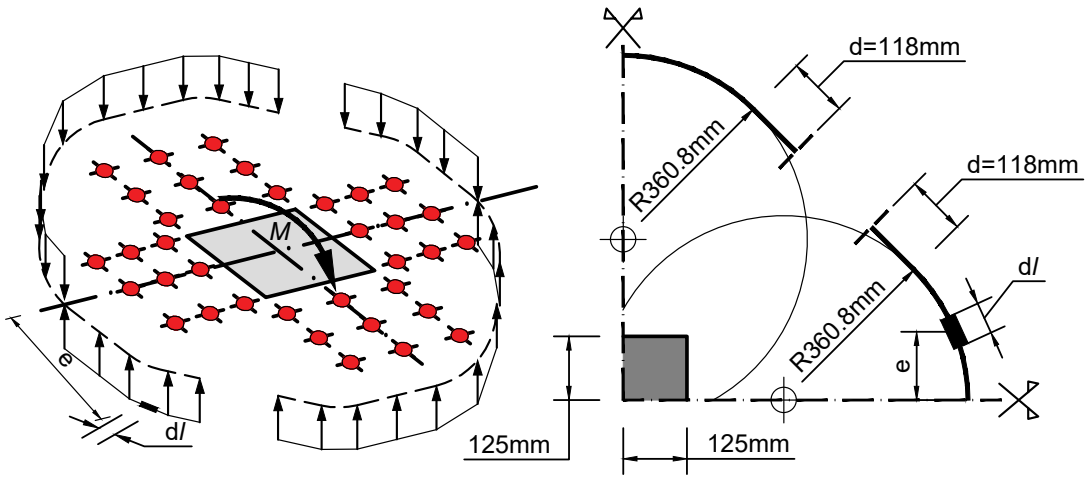


Figure 4.48: Calculation of $W_{out}$

The calculations and results are summarized in Table 4.4 along with the experimental unbalanced moments $M_{unb,max}$. The table shows that the unbalanced moment calculated based on EC2 (CEN 2004c) for failure outside the shear-reinforced zone is overestimated for all specimens. This indicates that the "force-based" approach based on EC2 (CEN 2004c) is not appropriate for predicting the unbalanced moment capacity under cyclic unbalanced moments, at least for this set of experimental results.

### 4.10.2 ACI 318

ACI 318 (ACI 2014) requires the safety checks to be performed for punching failure through the shear reinforcement ($V_{0c,s}$) and punching outside the shear-reinforced zone

Table 4.4: Resisting unbalanced moment considering failure outside the shear-reinforced zone in accordance with EC2

| Specimen | $v_{Rd,c}$ (MPa) | $V_g$ (kN) | $\beta$ | $W_{out}$ (mm) | $M_{unb,max}$ (kNm) | $M_{R,unb}$ (kNm) |
|---|---|---|---|---|---|---|
| C-SSR3 | 1.23 | 196.4 | 2.36 | 1038999 | 120.8 | 144.0 |
| C-SSR5a | 1.07 | 169.2 | 2.38 | 1263796 | 110.4 | 153.2 |
| C-SSR5b | 1.37 | 213.9 | 2.42 | 1263796 | 117.8 | 199.2 |
| C-SSR5c | 1.46 | 275.0 | 2.02 | 1263796 | 95.8 | 184.0 |

($V_{0,out}$). Referring to Section 2.2.2, the resistances for concentric loading conditions are calculated. The results are summarized in Table 4.5. In this table, the concentric punching shear resistance without shear reinforcement, $V_0$, is also given. Note that for EC2, the values of $V_0$ were provided earlier, in Table 3.5.

For the calculation of $V_{0,out}$, Equation 2.6 applies, but the control perimeter is located at a distance $d/2$ from the outermost layer of studs (Figure 4.49). Furthermore, the value of $V_{0,out}$ is limited to $0.17\lambda\sqrt{f_c}b_{out}d$ (where $b_{out}$ is the outer perimeter and the other symbols are defined in Section 2.2.2).

Table 4.5: Concentric ACI 318 punching shear resistance considering the shear reinforcement

| Specimen | $V_g$ (kN) | $V_0$ (kN) | $V_{0c,s}$ (kN) | $V_{0,out}$ (kN) | $d_{r,u}$ (%) |
|---|---|---|---|---|---|
| C-Ref | 224.8 | 452.9 | - | - | 1.0 |
| C-SSR3 | 196.4 | 367.4 | 556.7 | 321.8 | 4.0 |
| C-SSR5a | 169.2 | 296.2 | 448.7 | 341.9 | 6.0 |
| C-SSR5b | 213.9 | 430.7 | 652.6 | 497.7 | 5.5 |
| C-SSR5c | 275.0 | 479.7 | 726.8 | 552.8 | 4.0 |

Since spacing of the perimeters of studs was larger than $d/2$ but smaller than $3d/4$ (Section 2.2.2), Equation 2.10 was used to derive $V_{0c,s}$. It is noticed that, similarly to EC2 (CEN 2004c), the calculations for concentric loading in accordance with ACI 318 (ACI 2014) predict failure outside the shear-reinforced zone.

### 4.10.3 Model Code 2010 – CSCT

CSCT (Muttoni 2008) was used at the beginning of Chapter 3 for conceptual design purposes, due to its convenient graphical representation. Since CSCT forms the basis

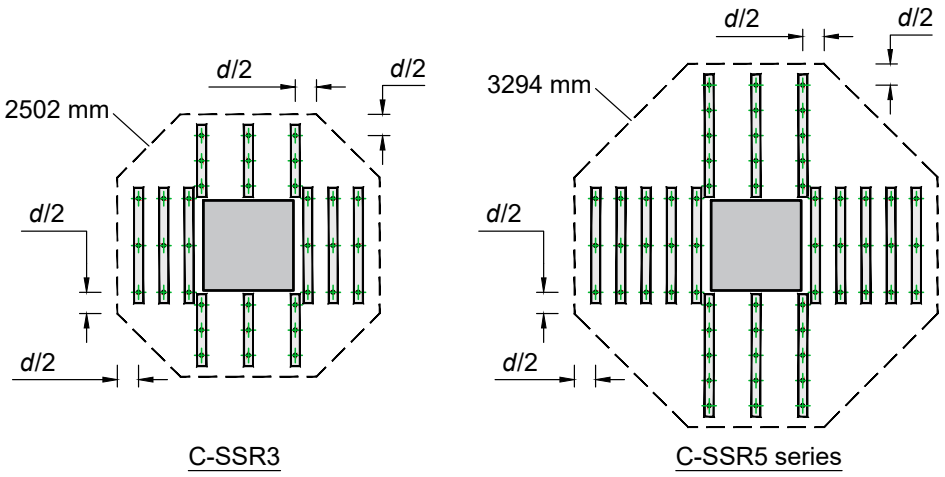


Figure 4.49: Outer control perimeter in accordance with ACI 318 (ACI 2014)

of MC2010 (*fib* 2013), this section continues with predictions of CSCT in its full form instead of the simplified formulation contained in MC2010.

Figure 3.1 is updated using the material properties determined from tests (Tables 3.3 -3.4), the measured effective depths (Table 3.2) and the aggregate sizes from Section 3.8.3. To account for the concentrated top reinforcement in vicinity of the column, the equilibrium of the sector elements was formulated by numerical integration, using two values of the longitudinal reinforcement ratio as a function of the radius (refer to Figure 3.2). The slab was divided into 360 sectors and the summation of internal forces (numerical integration) was performed every one millimetre of slab outside the critical shear crack in the radial direction. The numerical integration procedure was checked by comparing the results with the solution for uniform longitudinal reinforcement ratio (Muttoni 2008) and a good match was found. The radius $r_s$ was assumed equal to 845 mm. The results are presented in Figure 4.50.

The observations made in Section 3.1 based on Figure 3.1 still hold. More specifically:

- The outer perimeter is the most critical one for concentric punching shear loading conditions;

- The deformation capacity is increased when the extent of shear reinforcement is increased. This can be observed by looking at the criterion for failure outside the shear-reinforced zone. The intersection of this failure criterion curve with the load–rotation curve corresponds to a larger slab rotation in C-SSR5 series.

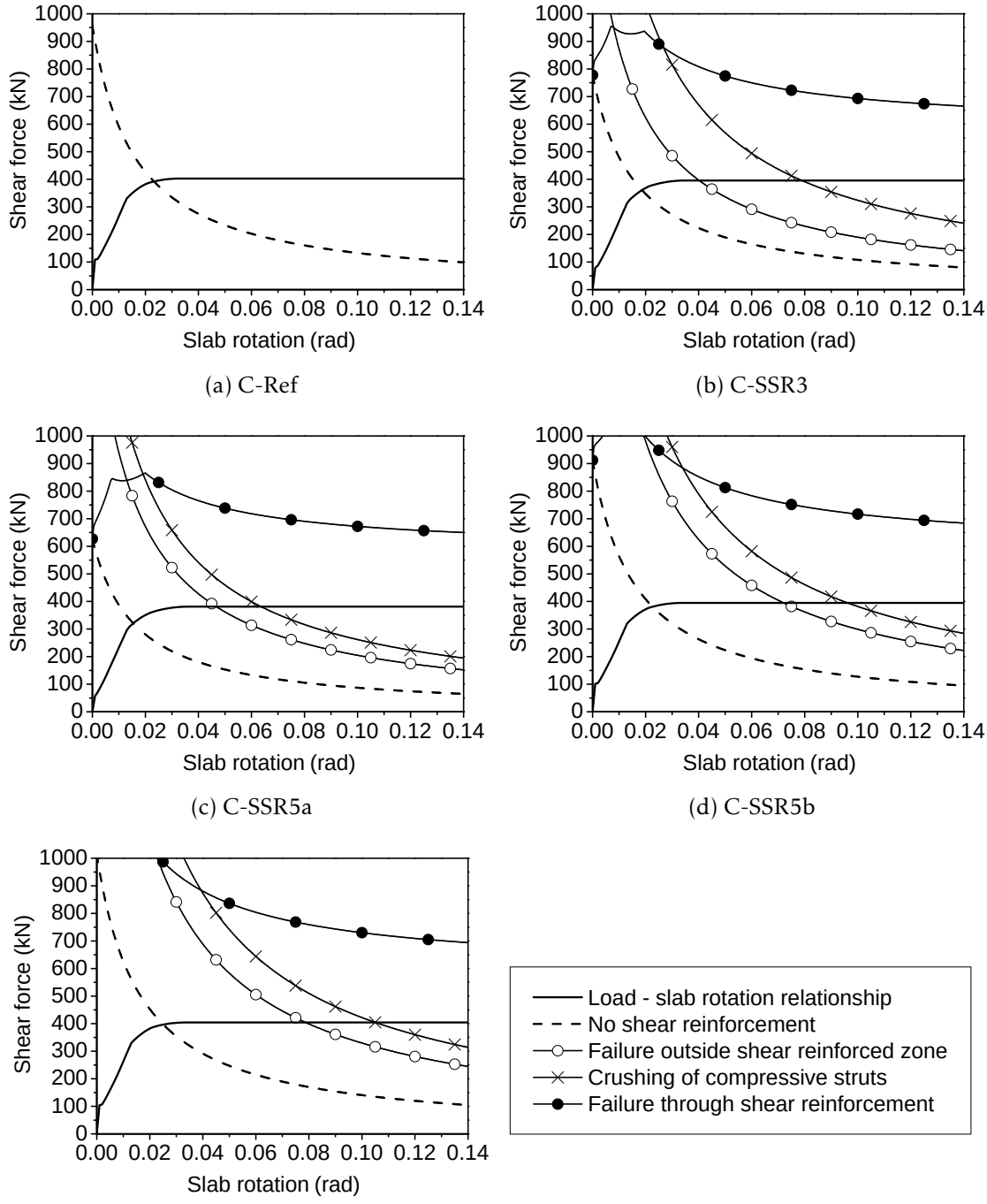


(a) C-Ref

(b) C-SSR3

(c) C-SSR5a

(d) C-SSR5b

(e) C-SSR5c

Figure 4.50: Predictions of CSCT for concentric loading of the specimens

### 4.10.4 Conclusion related to code predictions

An analysis based on three major design codes (EC2, ACI 318 and MC2010) was presented. Although the specimens were tested under constant gravity loads that constituted a relatively small fraction (around the half) of the concentric punching shear resistance, it was shown that the failure modes observed in the laboratory under horizontal cyclic loading were those that EC2 (CEN 2004c), MC2010 (*fib* 2013) and ACI 318 (ACI 2014) predicted to be the most critical ones under concentric loading conditions.

## 4.11 Comparison with analytical models

### 4.11.1 Comparison with Drakatos et al. 2018

Measurements from the displacement transducers were used to check the validity of the assumption of a sinusoidal law of rotations of sector elements (Equation 2.39) for the specimens presented in this study. Because of the finite number of measurement points on the top surface of the slab, fitted polynomials were adopted (Figure 4.51) to estimate the slab rotation at a radius $0.22 \times span$. The slab–column connection rotation was estimated considering the flexibility of the column.

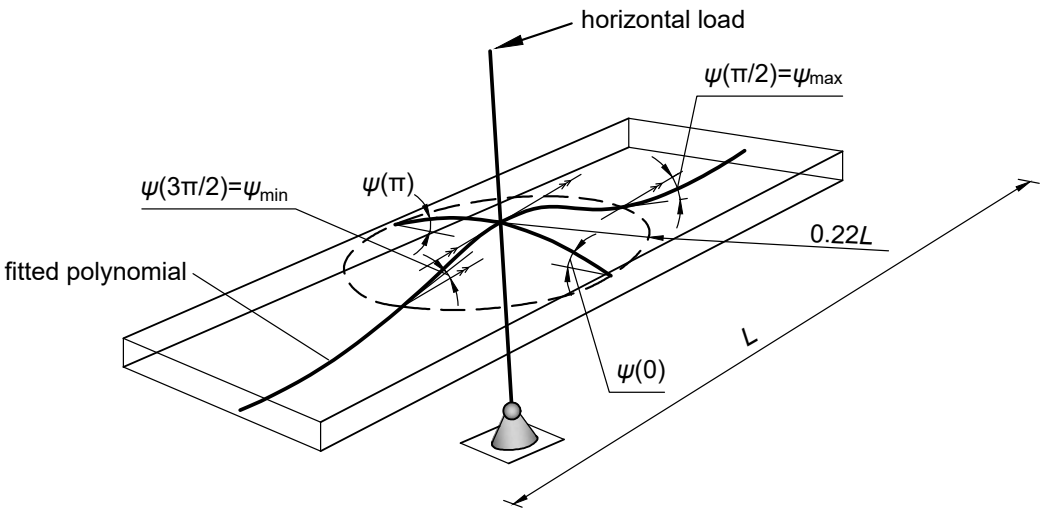


Figure 4.51: Definition of angles of rotation of slab sectors during horizontal loading

In Figure 4.52, the local slab rotations for the specimens presented in this study are compared to the sinusoidal law (Equation 2.39) for different horizontal load levels. Measurements are available only along the transversal and longitudinal direction of the slab, at locations indicated in Figure 3.23. Therefore, the comparison is possible only for angles 0, $\pi/2$, $\pi$ and $3\pi/2$. The figure shows that there is a good agreement between the measured rotations and the sinusoidal law adopted in the model of Drakatos et al. 2018. The same has also been experimentally verified in Drakatos et al. 2016.

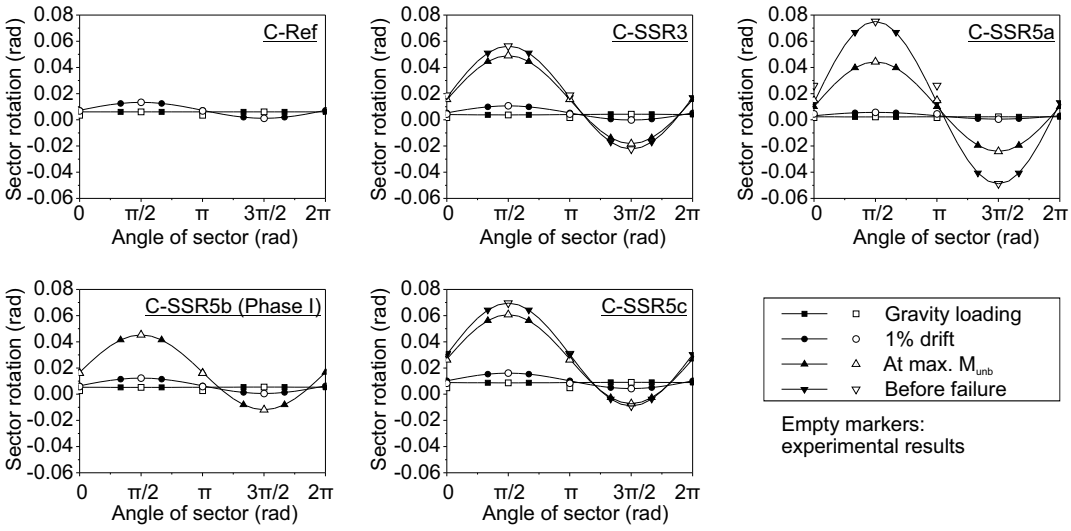


Figure 4.52: Verification of the assumption of a sinusoidal law of local slab rotations

For all the specimens presented in Chapter 3, a comparison is made in Figure 4.53 with the predictions of the mechanical model of Drakatos et al. 2018. The figure presents the relationship between the unbalanced moment and the slab–column connection rotation. For the experimental results, the connection rotation is calculated taking out the flexibility of the steel column used in the laboratory.

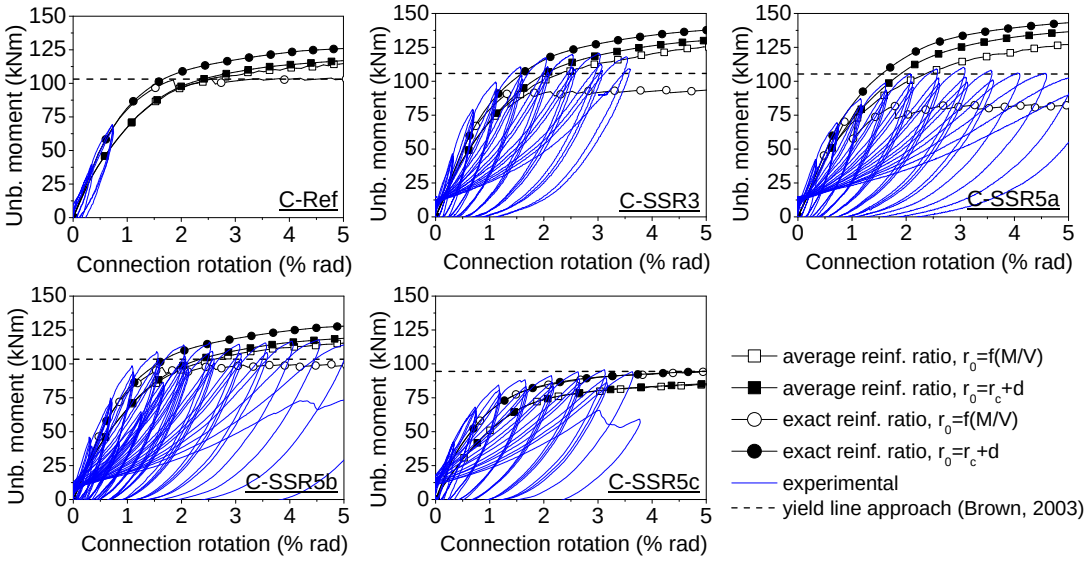


Figure 4.53: Comparison of the unbalanced moment–slab rotation relationship with the models of Drakatos et al. 2018 and Brown 2003

The radial and tangential moments at radius $r_s$ ($M_{rad}(\phi_i, r_s)$ and $M_{tan}(\phi_i, r_s)$ respectively) are assumed equal to zero in the following discussion. This means that the influence of the slab outside the radius $r_s = 0.22 \times span$ is not considered, and therefore, the

rotations that will be derived using the model are slab–column connection rotations. For a slab with full width, Drakatos et al. 2018 estimated that the slab–column connection is responsible for the major part (75%–80%) of the slab rotation under horizontal loading. Considering the limited width of the specimens, it is estimated that the influence of the slab outside radius $r_s$ is even smaller. A more rigorous approach would require modelling the portion of the slab outside radius $r_s$ with elastic equivalent beams in accordance with the Equivalent Beam Width approach, as described in Drakatos et al. 2018.

For the construction of curves corresponding to the model of Drakatos et al. 2018 in Figure 4.53, the slab was divided into 16 sector elements. As already observed by Drakatos et al. 2018, it is confirmed that a further increase of the number of sectors does not significantly affect the results. The tangential moments ($M_{tan}$) were calculated by numerical integration (to account for variable reinforcement, as will be discussed later). A quadrilinear moment–curvature was used for hogging moments and a simplified bilinear curve was adopted for sagging moments (Figure 4.54). In the radial direction, a discretization step of 2.5 mm was found to be suitable for the numerical integration of the tangential moments, in terms of accuracy and computational time.

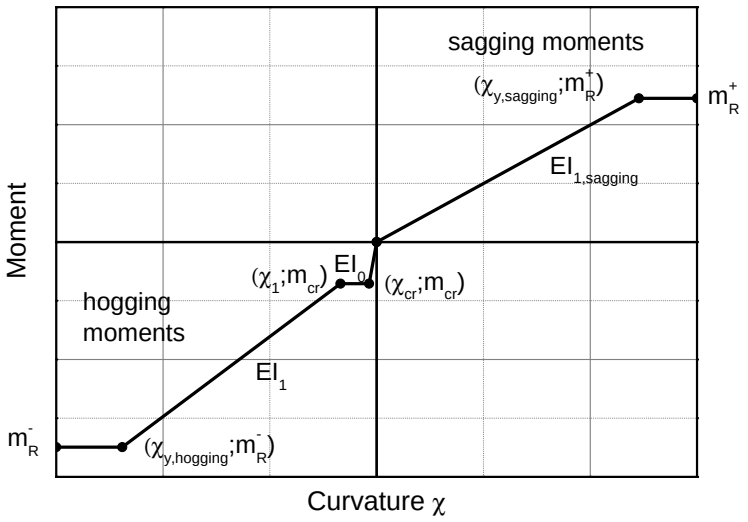


Figure 4.54: Adopted moment–curvature relationship

As described in Section 3.2, the longitudinal reinforcement is concentrated near the column. At a radius 450 mm from the centre of the slab, spacing of the longitudinal bars is doubled. In the original model proposed in Drakatos et al. 2018, the radius of the shear crack, $r_0$, is updated in each calculation step as a function of the attained eccentricity ($e = M/V$). This means that there is a sudden drop of the moments at radius $r_0$ (Figure 2.35) when $r_0$ exceeds 450 mm, and the resulting curve is not smooth. Results based on four variants of the mechanical model of Drakatos et al. 2018 are presented in Figure 4.53, with:

- average reinforcement ratio along the entire width of the specimen, and $r_0$ taken as a function of the attained eccentricity, in accordance with the recommendation of Drakatos et al. 2018;

- average reinforcement ratio along the entire width of the specimen but with $r_0$ assumed constant and equal to $r_c + d$, as in case of concentric loading (Muttoni 2008);

- exact reinforcement ratio along the width of the specimen, with a 50 mm linear transitory phase for numerical stability and $r_0$ taken as a function of the attained eccentricity;

- exact reinforcement ratio along the width of the specimen, but with $r_0$ assumed constant and equal to $r_c + d$.

The main observations based on Figure 4.53 are listed in the following:

- The mechanical model of Drakatos et al. 2018 captures reasonably well the response of the specimens under horizontal displacements. In all cases, the response in the analytical model is slightly softer than the experimental response;

- The curves corresponding to averaged top reinforcement ratio within the radius $r_s$ deviate considerably from the experiment in terms of initial stiffness, but they are close to the experiment in terms of maximum unbalanced moment;

- Using a variable radius $r_0$ has a limited effect on the curves when uniform longitudinal reinforcement is considered. When the longitudinal reinforcement is not uniform, the variable radius can lead to considerable numerical difficulties in determining the equilibrium state. Most importantly, using a variable $r_0$ can lead to an underestimation of the maximum unbalanced moment when the longitudinal reinforcement is concentrated over the column. To demonstrate why this happens, let's consider specimen C-SSR5c, which had the greatest gravity shear force, $V_g$ = 275 kN (see Table 3.5). For this shear force, the eccentricity becomes larger than the radius of the concentrated top reinforcement when the unbalanced moment exceeds 123.75 kNm (because $e$ = 123.75/275.00 = 0.45 m = radius within which the top reinforcing bars are spaced at 100 mm). However, the experimental specimen never reaches this high value of the unbalanced moment. In Figure 4.53 this is marked by a reduced unbalanced moment prediction, because the moments at radius $r_0$ are now calculated for a slab section that has half of the top reinforcement ratio. On the other hand, in the specimen C-SSR5a with the smallest gravity shear force, $V_g$ = 169.2 kN, the eccentricity becomes larger than the radius of the concentrated top reinforcement when the unbalanced moment exceeds 76.14 kNm.

- The analytical mechanical model worked best in predicting the maximum unbalanced moment of specimen C-SSR5c. The analytical results diverged most from the experiment in case of specimen C-SSR5a.

The updating of $r_0$ as proposed in Drakatos et al. 2018 was based on observations on tests of flat slab specimens without shear reinforcement (Drakatos et al. 2016). As demonstrated above, such an update of the radius should be considered with caution, especially when used for the purpose of estimating the unbalanced moment capacity.

### 4.11.2 Comparison with the yield line approach of Brown and Dilger 2004

Figure 4.53 also contains a comparison of the results with the yield line approach proposed in Brown and Dilger 2004. The yield line method gives only estimates of the maximum unbalanced moment and not the entire moment–rotation curve and it is represented by the horizontal dashed lines in Figure 4.53. It is noticed that the maximum unbalanced moment calculated using the yield line approach of Brown and Dilger 2004 is very close to the experiment for specimens C-SSR5a and C-SSR5c. For specimens C-SSR3 and C-SSR5b, the yield line approach slightly underestimates the unbalanced moment.

To get a broader view of the expected results using the yield line approach of Brown and Dilger 2004, $V_g$ in Equation 2.38 is expressed as follows:

$$V_g = GSR \times u_0 d C_{Rd,c} k (100 \rho_l f_c)^{1/3} \tag{4.7}$$

Neglecting compression reinforcement and assuming a rectangular stress–block for concrete as in Muttoni 2008 results in the following value of the moments $m_x$ ($m_y$):

$$m_{x(y)} = \rho_{x(y)} f_y d_{x(y)}^2 \left(1 - \frac{\rho_{x(y)} f_y}{2 f_c}\right) \tag{4.8}$$

where the subscripts $x$ and $y$ are used to denote the two main directions. Substituting equations 4.7 and 4.8 into Equation 2.38 results in:

$$M_{unb} = 2\pi c_y f_y d_x d_y \sqrt{\rho_x \rho_y \left(1 - \frac{\rho_y f_y}{2 f_c}\right)\left(1 - \frac{\rho_x f_y}{2 f_c}\right)} + 2 c_x \rho_x f_y d_x^2 \left(1 - \frac{\rho_x f_y}{2 f_c}\right) - \frac{3 c_y GSR \times u_0 d C_{Rd,c} k (100 \rho_l f_c)^{1/3}}{4} \tag{4.9}$$

Based on Equation 4.9, it is noticed that the unbalanced moment based on Brown and Dilger 2004 for the specimens presented in the current experimental campaign is a function of the Gravity Shear Ratio (GSR), the reinforcement ratios near the column in two directions ($\rho_x$ and $\rho_y$) and the average reinforcement ratio for punching shear calculation ($\rho_l$), steel yield stress ($f_y$), effective depths ($d_x$ and $d_y$), concrete strength ($f_c$) and column size ($c_x$, $c_y$). The values of $d$, $\rho$ and $f_y$ had only small changes between the specimens. The

column size was the same, $c_x = c_y = c = 250$ mm. Therefore, the only variables were $f_c$ and GSR. The unbalanced moment predictions of the yield line method of Brown 2003 for varying $f_c$ and GSR are plotted in 4.55. To facilitate comparison, nominal values are used for the effective depths and the corresponding reinforcement ratios. Steel yield stress is taken equal to 545 MPa.

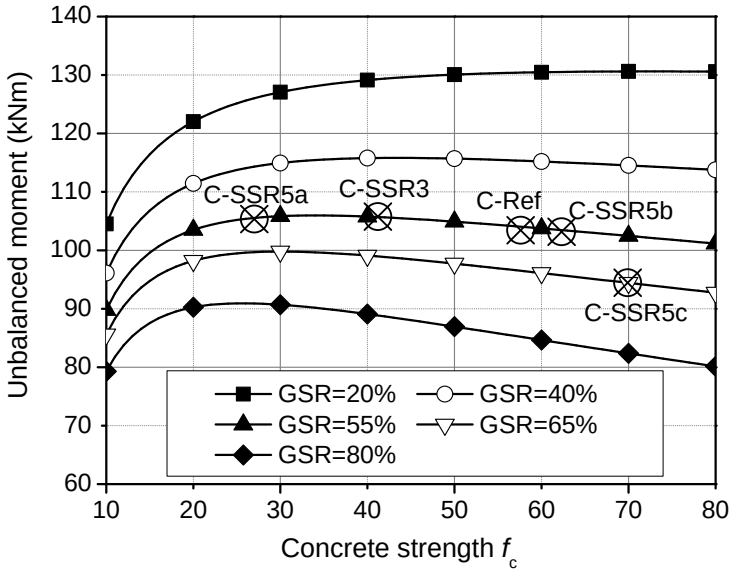


Figure 4.55: Unbalanced moment predictions of the yield line method of Brown 2003 for varying $f_c$ and GSR

Figure 4.55 shows that the yield line model of Brown and Dilger 2004 with gravity load assumed to be equal to a predefined percentage of the concentric punching shear resistance based on EC2 (CEN 2004c) predicts a rapid increase of the unbalanced moment with $f_c$, for concrete strengths lower than 20–30 MPa. The peak unbalanced moment is reached for a concrete strength that depends on GSR. For higher values of GSR, the peak unbalanced moment is reached for lower concrete strengths. For $f_c$ larger than that corresponding to the maximum unbalanced moment, the unbalanced moment is decreased. The rate of decrease is again depended on GSR. With higher values of GSR, the unbalanced moments are decreased more rapidly with the increase of $f_c$. It is noticed that the unbalanced moment predicted by the yield line approach of Brown and Dilger 2004 is not significantly influenced by concrete strength for $f_c$ between 30 and 40 MPa (common values in practice) and GSR around 50%.

The two curves of interest for the specimens under consideration are those corresponding to GSR=55% and GSR=65%. For the range of concrete strengths of the specimens, these two curves are almost parallel. The two specimens for which the unbalanced moment is underestimated by the yield line model (C-SSR3 and C-SSR5b, Figure 4.53) fall on the decreasing branch of the curve for GSR=55%. Although specimen C-SSR5c is also on the decreasing branch, the unbalanced moment predicted by the yield line model is

very close to the experimental result.

### 4.11.3 A refined analysis for C-SSR3

#### 4.11.3.1 Radius of the yielding zone

Specimen C-SSR3 is used in this section for a more detailed analysis. This specimen is chosen because of the intermediate value of concrete strength in relation to the other specimens. However, observations discussed herein are also applicable to the other specimens with shear reinforcement (C-SSR5 series).

As previously discussed, specimen C-SSR3 reached a horizontal plateau in the unbalanced moment–drift relationship before punching failure, which occurred outside the shear-reinforced zone after completing a full 4.0% drift cycle. It was shown in Figure 4.53 that three versions of the mechanical model of Drakatos et al. 2018 overestimated the unbalanced moment capacity of the specimen. In Figure 4.56, the radius $r_y$ based on the mechanical model is plotted for different slab–column rotations. This radius represents the extent of the zone upon which the flexural reinforcement has yielded (for the region beyond the radius $r_0$). For simplicity, average top reinforcement ratio was assumed for the entire width. Furthermore, the radius $r_0$ was assumed as fixed at a value $r_c + d$. The radius $r_y$ can be expressed as:

$$r_y = -\frac{\psi(\phi)}{\chi_y} \tag{4.10}$$

where $\psi(\phi)$ is given in Equation 2.39 and $\chi_y$ is the curvature at yielding. Substituting Equation 2.39 into Equation 4.10 and assuming a quadrilinear moment–curvature relationship (see notations in Figure 4.54):

$$r_y = +\frac{\frac{\psi_{max}+\psi_{min}}{2} + \frac{\psi_{max}-\psi_{min}}{2} sin(\phi)}{\frac{m_R}{EI_1} - \chi_{TS}} \tag{4.11}$$

where the decrease in curvature due to tension stiffening $\chi_{TS}$ is (Muttoni 2008):

$$\chi_{TS} = \frac{f_{ct}}{6\rho\beta E_s h} \tag{4.12}$$

with $\beta = 0.6$ for orthogonal layout of the flexural reinforcement (Muttoni 2008) and:

$$EI_1 = \rho\beta E_s d^3 \left(1 - \frac{c_c}{d}\right)\left(1 - \frac{c_c}{3d}\right) \tag{4.13}$$

The depth of the compression zone, $c_c$, can be expressed as (Muttoni 2008):

$$c_c = \rho\beta \frac{E_s}{E_c} d \left(\sqrt{1 + \frac{2E_c}{\rho\beta E_s}} - 1\right) \tag{4.14}$$

The denominator in Equations 4.10–4.11 is a constant value that depends on the section properties and material characteristics of the slab. The numerator represents the

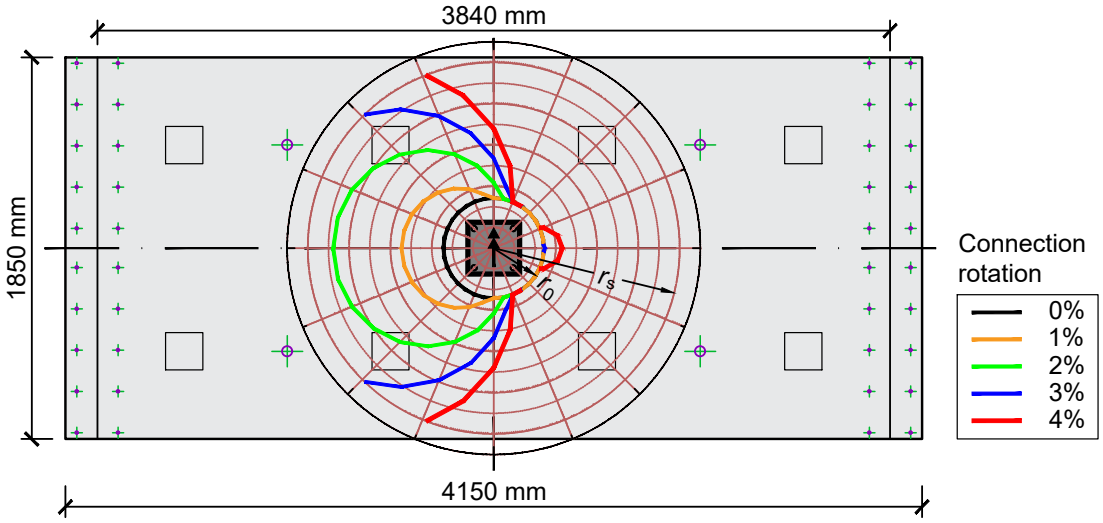


Figure 4.56: Radius of yielded region in C-SSR3 according to the model of Drakatos et al. 2018 for various connection rotations

adopted sinusoidal law (Drakatos et al. 2018). The equations show that the radius $r_y$ depends directly on the adopted law of rotations of slab sectors.

Comparing the readings of the strain gauges installed in the top bars (Figure 4.34) with Figure 4.56, it is noticed that yielding as measured by strain gauges in the experiment is reached for smaller slab–column connection rotations. For example, yielding of all instrumented bars was reached at around 2.0% drift (roughly 2.0% slab–column connection rotation). These bars cover nearly 70% of the width of the specimen (Figure 3.2). In contrast, the yielding zone does not extend as much as in the experiment for 2.0% connection rotation in Figure 4.56. To further investigate this discrepancy, a model was developed using the Finite Elements Method, as described in the following section.

#### 4.11.3.2 Finite Elements Analysis (FEA)

A nonlinear model was developed in the commercial computer program CSI Sap2000 (Computers and Structures. 2017). The model consists of four–node quadrilateral nonlinear layered shell elements with Mindlin/Reissner formulation. Smeared reinforcement in layers is used, corresponding to the top and bottom bars, in the longitudinal and transversal direction respectively (Figure 4.57). For the concrete section, 6 layers were used, adding up to a total of 10 layers through the thickness of the slab. Plane-stress behaviour is assumed in each layer. Although the Mindlin/Reissner formulation includes shear deformations, the model can only replicate the bending behaviour of the slab and no punching shear failure can occur in the model.

A general view of the model is shown in Figure 4.58. The model reproduces the test setup boundary conditions. The borders are constrained to have equal rotations and equal

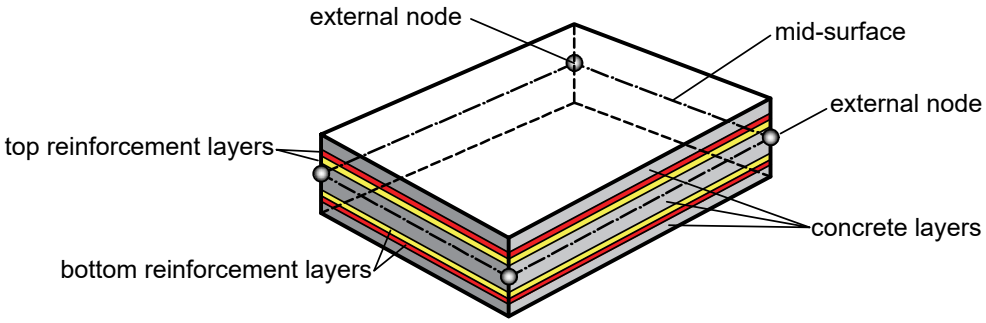


Figure 4.57: Nonlinear layered shell used

displacements (at mid–span locations). The nodes in the column region are constrained to behave as a rigid body. The stiffness properties of the column are modified to make the column rigid. The slab is meshed into regular rectangular elements with side dimension no larger than the thickness of the slab, $h$, as in Liu et al. 2015. Three shell sections were used, representing the region with concentrated top flexural reinforcement (Φ12 at 100 mm), another with Φ12 bars spaced at 200 mm and another section with Φ10 top bars spaced at 200 mm (see Figure 3.2). Gravity load is applied at the same locations it was applied in the experimental campaign. Increasing horizontal displacements are applied at the top node of the column.

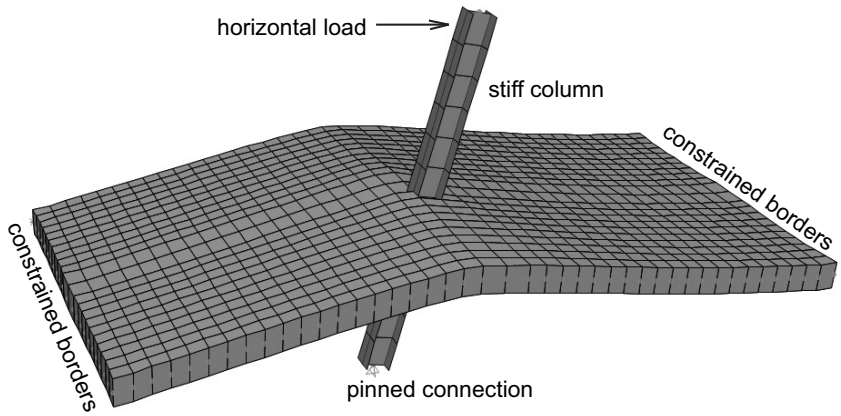


Figure 4.58: General view of the FEA model for specimen C-SSR3

Material properties are based on the experimental data for specimen C-SSR3 (see Section 3.8). The constitutive laws for concrete and steel reinforcement are shown in Figure 4.59. These constitutive laws are based on a combination of laboratory data (Section 3.8) and EC2 (CEN 2004c) provisions for material properties that were not directly obtained from tests. Tensile strength of concrete was reduced to 50% of its experimental value, as in Soares and Vollum 2015. It was found that the value of the tensile strength

influenced the deflections at the end of gravity loading and the adopted value led to matching results.

To account for torsional cracking, the shearing stress component of all the layers of the shell (both concrete and steel) is set as *inactive*. A reduction of the torsional stiffness to 1/8 of the uncracked stiffness has been found suitable in Sagaseta et al. 2011. The choice to reduce the torsional stiffness to zero was made after trying several values and comparing them to the experiment. Nonetheless, this choice is in accordance with the assumptions made in Drakatos et al. 2018 for the region of the slab outside the critical shear crack. A more rigorous approach would require the application of a non–constant shear modulus as a function of the principal tensile strain (for example, as in Polak 2005). The simplifications adopted herein are judged adequate for the purposes of this study.

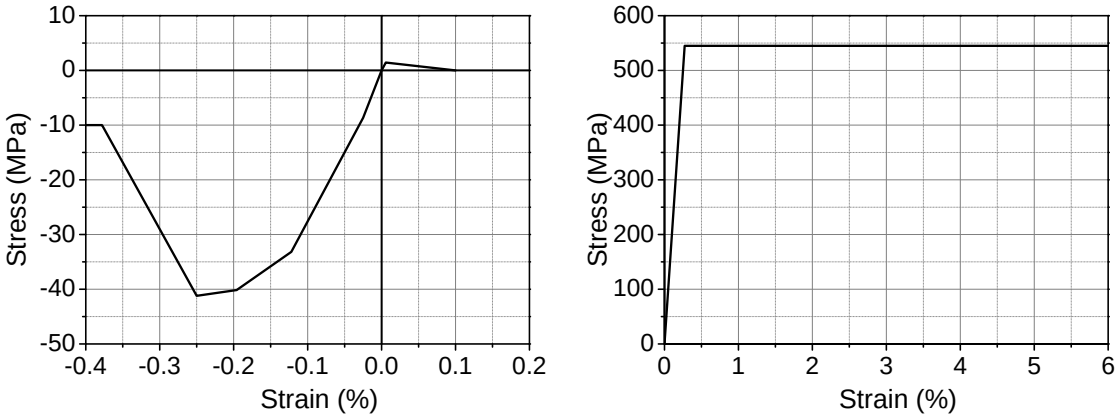


(a) Constitutive law for concrete

(b) Constitutive law for the reinforcement

Figure 4.59: Constitutive laws for materials used in the nonlinear shell model

In Figure 4.60, the experimental moment–rotation relationship is compared to the results of the FEA. In the model, the connection rotation is monitored in the central node. The unbalanced moment is calculated as the base shear force multiplied by the lever arm (2 m). The figure shows that a reasonably good match between the experimental result and the numerical model is achieved. The stiffness is slightly underestimated in the numerical model.

The stresses in the top bars after the application of gravity loading and stresses in top and bottom reinforcement layers at full global yielding based on the FEA are shown in Figure 4.61. The figure shows that, in agreement with the readings from the strain gauges installed in the longitudinal reinforcement (Figure 3.22), global yielding of the specimen is reached when yielding is extended through almost the entire width. Comparing with Figure 4.56, it is noticed that there is an apparent disagreement with the prediction based on the mechanical model of Drakatos et al. 2018. The FEA and the strain gauge readings show that yielding is extended over a greater width than the prediction of the mechanical model.

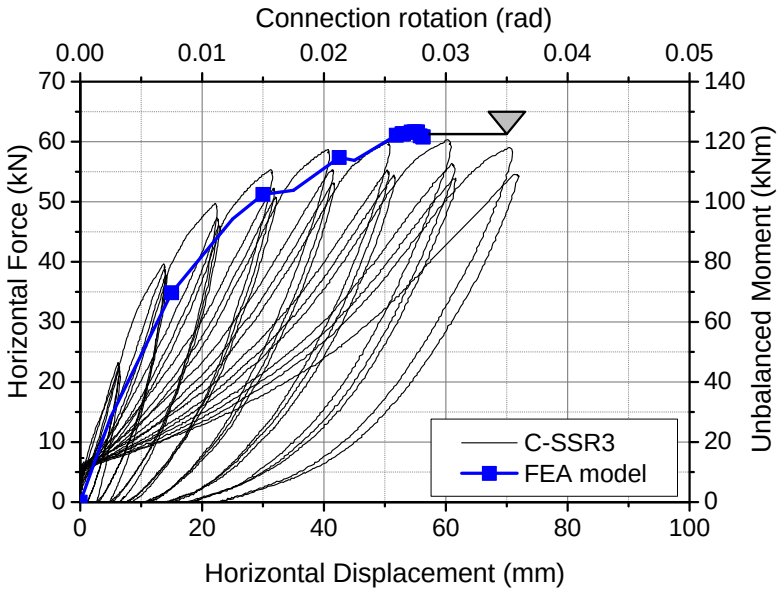


Figure 4.60: Comparison of FEA with experiment for specimen C-SSR3

To further investigate the reasons for the differences between the mechanical model and the experiment as well as the FEA, deflections of the slab are re-examined. Figure 4.62 shows the deflections of specimen C-SSR3 according to the FEA at the end of gravity loading and at global yielding (when the yielding unbalanced moment is reached). Comparing Figure 4.62 with Figure 4.12 and Figure 4.21, it is concluded that the FEA results are close to the experimental results for the gravity loading phase. For horizontal loading, the FEA model does not account for cyclic degradation of the slab and therefore underestimates the deflections. Nonetheless, the results are close to the experiment for drifts around 2.5%, when global yielding starts. Furthermore, the relationship between deflections in the longitudinal and transversal direction is reasonably preserved.

It is of interest to compare the iso-deflection lines of Figure 4.62 for gravity loading with those presented in Figure 4.22 based on measurements during the test of specimen C-SSR5c. Although the figures correspond to two different specimens, they confirm that:

- The assumed shape of the iso-deflection curves in Figure 4.22 is correct. Measurements during the experiments were available only along the two principal axes, and for the construction of the iso-deflection curves it was assumed that the shape was smooth and convex. The values differ between the figures because they correspond to two different specimens;
- The test setup simulates a marginally non-axisymmetric flat slab for gravity loading conditions. This can be regarded as a limitation of the test setup. Nevertheless, it is important to note that the test setup does effectively model a two-way slab, with significant deflections in both directions. For lateral loading, which is the main purpose of the test setup, the deflections in the transversal direction are indeed

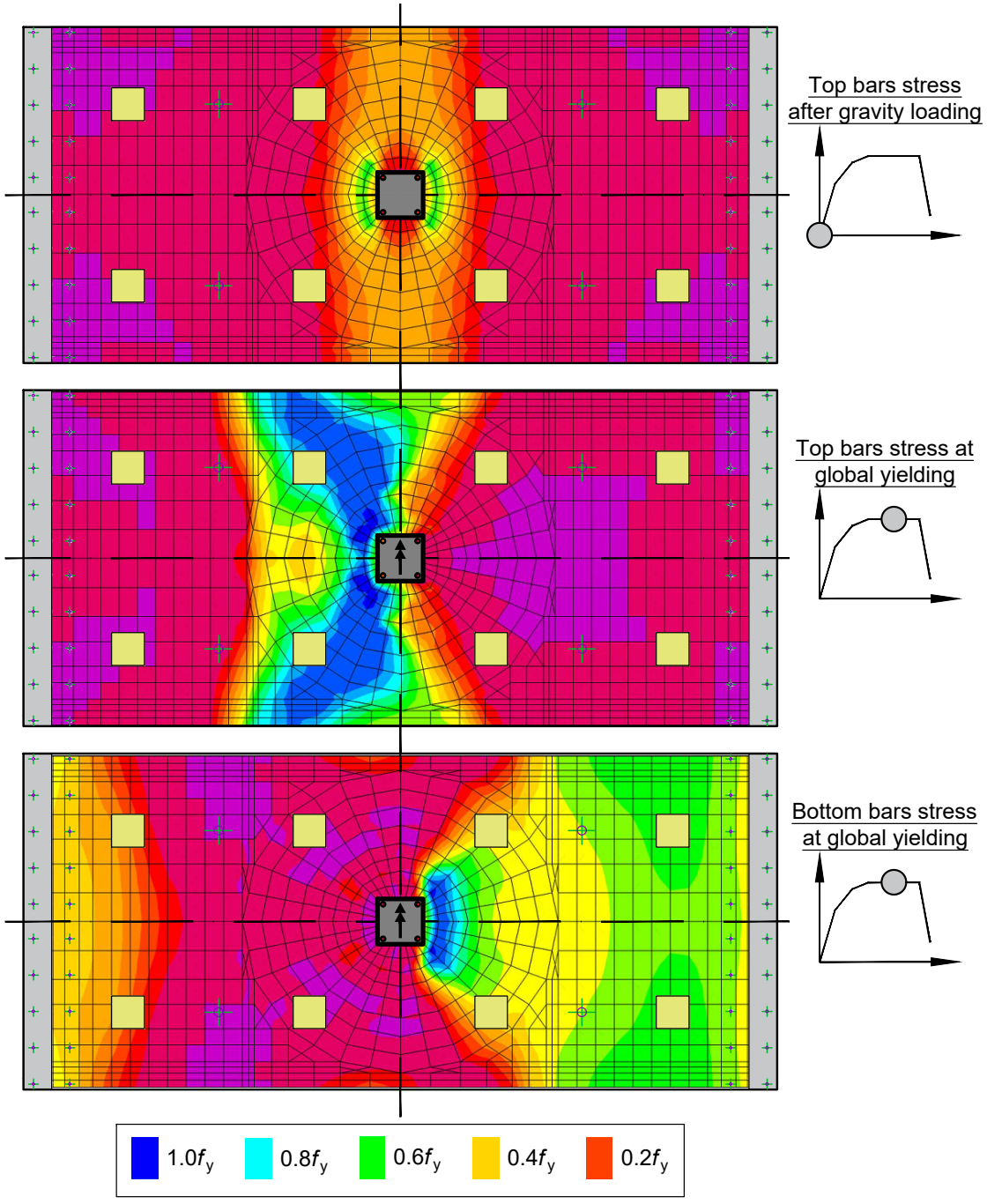


Figure 4.61: Stresses in longitudinal reinforcement after gravity loading and at global yielding

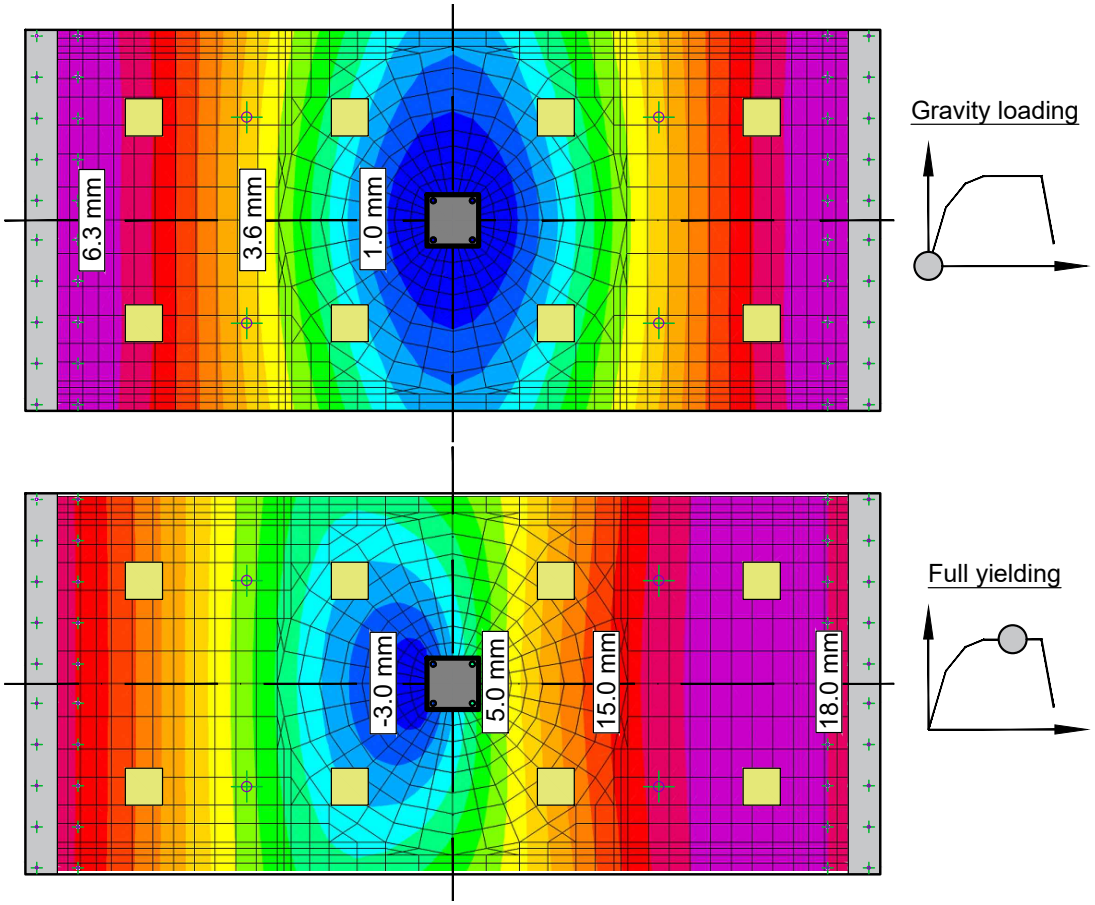


Figure 4.62: Specimen C-SSR3 deflections based on FEA

expected to be smaller than those in the longitudinal direction (refer for example to Equation 2.39, Drakatos et al. 2018) and the test setup reflects this feature reasonably well.

In Figure 4.63, a comparison is made between the sector rotation angles determined from the experiment (see Section 4.11.1 and Figure 4.52), from the FEA described above and from the sinusoidal law proposed in Drakatos et al. 2018. To facilitate the comparison, the rotations $\psi(\phi)$ of slab sectors at angle $\phi$ are divided by the rotation of the slab sector at angle $\pi/2$ (which is supposed to be the sector with the maximum rotation), such that the ordinate at $\pi/2$ is always equal to 1.

It is noticed that the major difference in shape occurs in Figure 4.63a, for gravity loading. Ideally, the slab sector rotations should have been constant at this phase, but there is a fluctuation of about 50% from angle 0 (sector perpendicular to the direction of loading) to $\pi/2$ (sector aligned with the direction of loading). Nonetheless, it is important to observe that at gravity loading, the rotations are considerably smaller than in eccentric loading. Referring to Figure 4.52, for example, such a fluctuation is barely visible.

At full yielding of the specimen (Figure 4.63c), the differences of the experiment and

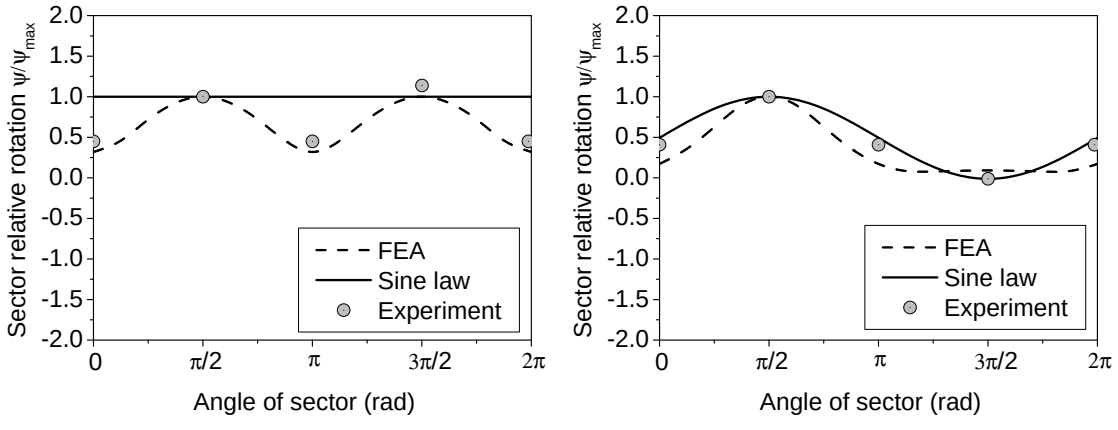


(a) After gravity loading

(b) At 1.0% drift

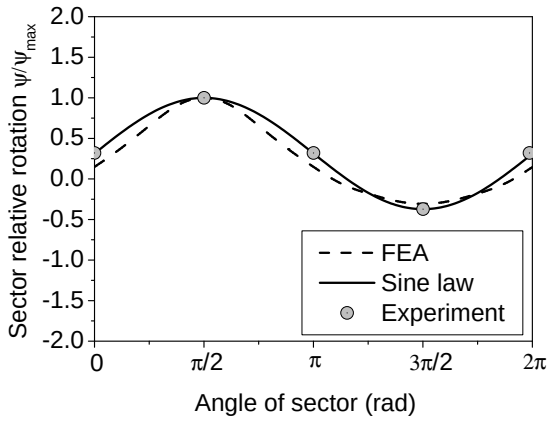


(c) At full specimen yielding

Figure 4.63: Comparison of C-SSR3 slab sector rotation angles determined from FEA, the experiment and Drakatos et al. 2018

FEA from the sinusoidal law are minimal. At intermediate drifts (Figure 4.63b), the results from the three different measurements are reasonably close with each other, but not as close as in case of full specimen yielding.

## 4.12 Comparison with specimens of Brown 2003

Brown 2003 presented a series of nine reinforced concrete flat slab specimens reinforced with headed shear studs. The specimens were tested under a constant gravity load of about 150 kN and reversed horizontal cyclic displacements. These specimens are chosen for a more detailed comparison in this section because they have several similarities with the slab specimens presented in the experimental campaign in Chapter 3. For instance, the specimens of Brown 2003 have the same slab thickness (150 mm), column side dimension (250 mm) and type of shear reinforcement (studs). Furthermore, the width of the specimens and the assumed radius of contraflexure is almost identical to that of the specimens of Chapter 3. The average effective depth of the specimens of Brown

2003 is slightly smaller, around 114 mm, compared to around 118 mm for specimens of the present study. In both experimental campaigns the clear concrete cover to the top bars was 20 mm, but a larger diameter of bars was used in Brown 2003 (16 mm bars versus 12 mm bars). A smaller amount of bottom longitudinal reinforcement was used in the specimens of Brown 2003 (11.3 mm bars at 210 mm versus 10 mm bars at 100 mm used in Chapter 3).

The specimens of Brown 2003 were square in plane, unlike the specimens of Chapter 3, which had a rectangular shape. As a result, this comparison will also serve as a benchmark for the obtained results using the test setup developed at FCT/UNL. The test setup used by Brown 2003 is shown in Figure 4.64. The borders of the specimen are pinned: rotations are allowed but all displacements are restrained. Lift-off of corners is not allowed. The gravity load, $V_g$, is applied directly to the column. Cyclic loading is applied through two coupled actuators attached to the ends of the column.

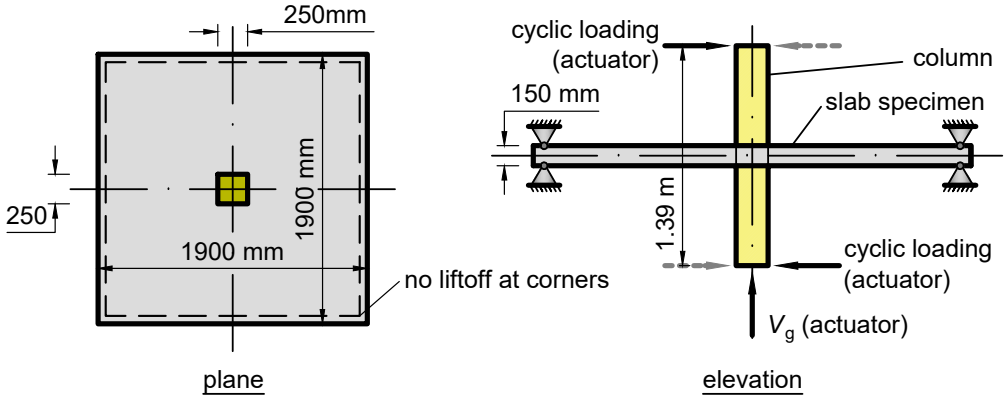


Figure 4.64: Test setup used in Brown 2003

The specimens of interest are named SJB-1, SJB-2, SJB-3, SJB-4 and SJB-5. Other specimens described in Brown 2003 had the column and the slab's reinforcement layout rotated by 45° and they are no longer considered herein for comparison with the specimens of the present experimental campaign. For all specimens, the steel yield stress was around 400 MPa. This value is lower than that used in Chapter 3. The area of studs in a perimeter around the column, $A_{sw}$, was approximately 567 mm$^2$ for all the specimens of interest in Brown 2003. The area of 12 studs with diameter 8 mm that was used for specimens C-SSR3 and C-SSR5 (a, b and c) is only slightly larger, approximately equal to 603 mm$^2$.

A summary of other main characteristics of the specimens of interest is given in Table 4.6. In this table, $\rho_l$ is the average top reinforcement ratio in vicinity of the column, $f_c$ is the concrete strength, $GSR_{EC2}$ is the Gravity Shear Ratio calculated in accordance with EC2 (CEN 2004c), $M_{unb,max}$ is the maximum attained unbalanced moment and $d_{r,max}$ is the maximum drift attained before failure.

Table 4.6: Summary of main characteristics of specimens of Brown 2003

| Specimen | No. rows of studs | $\rho_l$ (%) | $f_c$ (MPa) | $GSR_{EC2}$ | $M_{unb,max}$ (kNm) | $d_{r,max}$ (%) | Failure* |
|---|---|---|---|---|---|---|---|
| SJB-1 | 4 | 1.30 | 32.2 | 0.43 | 112 | 4.3 | O |
| SJB-2 | 4 | 1.45 | 34.3 | 0.41 | 138 | 4.6 | O |
| SJB-3 | 7 | 1.30 | 32.4 | 0.43 | 144 | 4.0 | I |
| SJB-4 | 7 | 1.45 | 39.7 | 0.39 | 137 | 6.4 | I, G |
| SJB-5 | 7 | 1.79 | 33.4 | 0.39 | 124 | 7.6 | O, G |

*O = outside shear-reinforced zone, I = inside shear-reinforced zone, G = gradual failure

In specimens of Brown 2003, the longitudinal reinforcement was higher and the concrete strength was lower, except for specimen C-SSR5a. The gravity shear ratio was lower for all the specimens of Brown 2003. From Table 4.6 it is noticed that the specimens of Brown 2003 had a higher scatter of peak unbalanced moments compared to the specimens of Chapter 3. For instance, the two similar specimens SJB-1 and SJB-3, differed only from the extent of shear reinforcement. However, the maximum unbalanced moment was more than 20% higher in the specimen with larger extent of studs. This phenomenon was not observed in the specimens presented in the experimental campaign. In terms of drift ratios, it is noticed that the specimens of Brown 2003 attained drift ratios that were all beyond 4.0%, similarly to the shear-reinforced specimens presented (C-SSR3 and C-SSR5 series).

A direct comparison of the backbone curves for specimens SJB-1 to SJB-5 (Brown 2003) with the specimens C-Ref, C-SSR3 and C-SSR5 series is shown in Figure 4.65. The figure shows that the initial stiffness of all the considered specimens was comparable. The results are somehow scattered in terms of maximum unbalanced moments. However, the specimens of Brown 2003 (which had a lower GSR), experienced higher unbalanced moments, except for specimen SJB-1 which was previously discussed.

## 4.13 Comparison with other similar specimens tested under the same conditions

Several specimens have been previously tested under conditions similar to those described in Chapter 3, using the same geometry of the specimens and the same longitudinal reinforcement detailing. Almeida et al. 2016 presented the reversed horizontal cyclic loading tests of three specimens named C-30, C-40 and C-50. The number in the name represents the GSR as a percentage. Specimen C-50 was similar to specimen C-Ref

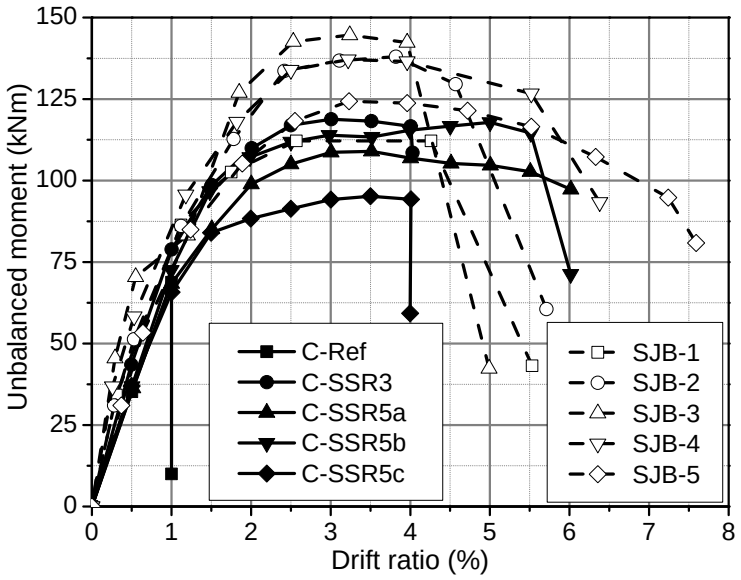


Figure 4.65: Comparison of backbone curves with experimental results from Brown 2003

presented herein, both in terms of geometry and loading. The concrete strength of specimen C-50 was slightly smaller than that of C-Ref (52.4 MPa vs. 62.3 MPa). Keeping approximately the same ratio between the applied gravity load $V_g$ and the concentric punching shear resistance calculated in accordance with EC2 (CEN 2004c),$V_0$, the value of $V_g$ for C-50 was slightly smaller than that of C-Ref (203.4 kN vs. 224.8 kN) to account for the lower concrete strength.

The force–displacement relationships for the two similar specimens are shown in Figure 4.66. The figure shows that the two test results were similar. Both specimens sustained a 1.0% drift ratio, but could not resist larger drifts. The maximum horizontal force (and unbalanced moment) was slightly larger in C-50. A possible explanation for this is the fact that the applied gravity load was slightly smaller in this specimen. Furthermore, the drift at which loading was reversed was slightly larger than 1.0% in C-50. The figure shows also that the loading and unloading stiffness, as well as the area enclosed by the hysteresis loops are almost identical in both specimens. As a conclusion, the test of specimen C-Ref effectively demonstrated the reproducibility of the experiments.

Two other specimens reported in Almeida et al. 2016 with lower GSR failed for larger drift ratios, confirming once again the inverse relationship between GSR and the ultimate drift ratio. A similar specimen, E-50, was tested under gravity loads comparable to C-50 and C-Ref but under monotonic horizontal displacements (Almeida et al. 2016). It was found that the ultimate drift capacity and ultimate horizontal force of specimen E-50 was higher, demonstrating the detrimental effect of cyclic loading compared to monotonic eccentric loading.

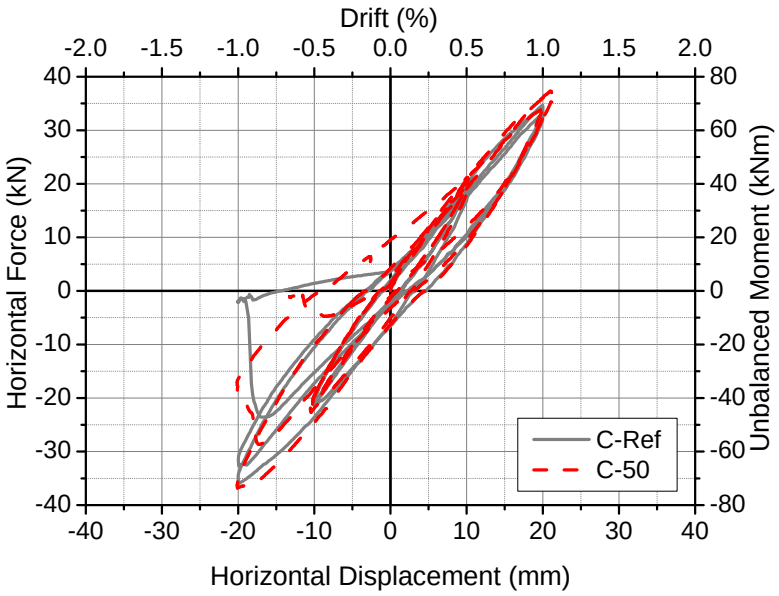


Figure 4.66: Comparison between specimen C-Ref and C-50 of Almeida et al. 2016

Steel fibre-reinforced concrete (SFRC) was found to be an effective means of enhancing the drift capacity of flat slab specimens tested under the test setup developed at FCT/UNL. Gouveia et al. 2018 presented the reversed horizontal cyclic loading test of four specimens, all similar to C-Ref and C-50, but with SFRC in various quantities in the region near the column. All the specimens failed for drifts larger than 3.0% (one of them reaching 6.0% without a brittle punching failure).

Inácio 2016 tested three similar specimens under cyclic loading. These specimens had High Strength Concrete (HSC) in the region near the column. In one of the specimens, HSC was used only in one third of the thickness. In the two other specimens, HSC was used through the entire depth of the slab but the extent of the zone with HSC was different in the two specimens. The compressive strength of the HSC was around 120 MPa. The applied gravity load was comparable with the load in specimens C-50 and C-Ref. Drift capacity was significantly enhanced by the use of HSC throughout the entire depth of the slab (the specimens reached a drift ratio of 3.0%). A smaller enhancement of the ultimate drift was observed in the specimen with partial application of HSC, where the ultimate drift ratio was 1.5%.

Particularly of interest is the comparison with similar specimens, reinforced with stirrups instead of studs. Almeida et al. 2018 described the horizontal cyclic loading test of four specimens reinforced with stirrups in a cruciform layout. Two of the specimens had three perimeters of stirrups around the column. The other two had five perimeters of stirrups. In two of the specimens (C-50 STR2 and C-50 STR4), the area of shear reinforcement in a perimeter was approximately the same as the area of the studs in a perimeter (Chapter 3). A total of 8Φ8 mm plus 8Φ6 mm vertical legs were placed in a perimeter of stirrups at specimens C-50 STR2 and C-50 STR4 (Figure 4.67), adding

up to a total area almost the same as the area of 12Φ8 mm studs used throughout the experimental campaign presented in Chapter 3. Furthermore, spacing of the vertical legs of shear reinforcement in the radial direction was the same for all specimens (with stirrups and studs). Specimen C-50 STR2 had three rows of stirrups around the column, whereas specimen C-50 STR4 had five rows of stirrups.

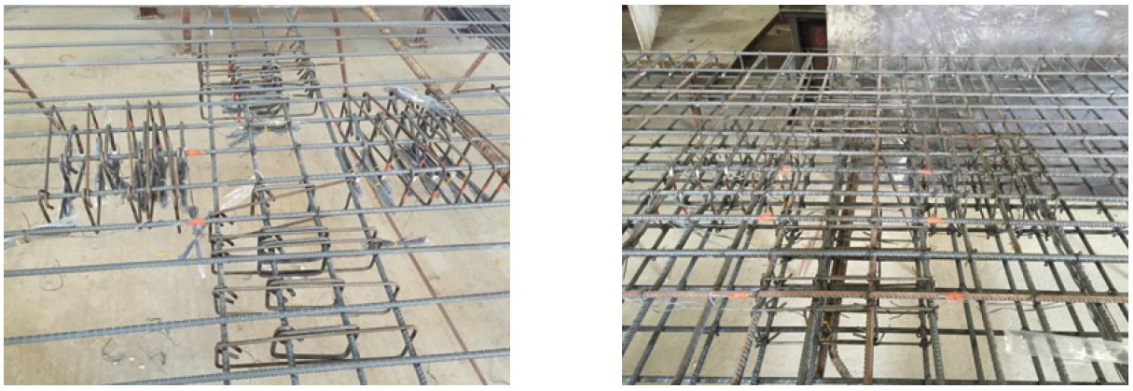

Figure 4.67: Stirrups used in specimens C-50 STR2 and C-50 STR4 (images from Ornelas 2017)

To facilitate comparison, the main characteristics of each specimen are summarized in Table 4.7. In this table, only the specimens with studs that had a comparable GSR with the specimens with stirrups are shown. Other properties that are not contained in the table, such as reinforcement yield stress and geometrical properties, were nominally identical between the specimens.

Table 4.7: Summary of main characteristics of comparable specimens with studs and stirrups

| Specimen | Shear reinf. | Perimeters of shear reinf. | $f_c$ (MPa) | $V_g$ (kN) | $d_{r,u}$ (%) | Failure mode |
|---|---|---|---|---|---|---|
| C-SSR3 | studs | 3 | 41.2 | 196.4 | 4.0 | Punching outside the shear-reinforced zone |
| C-SSR5a | studs | 5 | 27.0 | 169.2 | 6.0* | Gradual degradation, no punching |
| C-SSR5b | studs | 5 | 57.6 | 213.9 | 5.5 | Punching outside the shear-reinforced zone |
| C-50 STR2 | stirrups | 3 | 52.5 | 215.7 | 3.0 | Punching inside the shear-reinforced zone |
| C-50 STR4 | stirrups | 5 | 44.4 | 195.9 | 4.0* | Local flexural failure |

*at approximately 80% of the peak unbalanced moment.

Comparing the specimens with the same extent of shear reinforcement, it is concluded

that the drift capacity enhancement was larger in the specimens with studs. Nevertheless, the drift ratios attained by the specimens (including C-50 STR2, which failed for the lowest drift) are quite large for most practical purposes. This demonstrates once again that shear reinforcement in the form of stirrups or studs is very effective in the enhancement of the drift capacity of flat slab–column connections.

# Chapter 5

# Ultimate drift ratios in slab–column connections

This chapter contains an analysis of the experimentally observed drift ratios in slab–column connections from the literature, including the specimens presented in this dissertation. The aim is to identify the factors that influence the drift capacity the most and to estimate the influence of each factor. To this end, the database of tests from the literature is analysed in detail. A reorganization of the test setups into groups that better fit the purposes of this chapter is presented first.

The chapter is focused on specimens without shear reinforcement and with headed shear studs. For each group of specimens, the relationship between the ultimate drifts and various influencing factors (including punching shear and flexural strength) is studied.

For specimens with shear studs, a unitless factor incorporating the effect of gravity load, flexural strength and the extent of shear reinforcement is proposed. This factor describes reasonably well the relationship between the aforementioned factors and the ultimate drift capacity. The proposed factor and the main conclusions related to specimens with shear studs are published in Isufi et al. 2018b.

## 5.1 Regrouped test setups

A review of reversed horizontal cyclic loading tests on flat slab specimens with and without shear reinforcement was provided in Section 2.3. The main characteristics of the available test setups were summarized in Figure 2.18. As it was already discussed in Section 2.3, there exist considerable differences between the setups from different experimental campaigns, especially in the application of the gravity load (through the column or on the slab) and the number and arrangement of supports (continuous support on all four edges, continuous support on two opposite edges, support on struts located at the corners, support on struts with various configurations, etc.).

To simplify the analysis of the experimental results, the test setups are regrouped in Figure 5.1 based on the yield line patterns that can be used for the approximate estimation of the flexural strength, $V_{flex}$, defined as the slab's reaction on the column for which flexural failure of the specimen occurs.

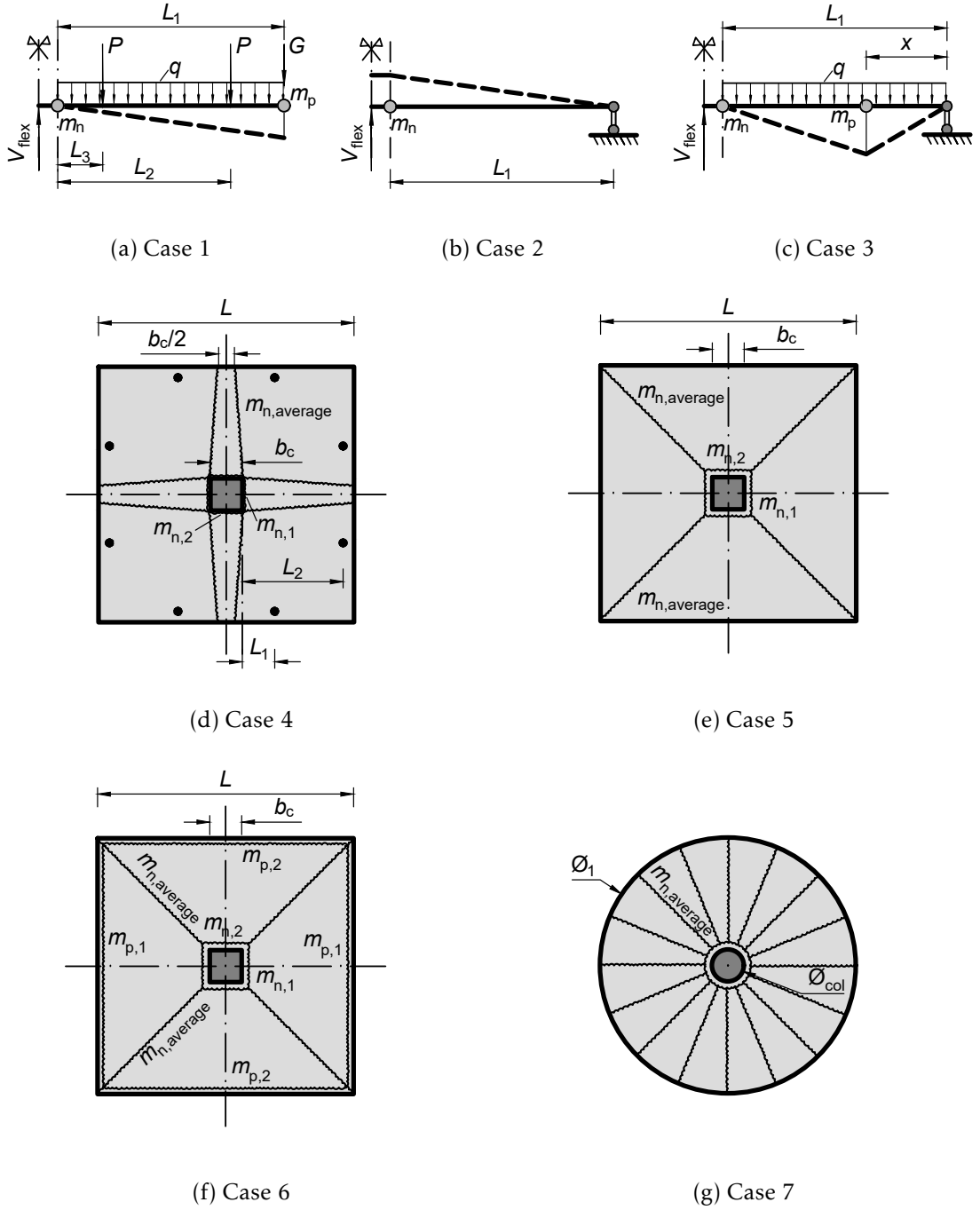


(a) Case 1 (b) Case 2 (c) Case 3

(d) Case 4 (e) Case 5

(f) Case 6 (g) Case 7

Figure 5.1: Test setups grouped by flexural yield line patterns for gravity loading

The yield lines in Figure 5.1 assume the gravity load is increased until a plastic mechanism is formed. In the experimental campaigns found in literature, the gravity load is usually kept constant, at a value smaller than $V_{flex}$ throughout the cyclic loading test.

However, the yield line patterns shown in the figure are meant to be used for the comparison of flexural strengths of the specimens. Figures 5.1a to 5.1c correspond to test setups and loading conditions that result in yield lines only in one direction, with length of all yield lines equal to the width of the specimen, $w$. Figures 5.1d to 5.1f correspond to yield lines stretched in two directions. The negative yield moments are denoted by $m_n$ and the positive yield moments are denoted by $m_p$. The last case (Figure 5.1g) represents a fan mechanism. The values of $V_{flex,i}$ for cases $i = 1$ to 7 are:

$$V_{flex,1} = 4\left(\frac{w(m_n + m_p) - GL_1 - qL_1^2/2}{L_2 + L_3}\right) + L_{tot}q + 2G \tag{5.1}$$

$$V_{flex,2} = 2\frac{wm_n}{L_1} \tag{5.2}$$

$$q_{flex,3} = \frac{m_n w/(L_1 - x) + m_p w[1/(L_1 - x) + 1/x]}{(L_1 - x)w/2 + xw/2} \tag{5.3}$$

$$V_{flex,4} \approx 4\frac{L}{(L_1 + L_2)}m_{n,av.} \tag{5.4}$$

$$V_{flex,5} = 8\frac{m_{n,av.}L}{L - b_c} \tag{5.5}$$

$$V_{flex,6} = 8\frac{m_{p,av.}L + b_c m_{n,av.} + (L - b_c)m_{n,av.}}{L - b_c} \tag{5.6}$$

$$V_{flex,7} = 2\pi\frac{\phi_1}{\phi_1 - \phi_{col}}m_{n,av.} \tag{5.7}$$

Equation 5.1 is specific for the test setup used at DEC/FCT/UNL, with $L_{tot}$ being the total length of the specimen. The loads $G$ and $q$ are constant, representing the self weight of the specimen and the relevant equipment. In Equation 5.3, the distributed load for which flexural failure occurs is given. Since the location of the positive yield line is unknown, the formula is iterated for different values of $x$ until a minimum ultimate load $q$ is found. The value of $V_{flex}$ is then calculated through a plastic analysis on a case-by-case basis.

## 5.2 Analysis of the observed ultimate drifts

### 5.2.1 Criteria for the compilation of the databases

For the compilation of databases with experimental results from literature, only interior slab–column assemblies subjected to unidirectional reversed cyclic loading are considered. The conclusions from experimental campaigns on specimens tested bidirectionally

are acknowledged, but these specimens are excluded from the databases in order to facilitate comparison with the specimens presented in the dissertation. For the same reason, tests on multi–panel specimens and full scale buildings are not further considered in this chapter. Other specimens are excluded from the database due to specifics compared to the rest of the specimens. For instance, the specimens reported in Tan and Teng 2005 have a very large ratio between the sides of the column (900/180 = 5), which is very different from the rest of the specimens and is classified as a "shear wall" in most codes. Also, tests in which after the completion of a certain number of cycles the load was monotonically increased to failure are excluded from the analysis of the data. High-strength concrete and lightweight concrete specimens are also not considered. A few specimens were excluded due to the lack of sufficient data for the purposes of this dissertation. Finally, the specimens tested under conditions that do not fall under the schemes given in Figure 5.1 are not further analysed due to the relatively high uncertainty in the determination of $V_{flex}$ and the ultimate drift.

For the specimens included in the databases, the following criteria were followed for the determination of the ultimate drift ratio, $d_{r,u}$ (Figure 5.2):

- If a punching failure occurred, $d_{r,u}$ is the maximum drift attained before failure;
- For specimens that did not fail in punching, $d_{r,u}$ is taken as the maximum drift attained before the horizontal load drops below 80% of the peak value attained throughout the test;
- When the behaviour of the specimen is non–symmetrical for positive and negative drifts, the smallest ultimate drift (in absolute value) is considered as $d_{r,u}$;
- Drifts are rounded to the nearest multiple of 0.1%.

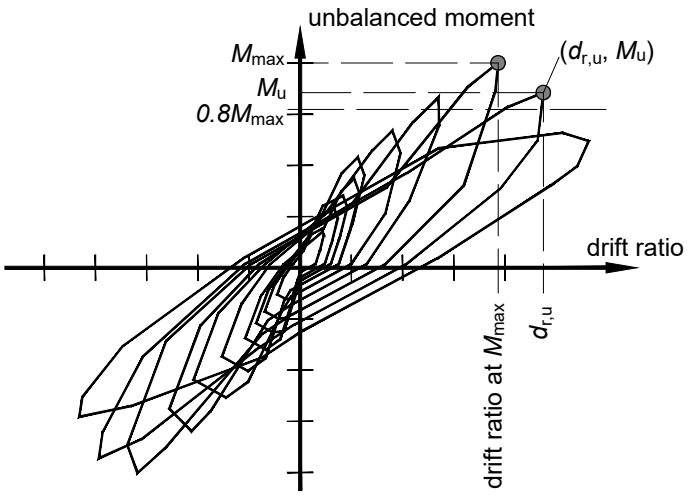


Figure 5.2: Determination of the ultimate drift ratio $d_{r,u}$

### 5.2.2 Ultimate drifts in flat slabs without shear reinforcement

Table 5.1 provides the main properties of the specimens without shear reinforcement included in the database. The ID is the name given by the authors of the publication, $d$ is the average effective depth of the longitudinal reinforcement, $\rho_l$ is the geometric mean of the longitudinal reinforcement ratio in the two main directions over a width equal to the column width plus $3d$ on each side. The table also contains the concrete strength $f_c$ and reinforcement yield stress $f_y$. The test setups are distinguished in the last column by the corresponding case for the calculation of $V_{flex}$, in accordance with Figure 5.1.

Table 5.2 summarizes the ultimate drift ratios, $d_{r,u}$. The table also contains the applied gravity load in the control perimeter $V_g$, the flexural strength $V_{flex}$ calculated as described in paragraph 5.1 and the concentric punching shear resistance $V_0$ in accordance with EC2 (CEN 2004c) for the specimens without shear reinforcement. The Gravity Shear Ratio (GSR) is:

$$GSR = \frac{V_g}{V_0} \tag{5.8}$$

and the Gravity Flexure Ratio (GFR) is defined as:

$$GFR = \frac{V_g}{V_{flex}} \tag{5.9}$$

Figure 5.3a shows the relationship between GSR and the ultimate drift ratio. The relationship between GFR and the ultimate drift is given in Figure 5.3b. The different test setup conditions are distinguished by different markers in accordance with Figure 5.1. As previously observed by various researchers (Pan and Moehle 1989; Luo and Durrani 1995; Hueste et al. 2007; Ramos et al. 2017), there is a trend of decreasing drifts with the increase of GSR. Figure 5.3b shows that there is a tendency to have lower drifts with larger values of GFR too, but this observation is inconclusive due to the large scatter.

An effort was made to establish a relationship between GSR, GFR and $d_{r,u}$ using symbolic regression with the help of the software Eureqa Desktop (Schmidt and Lipson 2014; Schmidt and Lipson 2009). This software uses Artificial Intelligence techniques to find expressions that relate the input and output variables. The best fit solutions generated by the program were too complicated for practical purposes. The mean absolute error was still relatively high even for very complex relationships between GSR and GFR. Due to the relatively large scatter of results (Figure 5.3), this was to be expected. An important observation was made: the generated relationships containing only GSR but not GFR had a comparable error with those containing both variables. In other words, including GFR led to complex relationships with no practical value, because the error was not substantially reduced.

Starting from the suggestions generated by Eureqa Desktop (Schmidt and Lipson 2014; Schmidt and Lipson 2009), a lower–bound curve similar to that proposed in ACI 318-14 (ACI 2014) and in Ramos et al. 2017 (for GSR calculated according to EC2 (CEN

Table 5.1: Main properties of specimens without shear reinforcement

| Reference | ID | $d$ (mm) | $\rho_l$ (%) | $f_c$ (MPa) | $f_y$ (MPa) | $V_{flex}$ case (Fig. 5.1) |
|---|---|---|---|---|---|---|
| Zee and Moehle 1984 | INT | 52 | 0.7 | 24.8 | 434 | 3 |
| Robertson 1990 | 8I | 90 | 0.7 | 39.3 | 525 | 3 |
| Pan and Moehle 1992 | AP1 | 104 | 0.8 | 33.3 | 472 | - |
| | AP3 | 104 | 0.8 | 31.4 | 472 | - |
| Cao 1993 | CD-1 | 107 | 1.3 | 40.4 | 395 | 5 |
| | CD-5 | 107 | 1.3 | 31.2 | 395 | 5 |
| | CD-8 | 107 | 1.3 | 27.0 | 395 | 5 |
| Farhey et al. 1993 | 2 | 62 | 0.8 | 29.2 | 458 | 2 |
| | 3 | 62 | 0.8 | 13.9 | 458 | 2 |
| | 4 | 62 | 0.8 | 13.9 | 458 | 2 |
| Emam et al. 1997 | HHHC0.5 | 119 | 0.5 | 75.8 | 460 | 5 |
| | HHHC1.0 | 119 | 1.0 | 72.3 | 460 | 5 |
| | NHHC0.5 | 119 | 0.5 | 36.8 | 460 | 5 |
| | NHHC1.0 | 119 | 1.0 | 35.4 | 460 | 5 |
| Marzouk et al. 2001 | NSNW0.5C | 119 | 0.5 | 35.0 | 400 | 5 |
| | NSNW1.0C | 119 | 1.0 | 35.0 | 400 | 5 |
| Ali and Alexander 2002 | SP-B | 106 | 1.3 | 34.1 | 415 | $\approx 6$ |
| Robertson et al. 2002 | 1C | 95 | 0.6 | 35.4 | 420 | 3 |
| Stark et al. 2005 | C-02 | 82 | 1.2 | 30.9 | 454 | 2 |
| | C-63 | 82 | 1.2 | 30.9 | 454 | 2 |
| Robertson and Johnson 2006 | ND1C | 100 | 0.6 | 29.6 | 400 | 3 |
| | ND4LL | 100 | 0.6 | 32.3 | 400 | 3 |
| | ND5XL | 100 | 0.6 | 24.1 | 400 | 3 |
| | ND6HR | 100 | 1.0 | 26.3 | 400 | 3 |
| | ND7LR | 100 | 0.4 | 18.8 | 400 | 3 |
| Kang and Wallace 2008 | C0 | 130 | 0.5 | 38.6 | 452 | 5 |
| Tian et al. 2008 | L0.5 | 127 | 0.5 | 25.6 | 469 | 4 |
| Park et al. 2012 | RC-A | 114 | 1.1 | 22.5 | 430 | 2 |
| | RC-B | 114 | 1.1 | 38.7 | 430 | 2 |
| Almeida et al. 2016 | C-50 | 118 | 1.0 | 52.4 | 526 | 1 |
| | C-40 | 119 | 1.0 | 53.1 | 526 | 1 |
| | C-30 | 118 | 1.0 | 66.5 | 526 | 1 |
| Drakatos et al. 2016 | PD8 | 214 | 0.8 | 34.4 | 575 | 4 |
| | PD6 | 214 | 0.8 | 40.3 | 507 | 4 |
| | PD2 | 214 | 0.8 | 38.8 | 558 | 4 |

Table 5.2: Ultimate drifts in specimens without shear reinforcement

| Reference | ID | $V_g$ (kN) | $V_{flex}$ (kN) | $V_0$ (kN) | GSR (%) | GFR (%) | $d_{r,u}$ (%) |
|---|---|---|---|---|---|---|---|
| Zee and Moehle 1984 | INT | 16 | 255 | 57 | 28 | 6 | 3.8 |
| Robertson 1990 | 8I | 47 | 732 | 211 | 22 | 6 | 4.3 |
| Pan and Moehle 1992 | AP1 | 104 | NC | 263 | 39 | NC | 1.6 |
| | AP3 | 53 | NC | 258 | 21 | NC | 3.7 |
| Cao 1993 | CD-1 | 300 | 470 | 340 | 88 | 64 | 0.6 |
| | CD-5 | 200 | 461 | 312 | 64 | 43 | 1.0 |
| | CD-8 | 150 | 455 | 297 | 50 | 33 | 1.2 |
| Farhey et al. 1993 | 2 | 0 | 45 | 112 | 0 | 0 | 4.0 |
| | 3 | 25 | 43 | 88 | 29 | 58 | 3.7 |
| | 4 | 25 | 43 | 80 | 31 | 58 | 2.5 |
| Emam et al. 1997 | HHHC0.5 | 125 | 315 | 359 | 35 | 40 | 5.2 |
| | HHHC1.0 | 125 | 620 | 445 | 28 | 20 | 5.0 |
| | NHHC0.5 | 125 | 310 | 282 | 44 | 40 | 3.7 |
| | NHHC1.0 | 125 | 597 | 351 | 36 | 21 | 3.7 |
| Marzouk et al. 2001 | NSNW0.5C | 125 | 270 | 278 | 45 | 46 | 4.0 |
| | NSNW1.0C | 125 | 524 | 350 | 36 | 24 | 4.9 |
| Ali and Alexander 2002 | SP-B | 94 | NC | 371 | 25 | NC | 3.5 |
| Robertson et al. 2002 | 1C | 40 | 461 | 209 | 19 | 9 | 3.0 |
| Stark et al. 2005 | C-02 | 90 | 98 | 220 | 41 | 91 | 2.4 |
| | C-63 | 90 | 98 | 220 | 41 | 91 | 2.3 |
| Robertson and Johnson 2006 | ND1C | 55 | 423 | 214 | 26 | 13 | 6.0 |
| | ND4LL | 71 | 424 | 220 | 32 | 17 | 3.0 |
| | ND5XL | 101 | 421 | 199 | 51 | 24 | 2.0 |
| | ND6HR | 66 | 780 | 247 | 27 | 8 | 3.0 |
| | ND7LR | 49 | 376 | 162 | 30 | 13 | 5.0 |
| Kang and Wallace 2008 | C0 | 125 | 259 | 342 | 37 | 48 | 1.9 |
| Tian et al. 2008 | L0.5 | 105 | 238 | 342 | 31 | 44 | 2.0 |
| Park et al. 2012 | RC-A | 134 | 223 | 316 | 42 | 60 | 1.5 |
| | RC-B | 161 | 230 | 379 | 42 | 70 | 1.9 |
| Almeida et al. 2016 | C-50 | 203 | 436 | 389 | 52 | 47 | 1.0 |
| | C-40 | 167 | 436 | 396 | 42 | 38 | 1.5 |
| | C-30 | 131 | 439 | 422 | 31 | 30 | 2.0 |
| Drakatos et al. 2016 | PD8 | 376 | 1412 | 952 | 39 | 27 | 1.7 |
| | PD6 | 517 | 1226 | 1004 | 52 | 41 | 0.8 |
| | PD2 | 734 | 1383 | 992 | 74 | 53 | 0.4 |

NC = not calculated

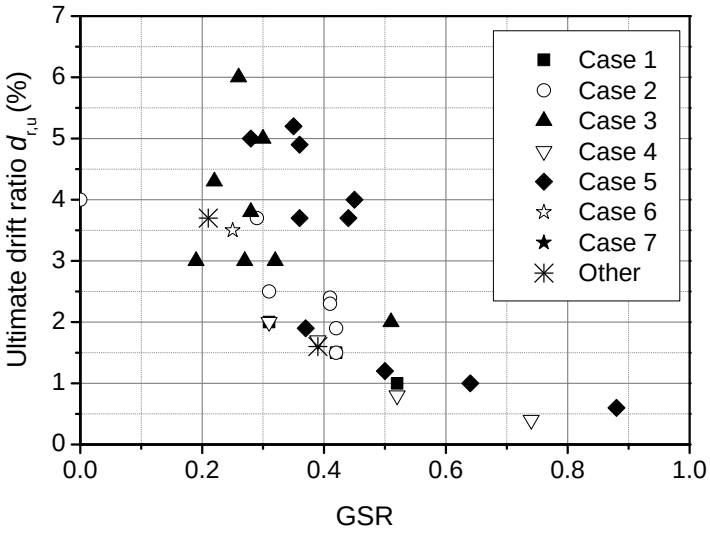


(a)

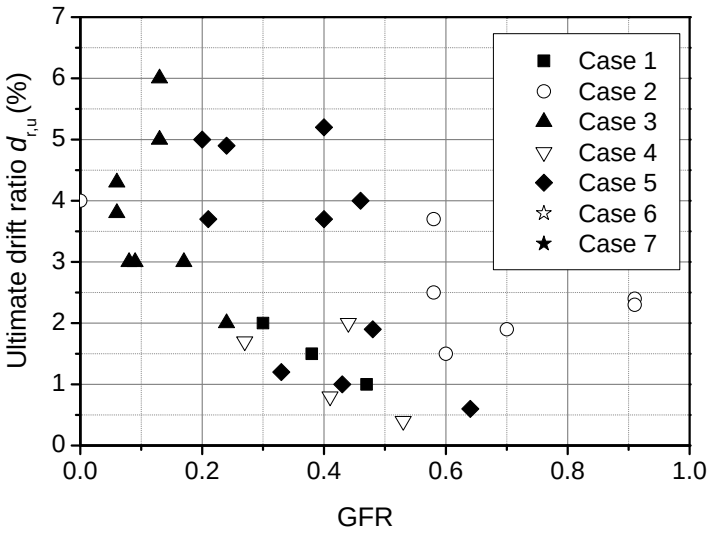


(b)

Figure 5.3: Ultimate drifts as a function of GSR and GFR for specimens without shear reinforcement

2004c)), is proposed herein using the following simple relationship:

$$d_{r,u} = \frac{1}{GSR} - 1 \leq 3 \tag{5.10}$$

where GSR is a unit-less decimal number and the result is a percentage. Figure 5.4 shows that Equation 5.10 is indeed close to the other alternatives.

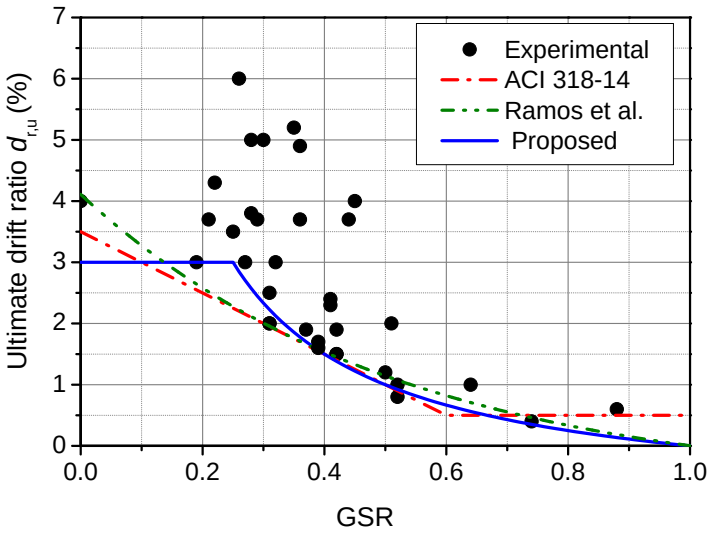


Figure 5.4: Comparison of various formulas describing the relationship between GSR and $d_{r,u}$

### 5.2.3 Ultimate drifts in flat slabs with headed shear studs

Table 5.3 provides the main properties of the specimens with shear studs found in literature fulfilling the criteria described in paragraph 5.2.1. The ultimate drift ratios are summarized in Table 5.4. The relationship between the ultimate drifts and GSR and GFR separately is shown in Figure 5.5. Here, it is noticed that the increase of GSR, as well as the increase of GFR, cause a decrease of the ultimate drift. Comparing Figure 5.5 with Figure 5.3, it can be noticed that the results are less scattered in case of specimens with shear studs and a linear trendline is reasonable. The linear trendlines are plotted in Figure 5.5 and the corresponding equations and $R^2$ values are given. GSR and GFR plots have almost the same scatter around the linear trendline. It should be noted here that the number of specimens with studs in the database is smaller than the number of specimens without shear reinforcement and not every test setup of Figure 5.1 is used.

Three of the specimens presented in this dissertation (C-SSR3, C-SSR5a and C-SSR5b) had a similar GSR, but different GFR. This resulted in different ultimate drift ratios for these three specimens, indicating that the ultimate drift is not only a function of GSR. Due to differences in the concrete strength (see Table 3.3), the predicted punching shear resistance of these specimens was significantly different. Therefore, the applied gravity

Table 5.3: Main properties of specimens with shear studs

| Reference | ID | $d$ (mm) | $\rho_l$ (%) | $f_c$ (MPa) | $f_y$ (MPa) | $V_{flex}$ case (Fig. 5.1) |
|---|---|---|---|---|---|---|
| Cao 1993 | CD-3 | 107 | 1.3 | 36.0 | 395 | 5 |
| | CD-4 | 107 | 1.3 | 34.0 | 395 | 5 |
| | CD-6 | 107 | 1.3 | 31.0 | 395 | 5 |
| | CD-7 | 107 | 1.3 | 29.0 | 395 | 5 |
| Robertson et al. 2002 | 4HS | 95 | 0.6 | 38.2 | 420 | 3 |
| Brown 2003 | SJB-1 | 114 | 1.3 | 32.0 | 400 | 5 |
| | SJB-2 | 114 | 1.4 | 34.0 | 400 | 5 |
| | SJB-3 | 114 | 1.3 | 32.0 | 400 | 5 |
| | SJB-4 | 114 | 1.4 | 40.0 | 400 | 5 |
| | SJB-5 | 114 | 1.8 | 33.0 | 400 | 5 |
| Broms 2007 | 18c | 150 | 1.0 | 34.6 | 563 | 7 |
| | 18d | 150 | 0.7 | 34.6 | 541 | 7 |
| Kang and Wallace 2008 | HS2.5 | 130 | 0.5 | 35.1 | 452 | 5 |
| Park et al. 2012 | SR-A | 114 | 1.1 | 22.5 | 430 | 2 |
| | SR-B | 114 | 1.1 | 38.7 | 430 | 2 |
| Present study | C-SSR3 | 118 | 1.0 | 41.2 | 545 | 1 |
| | C-SSR5a | 117 | 1.0 | 27.0 | 545 | 1 |
| | C-SSR5b | 117 | 1.0 | 57.6 | 542 | 1 |
| | C-SSR5c | 118 | 1.0 | 69.9 | 542 | 1 |

load varied considerably between the specimens, because GSR was kept constant. On the other hand, the flexural strength is less depended on the concrete strength, and the flexural resistance of the specimens was therefore not very different. This indicates that a combination of the influences from both GSR and GFR would be more appropriate for the description of the observed behaviour of the specimens presented in this study.

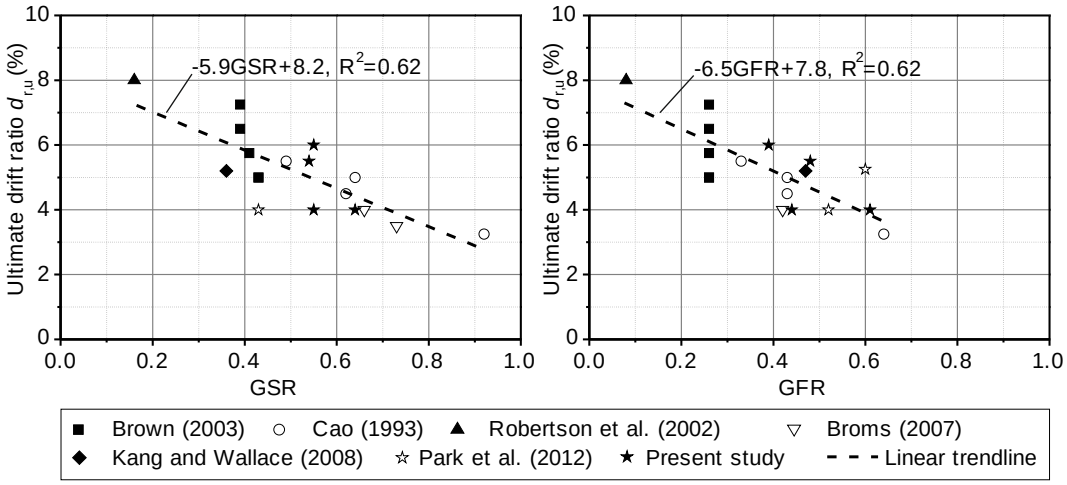


Figure 5.5: Ultimate drifts as a function of GSR and GFR for specimens with shear studs

For the four specimens with shear reinforcement described in this dissertation, the

Table 5.4: Ultimate drifts in specimens with shear studs

| Reference | ID | $V_g$ (kN) | $V_{flex}$ (kN) | $V_0$ (kN) | GSR (%) | GFR (%) | $d_{r,u}$ (%) | $\frac{u_{out,ef}}{u_{out}}$ (-) | $\zeta$ (%) |
|---|---|---|---|---|---|---|---|---|---|
| Cao 1993 | CD-3 | 300 | 466 | 327 | 92 | 64 | 3.3 | 0.59 | 35 |
| | CD-4 | 200 | 464 | 320 | 62 | 43 | 4.5 | 0.59 | 16 |
| | CD-6 | 200 | 461 | 311 | 64 | 43 | 5.0 | 0.59 | 16 |
| | CD-7 | 150 | 458 | 304 | 49 | 33 | 5.5 | 0.59 | 9 |
| Robertson et al. 2002 | 4HS | 35 | 461 | 214 | 16 | 8 | 8.0 | 0.45 | 1 |
| Brown 2003 | SJB-1 | 150 | 577 | 346 | 43 | 26 | 5.0 | 0.85 | 10 |
| | SJB-2 | 150 | 580 | 366 | 41 | 26 | 5.8 | 0.85 | 9 |
| | SJB-3 | 150 | 577 | 346 | 43 | 26 | 5.0 | 0.65 | 7 |
| | SJB-4 | 150 | 587 | 386 | 39 | 26 | 6.5 | 0.65 | 6 |
| | SJB-5 | 150 | 578 | 388 | 39 | 26 | 7.3 | 0.65 | 6 |
| Broms 2007 | 18c | 355 | 837 | 539 | 66 | 42 | 4.0 | 0.54 | 15 |
| | 18d | 355 | 616 | 485 | 73 | 58 | 3.5 | 0.54 | 23 |
| Kang and Wallace 2008 | HS2.5 | 120 | 258 | 331 | 36 | 47 | 5.2 | 0.88 | 15 |
| Park et al. 2012 | SR-A | 134 | 259 | 314 | 43 | 52 | 4.0 | 0.68 | 15 |
| | SR-B | 161 | 270 | 376 | 43 | 60 | 5.3 | 0.68 | 17 |
| Present study | C-SSR3 | 196.4 | 447 | 359 | 55 | 44 | 4.0 | 0.99 | 24 |
| | C-SSR5a | 169.2 | 435 | 310 | 55 | 39 | 6.0 | 0.79 | 17 |
| | C-SSR5b | 213.9 | 449 | 398 | 54 | 48 | 5.5 | 0.79 | 20 |
| | C-SSR5c | 275.0 | 453 | 429 | 64 | 61 | 4.0 | 0.79 | 31 |

punching shear resistances at the face of the column, at the control perimeter at a distance $2d$ from the face of the column and outside the shear-reinforced zone were summarized in Table 4.3. The results showed that the outer perimeter was the most critical one for all specimens. Indeed, except for C-SSR5a, all specimens failed outside the shear-reinforced zone. However, there is no apparent relationship between $V_{0,out}$ and $d_{r,u}$. For example, C-SSR5a had the lowest resistance but sustained the highest drift ratio. It should be noted that $V_{0,out}$ in Table 4.3 was calculated using the same value of $u_{out,ef}$ for all specimens (Figure 3.5). However, the results of the present experimental campaign indicate that drift capacity can be enhanced by increasing the number of perimeters of studs beyond the number of perimeters for which EC2 (CEN 2004c) does not recommend further increase of $u_{out,ef}$.

For the specimens with shear studs, a unitless factor, $\zeta$, is proposed to be used to describe the relationship between GSR, GFR, the extent of shear reinforcement beyond the point where EC2 (CEN 2004c) recommends outer perimeter reduction and the ultimate drift ratio:

$$\zeta = \frac{V_g^2}{V_0 V_{flex}} \left( \frac{u_{out,ef}}{u_{out}} \right) = GSR \times GFR \left( \frac{u_{out,ef}}{u_{out}} \right) \tag{5.11}$$

where $u_{out,ef}$ is the outer perimeter considering the recommendations of EC2 (CEN 2004c)

for the reduction of the perimeter for cruciform layout of the studs and distance between the studs larger than $2d$ along the perimeter. The quantity $u_{out}$ is the non–reduced outer perimeter, obtained by enclosing the effective outer perimeter $u_{out,ef}$ with straight lines if it consists of separated sections. The ratio $u_{out,ef}/u_{out}$ reflects the hypothesis that the extent of shear reinforcement influences the deformation capacity of shear-reinforced slab–column connections, even when the outer perimeter is no longer increased according to EC2. The values of ratios $u_{out,ef}/u_{out}$ and $\zeta$ are shown in Table 5.4. Figure 5.6 shows the ultimate drifts as a function of $\zeta$.

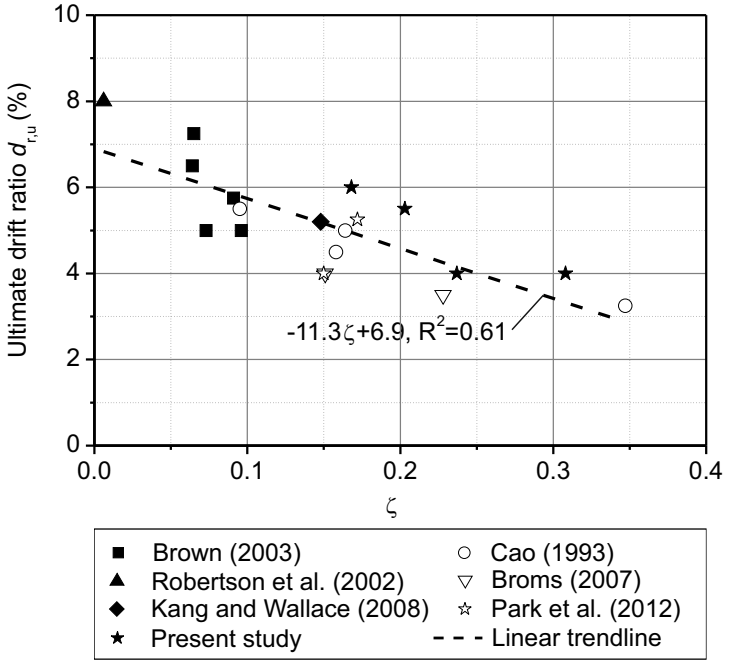


Figure 5.6: Ultimate drifts, $d_{r,u}$, as a function of $\zeta$

Figure 5.6 shows that $\zeta$ describes reasonably well the relationship between the ultimate drift ratio and the gravity load, punching shear capacity, flexural resistance and extent of shear reinforcement for the specimens in the present experimental campaign and for the specimens found in literature. Compared to the relationships presented in Figure 5.5, using the factor $\zeta$ results in a slightly smaller absolute maximum difference from the linear trendline (1.2%, compared to 1.7% for GSR and 1.3% for GFR) but comparable values of $R^2$. The four points marking the specimens of the present study have clearly distinct values of $\zeta$ and a noticeable trend of reducing the ultimate drift with the increase of $\zeta$. Such an observation was not possible in Figure 5.5.

For design purposes, it is proposed to use a lower-bound line, obtained by shifting the trendline of Figure 5.6 downwards until all the specimens remain above the line. The intercept is then rounded down to the nearest 0.5% drift, resulting in the following equation:

$$d_{r,u} = -11.3\zeta + 5.5 \tag{5.12}$$

The proposed lower bound line is shown in Figure 5.7. A characteristic formulation (in which 5% of the specimens would be allowed to fall under the curve) is not used herein due to the relatively small number of specimens.

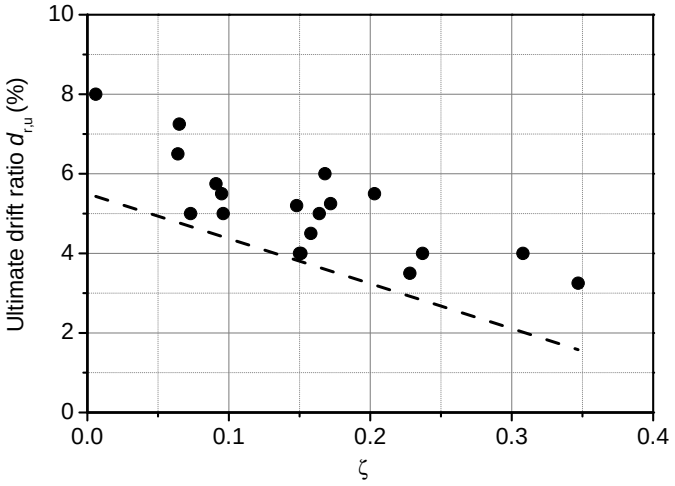


Figure 5.7: Proposed relationship of $d_{r,u}$ and $\zeta$ for design purposes

### 5.2.4 Limitations of the proposed factor for specimens with shear studs

All the specimens included in Figure 5.6 reached a nearly horizontal plateau in the unbalanced moment–drift enveloping curve. For this reason, the factor $\zeta$ is not checked for flat slabs that fail in punching prior to developing the full unbalanced moment transfer capacity. It should also be noted that most of the GFR values (Figure 5.5) correspond to slabs that are over-dimensioned for flexure under gravity loading and the validity of the trend described in Figure 5.6 is not checked for $\zeta > 0.35$. Also, a lower limit of the ratio $u_{out,ef}/u_{out}$ beyond which the drift capacity is no longer enhanced cannot be determined with the currently available experimental data. Furthermore, the ratio $u_{out,ef}/u_{out}$ should be understood as valid only for the cruciform layout of the studs, and only when the shear-reinforced zone extends beyond the point where outer perimeter reduction is required by EC2 (CEN 2004c). As an alternative to $u_{out,ef}/u_{out}$, it was found that similar conclusions to those made in this chapter can be obtained by using the ratio of the actual number of perimeters of studs around the column to the number of studs for which EC2 (CEN 2004c) starts to require outer perimeter reduction.

Finally, it should be noted that Figure 5.5 and Figure 5.6 were derived based on relatively thin specimens (including the specimens presented in this dissertation). Research has shown that size effects can play an important role in punching shear capacity of flat slabs. For this reason and for the reasons discussed above, more experimental research on shear-reinforced flat slabs under reversed horizontal cyclic is necessary to validate

whether the proposed factor $\zeta$ relates to the ultimate drift capacity of flat slab–column connections outside the presented limitations.

## 5.3 Drift ratios at yielding

Using the procedure described in Figure 4.9, the unbalanced moment–drift curves for all the specimens of Section5.2.3 are idealized into bilinear curves. In the bi-linearisation process, the curves are followed up to the maximum unbalanced moment. The results are shown in Figure 5.8. For the specimens tested in the present study, refer to Figure 4.9.

It is especially of interest to look at the bilinear curves of experimental campaigns containing more than two specimens (for example, Figure 5.8a and 5.8c). Usually, the same geometry of specimens is used within an experimental campaign (Table 5.3). This means that the specimens within an experimental campaign have the same thickness and geometry. Figure 5.8 demonstrates that, in such cases, the drift at yielding varies less than the strength (maximum unbalanced moment). In fact, specimens within the same experimental campaign have a maximum absolute difference between the drifts at yielding of less than 0.5%, regardless of the strength. The same observation is made referring to Figure 4.9 corresponding to the specimens presented in this study, in which the maximum absolute difference of the yield drifts is 0.3%.

Figure 5.9 shows the variation of drift at yielding with the slab's flexural strength, drift at maximum unbalanced moment and the ratio $\epsilon_y r_s/d$, where $\epsilon_y = f_y/E_s$ is the strain at yielding of the longitudinal reinforcement and $r_s$ is the radius of the zero-moment line. The ratio $r_s/d$ represents the slenderness of the slab. The figure shows that the relationship between the drifts at yielding and the slab's flexural strength is weak. However, there is a relatively strong correlation between the drift at maximum unbalanced moment and the drift at yielding (Figure 5.9b). This means that the ratio of drifts at maximum unbalanced moment to drifts at yielding is almost constant for all specimens. Indeed, the aforementioned ratio has a mean value of 1.92 and a relatively small standard deviation of 0.26.

The ratio $\epsilon_y r_s/d$ in Figure 5.9c was chosen in analogy with the expression proposed in Priestley et al. 2007 for the yield drift ($d_{r,y}$) in reinforced concrete frames, according to which:

$$d_{r,y} = 0.5\epsilon_y L_b/h_b \tag{5.13}$$

where $L_b$ is the span of the beam and $h_b$ is its depth. The large scatter of results in Figure 5.9c indicates that the expression developed for reinforced concrete frames (Equation 5.13) is not adequate for flat slab frames. Equation 5.13 has been developed based on the experimental investigation of beam–column sub-assemblies very similar to those represented in Figure 2.18a. The yielding drift is calculated by assuming a triangular distribution of the curvature along the span of the beam, with a value equal to the yield

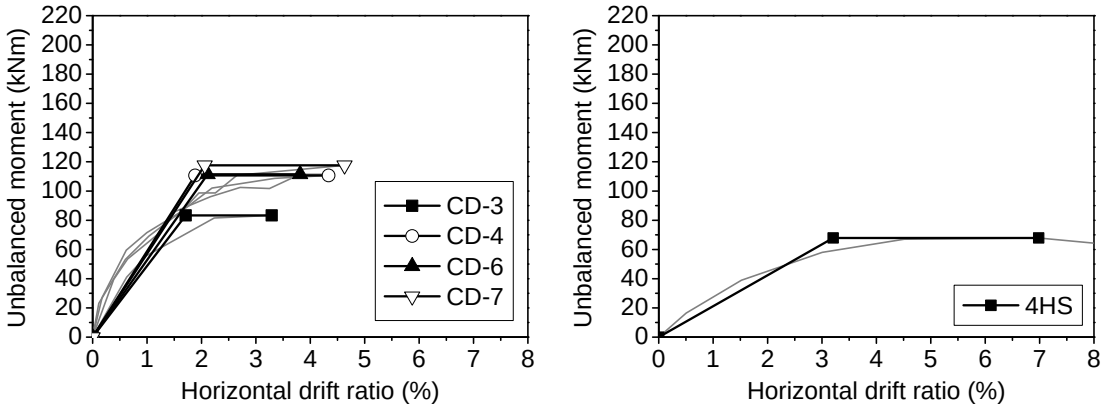


(a) Cao 1993




(b) Robertson et al. 2002

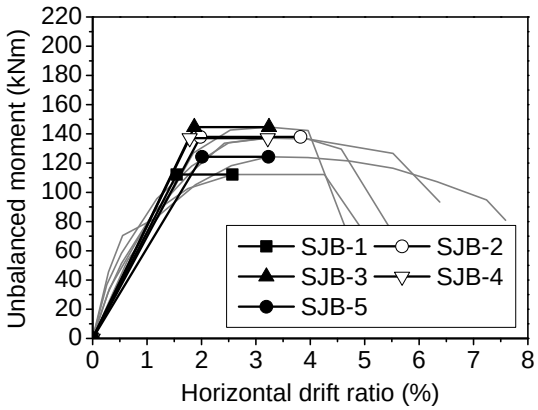


(c) Brown 2003

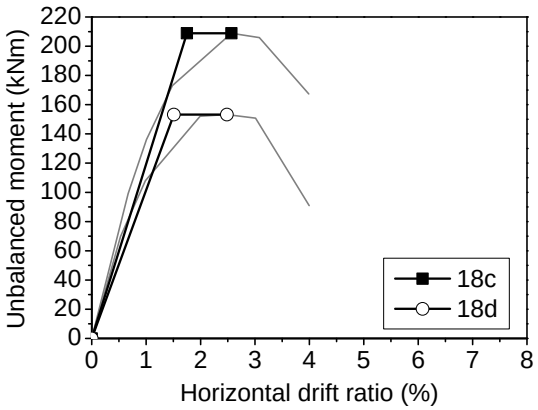


(d) Broms 2007

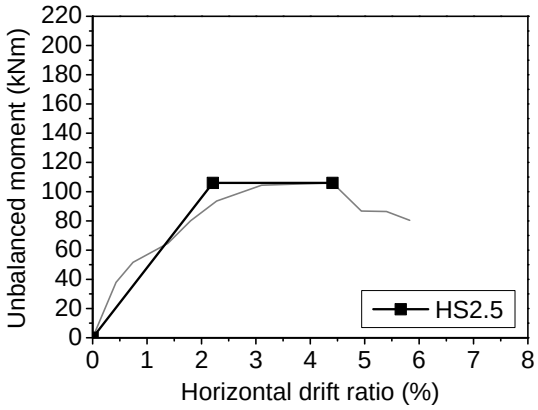


(e) Kang and Wallace 2008

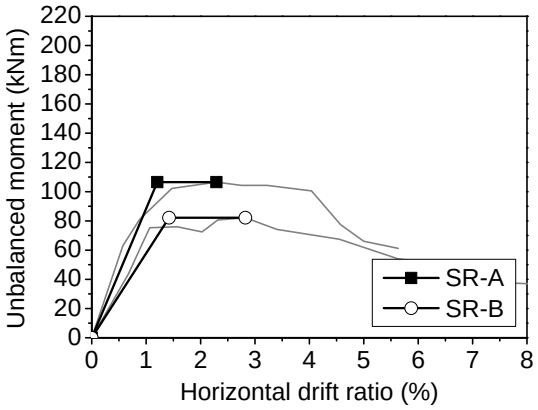


(f) Park et al. 2012

Figure 5.8: Idealized elasto – perfectly plastic curves for specimens with shear studs

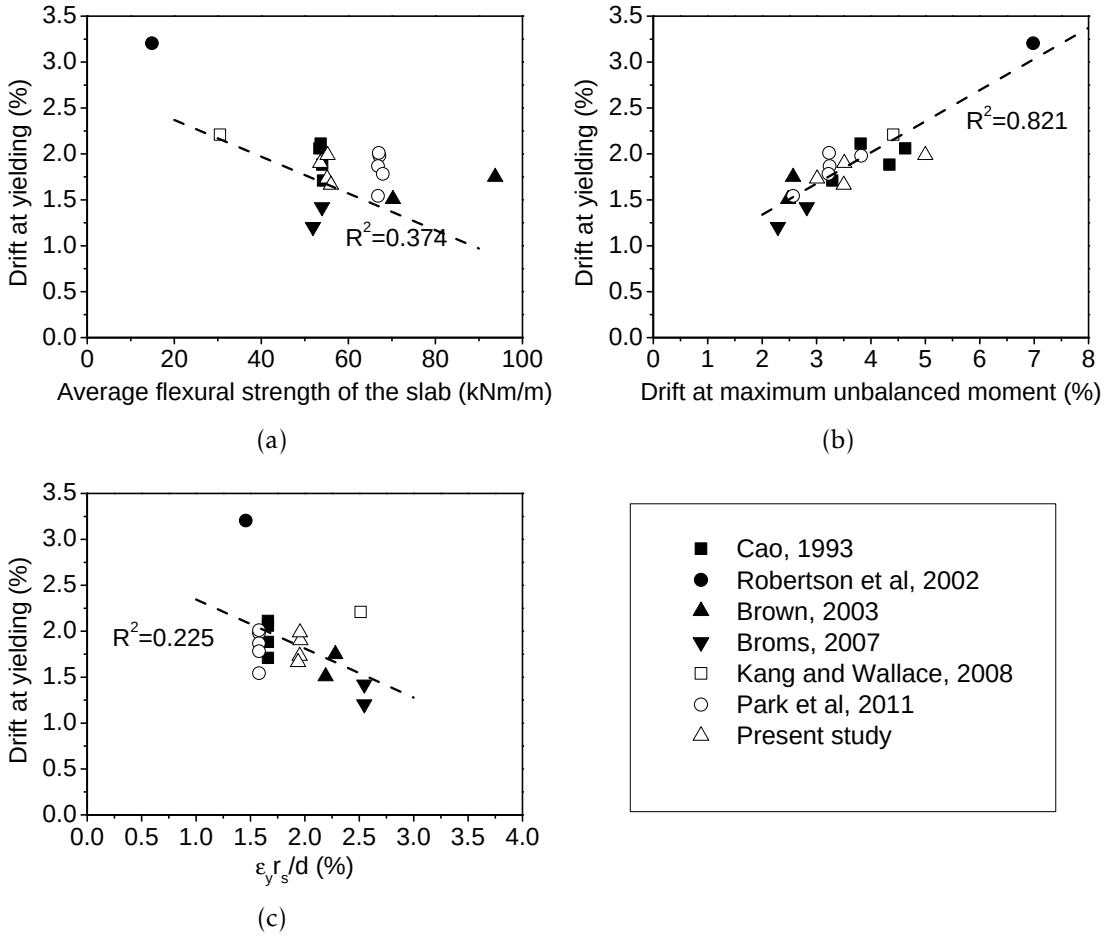


Figure 5.9: Variation of drift at yielding with a) slab's flexural strength, b) drift at maximum unbalanced moment and c) the ratio $\epsilon_y r_s/d$

curvature at the joint and zero at the mid-span. Furthermore, Equation 5.13 assumes a contribution of shear deformations and column deformation that are typical for beam–column connections. However, flat slabs are two-way elements, and the drift at yielding should be examined differently. The study of yielding drifts for flat slabs is outside the scope of this dissertation, but the benefits of future research on this topic are discussed in the following section.

## 5.4 Design implications

In this chapter, an analysis of the ultimate drift ratios for flat slabs with and without shear reinforcement (focused on shear studs) was presented. In accordance with previous research, it was shown that GSR is a good indicator of the ultimate drift ratio of flat slabs without shear reinforcement. For specimens with shear studs, a factor incorporating the influence of gravity load, flexural resistance and extent of shear reinforcement was proposed. It was shown that the proposed factor describes reasonably well the ultimate

drift ratios in flat slab–column connections with shear studs. Limitations were presented in Section 5.2.4. In this section, the benefits of knowing the ultimate drift ratio in the design process are discussed.

### 5.4.1 Force–based versus displacement–based design

Considering the flat slab specimens presented in Chapters 3–4 and those reported in the literature, it becomes apparent that drift ratios are more representative of the capacity of the slab–column connections than the forces (shear force and unbalanced moment). Figure 5.10 shows a typical unbalanced moment–drift curve for flat slab–column connections with shear reinforcement and sufficient flexural capacity enabling them to develop a ductile behaviour. Although the maximum unbalanced moment (therefore, the maximum shear stress) is reached at point A, the flat slab is able to safely sustain the gravity loads and the imposed unbalanced moment until point B, where a punching failure occurs for a certain drift ratio. Designing the flat slab for the stresses induced by the unbalanced moment and the gravity load at point A (i.e., Force Based Design) does not give sufficient information about the safety of the structure under seismic loading, which can vary substantially based on the drift capacity of the slab–column connection.

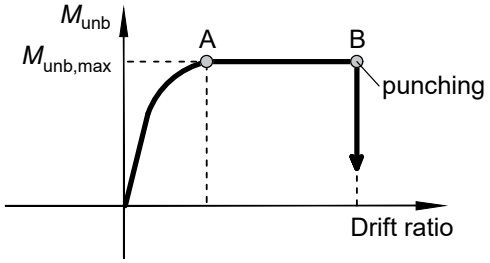


Figure 5.10: Typical unbalanced moment – drift relationship for a flat slab–column connection with shear reinforcement and sufficient flexural capacity

A comprehensive explanation of the *fallacies*[1] of the Force Based Design, in a broader sense, is presented in Priestley et al. 2007. In particular:

- Structural performance can be related to displacements but not to forces and strength. It is well acknowledged, for example, that damage to non-structural elements is related to the inter-storey drift ratio. Structural damage too, can be better represented by displacements (for example, refer to Figure 5.10);

- Force Based Design assumes that the elastic stiffness is known from the very beginning. It is shown (Priestley et al. 2007) that this is not the case, because the elastic stiffness depends on the strength, which is unknown at the beginning of the design.

[1] using the terminology adopted in the pioneering publication entitled "Myths and Fallacies in Earthquake Engineering" (Priestley 1997)

On the other hand, yield curvatures are less depended on the strength and can be determined satisfactorily based on geometry alone for most structural elements;

- Force Based Design employs a force reduction factor (behaviour factor $q$ in European practice, EC8 (CEN 2004d)). This force reduction factor cannot be determined accurately and uniquely for all structures of the same type. There is a very large variation of recommended values in different major design codes for the same structural type (Priestley et al. 2007);
- Displacements in Force Based Design are only checked at the end of the design process, using elastic response values, which might be non-realistic.

Pioneering work by Moehle 1992 and Priestley 1997 brought the attention to an alternative approach to the Force Based Design of structures: the Displacement Based Design (DBD), which solves the aforementioned issues related to Force Based Design. Priestley 1997 noticed that the philosophy of seismic design at that time was largely influenced by the proven design techniques commonly adopted for gravity loading. However, seismic design requires a substantially different mindset. For example, it is not expected to reach the ultimate strength of a structural element for gravity loading, but it is common to do so for seismic loading (Priestley 1997).

Based on previous work on DBD, Priestley et al. 2007 formulated the Direct Displacement Based Design (DDBD) approach. In DDBD, the displacements dictate the design, acknowledging that they are more important than forces in seismic design. The following steps are to be followed for a DDBD (based on Priestley 1997; Priestley et al. 2007; Chopra and Goel 2001):

1. Determine an acceptable plastic displacement, $\Delta_p$, from performance requirements or other limitations;
2. Provide an estimation of the yield displacement of the structure, $\Delta_y$;
3. Determine the design displacement as:

$$\Delta_d = \Delta_y + \Delta_p;$$

4. Estimate the total equivalent viscous damping based on the displacement ductility $\Delta_d/\Delta_y$;
5. Find the fundamental period of vibration, $T$, of an equivalent single degree of freedom system using displacement spectra with the equivalent damping ratio determined in the previous step. Determine the corresponding secant stiffness of the system with mass $M$

$$K = \frac{4\pi^2}{T} M;$$

6. Determine the yield resistance $V_R$ of the structure based on the stiffness $K$ and the displacement $\Delta_d$:

$$V_R = K\Delta_d;$$

7. Dimension structural elements to achieve the required global yielding resistance and check the design;

8. Iterate if necessary until a satisfactory solution is found.

Although DBD is relatively mature and backed by considerable research, it has found limited popularity in the European design practice. However, DBD is currently being considered to be included in the upcoming revised version of Eurocode 8 as an alternative procedure for the seismic design of structures (Bisch 2018; Fardis 2018).

### 5.4.2 DDBD of buildings with flat slabs

For the application of DDBD in buildings with flat slabs, it is necessary to distinguish two cases (using the EC8 (CEN 2004d) terminology):

1. Flat slabs as "primary seismic elements", i.e. they contribute to the lateral stiffness and resistance;

2. Flat slabs as "secondary seismic elements", i.e. they do not contribute to the lateral stiffness and resistance, but they follow the deformations imposed by the primary seismic elements (for example, shear walls, braces, moment resisting frames).

The first case (flat slabs as primary seismic elements) is currently not covered by EC8 (CEN 2004d). For the application of DDBD in these types of structures, it is necessary to fill the gap currently present in the literature related to the estimation of yield drifts (refer to Section 5.3). Nonetheless, the proposals for the ultimate drift ratios in flat slabs with and without shear reinforcement presented in this chapter can be useful in determining the acceptable plastic displacement, $\Delta_p$ (Section 5.4.1). Besides other performance requirements (for example, damage limitation in non-structural elements), the ultimate drift ratio of flat slabs should be an additional constrain in the determination of $\Delta_p$. Although GSR and GFR depend on the strength of the flat slabs, which is unknown in the beginning of the design process, they can be reasonably estimated using the known vertical loads, the thickness of the slab (which can be estimated from experience, based on serviceability requirements) and the concrete strength (which is normally known from the beginning). The flexural reinforcement ratio (unknown in the beginning) can influence the result and might require iteration of the design.

In the special case of primary seismic flat slabs without shear reinforcement, further research on the estimation of yield drifts for DDBD purposes is not advocated. The mechanical model proposed by Drakatos et al. 2018 was verified on a relatively large

number of specimens without shear reinforcement. Since the model can provide the entire force–displacement curve up to failure, it can be used in the framework of DDBD to assess safety starting from displacements (drifts). However, the yielding plateau is rarely reached for specimens without shear reinforcement. Therefore, the behaviour is usually brittle (non-ductile). Following the DDBD procedure (Section 5.4.1), this means that the total equivalent viscous damping of such structures is low. As a result, the required stiffness of the structure is relatively high, which means high cost for the structure. In Chapter 6 it will be shown that the seismicity level for which punching failures occur in a typical structure of this kind is relatively low. On the other hand, adding shear reinforcement in the flat slab around the columns adds to the cost of the slab, but it can significantly reduce the cost of the vertical structural elements (columns in this case) while allowing a lower stiffness due to the increased drift capacity. Based on this reasoning, the use of shear reinforcement is recommended, even in cases of low to moderate seismicity (in which flat slabs as primary seismic elements are permitted in the North American practice). Even when shear reinforcement is provided, it was shown in Section 4.5 that the lateral stiffness of the flat slabs is very low compared to the stiffness of the uncracked full section. As a consequence, the flexibility is expected to be high and deformations (drifts) become difficult to control. In general, the use of flat slabs as primary seismic elements should be considered with caution, even in low seismicity cases.

Examples of the application of DDBD for the second case (flat slabs as secondary seismic elements) are already present. A worked example of a six storey building with perimeter shear walls and secondary columns supporting the flat slab is presented in Priestley et al. 2007. In this example, no special consideration for the punching failure mode of the flat slabs was given (flat slabs were to be designed separately, because they did not contribute to the lateral load resisting system). An approach for proportioning shear walls in buildings with flat slabs based on DDBD was presented in Sen and Singh 2016. In this case, the design of the flat slabs was treated in conjunction with that of the primary load resisting system, considering the drift limits for the punching shear failure of the flat slabs in accordance with ACI 318 (ACI 2014). Flat slabs were designed for gravity loading, and the corresponding drift limits were used as performance criteria.

It is apparent that knowing the yield drift is not necessary when designing buildings in which the flat slabs do not contribute in the earthquake resisting system, because the displacement ductility $\Delta_m/\Delta_y$ is determined based on the yield displacement $\Delta_y$ of the primary system (shear walls for example). On the other hand, the ultimate drift capacity is needed, because it constrains the value of $\Delta_m$ in case it is not already limited by other performance criteria. It is proposed herein to estimate the displacements $\Delta_m$ for DDBD based on the ultimate drift ratio relationships proposed in this dissertation (Equation 5.10 and Equation 5.12).

### 5.4.3 Design of the shear reinforcement

Ultimately, it is necessary to design the quantity and layout of shear reinforcement to achieve the required deformation capacity. Again, it is necessary to distinguish between flat slabs considered as primary and secondary seismic elements. For the reasons discussed in the previous section, flat slabs as primary seismic elements are no longer discussed in this chapter.

In the most common case, of flat slabs being secondary seismic elements, the shear reinforcement can be designed for gravity loading at first. This can be done independently from the design of the primary seismic elements in most cases. If no shear reinforcement is required, the ultimate drift ratio can be calculated using Equation 5.10. If the calculated drift ratio is smaller than drift ratios marking other performance criteria, then shear reinforcement should be provided or DDBD must be followed with the smallest of the drifts, which can lead to a design that is not economical.

In case shear reinforcement is provided, the designer should make sure the punching shear strength is high enough for the yielding plateau of the slab–column connection to be reached without a punching shear failure. To achieve this, the slab–column connection must be designed for a combination of the gravity load with the unbalanced moment larger than the one that causes flexural failure of the connection. One way of calculating this unbalanced moment is to use the yield line approach proposed in Brown and Dilger 2004. In Section 4.11.2 it was shown that, for the specimens presented in this dissertation, the yield line approach of Brown and Dilger 2004 produced good results, but not consistently conservative. Another approach, more laborious, is to use the mechanical model proposed by Drakatos et al. 2018 to determine the yielding unbalanced moment of the connection and to design for that unbalanced moment.

After the design of the shear reinforcement, Equation 5.12 can be used to determine the ultimate drift ratio. If the ultimate drift ratio is smaller than the drift ratios corresponding to other performance states, it is to be used to calculate the maximum displacement in the DDBD approach. Note that, it is not required to perform a structural analysis of the flat slabs under horizontal loading in any of the steps described. This is advantageous because it saves time and reduces uncertainties associated with modelling of flat slabs for horizontal actions (Section 2.7).

### 5.4.4 Design example

To illustrate how the relationships developed in this chapter can be used in design, consider the six storey regular tower building shown in Figure 5.11. In these calculations, reference is made to the Eurocodes. Nonetheless, the design procedure can be applied similarly for materials and loading in accordance with other codes.

The earthquake resisting system consists of moment resisting frames in the exterior

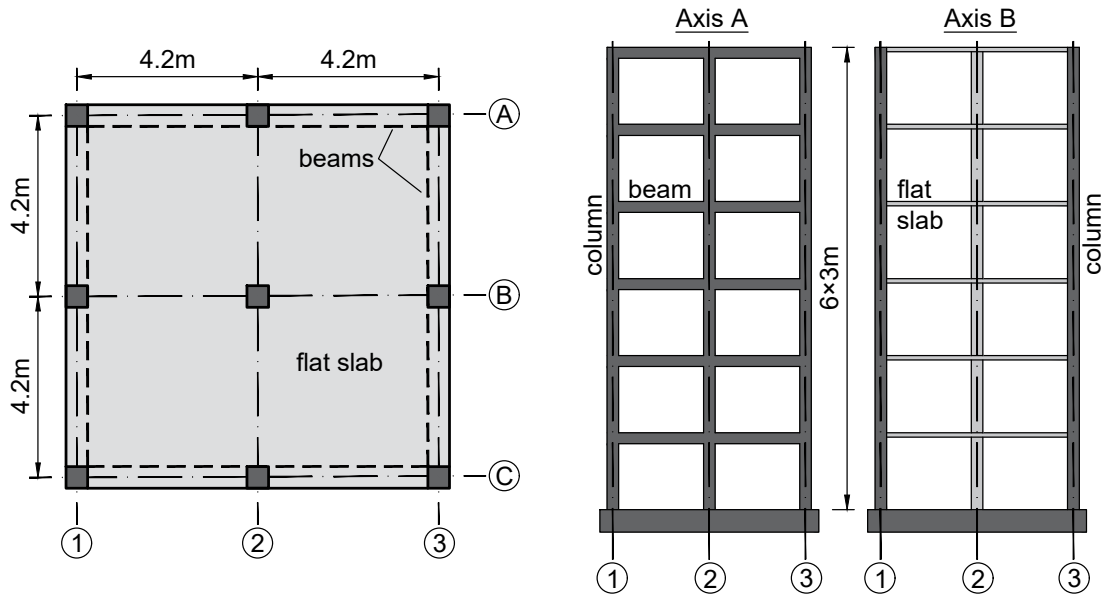


(a) Plan (b) Elevation

Figure 5.11: Example structure

axes (1, 3, A and C). The central column and the flat slab are secondary seismic elements and their contribution to lateral stiffness is neglected. Due to regularity of the building, only one frame is considered. Concrete class C30/37 and steel with characteristic yield stress $f_{yk}$ = 500 MPa will be used. The structure is situated in a site where the reference ground acceleration is $a_{gR} = 0.20g$, ground type C and spectrum type 1 (CEN 2004d).

The preliminary depth of the slab can be estimated by limiting the span to depth ratio ($l/d$) as recommended in EC2 (CEN 2004c), according to which $l/d$ varies from 17 to 24 (for reinforcement ratio 1.5% and 0.5% respectively) for the current conditions. It is assumed herein that a value $d$ = 180 mm fulfils the deflection control criteria. The total thickness of the slab is $h$ = 210 mm. The self-weight (including the weight of the slab) is $g$ = 7.0 kN/m$^2$ and the imposed load on the slab is $q$ = 3.0 kN/m$^2$. It is assumed that the mass contributing to the dynamic response under earthquake loading is constant along the height, equal to 56 tonnes for each storey level. This value of the mass is derived from the gravity loads, assuming a combination of actions $1.00g + 0.24q$, in accordance with EC8 (CEN 2004d) for storeys with correlated occupancies.

For the Ultimate Limit State with a combination of actions $1.35g + 1.5q$, the design value of the shear force in the slab–column connection is approximately[2] $V_{gd}$ = 355 kN. For this combination of actions, the slab–column connection is reinforced with a longitudinal reinforcement ratio of 0.5%. With this reinforcement ratio, the span to depth ratio remains within the permissible limits, and no further verification of the deflections is

[2] in the interest of the example, a conservative value is used, considering the fact that the depth of the beams in the exterior axes in not known at this stage of the design.

necessary.

The central column supporting the flat slab is assumed to have a square cross section with dimensions $400 \times 400$ mm (the design of this column is not treated in this example). The punching shear strength calculations are summarized in Table 5.5 for the fundamental and seismic combination of gravity loads. The control perimeter is $u_1 = 3862$ mm, the size effect factor $k = 2$ and $C_{Rd} = 0.12$.

Table 5.5: Calculation of punching shear resistance

| Combination | Description | $V_g$ | $v_{Rd,c}$ | $\beta$ | $V_R$ | GSR |
|---|---|---|---|---|---|---|
| | | kN | MPa | | kN | % |
| Fundamental (for design) | $1.35g + 1.50q$ | 355 | 0.59 | 1.15 | 357 | 99 |
| Seismic (for calculation of GSR only) | $1.00g + 0.30q$ | 201 | 0.59 | 1.00 | 410 | 49 |

Table 5.5 shows that punching shear reinforcement is not required (however, the ratio between the design load and the design resistance is very close to 1). In the next sections, the procedure is followed for two cases. In the first case, the designer decides to keep the flat slabs without shear reinforcement. In the second case, shear reinforcement is provided.

#### 5.4.4.1 Design of the structure without punching shear reinforcement

With the value of GSR calculated for concentric loading conditions under the gravity load present in the seismic design situation, the ultimate drift capacity can be calculated from Equation 5.10, resulting in $d_{r,u} = 1.0\%$ (rounded down value). The structure will be designed to safely achieve this drift ratio. Note that, for design of real structures, a safety factor should be applied to the drift calculated in accordance with Equation 5.10. Note also, that for the damage limitation state (CEN 2004d), the design seismic action is not the same (it is normally a reduced one, with a lower return period) and a separate verification is necessary.

To design the structure for this target drift, it must first be transformed into an equivalent single degree of freedom (SDOF) system with mass $m_e$ and effective height $H_e$ as shown in Figure 5.12a. This transformation is achieved through the following equation (Priestley et al. 2007):

$$\Delta_d = \frac{\sum_{i=1}^{n} m_i \Delta_i^2}{\sum_{i=1}^{n} m_i \Delta_i} \tag{5.14}$$

where $\Delta_d$ is the equivalent design displacement of the SDOF system (Figure 5.12b), $n$ is the number of storeys, $m_i$ is the mass of storey $i$ and $\Delta_i$ is the displacement at storey $i$, at a height $H_i$ from the base of the building. The mass of the SDOF system is:

$$m_e = \frac{\sum_{i=1}^{n} m_i \Delta_i}{\Delta_d} \tag{5.15}$$

and the effective height is:

$$H_e = \frac{\sum_{i=1}^{n} m_i \Delta_i H_i}{\sum_{i=1}^{n} m_i \Delta_i} \tag{5.16}$$

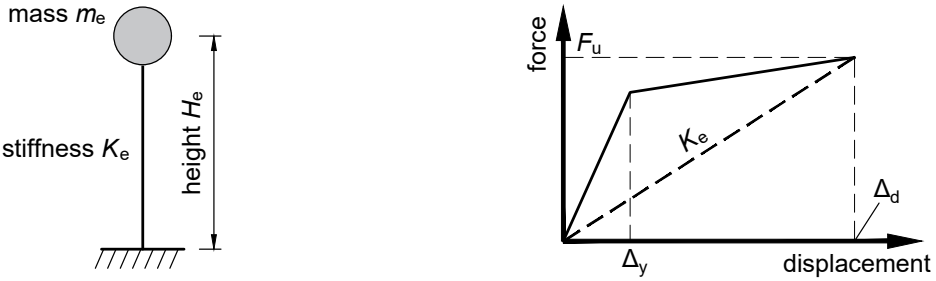


(a) Single degree of freedom system

(b) Behaviour of the SDOF system

Figure 5.12: Equivalent single degree of freedom system

In similarity with Example 5.1 in Priestley et al. 2007, the calculations are presented in tabular form in Table 5.6. Figure 5.13 shows the inelastic mode shape for frames (Priestley et al. 2007). From it, it is noticed that the maximum drift occurs in the ground storey. Starting from the limiting drift $d_{r,u}$ of punching failures, the horizontal displacement at the first storey is estimated as $\Delta_1 = d_{r,u} \times 3$ m= 0.030 m (Table 5.6). From there, the other displacements $\Delta_i$ are calculated in proportion to $\delta_i$ (more precisely, $\Delta_i = \delta_i \Delta_1 / \delta_1$).

Table 5.6: Calculation of the characteristics of the SDOF system, no punching shear reinforcement case

| Storey | $H_i$ (m) | $m_i$ (tonnes) | $\delta_i$ | $\Delta_i$ (m) | $m_i\Delta_i$ | $m_i\Delta_i^2$ | $m_i\Delta_i H_i$ |
|---|---|---|---|---|---|---|---|
| 6 | 18 | 56 | 1.00 | 0.143 | 8.01 | 1.15 | 144.18 |
| 5 | 15 | 56 | 0.88 | 0.126 | 7.06 | 0.89 | 105.90 |
| 4 | 12 | 56 | 0.74 | 0.106 | 5.94 | 0.63 | 71.28 |
| 3 | 9 | 56 | 0.58 | 0.083 | 4.65 | 0.39 | 41.85 |
| 2 | 6 | 56 | 0.41 | 0.059 | 3.30 | 0.19 | 19.80 |
| 1 | 3 | 56 | 0.21 | 0.030 | 1.68 | 0.05 | 5.04 |
| Sum | | | | | 30.64 | 3.3 | 388.05 |

From Equations 5.14 – 5.16, the following results are obtained: $\Delta_d = 0.108$ m, $H_e = 12.665$ m and $m_e = 283.7$ tonnes. To determine the yield displacement, and therefore the displacement ductility, it is necessary to choose the depth of the beams. For beams with depth $h_b = 500$ mm, the yield drift is (Priestley et al. 2007):

$$\theta_y = 0.5\epsilon_y \frac{L_b}{h_b} = 1.05\% \tag{5.17}$$

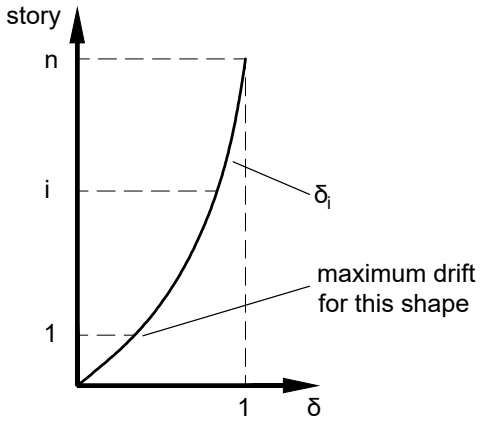


(a) Inelastic mode shape for frames

$$\delta_i = \frac{4}{3}\left(\frac{H_i}{H_n}\right)\left(1 - \frac{H_i}{4H_n}\right)$$

(b) Equation

Figure 5.13: Inelastic displacements profile for frames according to Priestley et al. 2007

where $\epsilon_y = f_{yk}/E_s = 0.25\%$ and $L_b$ is the span of the beam. Since the storey yield drift is larger than the punching failure drift, the depth of the beams should be increased. For $h_b = 600$ mm, $\theta_y = 0.88\%$, which is acceptable. Since the frame is regular, the yield displacement of the equivalent SDOF system can be calculated as follows (Priestley et al. 2007):

$$\Delta_y = \theta_y H_e = 0.111 \text{ m} \tag{5.18}$$

For the above equation to hold, the plastic mechanism must be a sway-type one (with plastic hinges forming at the base of the columns and at beam ends). Since $\Delta_y > \Delta_d$, it is necessary to further increase the depth of the beams. For beams with depth $h_b = 650$ mm, the yield displacement becomes:

$$\Delta_y = \theta_y H_e = 0.102 \text{ m} \tag{5.19}$$

The displacement ductility is therefore:

$$\mu = \Delta_y/\Delta_d = 1.06 \tag{5.20}$$

Equation 5.20 demonstrates that the structure must be designed to remain almost elastic in order to avoid punching failures in the slab–column connection under the design seismic action. To increase the displacement ductility, the depth of the beams can be further increased, but note that for an increase of the depth of the beams, the section and reinforcement of the columns is also increased, to comply with the Capacity Design rules. The solution is continued with $h_b = 650$ mm in the interest of the comparison with the case in which a shear-reinforced flat slab is used.

The next step is to estimate an equivalent viscous damping, which for reinforced concrete frames can be calculated based on the work of Priestley et al. 2007 as follows:

$$\xi_{eq} = 0.05 + 0.565\left(\frac{\mu - 1}{\mu\pi}\right) = 6.00\% \tag{5.21}$$

Knowing the equivalent viscous damping, the damped displacement spectrum can be constructed with the data provided at the beginning of this example. The EC8 (CEN 2004d) spectrum is used herein, according to which the damping correction factor $\eta$ should be used:

$$\eta = \sqrt{\frac{10}{5 + \xi_{eq}}} \geq 0.55 \tag{5.22}$$

The displacement spectrum, $S_{De}(T)$, is directly obtained by transforming the acceleration spectrum $S_e(T)$ as follows (CEN 2004d):

$$S_{De}(T) = S_e(T)\left(\frac{T}{2\pi}\right)^2 \tag{5.23}$$

where $T$ is the period.

The displacement spectrum, corrected for damping, is presented in Figure 5.14. Starting from the displacement $\Delta_d$, the period of the SDOF system is determined as shown in the figure. In this case, $T_e = 1.32$ s. From here, the effective stiffness of the SDOF system is calculated as:

$$K_e = \frac{4\pi^2 m_e}{T_e^2} = 6427.9 \text{ kN/m} \tag{5.24}$$

and finally, the design base shear force:

$$F = K_e \Delta_d = 694.2 \text{ kN} \tag{5.25}$$

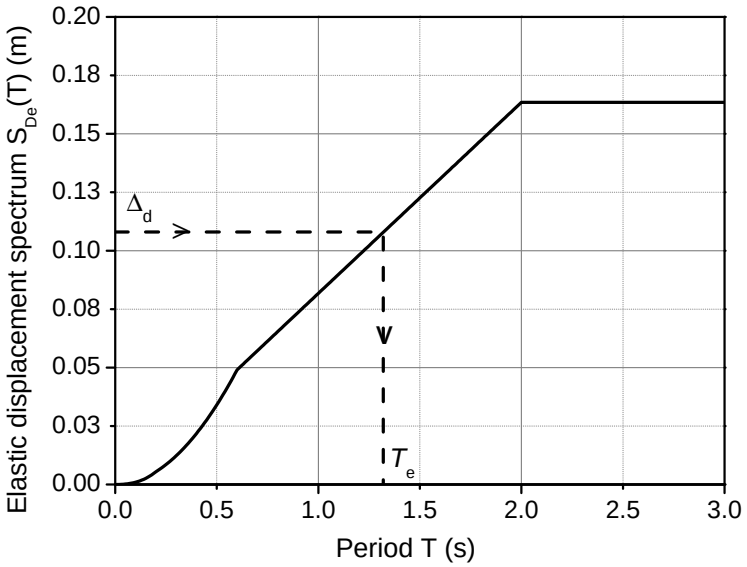


Figure 5.14: Determination of the period of the SDOF system

Note that the calculated base shear resistance should be distributed in two moment resisting frames, because the entire seismic mass of the storey was used for the calculations. The next design steps are not presented in this dissertation. They should consist

in the design of the beams and columns, in accordance with Capacity Design rules, to achieve the required strength (further details can be found in Priestley et al. 2007). Also, the feasibility of this design (i.e. whether it is possible to construct a frame with the required strength) is not checked. The force determined above, however, will be compared in the following section with that determined from an alternative design, in which shear reinforcement is used in the flat slabs.

#### 5.4.4.2 Design of the structure with punching shear reinforcement

In this section, an alternative design will be discussed. The structure will be designed to safely achieve a maximum storey drift ratio of 1.50%. The flat slab will be shear-reinforced to have sufficient deformation capacity to safely accommodate this drift. Again, the verifications for the Damage Limitation state are not presented. The thickness of the slab will be kept the same as in the first case (due to serviceability requirements).

**Design of the primary seismic frame** Following the same procedure as described in the previous section, the limiting drift at the first storey is determined as $\Delta_1 = d_{r,u} \times 3$ m$= 0.045$ m. The rest of the calculations for transformation into a SDOF system are summarized in Table 5.7.

Table 5.7: Calculation of the characteristics of the SDOF system, the case with punching shear reinforcement

| Storey | $H_i$ (m) | $m_i$ (tonnes) | $\delta_i$ | $\Delta_i$ (m) | $m_i\Delta_i$ | $m_i\Delta_i^2$ | $m_i\Delta_i H_i$ |
|---|---|---|---|---|---|---|---|
| 6 | 18 | 56 | 1.00 | 0.214 | 11.98 | 2.56 | 215.64 |
| 5 | 15 | 56 | 0.88 | 0.189 | 10.58 | 2.00 | 158.70 |
| 4 | 12 | 56 | 0.74 | 0.159 | 8.90 | 1.42 | 106.80 |
| 3 | 9 | 56 | 0.58 | 0.124 | 6.94 | 0.86 | 62.46 |
| 2 | 6 | 56 | 0.41 | 0.088 | 4.93 | 0.43 | 29.58 |
| 1 | 3 | 56 | 0.21 | 0.045 | 2.52 | 0.11 | 7.56 |
| Sum | | | | | 45.85 | 7.38 | 580.74 |

The calculations based on Equations 5.14 – 5.16 result in $\Delta_d = 0.161$ m, $H_e = 12.666$ m and $m_e = 284.8$ tonnes. A reduced depth of the beams is now possible compared to the first case. Using beams with depth $h_b = 500$ mm results in a yield drift ratio of 1.05%, which is lower than the limiting drift considered. The yield displacement of the SDOF system is therefore $\Delta_y = 0.133$ m and the displacement ductility is $\Delta_y/\Delta_d = 1.21$. Note that, the displacement ductility is now increased. As a result, the equivalent viscous damping will be increased: $\xi_{eq} = 8.13\%$. From the displacement spectrum corrected for damping (Figure 5.15), it is noticed that the displacement $\Delta_d$ is above the spectrum.

Since the design displacement remains below the horizontal plateau of the 5% damped spectrum, it is necessary to iterate the solution by reducing the design displacement (which consequently reduces the equivalent damping). The procedure is described in Figure 5.15.

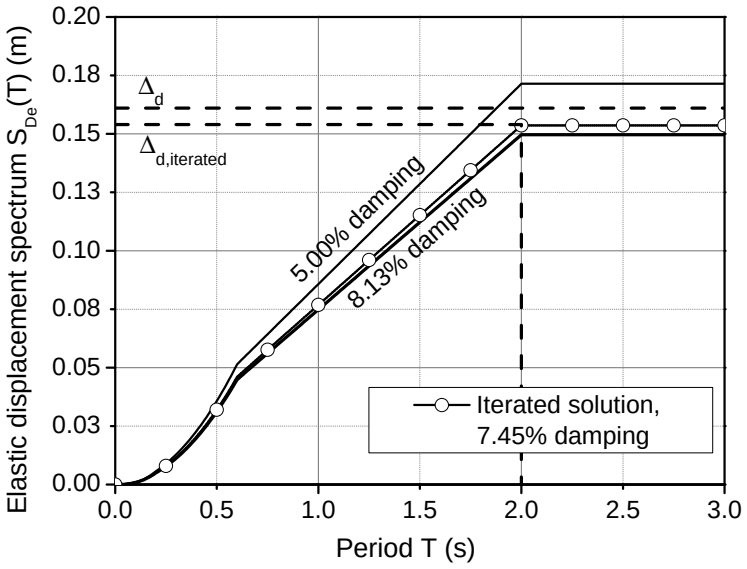


Figure 5.15: Determination of the period of the SDOF system, the case with shear-reinforced flat slabs

With the design displacement reduced to 0.154 m (only slightly smaller than the initial value and still larger than in the case of design without shear reinforcement in the flat slab), the corresponding required stiffness of the SDOF system is $K_e = 4\pi^2 m_e/T_e^2 =$ 2809.9 kN/m and the design base shear force for the entire structure is $F = K_e\Delta_d =$ 432.7 kN. As a result of the reduced design displacement, the design drift is also reduced, from 1.50% to 1.43%.

**Ensuring sufficient deformation capacity of the flat slab** From Figure 5.7 it is noticed that for $\zeta = 0.3$, the ultimate drift ratio is about 2%, which is larger than the drift ratio imposed by the design earthquake considered in this example. In other words, values of $\zeta$ smaller than 0.3 result in a sufficiently safe design. At this stage of the design, it is possible to check the value of $\zeta$ considering preliminary $u_{out,ef}/u_{out} = 1$ (i.e. extent of the shear-reinforced zone up to the point where reduction of the outer perimeter starts based on EC2 (CEN 2004c) rules). An approximate value of $V_{flex}$ is:

$$V_{flex} \approx 8m_R = 533 \text{ kN} \tag{5.26}$$

where $m_R = 66.6$ kNm/m is the resisting bending moment for unit length of the slab. From Equation 5.11, the factor $\zeta$ is therefore:

$$\zeta = \frac{201^2}{410 \times 533} \times 1 = 0.185 < 0.3 \tag{5.27}$$

Figure 5.7 indicates that the connection is therefore able to reach drift ratios larger than the target if sufficient shear reinforcement is provided.

To ensure that the relationships upon which the drift capacity was determined hold, the amount of punching shear reinforcement must be chosen such that the flexural yielding plateau of the slab–column connection can be reached. The unbalanced moment–drift relationship for the connection under consideration developed using the mechanical model proposed by Drakatos et al. 2018, with $r_q$ = 1.05 m (roughly corresponding to the zero moments line), bottom reinforcement ratio of 0.3% in the column region, a fixed radius $r_0$ (see Section 4.11.1) and characteristic material properties[3] is shown in Figure 5.16.

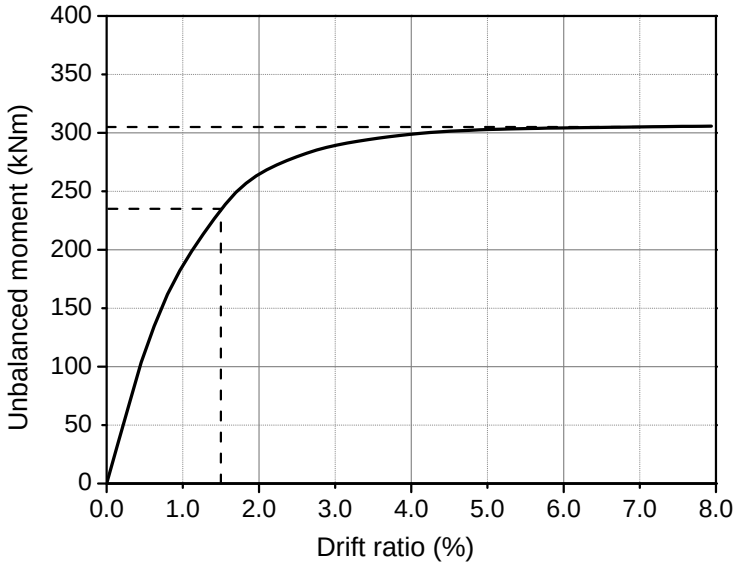


Figure 5.16: Determination of the unbalanced moment to be used for the design of shear reinforcement

A safe design of the slab–column connection would be achieved using the following design action effects: $V_{Ed}$ = 197 kN and $M_{Ed}$ = 305 kNm (Figure 5.16). In the present case, the drift ratio was not limiting the design of the frame, because the design drift of 1.50% (then further reduced to 1.43%) was chosen smaller than the ultimate drift ratio of the slab–column connection. In such a case, where using the factor $\zeta$ is not necessary, the design unbalanced moment can be reduced to the value corresponding to the limiting drift, as demonstrated in Figure 5.16. However, to prevent brittle punching shear failures for earthquakes stronger than the design earthquake, this reduction of the design unbalanced moment is not recommended.

[3] conservative approach when determining the design unbalanced moment

#### 5.4.4.3 Concluding remarks

Comparing the two design alternatives it is obvious that the second one is more economic. The required strength (base shear) in case the design drift is not limited by punching shear of the slab–column connections is reduced from 694.2 kN to 432.7 kN (approximately 38% reduction). The limiting drift of 1.43% is still relatively small for shear-reinforced flat slab–column connections (based on the available experimental data). A further increase of the design drift (and an even more economic design) might be possible in other structures if the damage limitation criteria are also met (for the corresponding earthquake, with a lower return period).

The example presented here is a simple one. It should be noted, however, that DDBD is also applicable to irregular buildings, bi-directional loading, $P-\Delta$ effects, effect of higher modes, buildings with shear walls and base isolated structures (Priestley et al. 2007).

# Chapter 6

# Seismic behaviour of flat slab frames

## 6.1 Introduction

Experimental investigation on full-scale building specimens remains to date the most comprehensive method of studying the seismic behaviour of flat slab buildings. However, very few such tests are reported in the literature (see Section 2.3.7). Although these tests have given a significant contribution in the understanding of the seismic behaviour of flat slab buildings, they are limited to the geometry, loading and material characteristics adopted in the experimental campaign. Testing of full scale buildings to cover the wide range of input variables is impractical. On the other hand, a considerable number of cyclic loading tests on isolated structural elements that constitute a flat slab building exist.

Considerably high drift ratios at failure have been reported in the literature corresponding to specimens with studs (Chapter 5). In a real building, however, it is often not possible to attain such high drift ratios without failure of other structural elements (for example, columns, shear walls and non-structural components). The use of flat slabs as primary seismic elements in highly seismic areas is discouraged due to their poor performance during earthquakes (notably the Mexico City earthquakes of 1985 (Butcher et al. 1988) and 2017 (Galvis et al. 2017)) and lack of code regulations. For example, Eurocode 8 (CEN 2004d) does not fully cover such structures. However, a better understanding of the seismic behaviour of these buildings would contribute in the risk mitigation of existing buildings and safer design of new ones.

As previously mentioned, the test setup developed at DEC/FCT/UNL (Section 3.5) simulates the entire span of the flat slab in the longitudinal direction (from mid-span to mid-span). As a result, it is rather convenient to assemble experimentally calibrated flat slab models to build flat slab frames (Figure 6.1).

A series of analyses on flat slab frames is described and discussed in this chapter. For the flat slabs, the specimens presented in Chapter 3 are used. As already described, one of

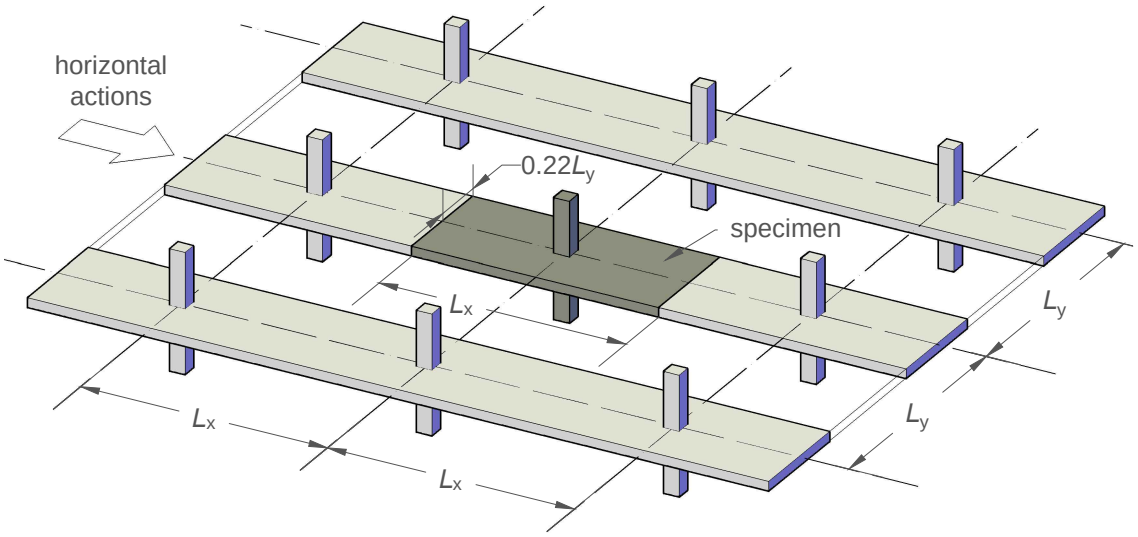


Figure 6.1: Assembling flat slab frames based on the experimentally tested specimens

the specimens had no shear reinforcement whereas the other specimens had shear studs around the column. The frames are therefore analysed for two versions of the flat slabs:

- without shear reinforcement;
- with shear reinforcement.

The focus of this chapter is therefore on the study of the role that punching shear reinforcement plays in the seismic behaviour and performance of flat slab frames.

All modelling and analyses are performed in the OpenSees platform (McKenna et al. 2009). The model adopted for the slab–column connections is described first. Then, pushover analyses are performed on a series of frame models. For two representative frames, further analyses based on nonlinear time history analyses are described.

## 6.2 Modelling of slab–column connections

A review of the modelling techniques for flat slabs and flat slab–column connections was presented in Section 2.8. Since the focus of this chapter is on the seismic behaviour of reinforced concrete flat slab frames, it is convenient to adopt simplified models for the slab–column connections. First, the model is calibrated based on the experimental results presented in Chapter 4. Then, the model is replicated to form reinforced concrete frames as it is discussed in the subsequent sections.

### 6.2.1 Description of the adopted model for the slab–column connections

The model used herein is based on that of Kang et al. 2009. However, some modifications are proposed to better fit to the purposes of this study. The first modification is related to

the slab-beam elements. A nonlinear fibre element modelling approach is adopted here (Figure 6.2) instead of using elastic elements and slab plastic hinges that are proposed in the original model (Figure 2.39).

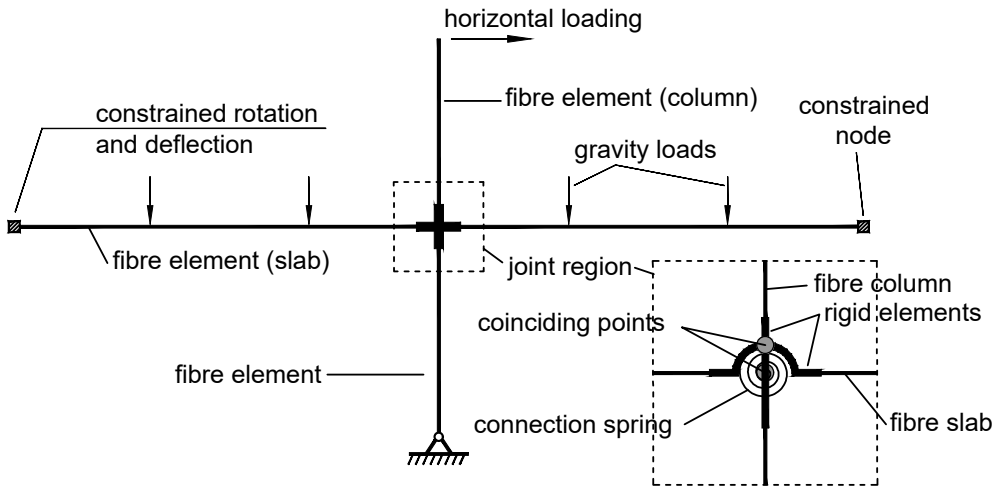


Figure 6.2: Adopted model for the specimens and the flat slab–column connections

The behaviour of the connection spring (see Figure 6.2) is shown in Figure 6.3. This spring controls the unbalanced moment transfer from the column to the flat slab. Since the slab–column connections herein are calibrated based on experimental tests, modifications are also made on the nonlinear behaviour characteristics of this spring. For instance, a linear transition zone is added between the rigid branch and the perfectly plastic branch in the connection spring (Figure 6.3) as it was found to produce results that better match the experiment. Regarding the loss of unbalanced moment transfer due to punching shear failure, there are two representative scenarios taken into account (Figure 6.3):

- Punching shear failure before global yielding (i.e. before reaching the horizontal plateau in the unbalanced moment–drift relationship). For the specimens presented in this dissertation, this is the case of specimen C-Ref (Figure 6.3a).
- Punching shear failure for a certain drift, after global yielding. This is the case of all the other specimens (C-SSR3 and C-SSR5 series, Figure 6.3b).

The spring is modelled using the LimitState (Elwood 2004) uniaxial material in OpenSees (McKenna et al. 2009), which has a trilinear backbone curve and a hysteretic behaviour. The limit state model is based on the global connection rotation. As a result, this approach is limited to buildings in which the global rotation at the slab–column connections is not significantly influenced by the flexural deformation of the entire building as a cantilever. The focus herein is on low-rise buildings with several spans, therefore this limitation does not apply.

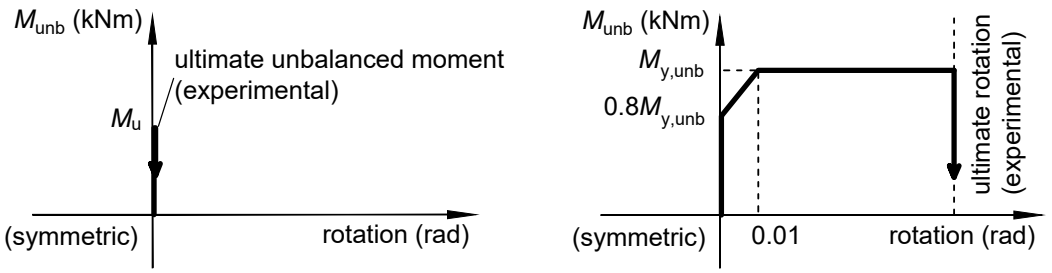


(a) Specimen C-Ref

(b) Specimen C-SSR3 and C-SSR5 series

Figure 6.3: Connection spring moment-rotation relationship

### 6.2.2 Model calibration

#### 6.2.2.1 Materials

For the calibration of the numerical models of the specimens, there are three materials to be considered:

- structural steel used in the steel column (see the experimental campaign, Chapter 3);
- concrete of the slab specimens;
- reinforcing steel of the slab specimens;

Structural steel and the reinforcement are modelled using a Giuffré-Menegotto-Pinto model with isotropic strain hardening (named Steel02 in OpenSees, Filippou et al. 1983; *Steel02 Material – Giuffré-Menegotto-Pinto Model with Isotropic Strain Hardening*). A concrete material with linear tension softening (named Concrete02 in OpenSees, *Concrete02 Material – Linear Tension Softening*) is used to model the slab-beams. However, it was found that neglecting the tensile strength leads to an initial stiffness that is closer to the experimental results. Therefore, tensile strength was set equal to zero for the subsequent analyses. The material characteristics determined from tests were used (Section 3.8). Assumptions were made for properties required by the material models that were not directly determined from tests. For instance, the strain hardening ratio of steel was assumed close to zero and the yield stress of structural steel was assumed equal to 275 MPa. The modulus of elasticity was taken equal to 210 GPa for structural steel and 200 GPa for reinforcement steel. Concrete ultimate strain was assumed equal to 0.35 % (CEN 2004c). Concrete strain at strength $f_c$ and crushing stress were taken as described in Figure 6.4.

#### 6.2.2.2 Yielding unbalanced moment

In the original model proposed by Kang et al. 2009, the ACI 318-14 (ACI 2014) eccentric shear model for moment transfer is used to determine the yield unbalanced moment of

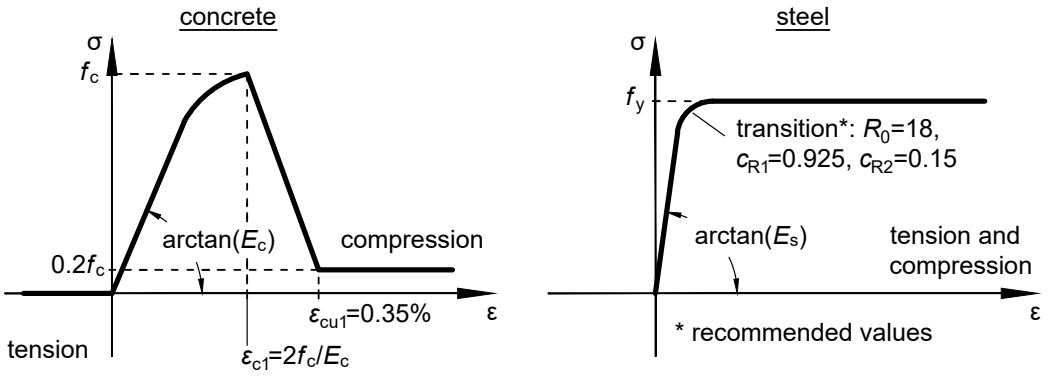


Figure 6.4: Adopted concrete and steel stress–strain relationships

the connection spring $M_{y,unb}$, as follows:

$$M_{y,unb} = \frac{M^{+}_{y,c+3h} + M^{-}_{y,c+3h}}{\gamma_f} \tag{6.1}$$

where $M^{+}_{y,c+3h}$ and $M^{-}_{y,c+3h}$ are the positive (sagging) and negative (hogging) slab yield moments calculated based on a section width equal to the dimension of the column's side plus three times the thickness of the slab ($h$). The factor $\gamma_f$ represents the portion of the unbalanced moment transferred by flexure in the eccentric shear model. Based on Equation 2.9, $\gamma_f = 0.6$ for a square column.

For the purposes of this study, it is not necessary to calculate the yielding unbalanced moment, because it is already available from the experimental campaign (Chapters 3 and 4). However, the experimental unbalanced moments ($M_{y,exp}$) are compared in Table 6.1 with the values obtained using Equation 6.1. The calculations are performed considering an effective depth equal to 124 mm for the top reinforcement 125 mm for the bottom reinforcement (in the direction of loading). The width over which the moments $M_{y,c+3h}$ are calculated is 700 mm. The comparison is expressed in Table 6.1 in terms of a factor $\gamma_f$ that results in a yielding unbalanced moment equal to the experimentally observed one. Since $\gamma_f$ does not depend on the applied gravity load (Equation 6.1), a unique value that can be applicable to all the specimens is not possible. For instance, the value corresponding to the specimen with increased GSR (specimen C-SSR5c) is notably higher than that of the rest of the specimens in Table 6.1.

It should be noted that the original model of Kang et al. 2009 considers an increase of the unbalanced moment even after reaching $M_{y,unb}$, as shown in Figure 2.40, due to eccentric shear. However, the behaviour of the rotational spring is simplified as described in Figure 6.3b to match with the experimental results. To this end, a linear inelastic branch starting from $0.8M_{y,unb}$ and extended until around a connection rotation of 0.01 radians is added. After reaching $M_{y,unb}$, the behaviour is assumed as perfectly plastic, in accordance with the experimental observations.

Table 6.1: Comparison of experimental unbalanced moments with the eccentric shear model (plus sign for sagging moments, minus for hogging moments)

| Specimen | $f_y^+$ (MPa) | $f_y^-$ (MPa) | $f_c$ (MPa) | $M_R^+$ (kNm) | $M_R^-$ (kNm) | $M_{y,exp}$ (kNm) | $\gamma_f$ |
|---|---|---|---|---|---|---|---|
| C-SSR3 | 523.9 | 544.9 | 41.2 | 34.6 | 50.3 | 120.8 | 0.70 |
| C-SSR5a | 523.9 | 544.9 | 27.0 | 33.8 | 48.6 | 110.4 | 0.75 |
| C-SSR5b | 549.5 | 541.9 | 57.6 | 36.6 | 50.9 | 117.8 | 0.74 |
| C-SSR5c | 549.5 | 541.9 | 69.9 | 36.8 | 51.3 | 95.8 | 0.92 |

#### 6.2.2.3 Hysteretic behaviour

The hysteretic characteristics to be determined are the pinching factors for deformation and force ($p_X$ and $p_Y$ in Figure 6.5) and a factor $\beta$ which is used to determine the degraded unloading stiffness, $K_{unload}$, based on ductility, $\mu$, as follows (after *OpenSees Command Manual - Hysteretic Material*):

$$K_{unload} = \mu^{-\beta} K_0 \tag{6.2}$$

where $K_0$ is the initial loading stiffness.

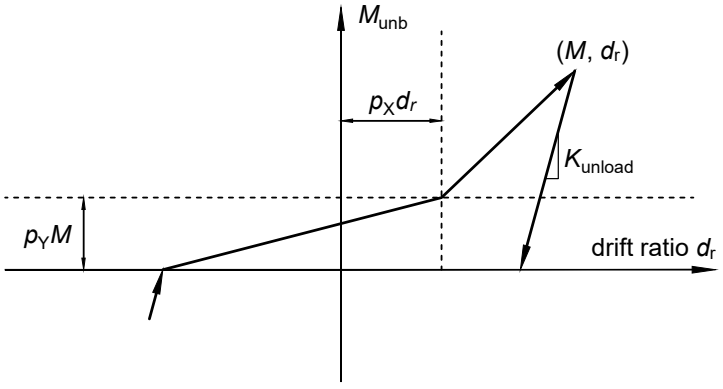


Figure 6.5: Pinching parameters to be determined

A parametric study was conducted to estimate the parameters $p_X$ (for displacement), $p_Y$ (for force) and $\beta$ based on two criteria:

- the minimization of the difference between the energy dissipated during the test and in the numerical model and
- numerical stability.

The model of the specimen C-SSR3 was used as a reference. The pinching factors were varied from 0.20 to 0.80 in steps of 0.05 while keeping $\beta$ equal to 0.90, which was found suitable for numerical stability reasons. Figure 6.6 shows the results of the parametric analysis in terms of absolute difference in energy dissipation between the test and the numerical model. For clarity, the axes values are bounded to values close to the optimum (the absolute difference was larger for the region not shown in the figure). The loading history was tracked up to one full cycle at 4.0% drift ratio, thus avoiding the cycle in which the punching failure occurred for specimen C-SSR3. The minimum absolute difference in dissipated energy between the experiment (up to one cycle of 4.0% drift) and the numerical model was 0.02 kNm (0.1% of the dissipated energy during the test), corresponding to pinching factors $p_X = 0.8$ (for displacement) and $p_Y = 0.3$ (for force).

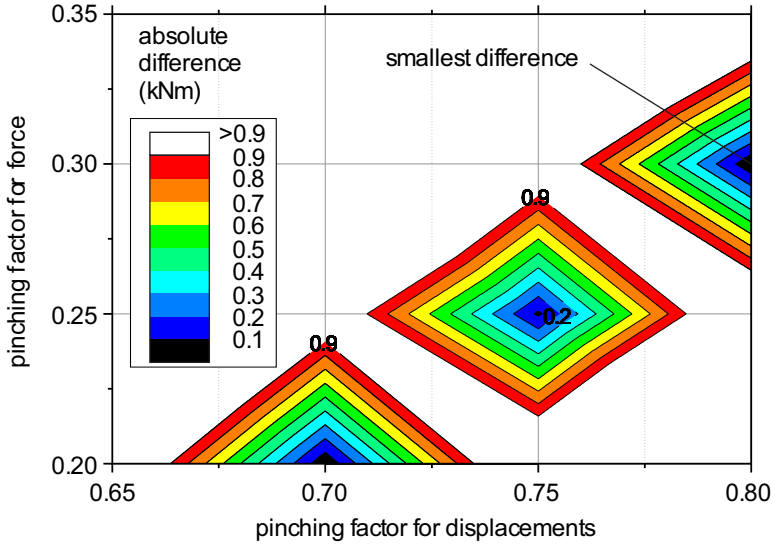


Figure 6.6: Results of the parametric study on the optimum pinching parameters

The hysteretic response of the other specimens with shear reinforcement was similar, and the same pinching factors were found to be suitable. In specimen C-Ref, it is not possible to apply the pinching characteristics described above, because the connection spring remains in the rigid branch for this specimen until punching failure. Nevertheless, it was found that for cyclic loading up to the second cycle of 1.0% drift ratio (ignoring the limit state model that would trigger punching failure), the absolute hysteretic energy difference between the experiment and the numerical model was less than 0.6% of the energy dissipated during the test.

#### 6.2.2.4 Analysis and comparison with the experiments

The model used for calibration of the connection spring characteristics is shown in Figure 6.2. This model replicates the boundary conditions of the test setup. Equal deflections and rotations are enforced at the opposite slab borders (i.e. at mid-spans) through constraints. The column is made of two force-based elements with a cross section discretized

in nonlinear fibres. Four integration points are used along each column element. The slab is modelled by 6 force-based elements with fibre cross section. The division into six elements was made in order to apply the gravity load in the correct position (Figure 6.2). The cross section was made of five stacked layers of concrete fibres and two layers of steel representing the top and bottom reinforcement respectively. Three integration points were used along each slab element. The rigid elements in the slab–column connection region were modelled using elastic elements with sufficiently large axial, shear and bending stiffness.

For specimen C-Ref, a force–based limit state model was adopted (Figure 6.3a). For all the other specimens, the limit state was based on the slab–column connection rotations measured experimentally (Figure 6.3b). A slight increase of the ultimate rotation was applied in cases where the specimen failed in the second cycle of a certain drift level, to ensure that the model completes a full cycle at that drift level before punching failure. For all the specimens that failed in punching (i.e., excluding C-SSR5a), the comparison of the numerical results with the experiments is given in Figure 6.7.

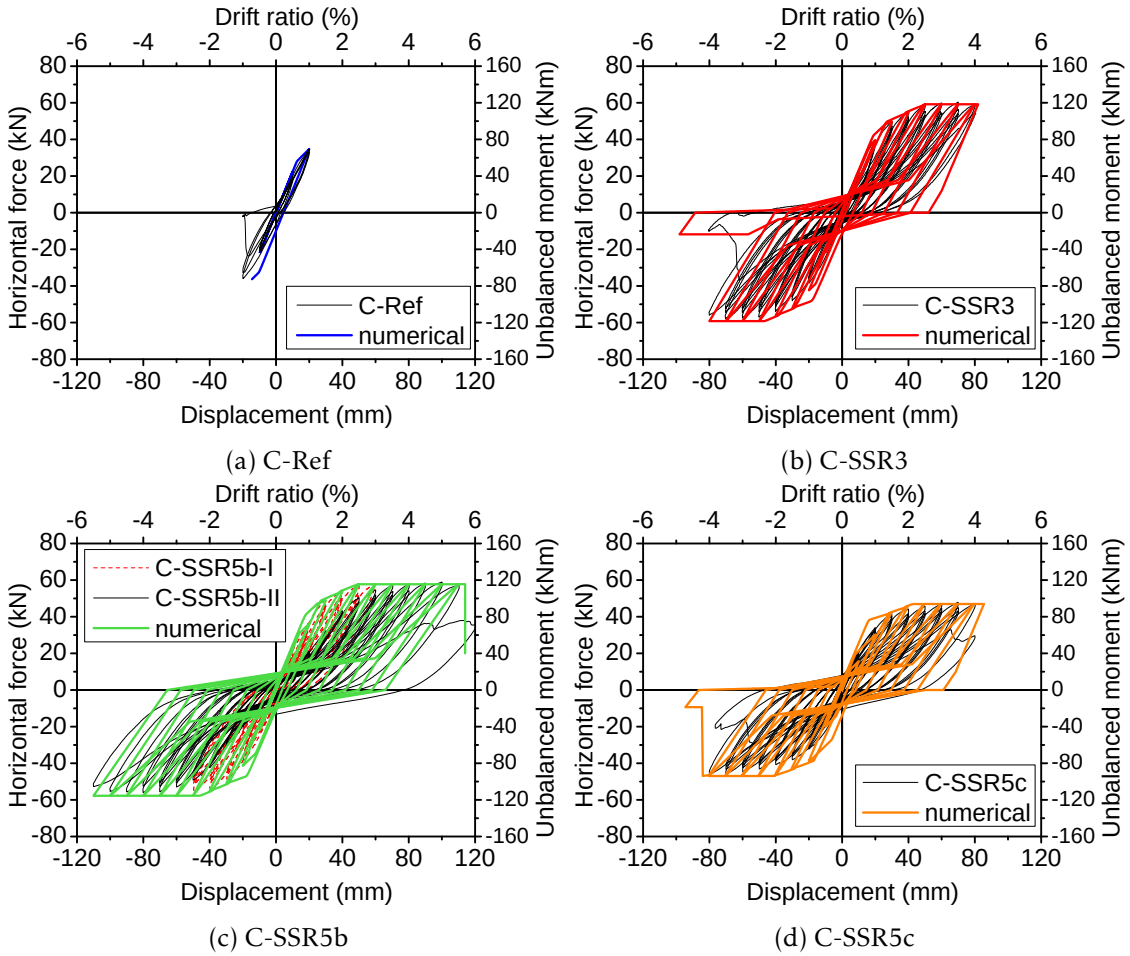


(a) C-Ref (b) C-SSR3

(c) C-SSR5b (d) C-SSR5c

Figure 6.7: Comparison of the specimen numerical models with the experimental results

For specimen C-SSR5a that did not have a clear punching failure, the limit state model

that triggers punching failure is not applied as in the other specimens. However, it is possible to model the softening behaviour of this specimen by adjusting the behaviour of the connection spring. As an alternative, the limit state can be triggered at the peak unbalanced moment and an appropriate degrading stiffness can be chosen. The connection spring backbone relationship modification approach is chosen and the comparison with the experiment is shown in Figure 6.8.

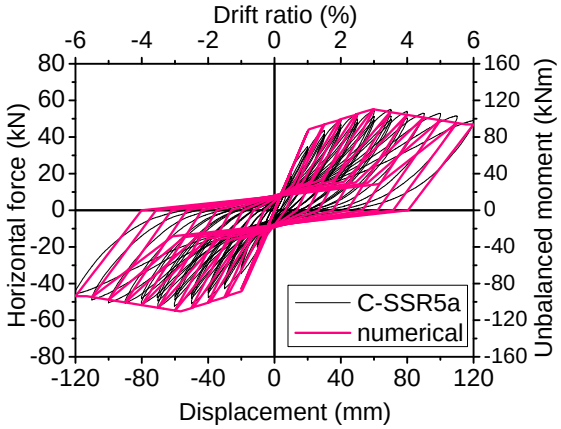


Figure 6.8: Comparison of the numerical results for C-SSR5a with the experiment

#### 6.2.2.5 Modelling damage

In Section 6.2.2.4, the numerical models used for comparison with the experiments followed a horizontal displacement history with no repetition of the drift cycles. As it was described in Section 3.6, the horizontal displacements history used in the experimental campaign involved three repetitions of cycles up to 3.5% drift, two repetitions for the 4.0% drifts and then no repetition for the subsequent drifts. Furthermore, specimen C-SSR5b was tested following a two–phase displacements history. It was shown that drift repetition resulted in stiffness and strength degradation.

Without further modification, the model of specimen C-SSR5b is tested with a two-phase loading protocol and the comparison with the experiment is shown in Figure 6.9. The figure shows that, even without special consideration regarding damage, the model follows reasonably well the experimental force–displacement hysteretic relationship. It is noticed that the model and the experiment diverge the most in the second phase up to 3.0% drift (Figure 6.9b).

The limit state material in OpenSees (McKenna et al. 2009) can model damage by introducing two parameters, one related to damage due to ductility ($D_1$) and another related to energy ($D_2$). These parameters cause a reduction of the strength as a function of ductility and the dissipated energy, respectively. The parameter $D_1$ is a function of $(\mu - 1)$, where $\mu$ is the displacement ductility. The parameter $D_2$ is a function of the ratio $E_{ii}/E_{ult}$, where $E_{ii}$ is the energy dissipated up to a certain analysis step and $E_{ult}$ is the

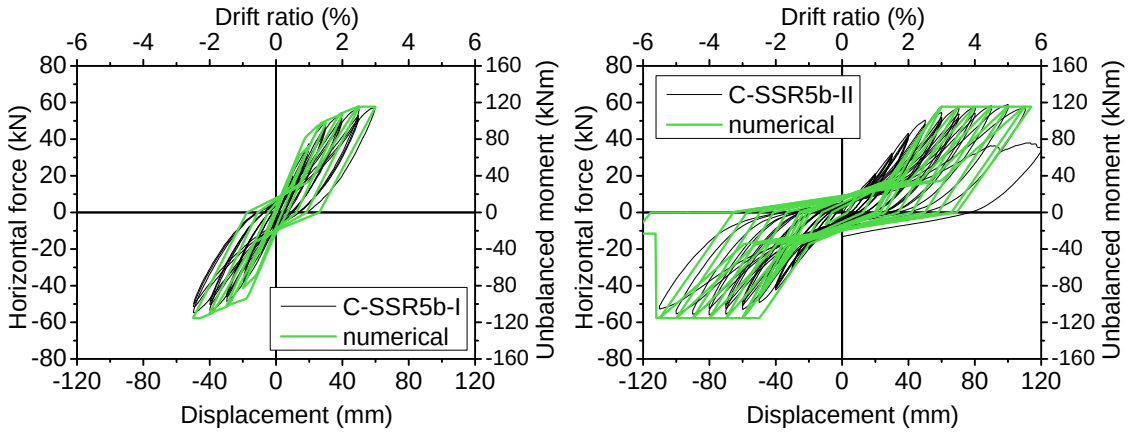


(a) Phase-I (b) Phase-II

Figure 6.9: Comparison of the numerical models with the experimental results for the two phases of loading of specimen C-SSR5b

total energy dissipated up to failure.

Although a more refined modelling including damage is possible, it is not used in the subsequent analyses, for the following reasons:

- It is an additional burden for the analysis. It can cause an increase of the run-time and convergence issues. Considering the fact that a large number of analyses will be performed herein, these factors become important.

- It does not substantially improve the model. It was shown in Figure 6.9 that satisfactory results are achieved even without these special considerations.

However, a model explicitly incorporating damage can be a starting point for a more refined analysis in the future, including a more generalized treatment of damage due to repeated loading.

## 6.3 Pushover analyses of flat slab frames

In this section, pushover analyses on a number of flat slab frames are presented. The purpose is to understand the influence of several modelling variables in order to make appropriate decisions regarding the frames to be further considered for a more detailed analysis. Besides the above-mentioned purpose, this section provides insight on the comparison between shear-reinforced flat slab frames and frames with flat slabs without shear reinforcement under seismic loading conditions. Preliminary analyses were presented in Isufi et al. 2018a.

### 6.3.1 Description of the frames

A total of 12 frames were modelled and analysed in the OpenSees (McKenna et al. 2009) platform. The frame models presented herein consist of an array of basic sub-assembly units such as that shown in Figure 6.2, therefore they are "scale models" of the prototype building corresponding to the laboratory tests (Figure 6.11a). The models are given names based on the following convention: number of storeys followed by the type of slab–column connections followed by a description of the columns in brackets. The types of slab–column connections are:

- R – for rigid connections. This type of connection is created by directly connecting the rigid end zones of the column and the slab. As a result, this type of connection is not expected to account for the unbalanced moment transfer mechanism over a width smaller than the full width of the slab specimen. Furthermore, punching shear failure is not simulated, due to the lack of a connection spring.
- NoSr – for connections calibrated based on specimen C-Ref, without shear reinforcement.
- SSR – for connections calibrated based on specimen C-SSR5b, reinforced with studs. This specimen is chosen due to the comparable material properties (especially concrete) with specimen C-Ref.

The considered column types are (Figure 6.10):

- C1 – for reinforced concrete square $250 \times 250$ *mm* columns reinforced with 12Φ12 bars.
- C2 – for reinforced concrete square $250 \times 250$ *mm* columns reinforced with 12Φ16 bars.

The strength of column C1 for low axial loads is comparable to the strength of the slab–beams connected to it (with section width equal to the full width of the specimen). The strength of column C2 for low axial loads is approximately 1.3 times the strength of the slab–beams connected to it.

The designation "S" is used in Figure 6.10 for steel HE120M columns. These columns are the same as the column used in the laboratory campaign. Note that, for the expected range of deformations in the laboratory, the column is designed to remain elastic. It can, however, be plasticized for larger deformations.

Steel columns of type "S" are impractical for real buildings, and are shown here only for reference with the laboratory work. Pushover analyses with such columns are not presented herein. In Isufi et al. 2018a, however, it was shown that these columns lead

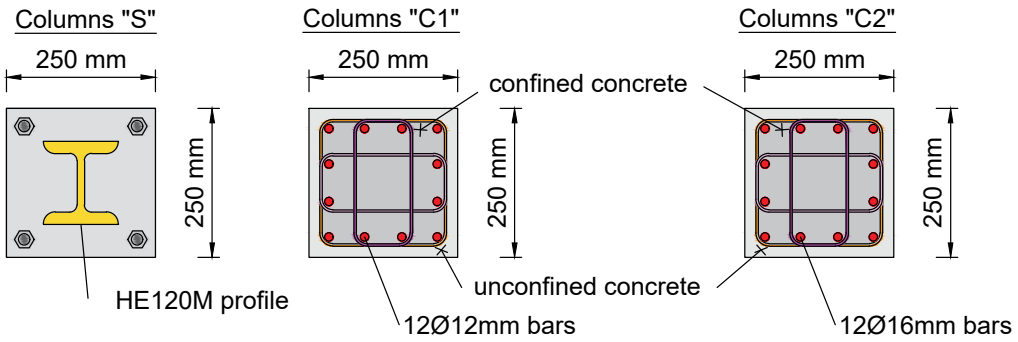


Figure 6.10: Column cross sections considered for the frames

to a less stiff global behaviour, which is not directly comparable with that of the other considered frames.

The cross-section dimensions are kept the same as the steel base plate dimensions, and since the slab–column connections are calibrated based on joint rotations, using reinforced concrete columns instead of the steel column in the structural models is acceptable. As an example of the nomenclature used for the frames, the model 3-NoSr(C2) is a three-story frame with reinforced concrete columns C2 and flat slabs without shear reinforcement.

All the frames have 5 bays (Figure 6.11). It is assumed that punching failures cannot occur in the exterior connections due to the presence of a continuous support (a beam) for the slab, therefore no rotational spring is modelled in the exterior connections. All columns within a model have the same cross section properties. Frames with three and five storeys are considered. The model is described in Figure 6.11b.

For the pushover analyses, a lateral load pattern compatible with the first mode of vibration of the structure is applied. $P-\Delta$ effects are included in the analysis. The analyses are terminated when the monitored displacement reaches a value of 400 mm (which was found to be a sufficiently large displacement based on preliminary analyses) or when analysis convergence is no longer achieved. For the slabs, material characteristics were taken as described in Section 6.2.2.1.

Gravity load is applied in locations distributed along the slab-beam elements, resulting in a shear force in the slab–column connections equal to $V_g = 215$ kN. This is close to the value applied in the experiments and it is kept the same for all frame models to minimize the effect on the columns and to facilitate the comparison of the frames. Modelling of the reinforced concrete columns is described in Section 6.3.2.

For nonlinear time history analyses (Section 6.4), it is assumed that the mass is consistent with the gravity load. The mass is lumped at the points of application of the gravity

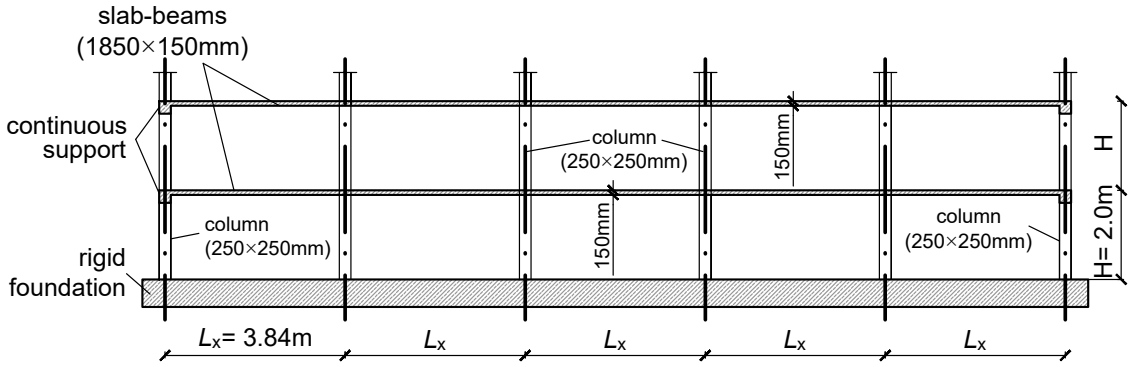


(a) Scaled prototype building

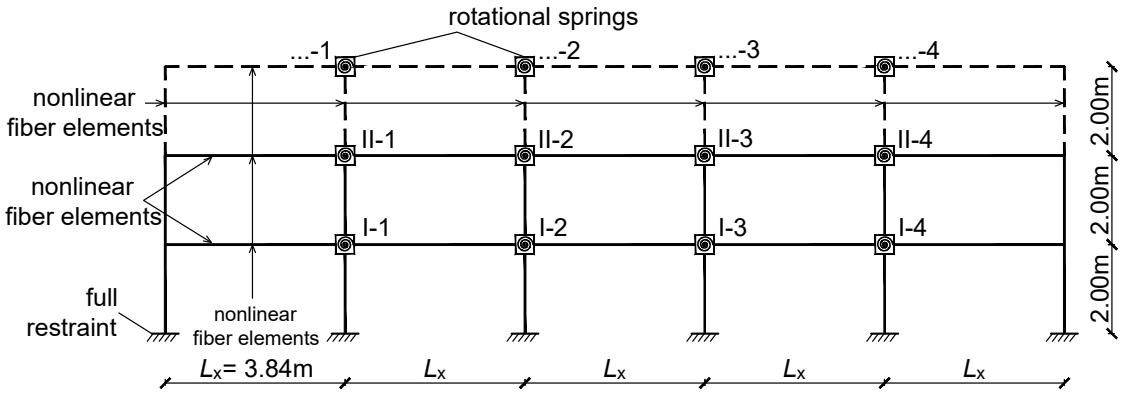


(b) Model

Figure 6.11: Description of the frame models (variable number of storeys)

load.

### 6.3.2 Modelling of the columns

A fibre modelling approach is adopted for the reinforced concrete columns. Two concrete materials are defined: an unconfined concrete material that is used for the fibres outside the confined core and an confined concrete model. For the unconfined concrete model, a Kent-Scott-Park concrete material model with no tensile strength is used (*Concrete01 Material – Zero tensile strength*). The unconfined concrete strength is assumed equal to 60 MPa for all the columns (in all frames). This value is close to the concrete strength used for the slabs in the experimental campaign (Table 3.3). Confined concrete is modelled based on the work of Braga et al. 2006. The model for the confined concrete requires the following inputs: unconfined concrete strength, initial modulus of elasticity of unconfined concrete, the ultimate strain of confined concrete, geometry of the hoops (diameter, configuration and spacing), steel characteristics of the hoops and the diameter of the longitudinal bars. For the unconfined concrete strength, the same value used for the concrete cover (60 MPa) was used. The modulus of elasticity was calculated in accordance with Eurocode 2 (CEN 2004c).

For the ultimate strain of confined concrete, $\epsilon_{cu,c}$, the formulation proposed by Scott et al. 1982 was used, according to which:

$$\epsilon_{cu,c} = 0.004 + 0.9\rho_s\left(\frac{f_{yw}}{300}\right) \tag{6.3}$$

where $\rho_s$ is the ratio of the volume of hoops to the volume of the confined concrete and $f_{yw}$ is the yield stress of the hoops.

The geometry of the confining steel is shown in Figure 6.12, along with the cross section of the columns and the shape of the stress–strain curves for confined and unconfined concrete. With the input parameters as described above, the confined concrete stress–strain relationship is obtained following the procedure described in Braga et al. 2006.

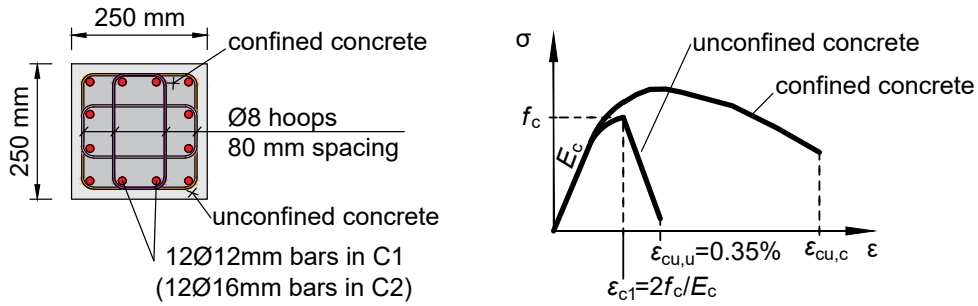


Figure 6.12: Cross section of the columns and confining reinforcement

The reinforcement model for the column is the same as that used for the slab–beam elements.

### 6.3.3 Pushover curves

The obtained pushover curves are given in Figure 6.13. The curves corresponding to models with rigid joints (i.e., without rotational springs) are also given for reference. Since these models do not accurately account for the portion of the unbalanced moment that is transferred to the slab and because they assume that the full width of the slab-beam participates in the load resisting frame, they overestimate the strength of the structure, as expected. However, the initial stiffness of these models closely matches the initial stiffness of models with connection springs. Obtaining an accurate force-displacement relationship with the rigid joint model technique would require a modification of the width of the slab-beam, as for example in Dovich and Wight 2005. Such models are not further discussed herein.

From the pushover curves it is noticed that, regardless of the columns' type, the frames with slabs without shear reinforcement have considerably lower strength and deformation capacity. The models with reinforced concrete columns have closely matching initial

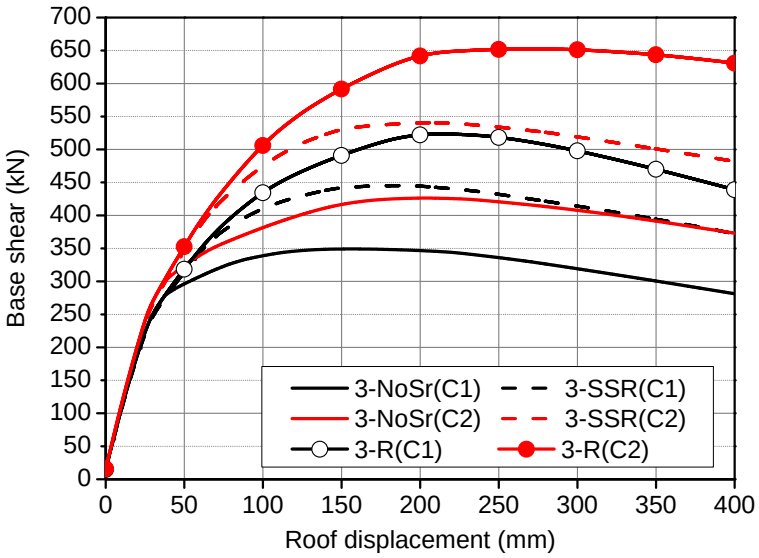


(a) Three storeys

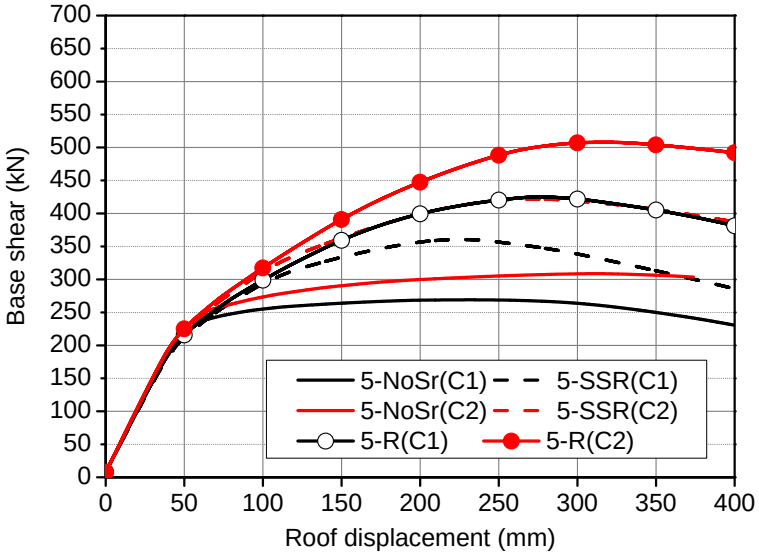


(b) Five storeys

Figure 6.13: Pushover curves for three and five story frames

branches. The models with highly reinforced columns (i.e. C2) attained considerably higher maximum base shear forces for all building heights.

### 6.3.4 Role of punching failures

The unbalanced moments in the rotational springs used in the slab–column connections are analysed in this section. It was noticed that, due to the regularity of the frames and the uniformity of the cross sections, there were no significant differences in terms of unbalanced moment–rotation relationship between the slab–column connections within

the same story. Therefore, in Figure 6.14 to Figure 6.17 the unbalanced moments are given for one representative flat slab–column connection per story, in the secondary axis. The corresponding global pushover curve is plotted in the primary vertical axis, with shaded area under the curve, to facilitate the comparison. The connection names are in accordance with Figure 6.11b.

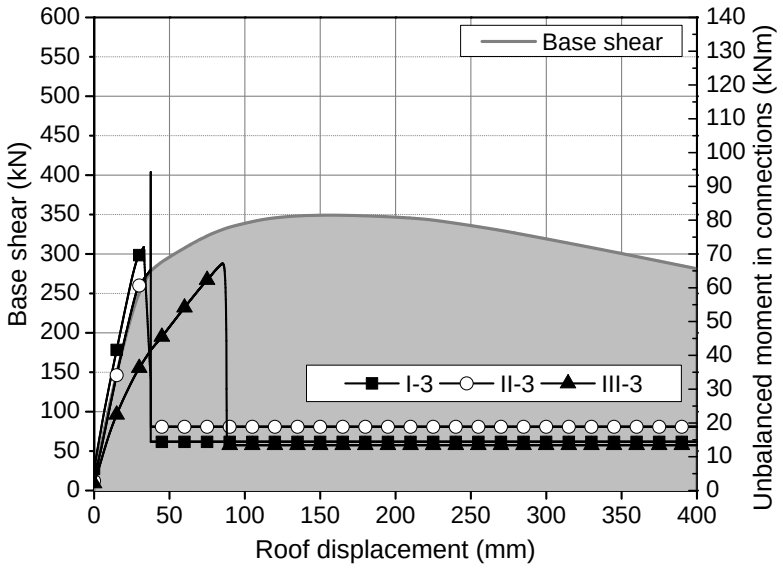


(a) 3-NoSr(C1)

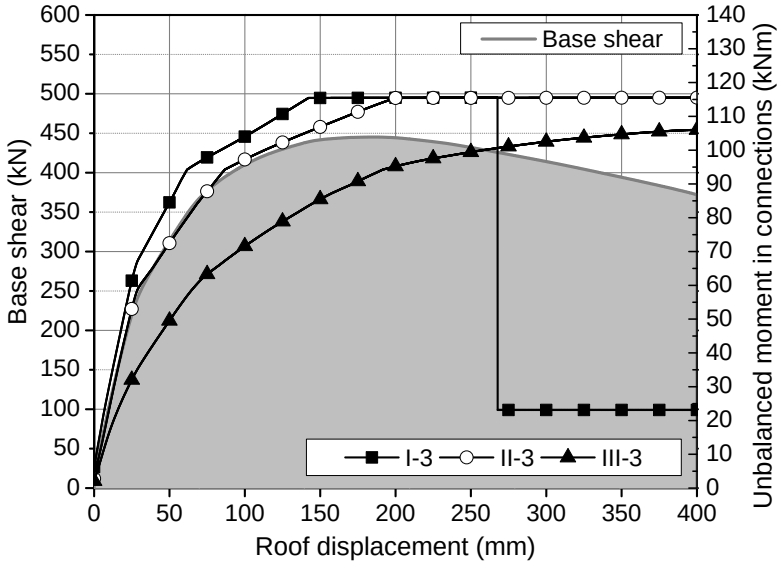


(b) 3-SSR(C1)

Figure 6.14: Unbalanced moment in slab–column connections versus global pushover curve in three storey frames with columns C1

As it was shown in the previous section, the pushover curves for frames with slabs with and without shear reinforcement have substantial differences. From the figures it is

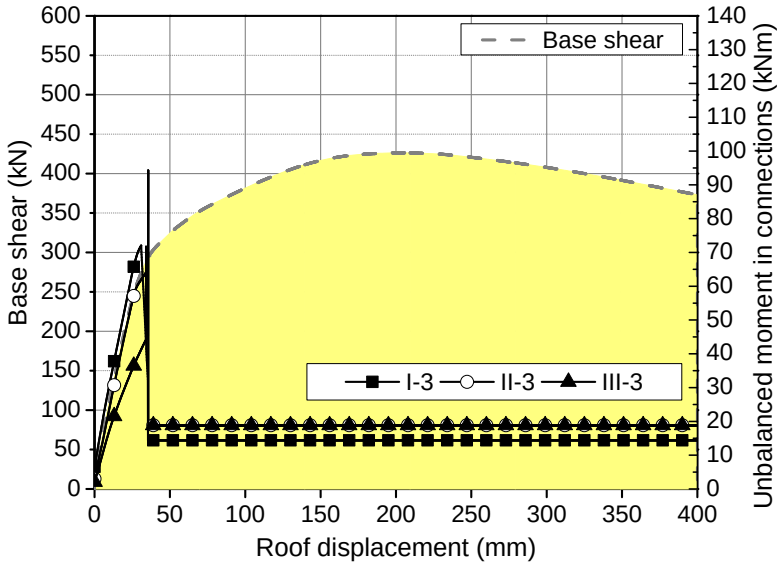


(a) 3-NoSr(C2)

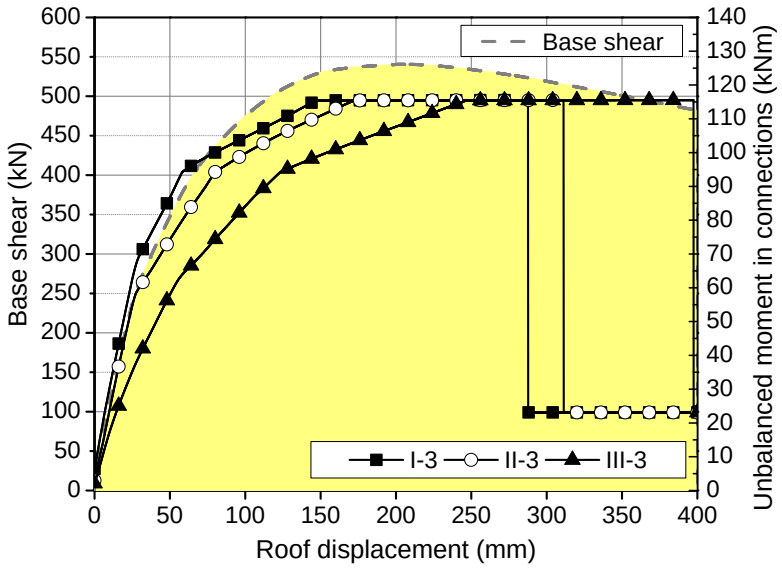


(b) 3-SSR(C2)

Figure 6.15: Unbalanced moment in slab–column connections versus global pushover curve in three storey frames with columns C2

noticed that the pushover curves of building models with flat slabs with no shear reinforcement are considerably influenced by the premature punching failure of the connections, leading to lower global base shear forces. In all models without shear reinforcement, the base shear continues to increase slightly even after punching failures, however, it remained lower than that of the corresponding models with shear-reinforced slabs. Looking at the figures corresponding to frames without shear reinforcement (Figures 6.14a, 6.15a, 6.16a and 6.17a) it is observed that punching failures correspond to a change of

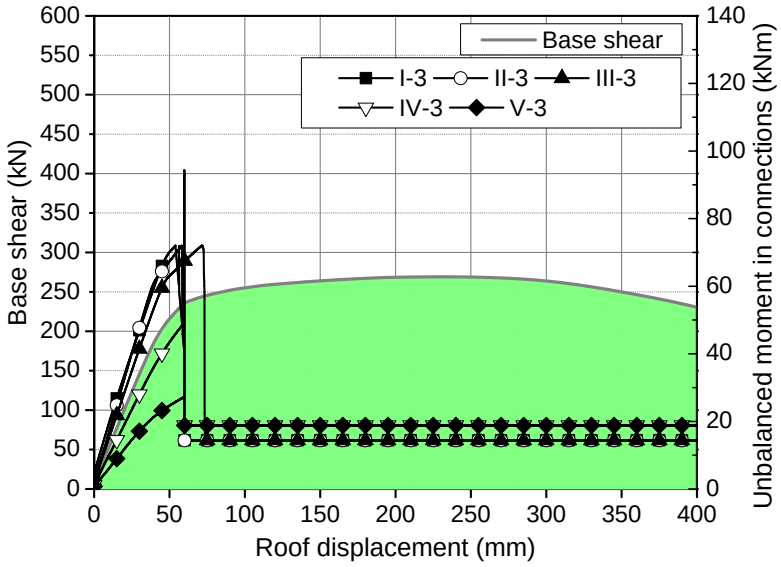


(a) 5-NoSr(C1)

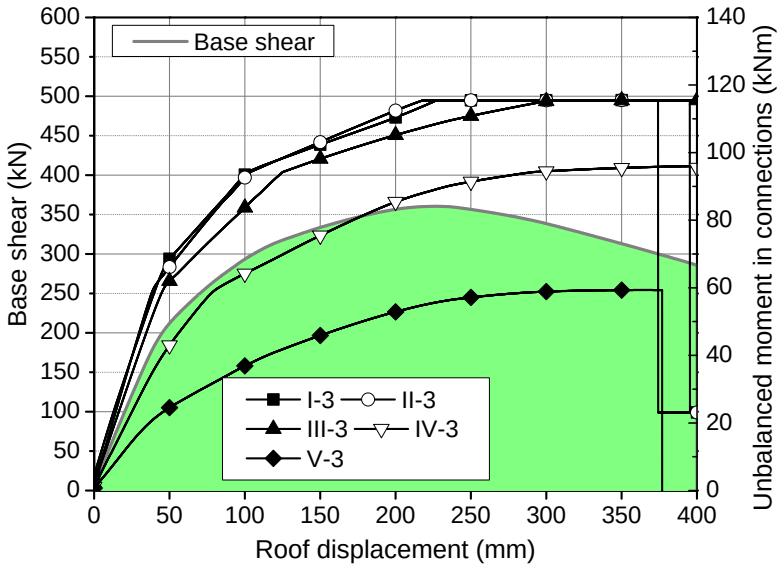


(b) 5-SSR(C1)

Figure 6.16: Unbalanced moment in slab–column connections versus global pushover curve in five storey frames with columns C1

slope in the global pushover curve.

In contrast to frames without shear reinforcement, it is observed that punching failures are not associated with major noticeable changes of slope in the global pushover curves of frames with shear-reinforced flat slabs. This is because punching failures occur for considerably large roof displacements in these frames, for which column plastic hinges are already formed (for much smaller global displacements). It is noticed, however, that the attainment of the maximum base shear force roughly corresponds to full

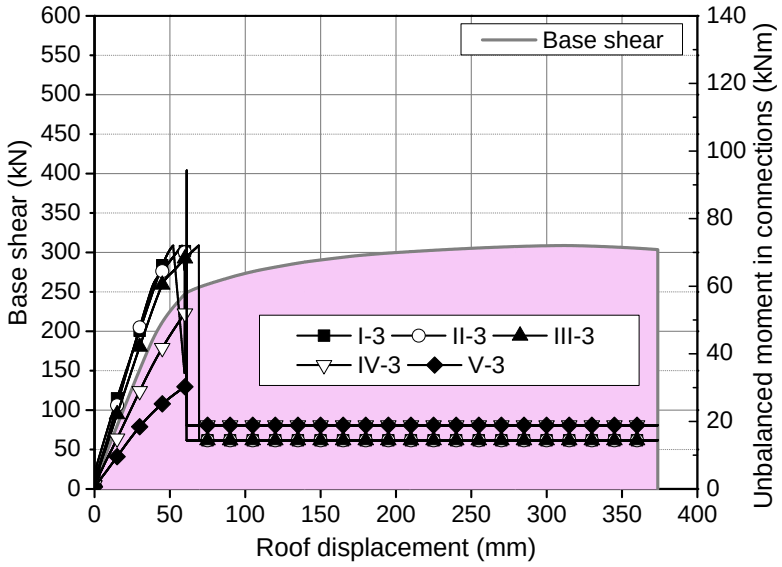


(a) 5-NoSr(C2)

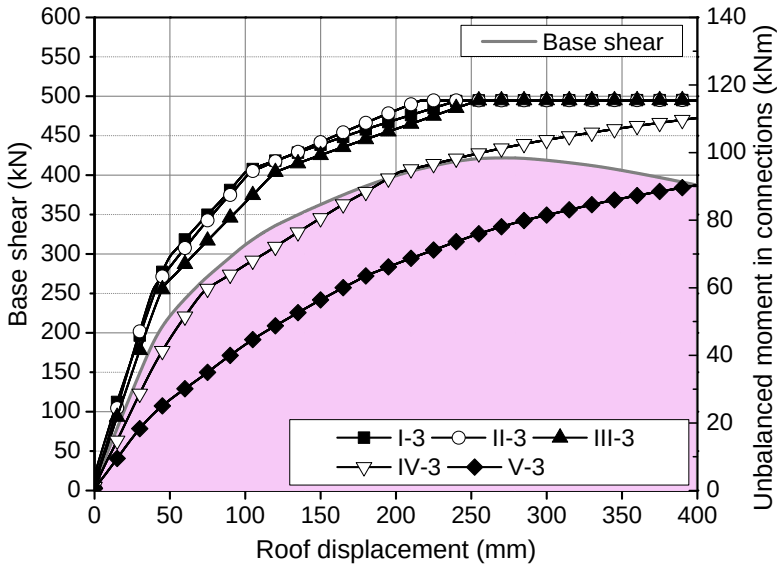


(b) 5-SSR(C2)

Figure 6.17: Unbalanced moment in slab–column connections versus global pushover curve in five storey frames with columns C2

yielding of the connection springs (i.e., $M_{y,unb}$ is reached in slab–column connections) for all the frames with shear-reinforced flat slabs. Figure 6.13 is a further confirmation of this observation, because it shows that when "R" (rigid) connections are used, the strength of the frame is further increased.

The drift capacity of the slab–column connections based on specimen C-SSR5b was so high that punching failures were not detected at all in some connections (for example, Figure 6.14b and Figure 6.17b). In all the frames that suffered punching failures, the

first story connections failed first, followed by the second story connections. The roof connections failed at a later stage, for considerably larger horizontal displacements.

Slab–column connections fail in a brittle manner which results in a zero or very low residual unbalanced moment transfer capacity. Although connection failures were observed in both with and without shear reinforcement models, there are significant differences between them. For instance, it is not possible to have a yielding plateau in the slab–column connection springs for slabs without shear reinforcement. After a punching failure, the column plastic hinges become the only barrier against global collapse. This mechanism can be significantly affected by the increased eccentricity of the vertical loads ($P-\Delta$ effect).

### 6.3.5 Hierarchy of resistances

A moment–curvature analysis of the cross sections used for the columns is described in this section. The analysis is performed in the OpenSees platform (McKenna et al. 2009). A zero-length element with cross section discretized in fibres is used, as described in Figure 6.18. The cross section and the materials assigned to the fibres are the same as those used in the frame models (see Section 6.3.1). One node of the zero-length element is fully fixed (node 1 in Figure 6.18). The other node (node 2 in Figure 6.18) has only the shear deformations restrained, and an axial load is applied to this node in a force controlled manner. After the application of the axial load, the rotations at node 2 are increased in a deformation controlled manner. Since the length of the section is zero, the nodal rotation is in fact the curvature, $\chi$. The moment that causes such a nodal rotation (curvature) is then recorded.

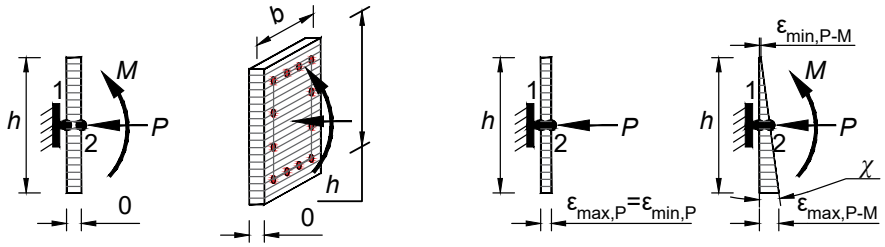


Figure 6.18: Description of the moment–curvature analysis model

The moment–curvature relationships are constructed for three levels of the axial load, corresponding roughly to the gravity load, $V_g$, applied in the experimental campaign (herein, a value of 200 kN is used), three times the value of $V_g$ (600 kN) and five times $V_g$ (1000 kN). These axial loads roughly correspond to the axial loads in the ground floor of frames with three and five storeys, except for column sections with an axial load of 200 kN, which correspond to the top storey of the frames. The results are presented in Figure 6.19.

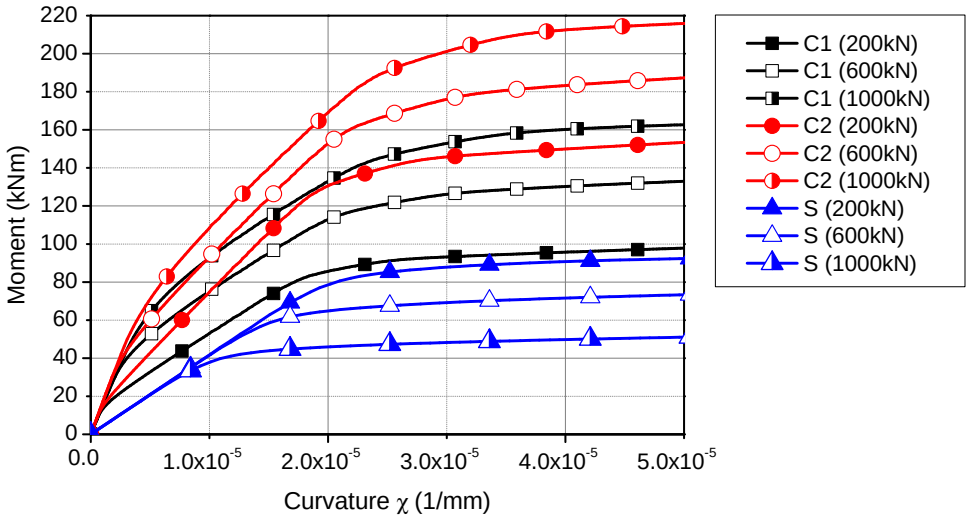


Figure 6.19: Moment–curvature relationships for the column sections

The figure shows that the moment–curvature relationship for column C1 with an axial load of 200 kN is very similar to that of the steel column under similar loading conditions. However, the initial stiffness is larger for the reinforced concrete columns. Again, since the behaviour of the slab–column connection is modelled based on connection rotations, using a stiffer column is not an issue as long as the same cross section outer dimensions are used.

Modern seismic design codes advocate the Capacity Design (CD) of structures. In principle, CD leads to a structure that is able to withstand the seismic action by favouring ductile plastic mechanisms of failure with high energy dissipation and by avoiding brittle failure modes. In a reinforced concrete building with moment resisting frames, a desirable plastic mechanism is the one in which plastic hinges form at the beam ends and at the column bases at the ground level (Figure 6.21a). In EC8 (CEN 2004d), for frames with at least two storeys, this is achieved by designing the column and the intersecting beams such that:

$$\sum M_{Rc} \geq 1.3 \sum M_{Rb} \tag{6.4}$$

where $\sum M_{Rc}$ and $\sum M_{Rb}$ represent the sum of the design values of the resisting moments of the columns and beams framing the joint, respectively.

As previously discussed, EC8 (CEN 2004d) does not fully cover buildings such as those described in Section 6.3.1. However, the relationship between the resistances of the columns and slab–beams is taken into consideration herein in order to study the applicability of Capacity Design rules in flat slab frames. To this end, the sum $\sum M_{Rb}$ is substituted with the yield unbalanced moment $M_{y,unb}$, as described in Figure 6.20. The value of $M_{y,unb}$ is smaller than the sum of the resisting moments of the slab–beams framing the slab–column connection (see Section 6.2.2.2) and it is rather easy to have "strong columns" in flat slab buildings.

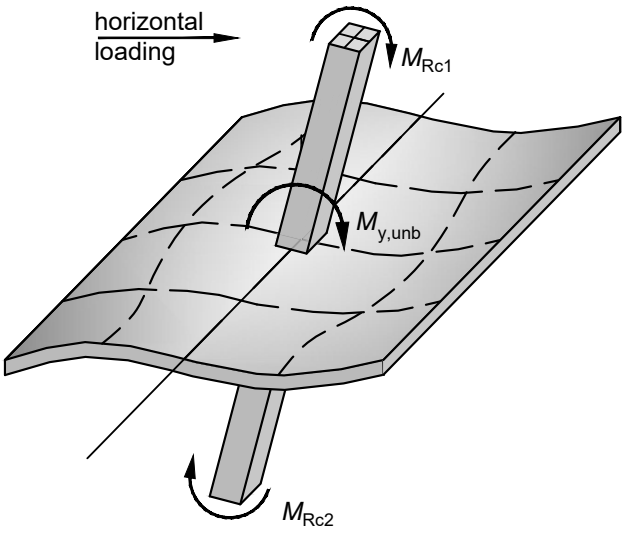


Figure 6.20: Resistance of elements framing into a slab–column connection

The column resistances $M_{Rc1}$ and $M_{Rc2}$ are equal, due to symmetry of the considered sections. The ratios $\sum M_{Rc}/M_{y,unb}$ for all three types of columns are given in Table 6.2. Although the ratios are shown for a five-storey frame, the information for lower frames can be obtained by looking at the last rows corresponding to the number of storeys. Note that an approximate value of $M_{y,unb}$ equal to 120 kNm is used to derive the values in the table. This value is used to detach the discussion from a specific flat slab specimen. It is, however, approximate with the experimentally observed yielding unbalanced moments (Chapter 4) for all specimens with GSR around 55 %.

Table 6.2: Ratios $\sum M_{Rc}/M_{y,unb}$ for the slab–column connections in the considered frame models

| | $\sum M_{Rc}/M_{y,unb}$ | |
|---|---|---|
| Storey | Column C1 | Column C2 |
| 1 | 1.90 | 3.00 |
| 3 | 2.38 | 3.42 |
| 5 | 2.76 | 3.75 |

The ratios in Table 6.2 are well beyond 1.3 for all the cases with reinforced concrete columns. As a result, the global mechanism of Figure 6.21c is favoured. The value of $M_{Rc1}$ would have to be smaller than 60 kNm for a "soft storey" to form (i.e., a storey in which column plastic hinges are developed, leading to a potential local mechanism of the storey, Figure 6.21b). By trial-and-error, it is found that the longitudinal reinforcement of the columns would have to be less than 12Φ8 for this to happen. However, this amount of longitudinal reinforcement is lower than the minimum reinforcement required by EC8 (CEN

2004d) for seismic design. In other words, for the given geometry and loading conditions, it is not possible to have a "soft storey" mechanism of the frames under consideration. This can be regarded as an advantage of flat slab buildings, given the disadvantages are dealt with properly (namely, avoiding punching shear failures and controlling deformations).

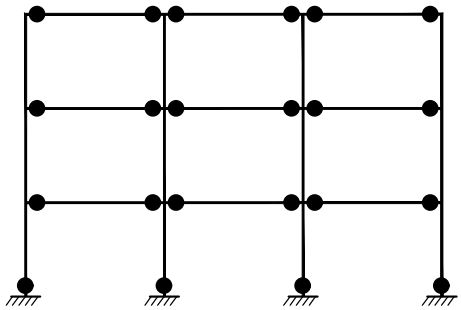

(a) Preferred mechanism

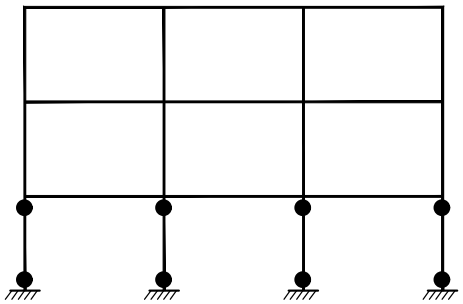

(b) Soft storey

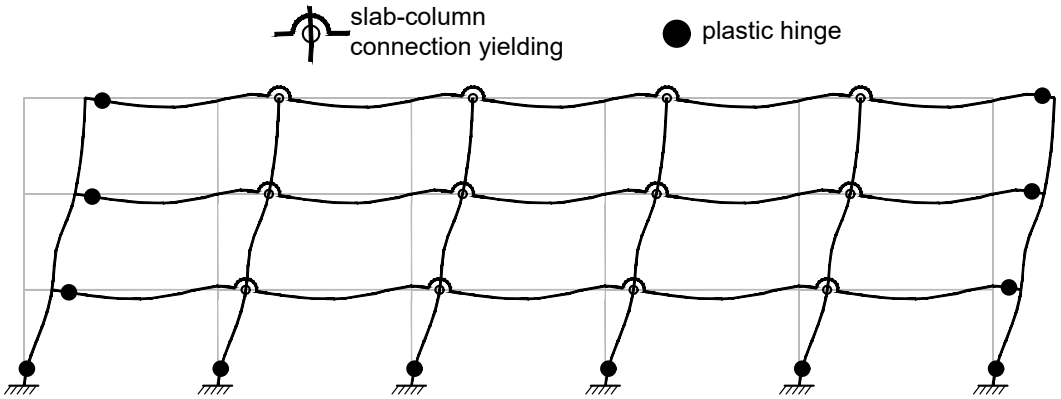


(c) Predisposed global mechanism in flat slab frames

Figure 6.21: Global mechanisms at failure

### 6.3.6 Capacity assessment of the three storey frames

The three storey frame models with columns C1 are chosen for a seismic fragility analysis in this dissertation (Section 6.4). To compare the pushover curves of frames with columns C1 and C2 and to evaluate the performance of each frame, the curves are transformed into idealized elasto–perfectly plastic curves for an equivalent Single Degree of Freedom (SDOF) system following the N2 procedure (Fajfar 2000), as recommended in Annex B of EC8, Part 1 (CEN 2004d). The formation of the plastic mechanism is assumed to correspond to the point in the curve with maximum base shear force. The resulting capacity curves are plotted in Figure 6.22 for the three storey frames, in Spectral Displacement – Spectral Acceleration coordinates (Acceleration Displacement Response Spectrum, ADRS

format).

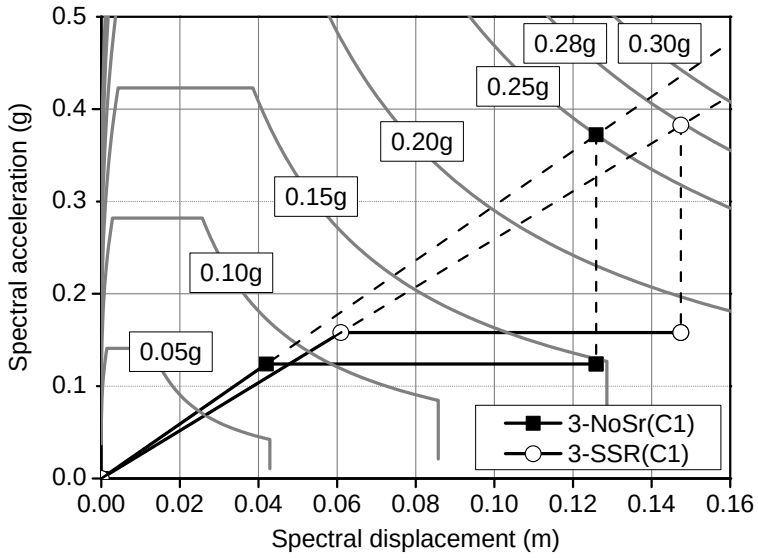


Figure 6.22: Comparison of the capacities of the two three storey frame models

Response spectra for different values of the reference ground acceleration, $a_{gR}$, are shown in Figure 6.22. These spectra are constructed in accordance with EC8 (CEN 2004d), for ground type C and spectrum type 1. The values of $a_{gR}$ that correspond to a complete exhaustion of the capacity of the structure are 0.25g and 0.28g for the frame 3-NoSr(C1) and 3-SSR(C1) respectively. These values are not far from each other. Furthermore, the two capacity curves demonstrate comparable ductility of the two frames, although one of them had shear reinforcement. There is some difference between the two frames in the reference ground acceleration for which the behaviour becomes plastic (both are around 0.10g, but global yielding is reached for a lower $a_{gR}$ in 3-NoSr(C1)).

Due to the high flexibility, the frames under consideration are subjected to lower seismic forces compared to stiffer structures. The intersection of the constant period line (elastic branch of the capacity curve and its extension in Figure 6.22) with the response spectra occurs in the constant spectral velocity region of the spectra, i.e. the fundamental period of the frames is between $T_C$ and $T_D$ (EC8, CEN 2004d). On the other hand, this means that the displacements of the structure are larger compared to stiffer structures.

It should be noted that the capacity assessment presented in Figure 6.22 does not provide any explicit information regarding damage suffered by the frames. As it will be discussed in the following sections, punching failures occur rather early (for small spectral accelerations and displacements) in frame 3-NoSr(C1).

### 6.3.7 Concluding remarks based on the pushover analyses

Pushover analyses of 3 and 5 story flat slab–column frames were presented. It was shown that models with no explicit consideration of the behaviour of the connections overestimated the global strength (connection type "R"). The presence of shear reinforcement in flat slabs played an important role in the global behaviour of the frames under consideration. Frames with flat slabs without shear reinforcement had lower strength compared to frames in which the slabs were reinforced with shear studs. However, the behaviour was found to be largely depended on the columns. In all cases, the ability of the column base sections to resist and to deform governed the behaviour of the frames under large horizontal displacements. As a result, a further increase of the ultimate drift ratio (for example, by increasing the amount and extent of shear reinforcement) would not lead to a substantially better seismic behaviour of the considered frames, although it would contribute in the limitation of local damage for strong earthquakes. Nonetheless, introduction of shear reinforcement in the slabs contributed in avoiding punching failures at the early stages of horizontal loading (i.e., prior to reaching the maximum global base shear force). Such failures are associated with considerable and potentially unrepairable damage to the structure and should therefore be avoided.

## 6.4 Seismic fragility analysis

### 6.4.1 Introduction

Fragility functions describe the probability of exceedance of a Damage State (DS)[1] as a function of a seismic Intensity Measure (IM). The IM reflects the severity of the ground motion and it can be expressed in many forms, including in terms of peak ground acceleration, spectral acceleration, spectral velocity and displacement, drift ratio, roof displacement, etc.

To better understand the concept of seismic fragility functions, a comparison is given in Figure 6.23 with the information obtained from a typical structural verification resulting from the comparison of the action effects with the corresponding resistances. Assuming the material properties, loading and geometrical properties are well defined and known, a value $IM_0$ of the IM for which the DS is exceeded can be found. Figure 6.23 describes the case of mean values of variables. As a result, the vertical line representing the structural verification is expected to intersect the fragility curve at a probability value of 0.5. A single structural verification does not provide any information about the probability of the DS being exceeded for a slightly lower or higher value of the IM.

In reality, structures are subjected to numerous uncertainties. Slight changes in the

[1] In design, it is common to refer to Limit States (LS) instead of Damage States. The term "Damage State" is used herein, because it is more common in seismic fragility analysis. However, the DS can be a code specified LS.

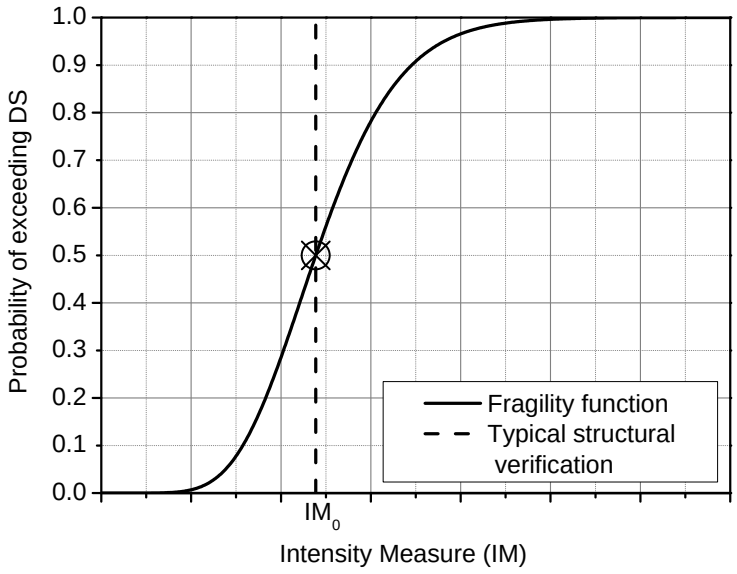


Figure 6.23: A fragility function and a typical structural verification

IM do not normally lead to drastic changes in the response. Fragility functions incorporate the uncertainties explicitly and provide continuous information over a wide range of IM values. As a result, the information obtained from the fragility functions is more representative of the real state of the structure. Especially in earthquake loading conditions, it is important to have such a type of information because it can substantially influence decision making in design and risk mitigation policies.

Fragility functions are convenient especially for the following purposes:

- *Seismic assessment of existing structures*. In seismic assessment, it is important to have realistic estimates of the structural response under the expected earthquake loading conditions.

- *Loss assessment*. Damage States are directly related to losses after a seismic event. Fragility functions provide a tool to quantify the expected damage and losses as a function of the seismic intensity measure. This information is useful for insurance purposes, decision making after structural assessment and emergency preparedness policies.

- *Performance Based Seismic Design* (PBSD). Fragility functions are suitable for PBSD, because they provide continuous information over a wide range of earthquake loading conditions, for various performance levels.

- *Vulnerability assessment and risk mitigation*. Fragility functions corresponding to typical structures or structural components can be used for rapid assessment of large areas (for example, entire cities). This turns them useful for the stated purposes.

There is no general consensus regarding the methodology of derivation of fragility functions and several methods can be found in the literature. A summary of the available methods is given in Porter et al. 2007, according to which there are six main groups of methods, based on six methods of obtaining knowledge on the IM. The method used in this dissertation falls under the category of "derived fragility curves", where the fragility functions are derived through numerical analyses. Other ways of obtaining the earthquake demand parameters (or IM) include laboratory testing of specimens for this specific purpose, post-earthquake observations, expert opinion and updating of existing fragility functions (Porter et al. 2007; Bradley 2010). All analytical methods have in common the fact that some variability of the structural capacity and the seismic demand is fundamental in the derivation of the fragility functions.

### 6.4.2 Literature review

Fragility analyses specific for flat slab buildings are scarce in literature. The fragility analysis of a 5 storey flat slab building was presented by Erberik and Elnashai 2003; Erberik and Elnashai 2004. The building was regular, with 6.0 m spans in both directions, storey height of 2.8 m and column dimensions of $400 \times 400$ mm$^2$. The authors used simplified two-dimensional models for their nonlinear static analyses and dynamic time history analyses. It is important to mention that the authors designed the slab such that punching failures and progressive collapse would be avoided (they assumed there were embedded beams with sufficient shear reinforcement). Also, the authors took into consideration the contribution of the masonry infill walls to the lateral stiffness and resistance of the building. Erberik and Elnashai 2004 considered four damage limit states for the building: LS1 - none to slight damage, LS2 - slight to moderate damage, LS3 - moderate to extensive damage and LS4 - extensive to complete damage and presented fragility curves for these damage limit states.

In contrast to the aforementioned study, Hueste and Bai 2007a; Hueste and Bai 2007b included the possibility for a punching shear failure in their model of a five storey reinforced concrete building with flat slabs. They accomplished this by adding a drift limit for which punching is deemed to occur, based on the model proposed by Hueste and Wight 1999. The slabs were assumed to have no shear reinforcement. The lateral load resisting system of the building analysed by Hueste and Bai 2007b consisted of perimeter frames (i.e., the flat slabs were not considered as part of the main lateral load resisting system).

Studies on the fragility analysis focused on the slab–column connections rather than the entire building include Aslani and Miranda 2005; Gogus and Wallace 2015. These studies rely on experimental test results from literature to propose relationships between the probabilities associated with each damage limit state and the drift ratio and GSR. These types of studies are primarily focused on the PBSD aspect of the problem. Aslani

and Miranda 2005 defined the damage limit states as a function of observable damage on the specimens, namely a) LS1: light cracking; b) LS2: severe cracking; c) LS3: punching shear failure and d) LS4: loss of vertical carrying capacity. In their study, the authors proposed a fragility surface for LS3, which includes the influence of the gravity shear ratio in punching shear failure. Similarly, Gogus and Wallace 2015 proposed empirical fragility curves for a wide range of different types of slab–column connections, including slabs with shear reinforcement and post-tensioned slabs. The damage limit states were defined from the backbone curve and they were associated with two corresponding "repair limit states": minor repair (RS1) and major repair (RS2). The study proposed fragility surfaces, which represent the probability of damage versus both the inter-storey drift ratio and GSR.

No study was found in the literature dealing with the fragility analysis of bare flat slab frames containing specific punching shear reinforcement that is susceptible to failure. However, such an analysis would help in quantifying the benefits and limitations of punching shear reinforcement in the seismic design of flat slab buildings in the framework of PBSD.

### 6.4.3 Methodology

Figure 6.24 provides a flow-chart of the methodology used for the derivation of fragility functions in this chapter. The pushover analyses described in Section 6.3 constitute the first step. The structural model, including material characteristics and gravity loading, is the same as that described in Section 6.3. Frames 3-NoSr(C1) and 3-SSR(C1) are chosen for the seismic fragility analysis.

The frame models are subjected to a Multiple Stripes Analysis (MSA, Jalayer and Cornell 2009; Baker 2015). This type of analysis consists in multiple nonlinear dynamic time-history analyses for several Intensity Measure (IM) levels. MSA is similar to Incremental Dynamic Analysis (IDA, Vamvatsikos and Cornell 2002), but in contrast, different ground motion inputs can be used in MSA for different IM levels. First, uncertainties related to the ground motion variability are considered. A total of 360 analyses per frame are run, corresponding to three sets of thirty ground motion records each scaled in four levels (discussed in more detail in Section 6.4.4). The spectral acceleration at the fundamental period of vibration ($Sa(T_1)$) is chosen as IM.

Rayleigh damping with a damping ratio of 5% at the first two modes of vibration is modelled. Structural response is not sensitive to the adopted damping model when elements with distributed plasticity are used (Chopra and McKenna 2016), as in this dissertation.

Based on the pre-defined damage states (Section 6.4.5), a lognormal cumulative distribution function in the form given in Equation 6.5 is fitted to the results obtained from the analysis (Figure 6.24) by means of the "maximum likelihood" approach, as it was shown

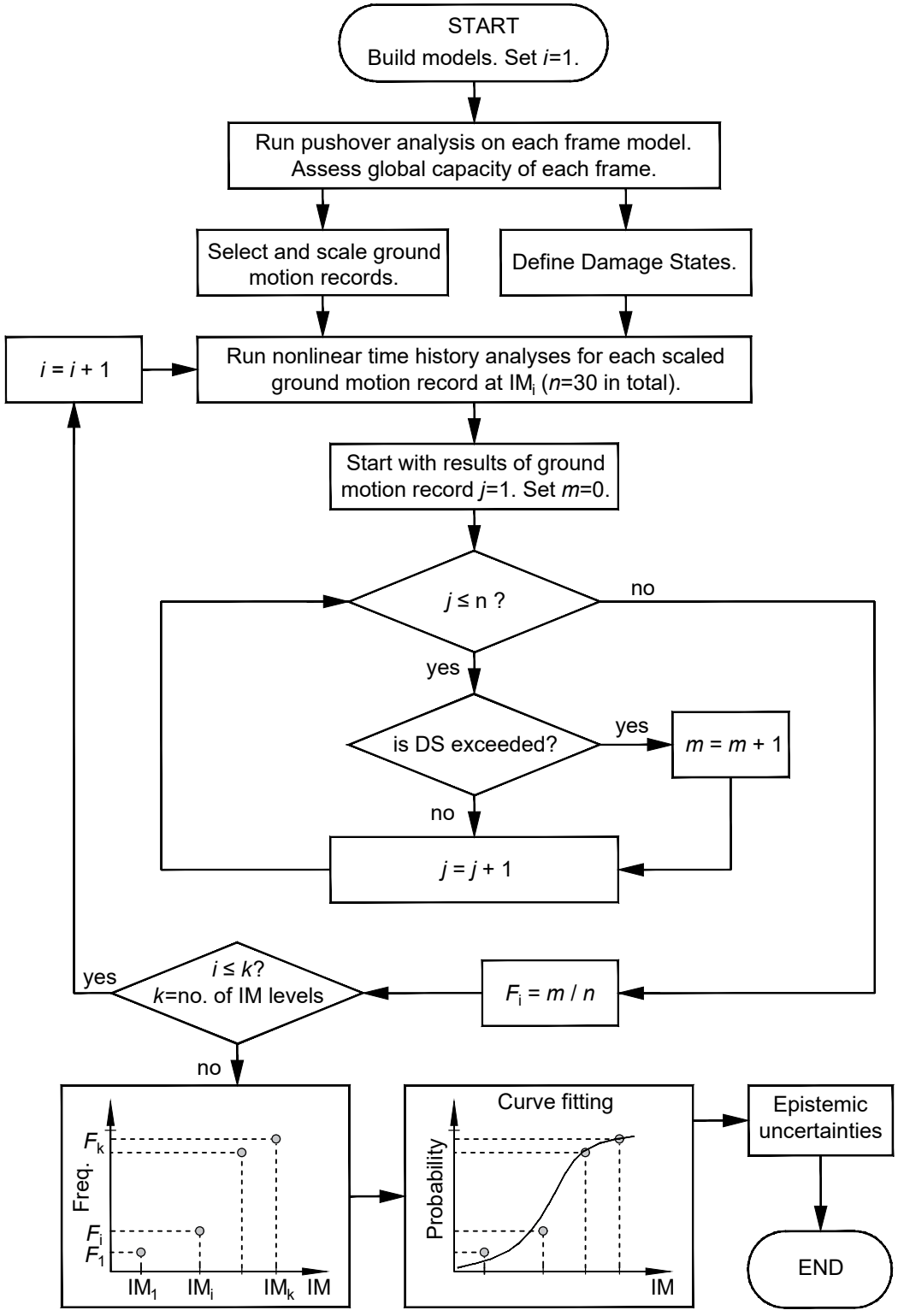


Figure 6.24: Flow-chart of the methodology used for the derivation of fragility functions

in Baker 2015 to be an appropriate method of fitting data from MSA. The procedure is further described by example in Section 6.4.6.

$$P(DS \mid Sa(T_1) = x) = \Phi\left(\frac{\ln(x/\theta)}{\beta}\right) \tag{6.5}$$

In Equation 6.5, the left-hand side represents the probability of reaching the damage state DS given the spectral acceleration $x$. This probability is shown in the right-hand side of the equation, where $\Phi$ is the standard Normal cumulative distribution function, $\theta$ is the median of the fragility function and $\beta$ is the dispersion (logarithmic standard deviation) of the spectral acceleration.

After obtaining the fragility functions under record-to-record variability of ground motion, an analysis and discussion on the epistemic uncertainties is provided in Section 6.4.5.3.

### 6.4.4 Ground motion selection and scaling

Selecting and scaling ground motion records for nonlinear dynamic analysis is an important task as it can impact the results of the analysis (Vamvatsikos and Cornell 2002). Direct scaling of ground motion records should be done with caution. To minimize the scaling factors applied to the accelerograms, therefore maintaining the accelerograms realistic, the following approach is followed in this dissertation.

Three sets containing 30 unscaled records each are chosen from the PEER NGA-West2 database (*PEER NGA-West2 Ground Motion Database*; Ancheta et al. 2013) based on their similarity (by means of mean squared errors) to three EC8 (CEN 2004d) target spectra. The chosen target spectra correspond to Ground Type C, Type 1 spectrum and reference ground accelerations $a_{gR}$ equal to 0.10g, 0.20g and 0.30g for Set I, II and III respectively. The unscaled ground motions in the PEER NGA database were chosen from all fault types, with magnitudes from 6.5 to 8.5, velocity $v_{s30}$ from 180 m/s to 360 m/s as recommended in EC8 for Ground Type C and distance from rupture surface limited from 10 to 80 km. The unscaled records and the target spectra for each set are shown in Figure 6.25 for the horizontal component and 5% damping. Basic information for each record is provided in Appendix C.

The mean squared errors of the chosen records in relation to the target spectrum were less than 0.15 $g^2$ for Set I, less than 0.28 $g^2$ for Set II and less than 0.57 $g^2$ for Set III. The larger error in Set III is due to the scarcity of records that closely match the corresponding target spectrum. For the same reason, some records belong to both Set II and Set III.

The ground motion records were scaled to spectral acceleration values for the fundamental period of vibrations of the structure $Sa(T_1)$. The fundamental period of vibrations $T_1$ that resulted after the application of the gravity load was used as a reference for scaling. The fundamental periods of the two frames were approximately the same. Eigenvalue

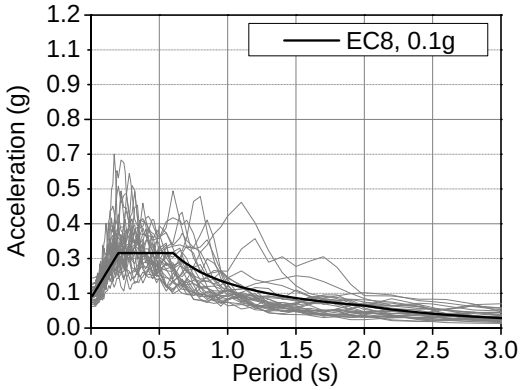


(a) Set I, $a_{gR} = 0.10g$

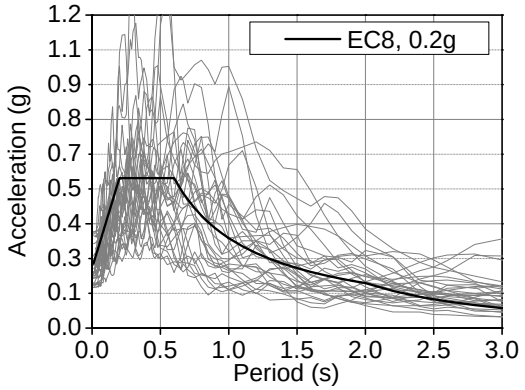


(b) Set II, $a_{gR} = 0.20g$

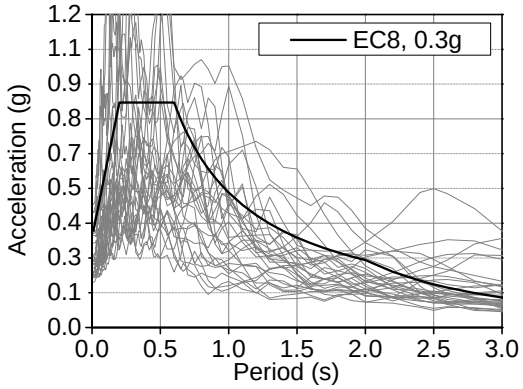


(c) Set III, $a_{gR} = 0.30g$

Figure 6.25: Five percent damped spectra for one horizontal component for the three sets of ground motion records

analysis resulted in $T_{1,el} = 0.52$ seconds for linear elastic analysis and $T_1 = 0.95$ seconds for eigenvalue analysis performed after the nonlinear analysis for the application of gravity loads.

The scaling scheme included direct scaling of the accelerograms of Set I to $Sa(T_1)$ values from 0.1g to 0.4g with steps of 0.1g. The Set II records were scaled to $Sa(T_1)$ values from 0.5g to 0.8g with steps of 0.1g, whereas the records of Set III were scaled to spectral accelerations from 0.9g to 1.2g, again with steps of 0.1g. The scaling scheme is demonstrated in Figure 6.26 for the smallest and largest scale factor in each set of ground motion records.

### 6.4.5 Definition of damage states

#### 6.4.5.1 Overview

Two types of damage states are defined. First, global damage states commonly adopted in seismic fragility analyses are described. Afterwards, three damage states that correspond

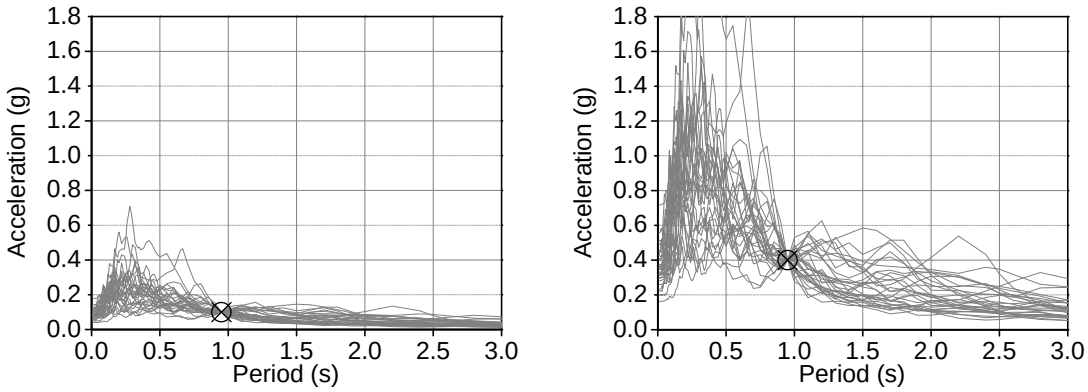


(a) Set I, $Sa(T_1) = 0.10g$

(b) Set I, $Sa(T_1) = 0.40g$

(c) Set II, $Sa(T_1) = 0.50g$

(d) Set II, $Sa(T_1) = 0.80g$

(e) Set III, $Sa(T_1) = 0.90g$

(f) Set III, $Sa(T_1) = 1.20g$

Figure 6.26: Scaled spectra at different spectral acceleration values (minimum and maximum scaling for each set)

specifically to the distribution of damage in the flat slabs are defined. The occurrence of a punching failure is a major, potentially unrepairable, event. The flat slab specific damage states are introduced to facilitate the interpretation of results from a performance-based perspective.

#### 6.4.5.2 Global damage states

In the current version of EC8 (CEN 2004d), two performance levels are defined for the design of new buildings: no-collapse and damage limitation.

The no-collapse requirement is fulfilled if the structure withstands the design seismic action without local or global failures. In the design of conventional buildings with moment resisting frames, local failures are not a concern when capacity design rules are followed. In case of the buildings with flat slabs, however, punching failures can occur, thus violating the no-collapse requirement. To account for this scenario, the following global damage states (DS) are proposed for the analysis of the flat slab frames under consideration:

- NCS (no-collapse state). This DS corresponds to the fulfilment of the no-collapse requirement as defined in EC8 (CEN 2004d). For the purposes of this study, it is reached when the maximum base shear of the frame is reached or when a punching failure occurs anywhere in the frame. For convenience, it is assumed that the maximum base shear is reached when the roof displacement exceeds the corresponding displacement from Figure 6.14 (namely, 156.7 mm for 3-NoSr(C1) and 186.1 mm for frame 3-SSR(C1));

- DLS (damage limitation state). This DS corresponds to the damage limitation requirement of EC8 (CEN 2004d). It is assumed that the building has ductile non-structural elements that do not interact significantly with the main structure. The criterion for DLS is set in terms of inter-story drift ratios. A limiting value of 0.75% is considered for the drift ratio, in accordance with EC8 (CEN 2004d) for the described type of non-structural elements.

#### 6.4.5.3 Flat slab specific damage states

The damage states described in this section correspond to various extends of punching failures throughout the structure. Three flat slab specific damage states are considered:

- FSDS1: damage state is reached when at least one punching failure occurs in the structure, regardless of whether any global damage state is reached. This is not to be confused with NCS described earlier, because FDS1 can be reached with NCS or after it;

- FSDS2: damage state is reached when punching failures are spread in more than one storey (i.e. when at least 5 slab–column connections have failed, considering the fact that there are 4 slab–column connections in each storey of the frames under consideration);
- FSDS3: damage state is reached when at least one roof level slab–column connection fails in punching.

Note that, by definition, a flat slab specific damage state may be reached regardless of whether a global damage state or another flat slab specific damage state is reached. This means that reaching one flat slab damage state does not mean that the previous damage state is reached. The flat slab specific damage states were intentionally defined independent from the global states so that the influence of punching failures in the global structural behaviour and damage can be observed in probabilistic terms.

### 6.4.6 Seismic fragility functions

#### 6.4.6.1 No-collapse

Figure 6.27 shows the maximum roof displacements during the MSA performed on each frame model. To obtain smooth fragility curves, the Set I of ground motion records was scaled into additional levels of 0.010g, 0.025g, 0.050g, 0.075g, 0.125g and 0.150g for frame 3-NoSr(C1), because it was found that failures occur for considerably low spectral accelerations for this frame. Especially for high spectral acceleration values, some of the time history analyses were interrupted before the end of the time history. It was found that this always occurred after local or global failures that caused dynamic instability. Due to the definition of the damage states considered herein (see Section 6.4.5), these analyses are valid. A different marker is used for these analyses to clarify the fact that although they cross the threshold for the NCS, the roof displacement value is not valid. These analysis results are stacked around roof displacement 400 mm and some random scatter is added to get a sense of the quantity of analyses.

In Figure 6.27, the threshold roof displacement for the NCS is shown with a vertical dashed line for each frame model. Counting the analyses that exceed the threshold and adding the ones in which localized punching failures occurred, the total number of analyses that exceed NCS is determined for each spectral acceleration value. Knowing the total number of analyses for each IM (spectral acceleration), the percentage of analyses that exceed NCS is calculated. In Figure 6.28, these calculated values are represented by markers. The fragility functions are obtained by fitting lognormal distribution functions to these markers, as described in Section 6.4.3.

Figure 6.28 demonstrates that the performance of the two frames is very different. It is almost impossible to fulfil the no-collapse requirement in frame 3-NoSr(C1) for spectral acceleration values higher than 0.2g. On the other hand, the no-collapse requirement

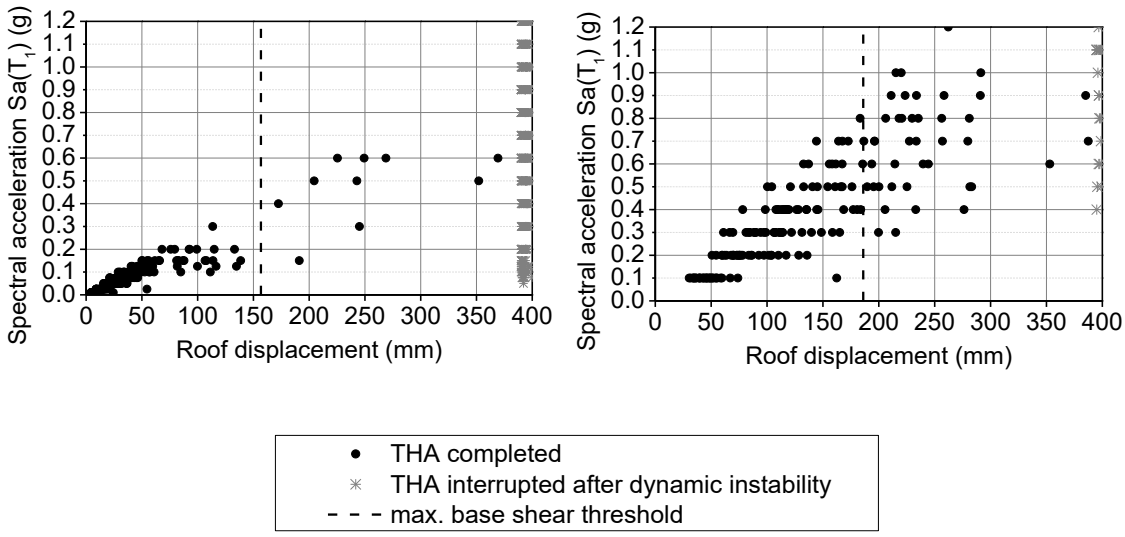


Figure 6.27: Results of the MSA: maximum roof displacements for each spectral acceleration level at frame a) 3-NoSr(C1) and b) 3-SSR(C1)

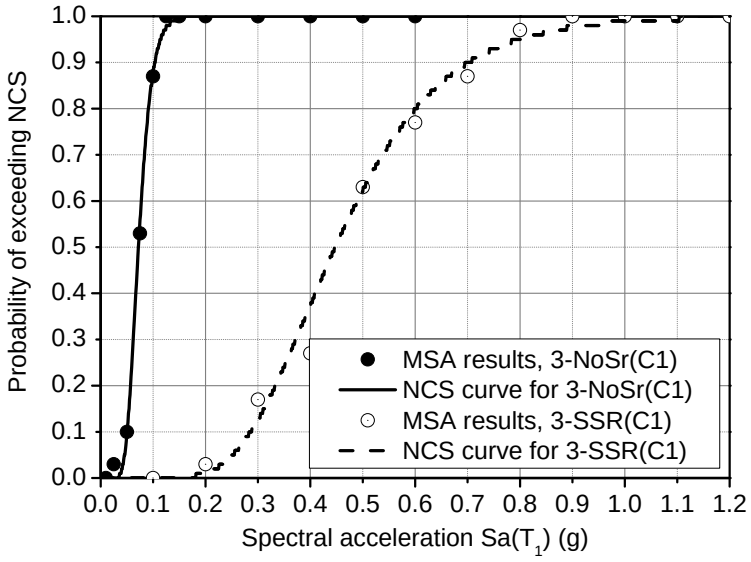


Figure 6.28: Fragility functions for NCS

is easily fulfilled in frame 3-SSR(C1) for similar spectral acceleration values. The ability of the frame 3-NoSr(C1) to resist seismic actions without local or global failures is very limited. A major improvement of the performance was achieved by adding shear reinforcement around the columns in the flat slabs.

The mean value of the lognormal fragility function corresponding to the NCS curve for 3-SSR(C1) is 0.45g (Table 6.3). For the target spectrum shape considered (see Section 6.4.4), this spectral acceleration value at period $T_1$ corresponds to a reference ground acceleration of 0.25g. This value is only slightly lower than the value determined using

the pushover analysis method described in EC8 (CEN 2004d, as described in Figure 6.22). This indicates that when sufficient drift capacity is provided for the slab–column connections (for example, through sufficient punching shear reinforcement), the rather convenient pushover analysis method can be used to estimate the performance of the structure.

On the other hand, the mean value of the lognormal curve corresponding to 3-NoSr(C1) is very far from the prediction of Figure 6.22. The reason for this is that the occurrence of local failures is not clearly visible in the pushover analysis. The base shear in the frame continued to increase even after punching failures (Figure 6.14a), because the columns had sufficient strength and deformation capacity. Since punching failures are major events for a structure (potentially leading to progressive collapse), they should be carefully considered in the structural model and in the post-processing of the results.

Using the maximum likelihood method was especially important for the fragility functions corresponding to frame 3-NoSr(C1), in which dynamic instabilities occurred for considerably low accelerations. The maximum likelihood method is appropriate for fitting such types of data (Baker 2015).

#### 6.4.6.2 Damage limitation

DLS is deemed to be reached when the limiting drift ratio is reached. The technique followed to derive the fragility functions for DLS was similar to that adopted for NCS, but the threshold here was the limiting drift ratio. For the two frame models, the corresponding fragility functions are plotted in Figure 6.29.

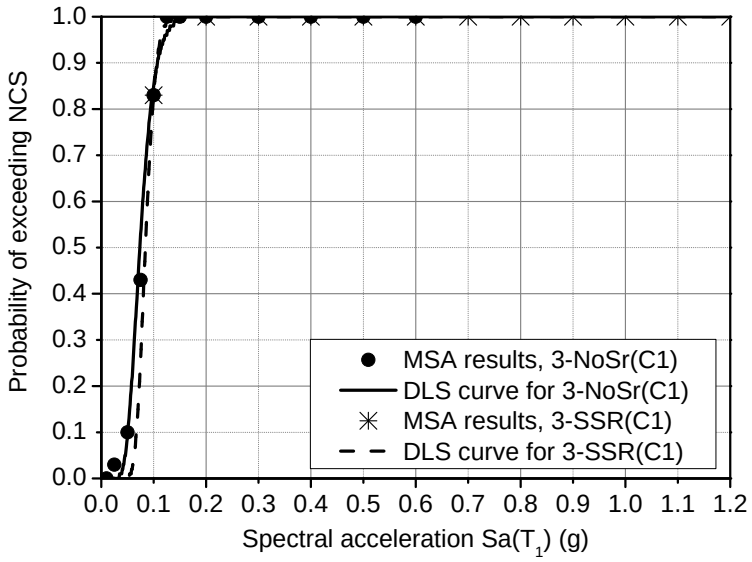


Figure 6.29: Fragility functions for DLS

It is noticed that the fragility curves corresponding to DLS are basically the same for both frame models. The minor differences in the figure are not of significant importance,

because they are caused by the additional scaling levels of spectral accelerations that were used in frame 3-NoSr(C1).

Although it was shown that the performance of the two frames was very different for the ultimate limit state (NCS in Section 6.4.6.1), Figure 6.29 proves that there is no difference towards the fulfilment of the damage limitation requirement of EC8 (CEN 2004d). In general, this holds true as long as the ultimate drift capacity of the slab–column connections is higher than the limiting drift of the damage limitation state. As it was discussed in Chapter 4, the ultimate drift of the specimen C-Ref (without shear reinforcement) was 1.00%, which is higher than the considered limiting drift of 0.75%. It should be noted here that the ultimate drift of the flat slabs in model 3-NoSr(C1) is lower than the experimental value of 1.00%, due to the stiffer columns compared to the laboratory.

#### 6.4.6.3 Damage state of the flat slabs

The occurrence of a punching shear failure in a building, whether with or without shear-reinforced flat slabs, is associated with damage that is very difficult and costly to repair and with the risk of progressive punching failures to the adjacent slab–column connections (Ruiz et al. 2013). To the author's knowledge up to date, there is a limited number of tests on repaired slab–column connections (see Section 4.9.1). Under these circumstances, the design of new flat slab structures or the design of retrofitting strategies in existing ones should be focused on reliably avoiding the occurrence of punching shear failures.

The fragility functions corresponding to the global damage states are plotted in Figure 6.30 along with the flat slab specific damage states. The lognormal parameters describing each fragility function are summarized in Table 6.3.

Table 6.3: Lognormal parameters of the fragility functions

| Damage state | 3-NoSr(C1) | | 3-SSR(C1) | |
|---|---|---|---|---|
| | $\theta$ | $\beta$ | $\theta$ | $\beta$ |
| DLS | 0.07 | 0.34 | 0.08 | 0.18 |
| NCS | 0.07 | 0.34 | 0.45 | 0.35 |
| FSDS1 | 0.07 | 0.34 | 0.69 | 0.45 |
| FSDS2 | 0.09 | 0.37 | 1.60 | 0.63 |
| FSDS3 | 0.11 | 0.43 | – | – |

Figure 6.30 shows that punching failures in the first storey are followed by progressive punching failures when the accelerations are increased (compare FSDS1 with FSDS2). In accordance with the observation made using the pushover analysis (Section 6.3), roof level slab–column connections failed last. Interestingly, no punching failure was detected in

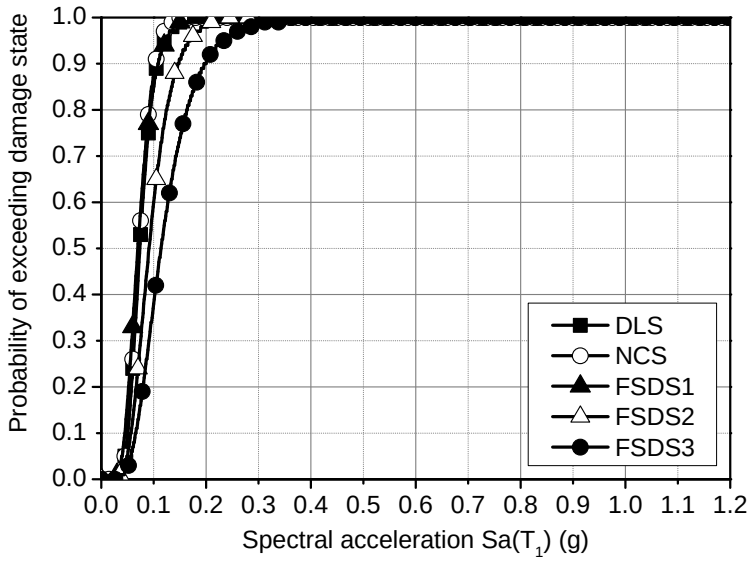


(a) 3-NoSr(C1)

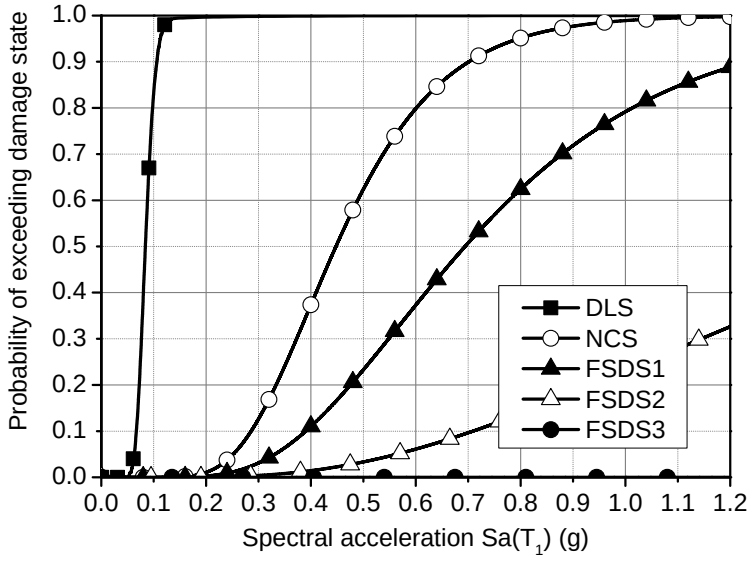


(b) 3-SSR(C1)

Figure 6.30: Fragility functions for all damage states

the roof level connections for frame 3-SSR(C1), even for very high spectral accelerations.

FSDS1 is reached with NCS in frame 3-NoSr(C1), whereas it is reached after the NCS in frame 3-SSR(C1). This demonstrates that the limiting factor in the frame without shear reinforcement was punching shear in slab–column connections. On the contrary, in the frame with studs, punching failures occurred after the structure had reached its maximum resistance.

In EC8 (CEN 2004d), damage limitation should be ensured for frequent earthquakes (with a shorter return period compared to the design earthquake, and normally, with a

lower ground acceleration). In Figure 6.30a and Table 6.3 it is noticed that the curves for NCS and DLS perfectly match for the frame 3-NoSr(C1). This means that the frame is not properly designed from a performance-based point of view. The earthquakes that cause exceedance of the DLS also cause exceedance of NCS. In frame 3-SSR(C1), on the other hand, the two performance levels are distinct. This major improvement of the seismic performance was achieved by just introducing shear reinforcement in the flat slabs.

### 6.4.7 Epistemic uncertainties

#### 6.4.7.1 Description of the uncertainty models

Besides the record-to-record variability of the ground motion, other sources of uncertainty can be considered when deriving fragility functions. Such uncertainties are, for example, related to the variability of material characteristics, gravity loading, geometry (dimensions, detailing, errors in construction, etc.) and the model itself. These are the result of limited knowledge and are commonly named "epistemic uncertainties", in contrast to the uncertainties related to the ground motion variability, which are commonly named "aleatory" (Bradley 2010).

In this section, the epistemic uncertainties related to the determination of the ultimate drift ratio of slab–column connections are addressed. The format of a typical fragility analysis is adopted for convenience in the presentation of the results. Nevertheless, the assigned distribution functions to the random variables considered herein do not necessarily correspond to real cases. Therefore, this section can be regarded as a parametric study, aiming to analyse the effect of uncertainties in slab–column connections to the global response of the frames under consideration.

In line with the modelling technique for the slab–column connections (Section 6.2.1), two cases are distinguished:

- force-induced punching (corresponding to specimen C-Ref);
- drift-induced punching (corresponding to specimen C-SSR5b).

For force-induced punching, current design codes such as EC2 (CEN 2004c), ACI 318 (ACI 2014), MC2010 (*fib* 2013) provide equations that can be reduced in the following form:

$$M_{unb,R} = \lambda(V_0 - V_g) \tag{6.6}$$

where $M_{unb,R}$ is the resisting unbalanced moment, $V_0$ is the punching shear resistance for concentric loading, $V_g$ is the applied gravity load and $\lambda$ is a coefficient taking into account the cross section of the column and the geometry of the control perimeter. Equation 6.6 was derived looking specifically at the EC2 (CEN 2004c) formulation. Combining

Equation 2.4 with Equation 2.5:

$$\left(1 + k\frac{M_{Ed}}{V_{Ed}}\frac{u_1}{W_1}\right)\frac{V_{Ed}}{u_1 d} = v_{Ed} \tag{6.7}$$

In limit, the acting shear stress $v_{Ed}$ is equal to the punching shear resistance. Multiplying both sides with $u_1 d$:

$$\left(1 + k\frac{M_{Ed}}{V_{Ed}}\frac{u_1}{W_1}\right)V_{Ed} = V_0 \tag{6.8}$$

Rearranging Equation 6.8, the factor $\lambda$ to be used in Equation 6.6 is obtained:

$$\lambda = \frac{W_1}{k u_1} \tag{6.9}$$

For the other design codes, the formulation is similar in principle. From Equation 6.9, it is noticed that $\lambda$ can be considered as a coefficient that takes into account the cross section of the column and the geometry of the control perimeter.

The resistance $V_0$ depends on several factors, among which the concrete strength is one of the most influential and variable in practice. To keep the problem simple, concrete strength in flat slabs is assumed to be the only variable in frame 3-NoSr(C1). The resistance $V_0$ is calculated based on EC2 (CEN 2004c). Based on Equation 6.9, a value of $\lambda = 0.416$ is determined for specimen C-Ref (using units kN and m). To account for the simplification made regarding the applied gravity load (which was assumed to be equal to 215 kN for both frames), a value $\lambda = 0.364$ is assumed to be the controlling parameter in Equation 6.6 for frame 3-NoSr(C1).

Thirty pushover analyses are performed on the frame 3-NoSr(C1). In each of the analyses, the concrete strength took a random value using the Latin Hypercube sampling technique. It was assumed that the concrete strength followed a Normal distribution function, with mean value 60 MPa and standard deviation of 15 MPa (Figure 6.31). For each sample, the ultimate unbalanced moment used in the limit state model of the slab–column connections is calculated in accordance with Equation 6.6 and the resulting pushover curves are analysed in Section 6.4.7.2.

In Chapter 5, it was shown that the following equation fits reasonably well with the available experimental results on flat slab specimens with headed studs (Figure 5.6):

$$d_{r,u} = -11.3\left(\frac{V_g^2}{V_0 V_{flex}}\left(\frac{u_{out,ef}}{u_{out}}\right)\right) + 6.9 \quad (\%) \tag{6.10}$$

where $d_{r,u}$ is the ultimate drift ratio, $u_{out,ef}/u_{out}$ is a measure of the extent of shear reinforcement and $V_{flex}$ represents the flexural capacity of the slab specimen.

Again, the concrete strength of the flat slabs is considered as the only random variable in frame 3-SSR(C1). The same distribution function and sampling technique as in case of frame 3-NoSr(C1) is adopted (Figure 6.31). Thirty pushover analyses are performed. For each sample of the concrete strength, the corresponding ultimate drift is calculated

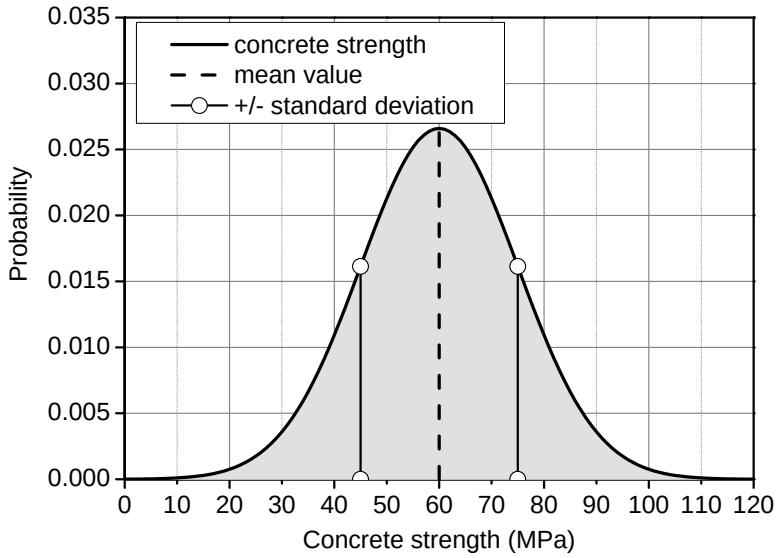


Figure 6.31: Probability density function of concrete strength

using Equation 6.10. The value is adapted to match with the experimental value. This adaptation is necessary for two reasons:

- the applied gravity load in the model is assumed equal to 215 kN, which is slightly different from the experimental value;
- there is some variability inherent to the experimental data from which Equation 6.10 was derived.

In other words, only the slope of the line represented by Equation 6.10 is assumed herein as the governing factor in the variation of the ultimate drift for varying values of concrete strength. The calculated ultimate drift is implemented in the limit state model of the slab–column connections of frame 3-SSR(C1).

The influence of concrete strength on the flexural capacity of the slab is small. Nevertheless, the value of the yielding unbalanced moment is updated in each analysis assuming a linear relationship with the resisting moment per unit width of the slab specimen.

In both models, the concrete of the columns is kept constant (deterministic) to facilitate comparison and to study the influence of the capacity variability of the slab–column connections.

#### 6.4.7.2 Analysis of results

The roof displacement–base shear curves from the pushover analyses performed with random input concrete strengths for the two frames are given in Figure 6.32. For clarity, the maximum base shear points for each curve are denoted with a marker.

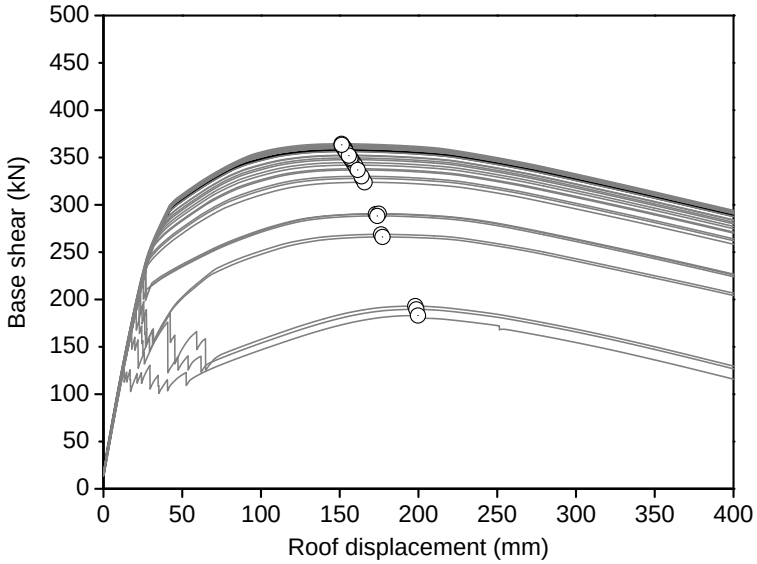


(a) 3-NoSr(C1)

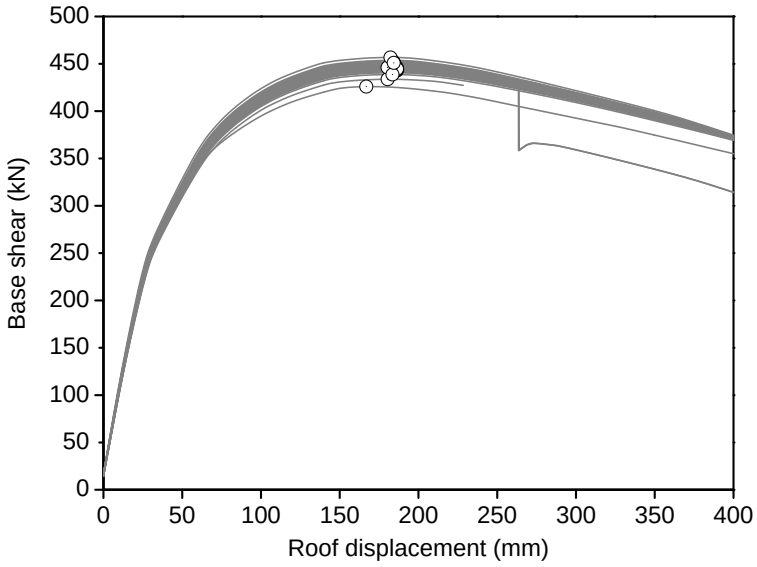


(b) 3-SSR(C1)

Figure 6.32: Pushover curves for random input concrete strengths

Comparing the results for the two frames, it is noticed that epistemic uncertainties play a larger role in the frame without shear reinforcement. The scatter of the displacements at maximum base shear is larger in frame 3-NoSr(C1). This is expected, because it was shown that punching failures play a decisive role in frame 3-NoSr(C1), and punching failures are strongly depended on the random variable: concrete strength.

Using the pushover curves of Figure 6.32, it is possible to assess the spectral acceleration that leads to the attainment of the maximum base shear force, by converting the

pushover curves into idealized elasto–perfectly plastic curves for an equivalent SDOF system in the ADRS format, as described earlier in Section 6.3.6. Note that, since punching failures occur after attaining the maximum base shear force in frame 3-SSR(C1), the spectral accelerations assessed as described can be fitted into a lognormal distribution function that represents the fragility function for the NCS, considering epistemic uncertainties alone (and deterministic ground motion characteristics). The resulting fragility curves are shown in Figure 6.33. Since punching failures occur before reaching the maximum base shear in frame 3-NoSr(C1), the fragility curve of Figure 6.33 for this frame does not correspond to NCS. Nevertheless, it is interesting to notice again that epistemic uncertainties have a higher influence on the frame 3-NoSr(C1) compared to 3-SSR(C1) in the attainment of the maximum base shear force. The dispersion of the fragility function corresponding to frame 3-NoSr(C1) is $\beta = 0.21$, whereas for the frame 3-SSR(C1), the dispersion is only $\beta = 0.03$ (see Equation 6.5).

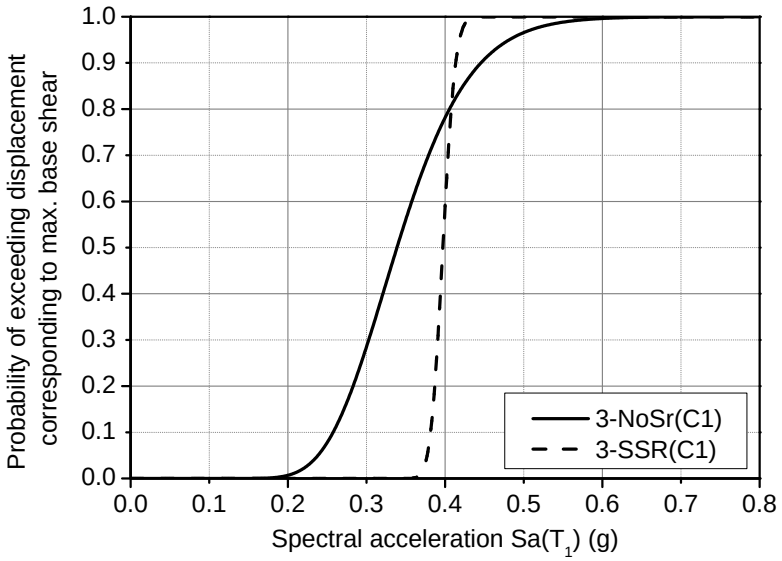


Figure 6.33: Fragility curves for exceedance of the displacement corresponding to the attainment of the maximum base shear force, considering epistemic uncertainties and deterministic ground motion characteristics

It is possible to combine the fragility functions from Figure 6.33 with those of Figure 6.28 to derive fragility functions that consider both aleatory and epistemic sources of uncertainty, using for example, a technique similar to the one described in Rota et al. 2010. However, it is of no practical interest for the purposes of this dissertation.

# Chapter 7

# Conclusions, recommendations and further research

This chapter contains a summary of the main conclusions derived from the experimental and numerical work presented in this dissertation. Based on these conclusions and other observations made throughout the dissertation, a list of recommendations for design is presented in Section 7.2. The chapter is concluded with possible future research directions starting from the work presented herein.

## 7.1 Conclusions

### 7.1.1 Experimental campaign

Horizontal cyclic loading tests of five reinforced concrete flat slab specimens were described in this dissertation. Four of the specimens were reinforced with shear studs and the other one served as a reference specimen. Shear reinforcement was provided in the form of headed shear studs, in cruciform layout and in two levels of extent: 3 rows and 5 rows. The gravity load was kept constant during the application of the reversed horizontal cyclic drifts. The following main conclusions are drawn from the experimental campaign:

- All shear-reinforced specimens attained high drift ratios before failure. A significant increase in the drift capacity of the specimens was observed due to the introduction of shear studs. No shear-reinforced specimen failed before 4.0% drift, which is a significantly high drift ratio for most common reinforced concrete applications. On the other hand, the very low drift capacity attained by the specimen without shear reinforcement (only 1.0%) is in line with experimental results from the literature;

- The reference specimen (C-Ref) failed in a punching failure mode. The specimen C-SSR5a which had the lowest absolute gravity load did not have a clear failure,

but rather a gradual loss of strength. The other three specimens, which had relatively high gravity loads in absolute terms and shear stud reinforcement, failed in a brittle punching failure mode outside the shear-reinforced zone, after reaching a horizontal plateau in the force-displacement relationship. Among the three specimens with high absolute gravity loads, one of them (C-SSR5c) had a higher GSR (approximately 0.10 higher than the other specimens). The increased GSR led to a failure for a lower drift compared to the similar specimen with lower GSR (more precisely, C-SSR5b);

- The energy dissipation characteristics measured via the equivalent damping coefficient were quite similar between the specimens with shear reinforcement, regardless of their differences. Repeated cyclic loading resulted in an increase of damage and stiffness deterioration, associated by a reduction of the equivalent damping coefficient. It was observed that the first cycle repetitions were the most detrimental. With increasing drifts, the difference between the equivalent damping coefficients calculated on consecutive cycles of the same drift level became smaller;

- It was shown that horizontal loading stiffness of flat slabs is rapidly decreased with the increase of horizontal displacements. The first drift cycles were the most detrimental ones. Afterwards, stiffness degradation was slower, following approximately a logarithmic law as a function of the dissipated energy.

One of the specimens was tested in a two-phase loading protocol to examine the post-earthquake behaviour of flat slabs that survive a major earthquake event without a punching shear failure. The specimen was reinforced with studs arranged in 5 rows around the column, with a layout similar to that of the other specimens. In the first phase, the specimen was loaded up to 3.0% horizontal drifts, after which the loading protocol was restarted and followed until failure. The main conclusions are summarized below:

- Although the specimen was loaded up to considerably high drift ratios in the first phase (3.0% drift), it was able to sustain further deformations in the second phase, while successfully carrying the imposed gravity loads. The ultimate drift capacity of the specimen was comparable with that of similar specimens tested under reversed horizontal cyclic loading in a single phase. This is a desirable feature for flat slabs that are secondary seismic elements, because carrying the gravity load while surviving the imposed deformations is of paramount importance;

- The second phase was characterized by a reduced loading stiffness and lower horizontal forces for the same drift, which can be regarded as a negative aspect of the post-earthquake behaviour for flat slabs that are primary seismic elements. In this case, both the deformation capacity and the stiffness are important in resisting

future earthquakes. It was shown, however, that significant stiffness degradation occurred only for strong returning earthquakes, and almost no additional degradation occurred for repeated drifts smaller than the yielding drift;

- Repeated horizontal loading caused significant degradation of the bending stiffness of the slab, resulting in a continuous increase of deflections throughout the entire test. It was shown that repeated horizontal loading causes irreversible deflections of the slab, which can become critical for the serviceability of the structure after a seismic event.

Comparing the experimental results with code provisions and analytical models proposed in the literature, the following conclusions are derived:

- The EC2 (CEN 2004c) calculations showed that, for gravity loading conditions, punching failure outside the shear-reinforced zone was the most critical failure mode. Indeed, all specimens with shear reinforcement failed outside the shear-reinforced zone. Furthermore, EC2 (CEN 2004c) requires a reduction of the perimeter in which shear stresses should be checked to determine the extent of shear reinforcement. As a result of the chosen geometry, all specimens had the same outer perimeter when calculated in accordance with EC2. However, there was an increase of the deformation capacity of the specimens with 5 rows compared to the specimen with 3 rows of studs. Therefore, the extension of shear reinforcement beyond the point where the EC2 outer perimeter is no longer increased is encouraged;

- CSCT (Muttoni 2008; *fib* 2013) predicted failure modes for concentric loading that matched with the experimental failure modes for horizontal loading. The same observation holds true when calculations are based on ACI 318 (ACI 2014);

- It was shown that the mechanical model proposed in Drakatos et al. 2018 describes reasonably well the response of the specimens presented in this dissertation. The yield line approach proposed by Brown and Dilger 2004 predicted reasonably well the maximum unbalanced moment of the specimens, but the results were not consistently on the conservative side.

Direct measurements throughout the tests demonstrated that the test setup worked as intended, with equal deflections and rotations at mid-spans. A nonlinear static finite element analysis confirmed that the test setup simulates well the behaviour of flat slabs under horizontal loading. For gravity loading, however, the test setup is somehow limited, because it simulates marginally non-axisymmetric conditions.

The following conclusions are derived comparing the results with previous experimental campaigns on similar specimens:

- Similar specimens, with comparable geometrical features and shear reinforcement were presented in Brown 2003. The main difference was the test setup, which modelled an isolated flat slab in Brown 2003 , in contrast to the test setup used herein, which modelled a continuous slab in the longitudinal direction. The specimens of Brown 2003 had higher longitudinal reinforcement ratio and a lower GSR. As a result, the yielding unbalanced moments were higher compared to those of the specimens presented in this dissertation. The initial stiffness in all specimens was comparable. The ultimate drift ratios from the two experimental campaigns are comparable;

- Several specimens have been tested in the past few years using the test setup that was used in the present experimental campaign. Comparing the results with similar specimens, it was shown that:

  – the tests performed using this test setup have a reasonable level of reproducibility and consistency. This was demonstrated by comparing the specimen C-Ref with a previously tested specimen without shear reinforcement, which behaved very similarly in terms of load–deformation response and failure;

  – the results indicate that studs are slightly more effective than stirrups in the enhancement of the deformation capacity for the presented conditions. However, the ultimate drift capacity was relatively high with both solutions.

### 7.1.2 Ultimate drift ratios in slab–column connections

A database of horizontal cyclic loading tests on specimens without shear reinforcement and with shear studs was compiled to study the drift capacity of flat slab–column connections subjected to seismic actions. Results from the literature and results from the described experimental campaign were studied collectively. The main conclusions are summarized below:

- For specimens without shear reinforcement, the Gravity Shear Ratio (GSR) describes reasonably well the ultimate drift capacity of flat slab–column connections, as observed by several researchers in the past. As a result of the high scatter of results, it was found that involving other variables is not advantageous for practical purposes;

- It was found that the observations on the shear-reinforced specimens presented in this dissertation can be better explained if the following variables are considered simultaneously: the applied gravity load, punching shear strength under concentric loading conditions, flexural strength and extent of shear reinforcement.

- A unitless factor incorporating the aforementioned variables was proposed. It was found that the factor describes reasonably well the ultimate drift ratios observed in the experimental campaign;

- Using the proposed factor on specimens found in the literature, it was shown that it reasonably describes the ultimate drift ratios of the available specimens.

### 7.1.3 Role of punching shear reinforcement in the global behaviour of flat slab frames

Taking advantage of the features of the test setup that allow the tested specimens to represent the entire span in the direction of horizontal loading, a numerical investigation was performed by calibrating numerical models of the specimens and replicating them to form entire flat slab frames. By calibrating the flat slabs based on specimens C-Ref and C-SSR5b, the frames represented two cases: flat slabs without shear reinforcement and with shear studs, respectively. The frames were tested under monotonically increasing horizontal displacements (pushover analysis) and a suite of ground motion records that led to the development of a set of fragility functions for various damage states. It was assumed that sufficient measures were taken to prevent the progressive collapse of the frames after the occurrence of a punching failure. The main conclusions are summarized below:

- The behaviour of the slab–column connections influences the global capacity of the frames. However, two cases should be distinguished:

  1. punching failures occur for low drifts (for example, the case of no punching shear reinforcement);
  2. punching failures occur for high drifts (for example, the case of slabs with punching shear reinforcement).

  In the first case, punching failures lead to a reduced base shear capacity of the frame. In the second case, however, the effect of punching failures can be more subtle, and the flat slabs can be no longer the governing factor in the global response of the frame;

- For the case of flat slabs with shear reinforcement, yielding of the slab–column connections was related to the attainment of the maximum base shear of the frame, the value of which was shown to be largely depended on the columns. Since punching failures occurred for very large drifts, their influence was not significant in the capacity of the frame. In these cases, it was shown that the capacity of the frames can be assessed reasonably well through a conventional pushover analysis;

- Punching shear reinforcement, if properly designed, can substantially improve the performance of the frames under seismic loading conditions;

- It was shown that the damage limitation requirement was violated for very low spectral accelerations in both cases (flat slabs with and without punching shear

reinforcement). This means that the damage in the non-structural elements might remain a limiting factor for the use of bare flat slab frames in seismic regions, even when sufficient shear reinforcement is provided;

- It was found that the frame with flat slabs without shear reinforcement is more susceptible to changes in the concrete strength than the frame equipped with studs in the flat slab. This means that the entire frame became more robust by adding punching shear reinforcement in the flat slabs.

## 7.2 Recommendations for design

Especially in the European practice and in seismic design situations, designers are faced with several uncertainties when dealing with buildings containing flat slabs. Lack of full coverage by the Eurocodes (more specifically, EC8 (CEN 2004d)), contributes to the uncertainty during the design process. The new generation of Eurocodes, which is currently under way, aims to include rules for the seismic design of flat slabs that are part of the primary earthquake resisting system (Bisch 2018). Based on the experimental and numerical work presented in this dissertation, a set of recommendations and tentative code provisions is listed in the following.

1. *Flat slabs without shear reinforcement should not be considered as primary seismic elements*. In the EC8 (CEN 2004d) terminology, primary seismic elements are those that take part in the earthquake resisting system of the building. In this dissertation, it was shown that flat slabs without shear reinforcement have a number of deficiencies, that render them inappropriate for seismic design situations. More specifically:

    - *Low deformation capacity*. The drift ratio at punching was only 1.0% for the specimen C-Ref presented in this dissertation. Analysing results from the literature (Section 5.2.2), it was shown that higher drifts can be achieved for lower GSR values (i.e., lower gravity loads in relation to the punching shear capacity under concentric loading). Although the trend is clear considering specimens tested under similar conditions (for example, those reported in Almeida et al. 2016), there is a considerable scatter of results from the literature. Furthermore, there is no sufficient experimental evidence of the trend for thicker slabs (most of the slabs available in the literature are relatively thin). Analytical considerations (Drakatos et al. 2018) and few experimental ones (Drakatos et al. 2016), on the other hand, indicate that there is a decrease of the drift capacity with the increase of thickness (in relative terms);
    - *Lack of robustness*. Robustness is important for a structure, not only in seismic

design. A structure should be able to resist extreme events without disproportional damage and collapse (CEN 2002). For example, a localized failure somewhere in the structure should not trigger global collapse. Flat slabs without shear reinforcement are prone to progressive collapse if a localized punching failure occurs in a slab–column connection. Several studies have been devoted to the post-punching behaviour of flat slab–column connections, leading to the development of provisions to avoid progressive collapse (Sections 2.4.5 and 4.9). However, it was shown in this dissertation that such flat slab buildings have a very low robustness, even when appropriate measures are taken to prevent progressive collapse (Section 6.4.7).

2. *Flat slabs with shear reinforcement can be considered as primary seismic elements only in low seismicity areas, base isolated buildings or when their suitability is proven by advanced nonlinear methods of analysis*. It was shown in this dissertation that, in accordance with previous research, the drift capacity of flat slab–column connections can be relatively high. However, the following issues should be addressed before considering the flat slabs as primary seismic elements:

   - *High flexibility*. The high flexibility of slab–column connections was pointed out in several occasions in this dissertation (specifically, Section 4.5 and Section 6.4.6). As a result, switching to shear walls, braces or moment resisting frames may come as a natural consequence of the Damage Limitation requirement (referring to the current version of EC8, CEN 2004d). In Chapter 6, it was shown that the flat slab frames under consideration failed to meet the damage limitation requirements for very low earthquake ground motion intensities, even though it was shown that the global behaviour under severe earthquake loading can be satisfactory in terms of safety against collapse;
   - *Necessity for increased complexity of the analysis methods*. Although there may exist building configurations (for example, a combination of primary flat slab frames with few shear walls) and seismicity levels for which the design can be shown to be satisfactory when considering the contribution of flat slab frames in the earthquake resistance, it is recommended herein to use more detailed analysis approaches before accepting the design. The stiffness reduction for linear analysis determined for the specimens presented in this dissertation (see Section 4.5) is considerably lower than that recommended by current major design codes. Furthermore, the role of potential punching failures needs to be included in the analysis. As a result, it is recommended herein to verify the design performed through linear methods of analysis with nonlinear analyses. These analyses are normally more time and resource consuming and they require a high level of expertise. The method proposed by Kang et al. 2009 (which was adopted in Chapter 6 with few modifications) in combination

with approaches for determining the yield unbalanced moment (for example, Drakatos et al. 2018) can be a suitable choice in these cases. However, the following issues need to be solved:

  - The model needs to be incorporated in commercial design software accessible to design engineers;
  - The model proposed by Drakatos et al. 2018 needs to be validated with more specimens that reach the yielding plateau before being used in the design practice to model the behaviour of nonlinear springs in the model of Kang et al. 2009. The model has been validated by a considerable number of tests on specimens that fail before reaching the yielding unbalanced moment (see also Section 4.11.1).

3. *It is recommended to use the Direct Displacement Based Design (DDBD, Priestley et al. 2007) approach to guide the design of buildings with flat slabs.* Currently, elements of DDBD are being considered for inclusion as an alternative design approach for structures in the new generation of the Eurocodes (Bisch 2018; Fardis 2018). Based on Section 5.4, it is recommended to use DDBD as a primary choice when designing buildings that contain flat slabs. Besides addressing the well acknowledged deficiencies of force-based design (Section 5.4.1), DDBD was shown to be suitable for making rational decisions in the design of buildings in which flat slabs are secondary seismic elements (Section 5.4.4). Since the punching failure mode is a brittle one that must not occur during the design earthquake, and since it has been shown to be a "drift-induced" phenomenon in many cases[1], designing for displacements is reasonable. The relationships between the ultimate drift ratio and other factors, developed in Chapter 5, are recommended to be used in the DDBD framework if appropriate safety factors are applied. These limiting drifts can guide the design if other performance criteria are not prevailing, or they can be used to verify that the drift capacity of the connections is sufficient under the design displacement corresponding to other performance criteria;

4. *It is recommended to use shear reinforcement in flat slabs in seismic regions.* The results from the experimental campaign showed that the drift capacity can be significantly enhanced in flat slabs with shear reinforcement compared to similar ones without shear reinforcement. Although adding shear reinforcement might increase the cost of the building, the following additional remarks should be considered:

    - The robustness of the structure is increased if shear reinforcement is used. This was demonstrated in Section 6.4.7, where it was shown that the variation of the ultimate drift capacity is small in frames with punching shear-reinforced slabs when there is a variation in the concrete strength over a relatively wide range

[1] the force-induced problem can be incorporated in the design, where relevant

of values. For this added benefit, it is recommended to use shear reinforcement even when it is not required by calculation;

- Simple products such as the one used in the experimental campaign (Section 3.3), or alternative products such as stirrups, do not significantly increase the cost of the building.

5. *For seismic loading conditions, it is recommended to allow the extension of the shear-reinforced zone beyond the current limitations imposed in EC2 (CEN 2004c).* The experimental campaign and the subsequent analysis showed that extending the shear-reinforced zone enhances the drift capacity of slab–column connections. Extending the shear-reinforced zone beyond the point where EC2 requires perimeter reduction is therefore encouraged for seismic design. Even though this might not lead to an increased strength, it can enhance the deformation capacity. With the available data, it was not possible to define an upper limit of the extent of shear reinforcement beyond which the drift capacity is no longer enhanced. As discussed in Section 2.4.4, the North American practice is to extend the shear-reinforced zone $3.5d$–$4.0d$ from the face of the column.

6. *For preliminary analysis, the most critical failure mode can be estimated based on concentric loading calculations.* In Section 4.10, it was shown that punching failure modes under horizontal loading (within the shear reinforcement or outside the shear-reinforced zone) were predicted reasonably well by concentric punching shear calculations based on EC2 (CEN 2004c), MC2010 (*fib* 2013) and ACI 318 (ACI 2014);

7. *For linear analysis, when conventional force-based methods are used, the cracked stiffness properties should be reduced below current code recommendations.* The analysis in Section 4.5, indicates that the stiffness to be used for linear analysis of flat slabs under horizontal actions should be reduced down to 12% to 17% of the elastic stiffness. This means that a very small portion of the cross section should be considered to contribute in the stiffness towards horizontal actions. The reduction depends on the magnitude of the gravity load.

## 7.3 Further research

Based on the work presented in this dissertation, further research is recommended in several directions:

1. *Experimental work.* Based on the available database of shear-reinforced flat slab–column connections (including the specimens presented herein), it is apparent that the specimens are generally thin. Cyclic loading tests on thicker specimens with shear reinforcement are recommended. Experimental work directly related to the specimens presented in this dissertation could be of interest considering:

- different longitudinal reinforcement ratios;
- a smaller quantity of shear reinforcement and larger extent of the shear-reinforced zone, in order to attempt failure inside the shear-reinforced zone.

Further experimental work of interest that requires a modification of the test setup includes:

- *Testing slabs with higher and lower values of the GSR*. With the current test setup and longitudinal reinforcement, testing for higher GSR is not possible because excessive yielding occurs in the longitudinal reinforcement before even starting the horizontal drift cycles. Lower values of GSR are not currently possible with the shear reinforcement used in this dissertation because they are expected to result in specimens that survive drift ratios larger than 6% (currently impossible due to limitations of the test setup, and with little practical interest);
- *Testing of wider specimens*. It is of interest to test similar, but wider specimens, to analyse various non-symmetric configurations. In most cases in practice, the flat slabs have some sort of non-symmetry due to loading, reinforcement distribution or different span lengths. Wider specimens would be required also in case of extending the shear-reinforced zone more than in the presented specimens.

2. *Reducing the current limitations of the proposed factor describing the ultimate drift ratios in flat slabs with shear reinforcement*. A series of limitations of the proposed factor, $\zeta$, were presented in Section 5.2.4. To reduce these limitations, more experimental and numerical work is recommended. The experimental work should consist in testing thicker slabs (as described in the previous item on this list) and slabs with a reduced amount of flexural reinforcement. To determine a lower limit of the ratio $u_{out,ef}/u_{out}$ beyond which the drift capacity is no longer enhanced, it is necessary to carry out experimental campaigns specifically designed for this purpose (for example, several series of identical specimens with varying extent of shear reinforcement). To include also the effect of the layout of shear reinforcement in the drift capacity, it is recommended to perform experimental campaigns with radial layouts;

3. *Finite element modelling of the experiments*. Detailed finite element modelling of the experiments presented in this dissertation would be of interest, because – if successful – it could lead to the solution of some of the issues listed in this section without extensive experimental work;

4. *Work related to Direct Displacement Based Design of flat slabs taking part in the primary earthquake resisting system*. In this dissertation, it was shown that DDBD is suitable for buildings containing flat slabs, subjected to earthquake loading. An example application was provided for the case of flat slabs taking part as secondary seismic

elements. Extending the application of DDBD to primary flat slabs, some further research would be necessary, especially:

- Relating the yielding drift to geometric properties known from the beginning of the design process (for example, span and depth). In Section 5.3, it was shown that the existing formulas developed for moment resisting frames might not be suitable for this purpose. On the other hand, it was observed that the variation of yielding drifts within the same experimental campaign (i.e. on specimens with similar geometry) is relatively small and such a relationship might be possible;
- Determining the relationship between displacement ductility and the equivalent viscous damping. Such relationships are already available for several structural typologies and materials. It is necessary to check whether any of the existing relationships is valid for flat slab frames or to develop new relationships based on nonlinear dynamic analyses.

# Bibliography


ACI (1999). *Joint ACI-ASCE Committee 421. ACI 421.1R-99 - Shear reinforcement for slabs*.

— (2010). *Joint ACI-ASCE Committee 421. ACI 421.2R-10 - Guide to seismic design of punching shear reinforcement in flat plates*.

— (2014). *Building code requirements for structural concrete (ACI 318-14) and commentary on building code requirements for structural concrete (ACI 318R-14)*. Farmington Hills, MI, USA.

Akiyama, H. and N. M. Hawkins (1984). *Response of flat plate concrete structures to seismic and wind forces (Report SM 84-1)*. Tech. rep. Seattle, Washington, USA: Department of Civil Engineering, University of Washington.

Ali, M. A. and S. D. B. Alexander (2002). *Behaviour of slab–column connections with partially debonded reinforcement under cyclic lateral loading, Structural Engineering Report No. 243*. Tech. rep. Edmonton, Alberta, Canada: University of Alberta, Department of Civil & Environmental Engineering.

Allen, F. and P. Darvall (1977). "Lateral load equivalent frame." In: *Journal Proceedings*. Vol. 74. 7, pp. 294–299.

Almeida, A. F. O., M. M. G. Inácio, V. J. G. Lúcio, and A. P. Ramos (2016). "Punching behaviour of RC flat slabs under reversed horizontal cyclic loading." In: *Engineering Structures* 117, pp. 204–219.

Almeida, A., R. Marreiros, A. P. Ramos, M. Ornelas, and B. Alcobia (2018). "Behaviour of RC flat slabs with stirrups under reversed horizontal cyclic loading." In: *Magazine of Concrete Research*. In press.

Ancheta, T. D., R. B. Darragh, J. P. Stewart, W. J. Silva, B. S. J. Chiou, K. E. Wooddell, R. W. Graves, A. R. Kottke, D. M. Boore, T. Kishida, and J. L. Donahue (2013). *PEER NGA-West2 Database. PEER Report 2013/03*. Tech. rep. Berkeley, California, USA: Pacific Earthquake Engineering Research Center PEER.

Aslani, H. and E. Miranda (2005). "Fragility assessment of slab-column connections in existing non-ductile reinforced concrete buildings." In: *Journal of Earthquake Engineering* 9.06, pp. 777–804.

Attia, F., H. Salem, and N. Yehia (2017). "Progressive collapse assessment of medium-rise reinforced concrete flat slab structures." In: *Structural Concrete* 18.3, pp. 409–420.

Baker, J. W. (2015). "Efficient analytical fragility function fitting using dynamic structural analysis." In: *Earthquake Spectra* 31.1, pp. 579–599.

Birkle, G. and R. B. Gayed (2006). "Discussion of "Alternative shear reinforcement of reinforced concrete flat slabs" by K. Pilakoutas and X. Li." In: *ASCE Journal of Structural Engineering* 132.1, pp. 167–168.

Bisch, P. (2018). "Eurocode 8. Evolution or Revolution?" In: *Recent Advances in Earthquake Engineering in Europe*. Ed. by K. Pitilakis. 16th European Conference on Earthquake Engineering-Thessaloniki 2018. Springer International Publishing. Chap. 27, pp. 639–660.

Bischoff, P. H. and S. H. Perry (1991). "Compressive behaviour of concrete at high strain rates." In: *Materials and Structures* 24.6, pp. 425–450.

Bradley, B. A. (2010). "Epistemic uncertainties in component fragility functions." In: *Earthquake Spectra* 26.1, pp. 41–62.

Braga, F., R. Gigliotti, and M. Laterza (2006). "Analytical stress–strain relationship for concrete confined by steel stirrups and/or FRP jackets." In: *ASCE Journal of Structural Engineering* 132.9, pp. 1402–1416.

Broms, C. E. (2007). "Flat plates in seismic areas: Comparison of shear reinforcement systems." In: *ACI Structural Journal* 104.6, pp. 712–721.

— (2009). "Design method for imposed rotations of interior slab–column connections." In: *ACI Structural Journal* 106.5, pp. 636–645.

— (2016). "Tangential strain theory for punching failure of flat slabs." In: *ACI Structural Journal* 113.1, pp. 95–104.

Brown, S. and W. Dilger (2004). "Design of slab-column connections to resist seismic loading." In: *Proc., 13th World Conference on Earthquake Engineering, Paper*. Vol. 2832, p. 13.

Brown, S. J. (2003). "Seismic response of slab column connections." Doctoral dissertation. Calgary, Alberta, Canada: University of Calgary.

Butcher, G, D Hopkins, R Jury, W Massey, G McKay, and G McVerry (1988). "The September 1985 Mexico earthquakes: final report of the New Zealand reconnaissance team." In: *Bulletin of the New Zealand National Society for Earthquake Engineering* 21.1, pp. 3–96.

Cao, H. (1993). "Seismic design of slab-column connections." Master's thesis. Calgary, Alberta, Canada: University of Calgary.

CEN (2000). *NP EN 933-1. Tests for geometrical properties of aggregates. Part 1: Determination of particle size distribution. Sieving method.*

— (2002). *EN 1990, Eurocode - Basis of structural design*.

— (2004a). *EN 10025-1: 2004. Hot rolled products of structural steels. General technical delivery conditions*.

— (2004b). *EN 10025-2: 2004. Hot rolled products of structural steels. Technical delivery conditions for non-alloy structural steels*.

— (2004c). *EN 1992-1-1. Eurocode 2: Design of concrete structures - Part 1-1: General rules and rules for buildings*.

— (2004d). *EN 1998-1. Eurocode 8: Design of structures for earthquake resistance - Part 1: General rules, seismic actions and rules for buildings*.

— (Feb. 2009a). *EN 12390-3. Testing hardened concrete - Part 3: Compressive strength of test specimens*.

— (Dec. 2009b). *EN 12390-6. Testing hardened concrete - Part 6: Tensile splitting strength of test specimens*.

— (Dec. 2013). *EN 12390-13. Testing hardened concrete - Part 13: Determination of secant modulus of elasticity in compression*.

Cheng, M.-Y., G. J. Parra-Montesinos, and C. K. Shield (2010). "Shear strength and drift capacity of fiber-reinforced concrete slab-column connections subjected to biaxial displacements." In: *ASCE Journal of Structural Engineering* 136.9, pp. 1078–1088.

Choi, K.-K. and J.-C. Kim (2015). "Nonlinear model simulating load–deformation relationship of flat plate structures." In: *Engineering Structures* 85, pp. 26–35.

Chopra, A. K. and R. K. Goel (2001). "Direct displacement-based design: use of inelastic vs. elastic design spectra." In: *Earthquake Spectra* 17.1, pp. 47–64.

Chopra, A. K. and F. McKenna (2016). "Modeling viscous damping in nonlinear response history analysis of buildings for earthquake excitation." In: *Earthquake Engineering & Structural Dynamics* 45.2, pp. 193–211.

Computers and Structures. (2017). *SAP2000 V-19.2.1 (Trial version) - Integrated software for structural analysis and design*. URL: https://www.csiamerica.com/products/sap2000.

Corley, W. G. and N. M. Hawkins (1968). "Shearhead reinforcement for slabs." In: *ACI Journal Proceedings*. Vol. 65. 10, pp. 811–824.

Corley, W. G. and J. O. Jirsa (1970). "Equivalent frame analysis for slab design." In: *ACI Journal Proceedings* 67.11, pp. 875–884.

Corley, W. G., M. Sozen, and C. Siess (1961). *The equivalent frame analysis for reinforced concrete slabs*. Tech. rep. University of Illinois Engineering Experiment Station. College of Engineering. University of Illinois at Urbana-Champaign.

Coronelli, D. (2010). "Grid model for flat-slab structures." In: *ACI Structural Journal* 107.6, pp. 645–653.

CSA (2004). *CSA Standard, A23.3-04 Design of concrete structures*. Ontario, Canada.

Dam, T. X. and J. K. Wight (2016). "Flexurally–triggered punching shear failure of reinforced concrete slab–column connections reinforced with headed shear studs arranged in orthogonal and radial layouts." In: *Engineering Structures* 110, pp. 258–268.

Dam, T. X., J. K. Wight, and G. J. Parra-Montesinos (2017). "Behavior of monotonically loaded slab–column connections reinforced with shear studs." In: *ACI Structural Journal* 114.1, pp. 221–232.

Dilger, W., D. Dechka, and S. Brown (2005). "Slab–column connections under seismic actions." In: *ACI Special Publication* 232, pp. 127–146.

Dovich, L. M. and J. K. Wight (2005). "Effective slab width model for seismic analysis of flat slab frames." In: *ACI Structural Journal* 102.6, pp. 868–875.

Drakatos, I.-S., A. Muttoni, and K. Beyer (2016). "Internal slab-column connections under monotonic and cyclic imposed rotations." In: *Engineering Structures* 123, pp. 501–516.

— (2018). "Mechanical model for drift–induced punching of slab–column connections without transverse reinforcement." In: *ACI Structural Journal* 115.2, pp. 463–474.

Durrani, A., Y Du, and Y. Luo (1995). "Seismic resistance of nonductile slab-column connections in existing flat-slab buildings." In: *ACI Structural Journal* 92.4, pp. 479–487.

Dvorkin, E. N. and K.-J. Bathe (1984). "A continuum mechanics based four-node shell element for general non-linear analysis." In: *Engineering computations* 1.1, pp. 77–88.

Einpaul, J., M. F. Ruiz, and A. Muttoni (2015). "Influence of moment redistribution and compressive membrane action on punching strength of flat slabs." In: *Engineering Structures* 86, pp. 43–57.

Elwood, K. J. and J. P. Moehle (2003). *Shake table tests and analytical studies on the gravity load collapse of reinforced concrete frames. PEER 2003/01*. Tech. rep. Berkeley, California, USA: Pacific Earthquake Engineering Research Center, University of California Berkeley.

Elwood, K. J. (2004). "Modelling failures in existing reinforced concrete columns." In: *Canadian Journal of Civil Engineering* 31.5, pp. 846–859.

Emam, M., H Marzouk, and M. S. Hilal (1997). "Seismic response of slab-column connections constructed with high-strength concrete." In: *ACI Structural Journal* 94, pp. 197–205.

*fib* (2013). *fib Model Code for concrete structures 2010*. Wiley. DOI: 10.1002/9783433604090.

Eom, T.-S., J.-W. Song, J.-K. Song, G.-S. Kang, J.-K. Yoon, and S.-M. Kang (2017). "Punching-shear behavior of slabs with bar truss shear reinforcement on rectangular columns." In: *Engineering Structures* 134, pp. 390–399.

EOTA (2013). *European Technical Approval ETA-13/0151*. Tech. rep. Deutsches Institut für Bautechnik.

Erberik, M. A. and A. S. Elnashai (2003). *Seismic vulnerability of flat-slab structures – Technical Report, Mid-America Earthquake Center, DS-9 Project (Risk Assessment Modeling)*. Tech. rep. Urbana-Champaign, Illinois, USA: Civil and Environmental Engineering Department, University of Illinois.

— (2004). "Fragility analysis of flat-slab structures." In: *Engineering Structures* 26.7, pp. 937–948.

European Concrete Platform ASBL (2008). *Eurocode 2 Commentary*. Ed. by J.-P. Jacobs. European Concrete Platform ASBL.

Fajfar, P. (2000). "A nonlinear analysis method for performance-based seismic design." In: *Earthquake Spectra* 16.3, pp. 573–592.

Fardis, M. N. (2018). "From force- to displacement-based seismic design of concrete structures and beyond." In: *Recent Advances in Earthquake Engineering in Europe*. Ed.

by K. Pitilakis. 16th European Conference on Earthquake Engineering-Thessaloniki 2018. Springer International Publishing. Chap. 4, pp. 101–122.

Farhey, D. N., M. A. Adin, and D. Z. Yankelevsky (1993). "RC flat slab-column subassemblages under lateral loading." In: *ASCE Journal of Structural Engineering* 119.6, pp. 1903–1916.

— (1995). "Repaired RC flat-slab-column subassemblages under lateral loading." In: *ASCE Journal of Structural Engineering* 121.11, pp. 1710–1720.

Faria, D. M. V., V. J. G. Lúcio, and A. P. Ramos (2012). "Post-punching behaviour of flat slabs strengthened with a new technique using post-tensioning." In: *Engineering Structures* 40, pp. 383–397.

Ferreira, M. P., G. S. Melo, P. E. Regan, and R. L. Vollum (2014). "Punching of reinforced concrete flat slabs with double-headed shear reinforcement." In: *ACI Structural Journal* 111.2, pp. 363–374.

Fick, D. R., M. A. Sozen, and M. E. Kreger (2017). "Response of full-scale three-story flat-plate test structure to cycles of increasing lateral load." In: *ACI Structural Journal* 114.6, pp. 1507–1517.

Filippou, F. and S. Mazzoni. *Concrete01 Material – Zero tensile strength*. Online. Accessed: 2017-08-23. URL: http://opensees.berkeley.edu/wiki/index.php/Concrete01_Material_--_Zero_Tensile_Strength.

— *Concrete02 Material – Linear Tension Softening*. Online. Accessed: 2017-08-22. URL: http://opensees.berkeley.edu/wiki/index.php/Concrete02_Material_--_Linear_Tension_Softening.

— *Steel02 Material – Giuffré-Menegotto-Pinto Model with Isotropic Strain Hardening*. Online. Accessed: 2017-08-22. URL: http://opensees.berkeley.edu/wiki/index.php/Steel02_Material_--_Giuffr%C3%A9-Menegotto-Pinto_Model_with_Isotropic_Strain_Hardening.

Filippou, F. C., E. P. Popov, and V. V. Bertero (1983). *Effects of bond deterioration on hysteretic behavior of reinforced concrete joints. Report No. UCB/EERC-83/19*. Tech. rep. Berkeley, California, USA: Earthquake Engineering Research Center. College of Engineering, University of California, Berkeley.

Fu, H., M. Erki, and M Seckin (1991). "Review of effects of loading rate on reinforced concrete." In: *ASCE Journal of Structural Engineering* 117.12, pp. 3660–3679.

Galvis, F., E. Miranda, P. Heresi, H. Dávalos, and J. R. Silos (2017). *Preliminary statistics of collapsed buildings in Mexico City in the September 19, 2017 Puebla-Morelos earthquake*. Online. Accessed: 2017-10-20. URL: http://www.learningfromearthquakes.org/2017-09-19-puebla-mexico/resource/65-preliminary-statistics-of-collapsed-buildings-in-mexico-city-in-the-september-19-2017-puebla-morelos-earthquake.

Genikomsou, A. S. and M. A. Polak (2015). "Finite element analysis of punching shear of concrete slabs using damaged plasticity model in ABAQUS." In: *Engineering Structures* 98, pp. 38–48.

Ghali, A. and S. A. Youakim (2005). "Headed studs in concrete: state of the art." In: *ACI Structural Journal* 102.5, pp. 657–667.

Ghali, A., M. Z. Elmarsri, and W. Dilger (1976). "Punching of flat plates under static and dynamic horizontal forces." In: *Journal Proceedings*. Vol. 73. 10, pp. 566–572.

Gogus, A. and J. W. Wallace (2015). "Fragility assessment of slab-column connections." In: *Earthquake Spectra* 31.1, pp. 159–177.

Gomes, R. B. and P. E. Regan (1999a). "Punching resistance of RC flat slabs with shear reinforcement." In: *ASCE Journal of Structural Engineering* 125.6, pp. 684–692.

— (1999b). "Punching strength of slabs reinforced for shear with offcuts of rolled steel I-section beams." In: *Magazine of Concrete Research* 51.2, pp. 121–129.

Gouveia, N. D., D. M. V. Faria, and A. P. Ramos (2018). "Assessment of SFRC flat slab punching behaviour – Part II: reversed horizontal cyclic loading." In: *Magazine of Concrete Research* 0.0, pp. 1–70.

Grote, D., S. Park, and M. Zhou (2001). "Dynamic behavior of concrete at high strain rates and pressures: I. experimental characterization." In: *International Journal of Impact Engineering* 25.9, pp. 869–886.

Habibi, F., W. D. Cook, and D. Mitchell (2014). "Predicting post-punching shear response of slab-column connections." In: *ACI Structural Journal* 111.1, pp. 123–134.

Hanna, S. N., D. Mitchell, and N. M. Hawkins (1975). *Slab - column connections containing shear reinforcement and transferring high-intensity reversed moments. Structures & Mechanics Report SM 75-1*. Tech. rep. Seattle, Washington, USA: University of Washington.

Hawkins, N. M., D. Mitchell, and M. S. Sheu (1974). *Cyclic behavior of six reinforced concrete slab-column specimens transferring moment and shear (Progress Report 1973-74)*. Tech. rep. Seattle, Washington, USA: Department of Civil Engineering, University of Washington.

Hegger, J., A. G. Sherif, D. Kueres, and C. Siburg (2017). "Efficiency of various punching shear reinforcement systems for flat slabs." In: *ACI Structural Journal* 114.3, pp. 631–642.

Hose, Y. D. and F. Seible (1999). *Performance evaluation database for concrete bridge components and systems under simulated seismic loads. PEER 1999/11*. 11. Berkeley, California, USA: Pacific Earthquake Engineering Research Center, College of Engineering. University of California, Berkeley.

Hueste, M. B. D. and J.-W. Bai (2007a). "Seismic retrofit of a reinforced concrete flat-slab structure: Part I - seismic performance evaluation." In: *Engineering Structures* 29.6, pp. 1165–1177.

— (2007b). "Seismic retrofit of a reinforced concrete flat-slab structure: Part II - Seismic fragility analysis." In: *Engineering Structures* 29.6, pp. 1178–1188.

Hueste, M. B. D. and J. K. Wight (1999). "Nonlinear punching shear failure model for interior slab-column connections." In: *ASCE Journal of Structural Engineering* 125.9, pp. 997–1008.

Hueste, M. B. D., J. Browning, A. Lepage, and J. W. Wallace (2007). "Seismic design criteria for slab-column connections." In: *ACI Structural Journal* 104.4, pp. 448–458.

Hwang, S.-J. and J. P. Moehle (2000a). "Models for laterally loaded slab-column frames." In: *ACI Structural Journal* 97.2, pp. 345–352.

— (2000b). "Vertical and lateral load tests of nine-panel flat-plate frame." In: *ACI Structural Journal* 97.1, pp. 193–203.

Inácio, M. M. G. (2016). "Comportamento ao punçoamento de lajes fungiformes em betão de elevada resistência [in Portuguese]." Doctoral dissertation. Faculdade de Ciências e Tecnologia, Universidade NOVA de Lisboa. URL: http://hdl.handle.net/10362/19576.

Islam, S. and R. Park (1976). "Tests on slab-column connections with shear and unbalanced flexure." In: *Journal of the Structural Division* 102.3, pp. 549–568.

ISO (Oct. 2010). *ISO 15630-1. Steel for the reinforcement and prestressing of concrete — Test methods — Part 1: Reinforcing bars, wire rod and wire*. Second edition.

Isufi, B., A. M. P. Ramos, V. J. G. Lúcio, and I. Cismasiu (June 2018a). "Pushover analysis of flat slab buildings with shear studs punching reinforcement." In: *16th European Conference on Earthquake Engineering*. Thessaloniki, Greece.

Isufi, B., A. P. Ramos, and V. Lúcio (2018b). "Reversed horizontal cyclic loading tests of flat slab specimens with studs as shear reinforcement." In: *Structural Concrete*. DOI: 10.1002/suco.201800128.

Jalayer, F. and C. Cornell (2009). "Alternative non-linear demand estimation methods for probability-based seismic assessments." In: *Earthquake Engineering & Structural Dynamics* 38.8, pp. 951–972.

Kang, T. H.-K., J. W. Wallace, and K. J. Elwood (2009). "Nonlinear modeling of flat-plate systems." In: *ASCE Journal of Structural Engineering* 135.2, pp. 147–158.

Kang, T. H. and J. W. Wallace (2005). "Dynamic responses of flat plate systems with shear reinforcement." In: *ACI Structural Journal* 102.5, pp. 763–773.

— (2008). "Seismic performance of reinforced concrete slab-column connections with thin plate stirrups." In: *ACI Structural Journal* 105.5, pp. 617–625.

Kim, K. S., S.-H. Choi, H. Ju, D. H. Lee, J.-Y. Lee, and M. Shin (2014). "Unified equivalent frame method for flat plate slab structures under combined gravity and lateral loads–Part 1: derivation." In: *Earthquakes and Structures* 7.5, pp. 719–733.

Kinnunen, S. and H. Nylander (1960). *Punching of concrete slabs without shear reinforcement*. Tech. rep. 158. Stockholm, Sweden: Royal Institute of Technology.

Kokot, S., A. Anthoine, P. Negro, and G. Solomos (2012). "Static and dynamic analysis of a reinforced concrete flat slab frame building for progressive collapse." In: *Engineering Structures* 40, pp. 205–217.

Koppitz, R., A. Kenel, and T. Keller (2015). "Effect of load history on punching shear resistance of flat slabs." In: *Engineering Structures* 90, pp. 130–142.

Lips, S., M. Fernández Ruiz, and A. Muttoni (2012). "Experimental investigation on punching strength and deformation capacity of shear-reinforced slabs." In: *ACI Structural Journal* 109.6, pp. 889–900.

Liu, J., Y. Tian, S. L. Orton, and A. M. Said (2015). "Resistance of flat-plate buildings against progressive collapse. I: Modeling of slab-column connections." In: *ASCE Journal of Structural Engineering* 141.12, p. 04015053.

Lúcio, V. J. G. (1991). "Waffle slab structures under vertical and horizontal loading." Doctoral dissertation. Universidade Técnica de Lisboa, Instituto Superior Técnico.

Luo, Y. and A. Durrani (1995). "Equivalent beam model for flat-slab buildings: part I: interior connections." In: *ACI Structural Journal* 92.1, pp. 115–124.

Mamede, N. F. S., A. P. Ramos, and D. M. Faria (2013). "Experimental and parametric 3D nonlinear finite element analysis on punching of flat slabs with orthogonal reinforcement." In: *Engineering Structures* 48, pp. 442–457.

Marzouk, H, M. Osman, and A Hussein (2001). "Cyclic loading of high-strength lightweight concrete slabs." In: *ACI Structural Journal* 98.2, pp. 207–214.

Matzke, E. M., R. D. Lequesne, G. J. Parra-Montesinos, and C. K. Shield (2015). "Behavior of biaxially loaded slab-column connections with shear studs." In: *ACI Structural Journal* 112.3, pp. 335–346.

McKenna, F., M. H. Scott, and G. L. Fenves (2009). "Nonlinear finite-element analysis software architecture using object composition." In: *Journal of Computing in Civil Engineering* 24.1, pp. 95–107.

Megally, S. and A. Ghali (2000a). "Punching shear design of earthquake-resistant slab-column connections." In: *ACI Structural Journal* 97.5, pp. 720–730.

— (2000b). "Seismic behavior of edge column-slab connections with stud shear reinforcement." In: *ACI Structural Journal* 97.1, pp. 53–60.

Melo, G. and P. Regan (1998). "Post-punching resistance of connections between flat slabs and interior columns." In: *Magazine of Concrete Research* 50.4, pp. 319–327.

Mitchell, D. and W. D. Cook (1984). "Preventing progressive collapse of slab structures." In: *ASCE Journal of Structural Engineering* 110.7, pp. 1513–1532.

Mitchell, D., R. H. DeVall, M. Saatcioglu, R. Simpson, R. Tinawi, and R. Tremblay (1995). "Damage to concrete structures due to the 1994 Northridge earthquake." In: *Canadian journal of civil engineering* 22.2, pp. 361–377.

Moehle, J. P. (1996). "Seismic design considerations for flat-plate construction." In: *ACI Special Publication* 162, pp. 1–34.

Moehle, J. (1992). "Displacement-based design of RC structures subjected to earthquakes." In: *Earthquake Spectra* 8.3, pp. 403–428.

Mokhtar, A.-S., A. Ghali, and W. Dilger (1985). "Stud shear reinforcement for flat concrete plates." In: *Journal Proceedings*. Vol. 82. 5, pp. 676–683.

Morrison, D. G., I. Hirasawa, and M. A. Sozen (1983). "Lateral-load tests of R/C slab-column connections." In: *ASCE Journal of Structural Engineering* 109.11, pp. 2698–2714.

Muttoni, A. (2008). "Punching shear strength of reinforced concrete slabs without transverse reinforcement." In: *ACI Structural Journal* 105.4, pp. 440–450.

Muttoni, A. and M. F. Ruiz (2008). "Shear strength of members without transverse reinforcement as function of critical shear crack width." In: *ACI Structural Journal* 105.2, pp. 163–172.

Muttoni, A. and J. Schwartz (1991). "Behavior of beams and punching in slabs without shear reinforcement." In: *IABSE colloquium*. Vol. 62. IABSE Colloquium, pp. 703–708.

Ornelas, M. N.C. S. (2017). "Punçoamento Cíclico de Lajes Fungiformes com Estribos [in Portuguese]." Master's thesis. Faculdade de Ciências e Tecnologia, Universidade NOVA de Lisboa. URL: https://run.unl.pt/handle/10362/23406.

Pan, A. D. and J. P. Moehle (1989). "Lateral displacement ductility of reinforced concrete flat plates." In: *ACI Structural Journal* 86.3, pp. 250–258.

— (1992). "An experimental study of slab-column connections." In: *ACI Structural Journal* 89.6, pp. 626–638.

Park, H. gun, K. soo Ahn, K. kyu Choi, and L. Chung (2007). "Lattice shear reinforcement for slab–column connections." In: *ACI Structural Journal* 104.3, pp. 294–303.

Park, H.-G., Y.-N. Kim, J.-G. Song, and S.-M. Kang (2012). "Lattice shear reinforcement for enhancement of slab-column connections." In: *ASCE Journal of Structural Engineering* 138.3, pp. 425–437.

Park, T. W. (2012). "Inspection of collapse cause of Sampoong Department Store." In: *Forensic Science International* 217.1-3, pp. 119–126.

Park, Y.-M., S.-W. Han, and S.-H. Kee (2009). "A modified equivalent frame method for lateral load analysis." In: *Magazine of Concrete Research* 61.5, pp. 359–370.

Pecknold, D. A. (1975). "Slab effective width for equivalent frame analysis." In: *Journal Proceedings*. Vol. 72. 4, pp. 135–137.

PEER. *PEER NGA-West2 Ground Motion Database*. Online. Accessed: 2017-09-20. URL: http://ngawest2.berkeley.edu/.

Pilakoutas, K. and X Li (2003). "Alternative shear reinforcement for reinforced concrete flat slabs." In: *ASCE Journal of Structural Engineering* 129.9, pp. 1164–1172.

Polak, M. A. (1998). "Modeling punching shear of reinforced concrete slabs using layered finite elements." In: *ACI Structural Journal* 95.1, pp. 71–80.

— (2005). "Shell finite element analysis of RC plates supported on columns for punching shear and flexure." In: *Engineering Computations* 22.4, pp. 409–428.

Porter, K., R. Kennedy, and R. Bachman (2007). "Creating fragility functions for performance-based earthquake engineering." In: *Earthquake Spectra* 23.2, pp. 471–489.

Priestley, M. J. N. (1997). "Myths and fallacies in Earthquake Engineering." In: *ACI Concrete International* 19.2, pp. 54–63.

Priestley, M., G. Calvi, and M. Kowalsky (2007). *Displacement Based Seismic Design of Structures*. Pavia, Italy: IUSS Press. ISBN: 978-88-6198-000-6.

Qian, K. and B. Li (2016). "Resilience of flat slab structures in different phases of progressive collapse." In: *ACI Structural Journal* 113.3, p. 537.

Ramos, A. P. and V. Lúcio (2008). "Post-punching behaviour of prestressed concrete." In: *Magazine of Concrete Research* 60.4, pp. 245–251.

Ramos, A., R. Marreiros, A. Almeida, B. Isufi, and M. Inácio (2017). "Punching of flat slabs under reversed horizontal cyclic loading." In: *ACI/fib SP-315 Special Publication* 315, pp. 253–272.

Rha, C., T. H. Kang, M. Shin, and J. B. Yoon (2014). "Gravity and lateral load-carrying capacities of reinforced concrete flat plate systems." In: *ACI Structural Journal* 111.4, pp. 753–764.

Rizk, E and H Marzouk (2013). "Minimum shear reinforcement for thick plates and two-way slabs." In: *Engineering Structures* 46, pp. 1–13.

Robertson, I. and G. Johnson (2006). "Cyclic lateral loading of nonductile slab-column connections." In: *ACI Structural Journal* 103.3, pp. 356–364.

Robertson, I. N. and A. J. Durrani (1993). "Gravity load effect on seismic behavior of interior slab-column connections." In: *ACI Structural Journal* 89.1, pp. 37–45.

Robertson, I. N., T. Kawai, J. Lee, and B. Enomoto (2002). "Cyclic testing of slab-column connections with shear reinforcement." In: *ACI Structural Journal* 99.5, pp. 605–613.

Robertson, I. N. (1990). "Seismic response of connections in indeterminate flat-slab subassemblies." Doctoral dissertation. Rice University.

Robertson, I. N. and G. Johnson (2004). "Repair of slab–column connections using epoxy and carbon fiber reinforced polymer." In: *ASCE Journal of Composites for Construction* 8.5, pp. 376–383.

Rota, M, A Penna, and G Magenes (2010). "A methodology for deriving analytical fragility curves for masonry buildings based on stochastic nonlinear analyses." In: *Engineering Structures* 32.5, pp. 1312–1323.

Ruiz, M. F. and A. Muttoni (2009). "Applications of Critical Shear Crack Theory to punching of reinforced concrete slabs with transverse reinforcement." In: *ACI Structural Journal* 106.4, pp. 485–494.

Ruiz, M. F., Y. Mirzaei, and A. Muttoni (2013). "Post-punching behavior of flat slabs." In: *ACI Structural Journal* 110.5, pp. 801–812.

Sagaseta, J., A. Muttoni, M. Fernández Ruiz, and L. Tassinari (2011). "Non-axis-symmetrical punching shear around internal columns of RC slabs without transverse reinforcement." In: *Magazine of Concrete Research* 63.6, pp. 441–457.

Schmidt, M. and H. Lipson (2014). *Eureqa (Version 0.98 beta) [Software]*. URL: www.nutonian.com.

Schmidt, M. and H. Lipson (2009). "Distilling free-form natural laws from experimental data." In: *Science* 324.5923, pp. 81–85.

Scott, B. D., R. Park, and M. J. N. Priestley (1982). "Stress-strain behavior of concrete confined by overlapping hoops at low and high strain rates." In: *ACI Journal Proceedings* 79.1, pp. 13–27.

Scott, M., F. Filippou, and S. Mazzoni. *OpenSees Command Manual - Hysteretic Material*. Online. Accessed: 2017-06-07. URL: http://opensees.berkeley.edu/wiki/index.php/Hysteretic_Material.

Seible, F., A. Ghali, and W. H. Dilger (1980). "Preassembled shear reinforcing units for flat plates." In: *ACI Journal Proceedings*. Vol. 77. 1, pp. 28–35.

Sen, S. and Y. Singh (2016). "Displacement-based seismic design of flat slab-shear wall buildings." In: *Earthquake Engineering and Engineering Vibration* 15.2, pp. 209–221.

Soares, J (1993). "Punçoamento excêntrico em lajes fungiformes de betão armado (Eccentric punching in reinforced concrete flat slabs, in Portuguese)." Master's thesis. Universidade Técnica de Lisboa, Instituto Superior Técnico.

Soares, L. and R. Vollum (2015). "Comparison of punching shear requirements in BS 8110, EC2, and MC2010." In: *Magazine of Concrete Research* 67.24, pp. 1315–1328.

Stark, A., B. Binici, and O. Bayrak (2005). "Seismic upgrade of reinforced concrete slab-column connections using carbon fiber-reinforced polymers." In: *ACI Structural Journal* 102.2, pp. 324–333.

Symonds, D. W., D. Mitchell, and N. M. Hawkins (1976). *Slab-column connections subjected to high intensity shears and transferring reversed moments (Report SM 76-2)*. Tech. rep. Seattle, Washington, USA: Department of Civil Engineering, University of Washington.

Tan, Y and S Teng (2005). "Interior slab-rectangular column connections under biaxial lateral loadings." In: *ACI Special Publication* 232, pp. 147–174.

Tang, X. and S. C. Goel (1998). *DRAIN-2DM technical notes and user's guide. Research Rep. No. UMCE 88-1*. Tech. rep. Ann Arbor, Michigan, USA: University of Michigan.

Tian, Y., J. O. Jirsa, O. Bayrak, J. F. Argudo, et al. (2008). "Behavior of slab-column connections of existing flat-plate structures." In: *ACI Structural Journal* 105.5, pp. 561–569.

Tian, Y., J. O. Jirsa, and O. Bayrak (2009). "Nonlinear modeling of slab-column connections under cyclic loading." In: *ACI Structural Journal* 106.1, pp. 30–38.

University of Sheffield (2016). *Shearband System (marketed by ERICO as LENTON®STEEL FORTRESS)*. Online. Accessed: 2016-03-10. URL: https://www.sheffield.ac.uk/ci/research/concrete/sb.

Vamvatsikos, D. and C. A. Cornell (2002). "Incremental dynamic analysis." In: *Earthquake Engineering & Structural Dynamics* 31.3, pp. 491–514.

Vanderbilt, M. D. and W. G. Corley (1983). "Frame analysis of concrete buildings." In: *Concrete International* 5.12, pp. 33–43.

Vaz, A. P. R., R. B. Gomes, and L. d.C. D. Shehata (2009). "Study on minimum shear reinforcement of reinforced concrete flat slabs." In: *Revista IBRACON de Estruturas e Materiais* 2.1, pp. 1–24.

Voet, A. F.V. D., W. H. Dilger, and A. Ghali (1982). "Concrete flat plates with well-anchored shear reinforcement elements." In: *Canadian Journal of Civil Engineering* 9.1, pp. 107–114.

Vollum, R., T Abdel-Fattah, M Eder, and A. Elghazouli (2010). "Design of ACI–type punching shear reinforcement to Eurocode 2." In: *Magazine of Concrete Research* 62.1, pp. 3–16.

Wang, W. and S. Teng (2008). "Finite-element analysis of reinforced concrete flat plate structures by layered shell element." In: *ASCE Journal of Structural Engineering* 134.12, pp. 1862–1872.

Wey, E. H. and A. J. Durrani (1992). "Seismic response of interior slab-column connections with shear capitals." In: *ACI Structural Journal* 89.6, pp. 682–691.

Widianto, O. Bayrak, J. O. Jirsa, and Y. Tian (2010). "Seismic rehabilitation of slab-column connections." In: *ACI Structural Journal* 107.2, pp. 237–247.

Wood, J. G. (1997). *Pipers Row Car Park, Wolverhampton: Quantitative study of the causes of the partial collapse on 20th March*.

Zaharia, R., F. Taucer, A. Pinto, J. Molina, V Vidal, E Coelho, and P Candeias (2006). *Pseudodynamic earthquake tests on a full-scale RC flat-slab building structure. JRC scientific and technical reports, EUR 22192EN*. Tech. rep. Ispra, Italy: Joint Research Centre. Institute for the Protection and Security of the Citizen, European Laboratory for Structural Assessment (ELSA).

Zee, H. L. and J. P. Moehle (1984). *Behavior of interior and exterior flat plate connections subjected to inelastic load reversals (Report UCB/EERC-84/07)*. Tech. rep. Berkeley, California, USA: University of California, Earthquake Engineering Research Center.

# Appendix A

# Database of specimens from the literature

This Annex contains complementary details regarding specimens found in the literature, tested under a combination of constant gravity loads and reversed horizontal cyclic displacements. The information contained herein provides the basis for the construction of the histograms presented in Figure 2.23 and Figure 2.24 in Chapter 2 .

As previously mentioned, a sub-set of the experiments described here is chosen for the analysis of the ultimate drifts in slab–column connections in Chapter 5. The reader is referred to Section 5.2.1 for the criteria used for the compilation of such a database and to Sections 5.2.3 and 5.2.2 for more specific data relevant to the study of the ultimate drift ratios in specimens with and without shear reinforcement respectively.

## A.1 Specimens without shear reinforcement

In the following tables, $h$ is the thickness of the slab, $c$ represents the dimensions of the column (for square cross sections, only one dimension is shown), $f_c$ is concrete strength, $f_y$ is steel yield stress, $\rho_l$ is the geometric mean of the longitudinal reinforcement over $c + 6d$ over the column (where $d$ is the effective depth).

Table A.1: Complementary details on specimens without shear reinforcement

| No. | Publication | ID | $h$ (mm) | $c$ (mm) | $f_c$ (MPa) | $f_y$ (MPa) | $\rho_l$ (%) |
|---|---|---|---|---|---|---|---|
| 1 | Hawkins et al. 1974 | S-1 | 152 | 305 | 34.8 | 459 | 1.3 |
| 2 | | S-2 | 152 | 305 | 23.4 | 463 | 0.9 |
| 3 | | S-3 | 152 | 305 | 22.1 | 455 | 0.6 |
| 4 | | S-4 | 152 | 305 | 32.3 | 459 | 1.3 |

| No. | Publication | ID | $h$ (mm) | $c$ (mm) | $f_c$ (MPa) | $f_y$ (MPa) | $\rho_l$ (%) |
|---|---|---|---|---|---|---|---|
| 5 | Islam and Park 1976 | 3C | 89 | 229 | 29.7 | 316 | 1.2 |
| 6 | Symonds et al. 1976 | S-6 | 152 | 305 | 23.2 | 459 | 1.9 |
| 7 | | S-7 | 152 | 305 | 26.5 | 463 | 0.9 |
| 8 | Morrison et al. 1983 | S1 | 76 | 305 | 45.8 | 323 | 0.7 |
| 9 | | S2 | 76 | 305 | 35.1 | 330 | 1 |
| 10 | | S3 | 76 | 305 | 33.9 | 335 | 1.4 |
| 11 | | S4 | 76 | 305 | 34.9 | 320 | 1 |
| 12 | | S5 | 76 | 305 | 35.2 | 340 | 1 |
| 13 | Zee and Moehle 1984 | INT | 61 | 137 | 24.8 | 434 | 0.7 |
| 14 | Robertson 1990 | 8I | 114 | 254 | 39.3 | 525 | 0.7 |
| 15 | Pan and Moehle 1992 | AP1 | 122 | 274 | 33.3 | 472 | 0.7 |
| 16 | | AP2 | 122 | 274 | 33.3 | 472 | 0.7 |
| 17 | | AP3 | 122 | 274 | 31.4 | 472 | 0.7 |
| 18 | | AP4 | 122 | 274 | 31.4 | 472 | 0.7 |
| 19 | Wey and Durrani 1992 | SC6 | 203 | 254 | 34.6 | 568 | 0.3 |
| 20 | | SC4 | 203 | 254 | 36.8 | 568 | 0.3 |
| 21 | | SC2 | 203 | 254 | 39 | 568 | 0.3 |
| 22 | | SC0 | 114 | 254 | 39.3 | 525 | 0.6 |
| 23 | Cao 1993 | CD-1 | 150 | 250 | 40.4 | 395 | 1.3 |
| 24 | | CD-5 | 150 | 250 | 31.2 | 395 | 1.3 |
| 25 | | CD-8 | 150 | 250 | 27 | 395 | 1.3 |
| 26 | Farhey et al. 1993 | 1 | 80 | $300 \times 200$ | 29.2 | 458 | 0.8 |
| 27 | | 2 | 80 | $300 \times 200$ | 29.2 | 458 | 0.8 |
| 28 | | 3 | 80 | $300 \times 200$ | 13.9 | 458 | 0.8 |
| 29 | | 4 | 80 | $300 \times 120$ | 13.9 | 458 | 0.8 |
| 30 | Emam et al. 1997 | H.H.H.C.0.5 | 150 | 250 | 75.8 | 460 | 0.5 |
| 31 | | H.H.H.C.1.0 | 150 | 250 | 72.3 | 460 | 1 |
| 32 | | N.H.H.C.0.5 | 150 | 250 | 36.8 | 460 | 0.5 |
| 33 | | N.H.H.C.1.0 | 150 | 250 | 35.4 | 460 | 1 |
| 34 | Marzouk et al. 2001 | HSLW0.5C | 150 | 250 | 70 | 400 | 0.5 |
| 35 | | HSLW1.0C | 150 | 250 | 70 | 400 | 1 |
| 36 | | NSLW0.5C | 150 | 250 | 35 | 400 | 0.5 |

| No. | Publication | ID | $h$ (mm) | $c$ (mm) | $f_c$ (MPa) | $f_y$ (MPa) | $\rho_l$ (%) |
|---|---|---|---|---|---|---|---|
| 37 | | NSLW1.0C | 150 | 250 | 35 | 400 | 1 |
| 38 | | NSNW0.5C | 150 | 250 | 35 | 400 | 0.5 |
| 39 | | NSNW1.0C | 150 | 250 | 35 | 400 | 1 |
| 40 | Ali and Alexander 2002 | SP-A | 152 | 355 | 32.7 | 394 | 1.3 |
| 41 | | SP-B | 152 | 355 | 34.1 | 415 | 1.3 |
| 42 | Robertson et al. 2002 | 1C | 114 | 250 | 35.4 | 420 | 0.6 |
| 43 | Brown 2003 | SJB-7 | 150 | 250 | 28.8 | 400 | 1.3 |
| 44 | Stark et al. 2005 | C-02 | 115 | 305 | 30.9 | 454 | 1.2 |
| 45 | | C-63 | 115 | 305 | 30.9 | 454 | 1.2 |
| 46 | Tan and Teng 2005 | YL-L1 | 150 | $180 \times 900$ | 40 | 530 | 1.2 |
| 47 | | YL-H2 | 150 | $180 \times 900$ | 40 | 530 | 1.2 |
| 48 | | YL-L2 | 150 | $180 \times 900$ | 40 | 530 | 1.2 |
| 49 | Robertson and Johnson 2006 | ND8BU | 144 | 254 | 39.2 | 400 | 1 |
| 50 | | ND1C | 114 | 254 | 29.6 | 400 | 0.6 |
| 51 | | ND4LL | 114 | 254 | 32.3 | 400 | 0.6 |
| 52 | | ND5XL | 114 | 254 | 24.1 | 400 | 0.6 |
| 53 | | ND6HR | 114 | 254 | 26.3 | 400 | 1 |
| 54 | | ND7LR | 144 | 254 | 18.8 | 400 | 0.4 |
| 55 | Kang and Wallace 2008 | C0 | 152 | 254 | 38.6 | 452 | 0.5 |
| 56 | Tian et al. 2008 | LG0.5 | 152 | 406 | 33.2 | 455 | 0.5 |
| 57 | | LG1.0 | 152 | 406 | 27.6 | 421 | 0.9 |
| 58 | | L0.5 | 152 | 406 | 25.6 | 469 | 0.5 |
| 59 | Park et al. 2012 | RC-A | 135 | 300 | 22.5 | 430 | 1.1 |
| 60 | | RC-B | 135 | 300 | 38.7 | 430 | 1.1 |
| 61 | Almeida et al. 2016 | C-50 | 150 | 250 | 52.4 | 526 | 0.9 |
| 62 | | C-40 | 150 | 250 | 53.1 | 526 | 0.9 |
| 63 | | C-30 | 150 | 250 | 66.5 | 526 | 0.9 |
| 64 | Drakatos et al. 2016 | PD8 | 250 | 390 | 34.4 | 575 | 0.8 |
| 65 | | PD6 | 250 | 390 | 40.3 | 507 | 0.8 |
| 66 | | PD2 | 250 | 390 | 38.8 | 558 | 0.8 |
| 67 | | PD13 | 250 | 390 | 38.4 | 546 | 1.5 |

| No. | Publication | ID | $h$ (mm) | $c$ (mm) | $f_c$ (MPa) | $f_y$ (MPa) | $\rho_l$ (%) |
|---|---|---|---|---|---|---|---|
| 68 | | PD11 | 250 | 390 | 34.8 | 593 | 1.5 |

## A.2 Specimens with shear reinforcement

The following abbreviations are used for the type of shear reinforcement: ST - stirrups, SL - single leg stirrups, SSR - shear studs, THP - thin plate stirrups and LT - lattice type reinforcement. The area of shear reinforcement per perimeter is denoted as $A_{sw}$.

Table A.2: Complementary details on specimens with shear reinforcement

| No. | Publication | ID | $h$ (mm) | $c$ (mm) | $f_c$ (MPa) | $f_y$ (MPa) | $\rho_l$ (%) | Type | $A_{sw}$ (mm$^2$) |
|---|---|---|---|---|---|---|---|---|---|
| 1 | Hawkins et al. 1974 | SS-1 | 152 | 305 | 27.6 | 460 | 1.3 | ST | 570 |
| 2 | | SS-2 | 152 | 305 | 25.7 | 464 | 0.9 | ST | 253 |
| 3 | Hanna et al. 1975 | SS-3 | 152 | 305 | 25.9 | 456 | 1.9 | ST | 570 |
| 4 | | SS-4 | 152 | 305 | 27.6 | 456 | 1.9 | ST | 570 |
| 5 | | SS-5 | 152 | 305 | 32.2 | 464 | 0.9 | ST | 253 |
| 6 | Islam and Park 1976 | 6CS | 89 | 229 | 28.2 | 290 | 1.2 | ST | 285 |
| 7 | | 7CS | 89 | 229 | 29.7 | 304 | 1.2 | ST | 253 |
| 8 | | 8CS | 89 | 229 | 22.1 | 293 | 1.2 | ST | 143 |
| 9 | Symonds et al. 1976 | SS-6 | 152 | 305 | 24.2 | 463 | 0.9 | ST | 253 |
| 10 | | SS-7 | 152 | 305 | 26.9 | 459 | 1.9 | ST | 570 |
| 11 | Cao 1993 | CD-3 | 150 | 250 | 36.0 | 395 | 1.3 | SSR | 774 |
| 12 | | CD-4 | 150 | 250 | 34.0 | 395 | 1.3 | SSR | 774 |
| 13 | | CD-6 | 150 | 250 | 31.0 | 395 | 1.3 | SSR | var. |
| 14 | | CD-7 | 150 | 250 | 29.0 | 395 | 1.3 | SSR | 774 |
| 15 | Robertson et al. 2002 | 4HS | 114 | 250 | 38.2 | 420 | 0.6 | SSR | 567 |
| 16 | | 2CS | 114 | 250 | 31.4 | 420 | 0.6 | ST | 226 |
| 17 | | 3SL | 114 | 250 | 43.4 | 420 | 0.6 | SL | 226 |

| No. | Publication | ID | $h$ (mm) | $c$ (mm) | $f_c$ (MPa) | $f_y$ (MPa) | $\rho_l$ (%) | Type | $A_{sw}$ (mm$^2$) |
|---|---|---|---|---|---|---|---|---|---|
| 18 | Brown 2003 | SJB-1 | 150 | 250 | 32.0 | 400 | 1.3 | SSR | 567 |
| 19 | | SJB-2 | 150 | 250 | 34.0 | 400 | 1.4 | SSR | 567 |
| 20 | | SJB-3 | 150 | 250 | 32.0 | 400 | 1.3 | SSR | 567 |
| 21 | | SJB-4 | 150 | 250 | 40.0 | 400 | 1.4 | SSR | 567 |
| 22 | | SJB-5 | 150 | 250 | 33.0 | 400 | 1.8 | SSR | 567 |
| 23 | | SJB-8 | 150 | 250 | 35.0 | 400 | 1.3 | SSR | 567 |
| 24 | | SJB-9 | 150 | 250 | 31.0 | 400 | 1.8 | SSR | 567 |
| 25 | Tan and Teng 2005 | YL-H2V | 150 | $180 \times 900$ | 40.0 | 530 | 1.2 | SSR | 785 |
| 26 | | YL-H1V | 150 | $180 \times 900$ | 40.0 | 530 | 1.2 | SSR | 785 |
| 27 | Broms 2007 | 18c | 180 | 300 | 34.6 | 563 | 1 | SSR | 1232 |
| 28 | | 18d | 180 | 300 | 34.6 | 541 | 0.7 | SSR | 1232 |
| 29 | Kang and Wallace 2008 | PS2.5 | 152 | 254 | 35.1 | 452 | 0.5 | THP | 194 |
| 30 | | PS3.5 | 152 | 254 | 35.1 | 452 | 0.5 | THP | 194 |
| 31 | | HS2.5 | 152 | 254 | 35.1 | 452 | 0.5 | SSR | 142 |
| 32 | Cheng et al. 2010 | SB3 | 152 | 406 | 44.4 | 451 | 0.7 | SSR | 570 |
| 33 | Park et al. 2012 | SR-A | 135 | 300 | 22.5 | 430 | 1.1 | SSR | 628 |
| 34 | | SR-B | 135 | 300 | 38.7 | 430 | 1.1 | SSR | 628 |
| 35 | | LR-A1 | 135 | 300 | 22.5 | 430 | 1.1 | LT | - |
| 36 | | LR-A2 | 135 | 300 | 22.5 | 430 | 1.1 | LT | - |
| 37 | | SB-A | 135 | 300 | 22.5 | 430 | 1.1 | THP | 1080 |
| 38 | | ST-A | 135 | 300 | 22.5 | 430 | 1.1 | ST | 452 |
| 39 | | LR-B1 | 135 | 300 | 38.7 | 430 | 1.1 | LT | - |
| 40 | | LR-B2 | 135 | 300 | 38.7 | 430 | 1.1 | LT | - |
| 41 | | SB-B | 135 | 300 | 38.7 | 430 | 1.1 | THP | 1080 |
| 42 | | ST-B | 135 | 300 | 38.7 | 430 | 1.1 | ST | 452 |

| No. | Publication | ID | $h$ (mm) | $c$ (mm) | $f_c$ (MPa) | $f_y$ (MPa) | $\rho_l$ (%) | Type | $A_{sw}$ ($mm^2$) |
|---|---|---|---|---|---|---|---|---|---|
| 43 | Matzke et al. 2015 | B1 | 152 | 406 | 39.7 | 466 | 0.7 | SSR | 855 |
| 44 | | B2 | 152 | 406 | 32.9 | 483 | 0.7 | SSR | 855 |
| 45 | | B3 | 152 | 406 | 37.8 | 446 | 0.7 | SSR | 855 |
| 46 | | B4 | 152 | 406 | 40.7 | 465 | 0.7 | SSR | 1425 |

# Appendix B

# Strain gauge readings

The strain gauge readings along the entire duration of the tests are presented in this Annex. For locations in which two strain gauges were installed (top and bottom flexural reinforcement), the values in the figures are taken as the average value of the two readings. When strain gauges stop reading correctly (for example, when the reading jumps to a high or very low strain value), the graph is interrupted.

The graphs in this Annex are presented in the following order:

- top reinforcement for all specimens;
- bottom reinforcement for all specimens;
- strains in shear studs for shear reinforced specimens.

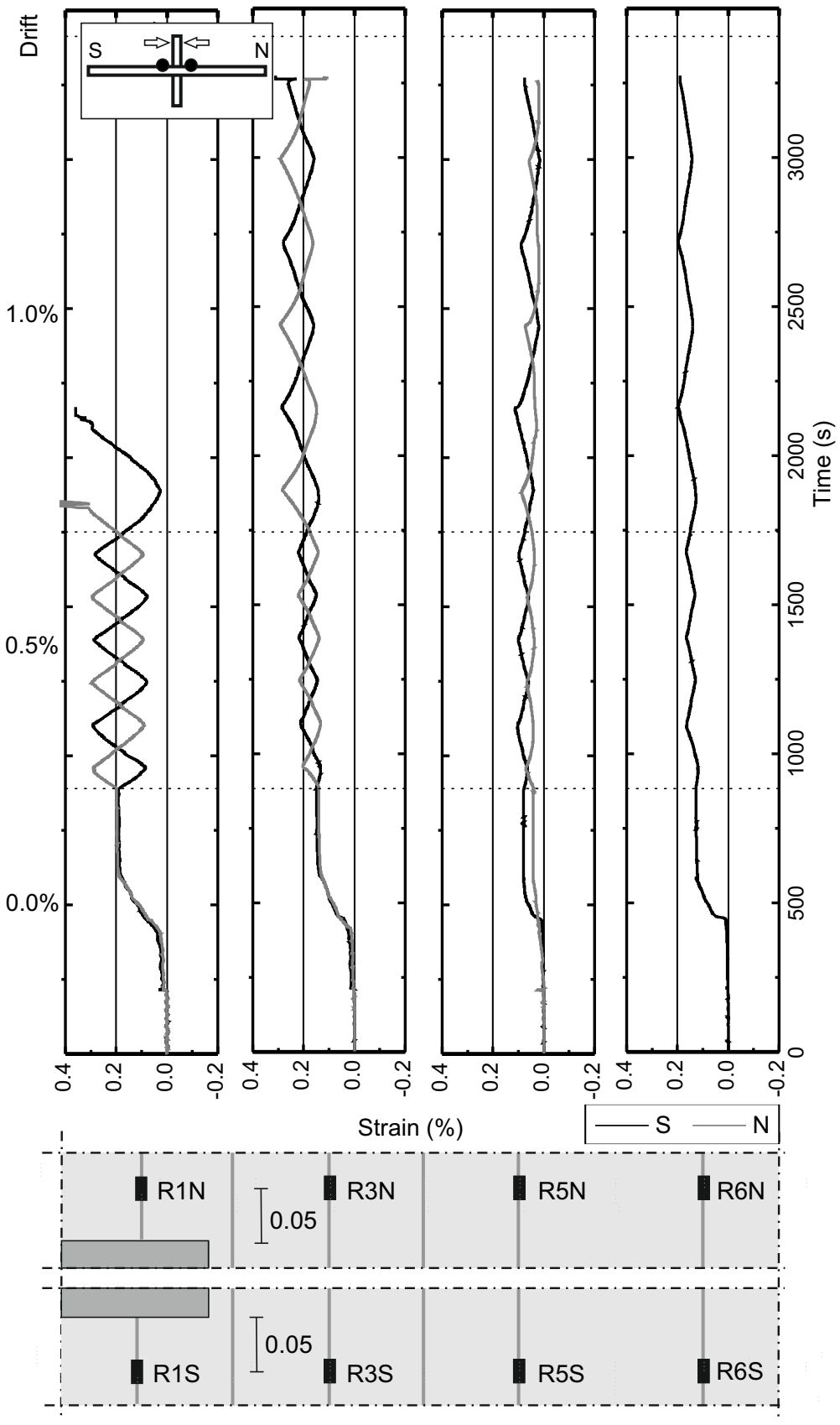


Figure B.1: Top reinforcement strains along the test, specimen C-Ref

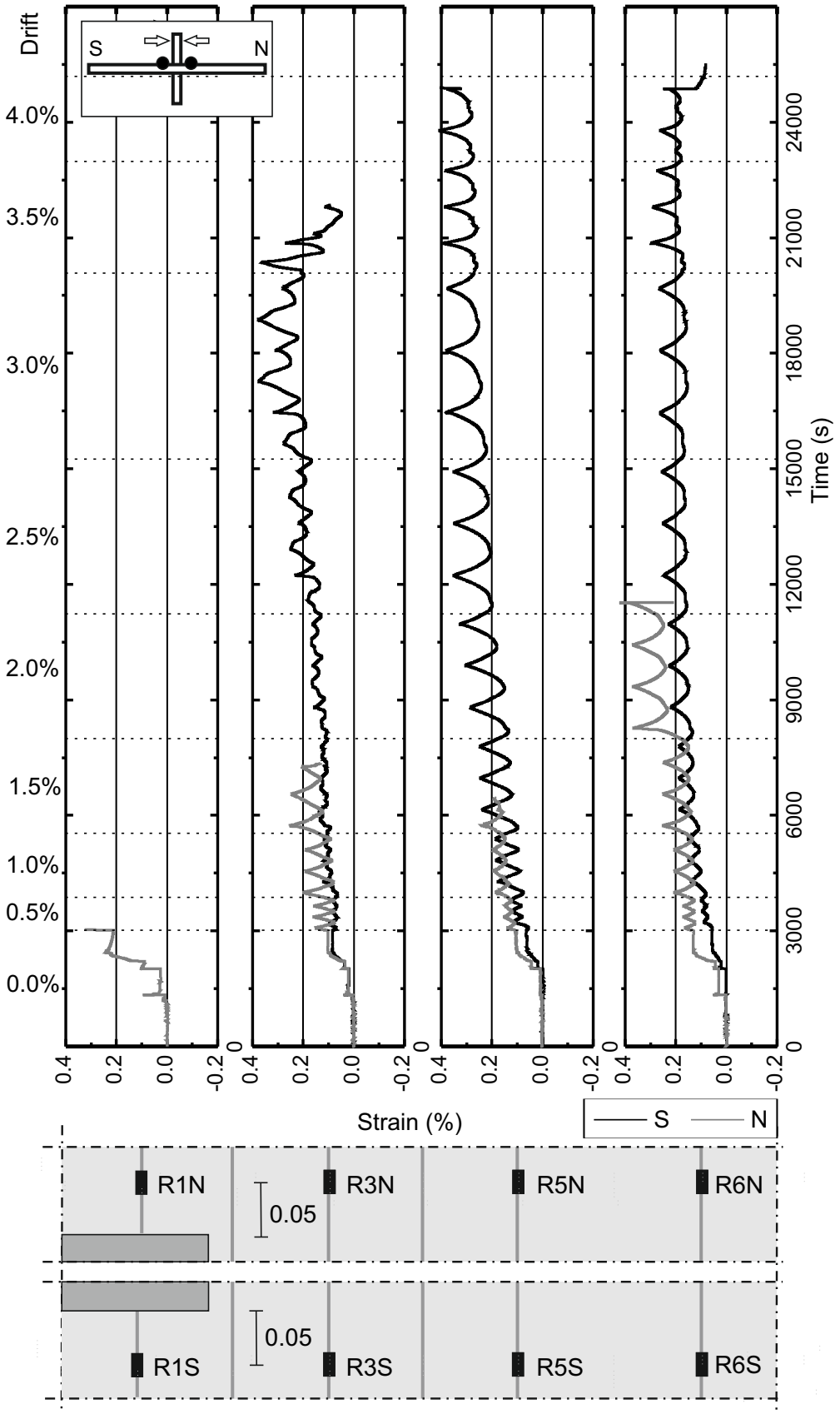


Figure B.2: Top reinforcement strains along the test, specimen C-SSR3

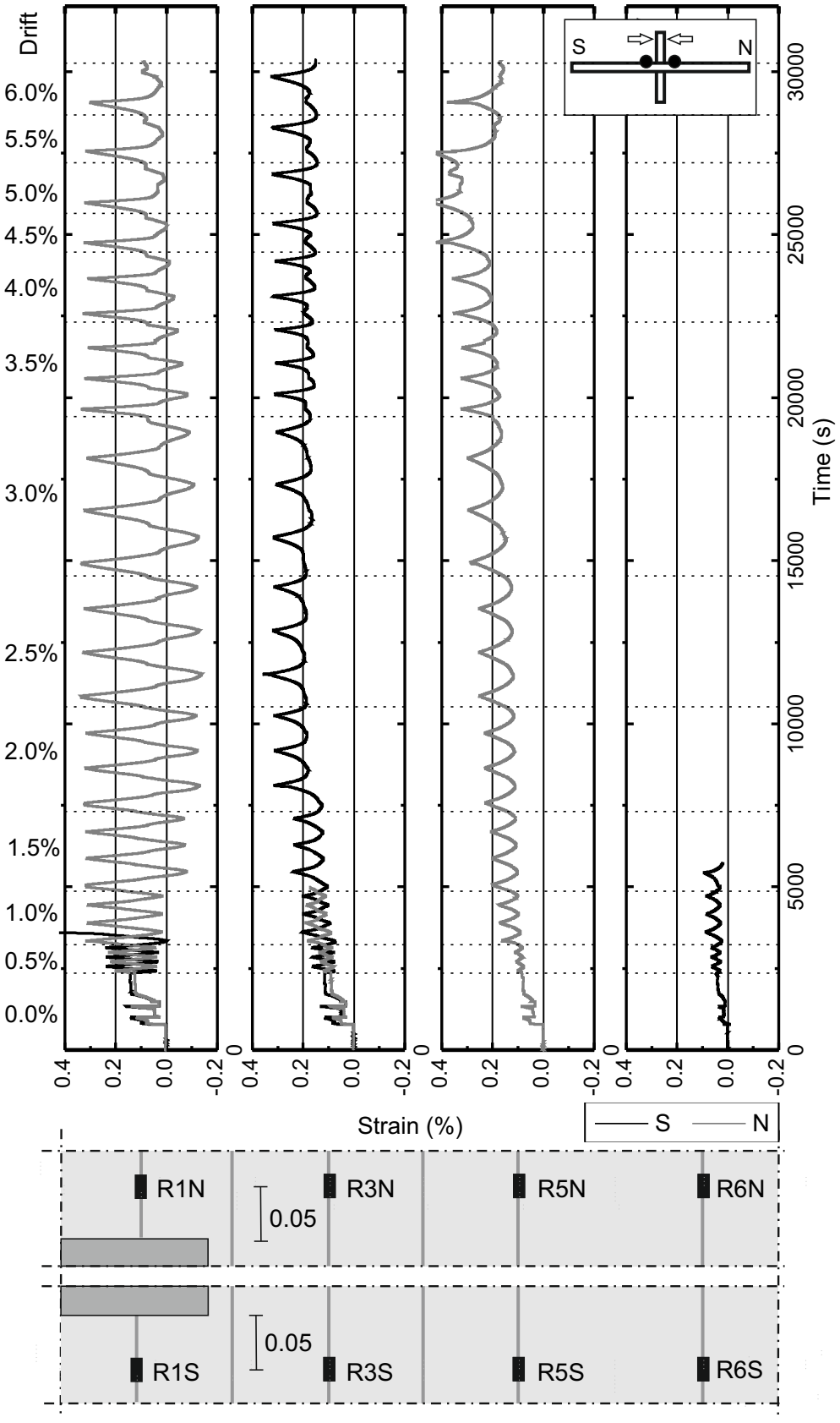


Figure B.3: Top reinforcement strains along the test, specimen C-SSR5a

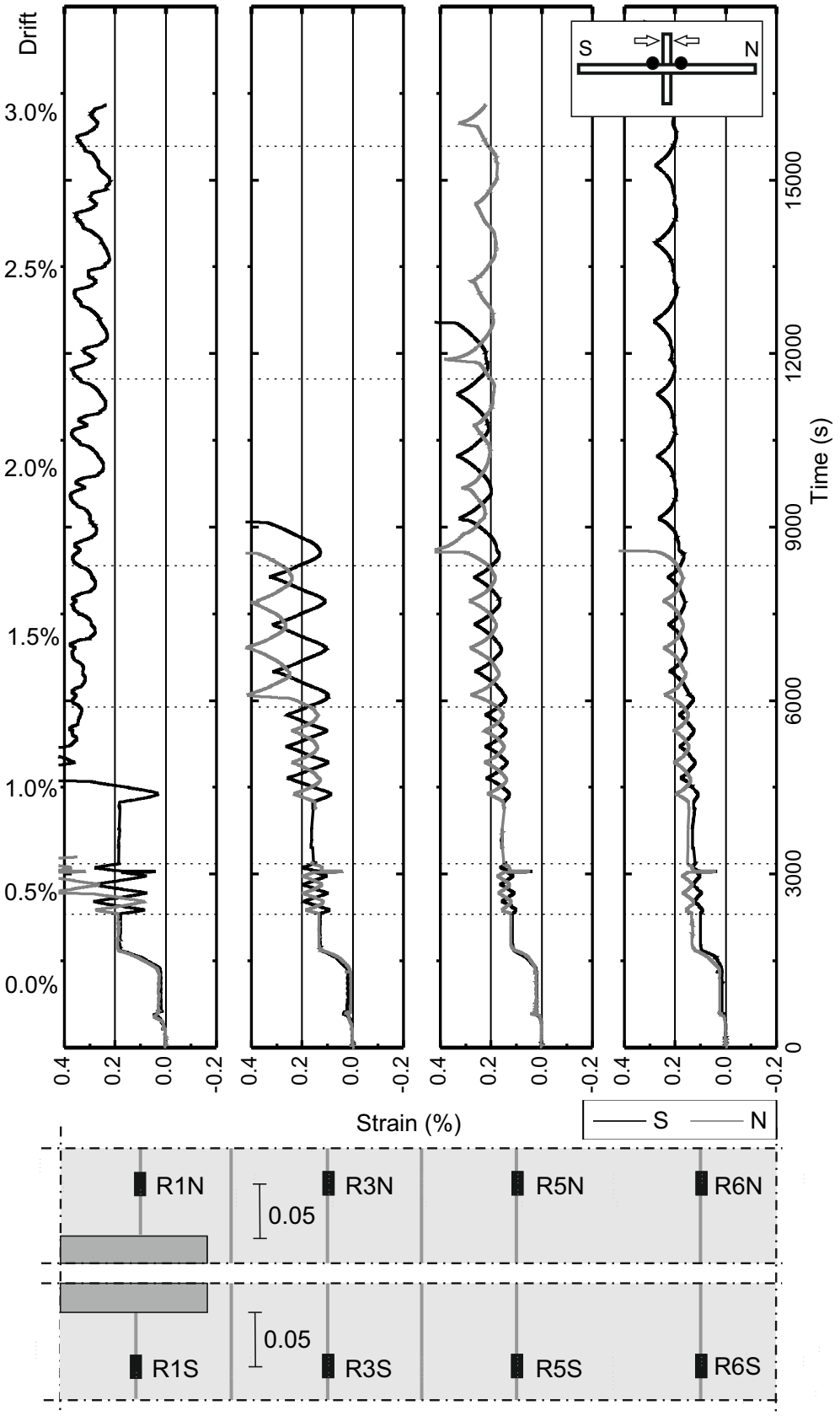


Figure B.4: Top reinforcement strains along the test, specimen C-SSR5b, Phase I

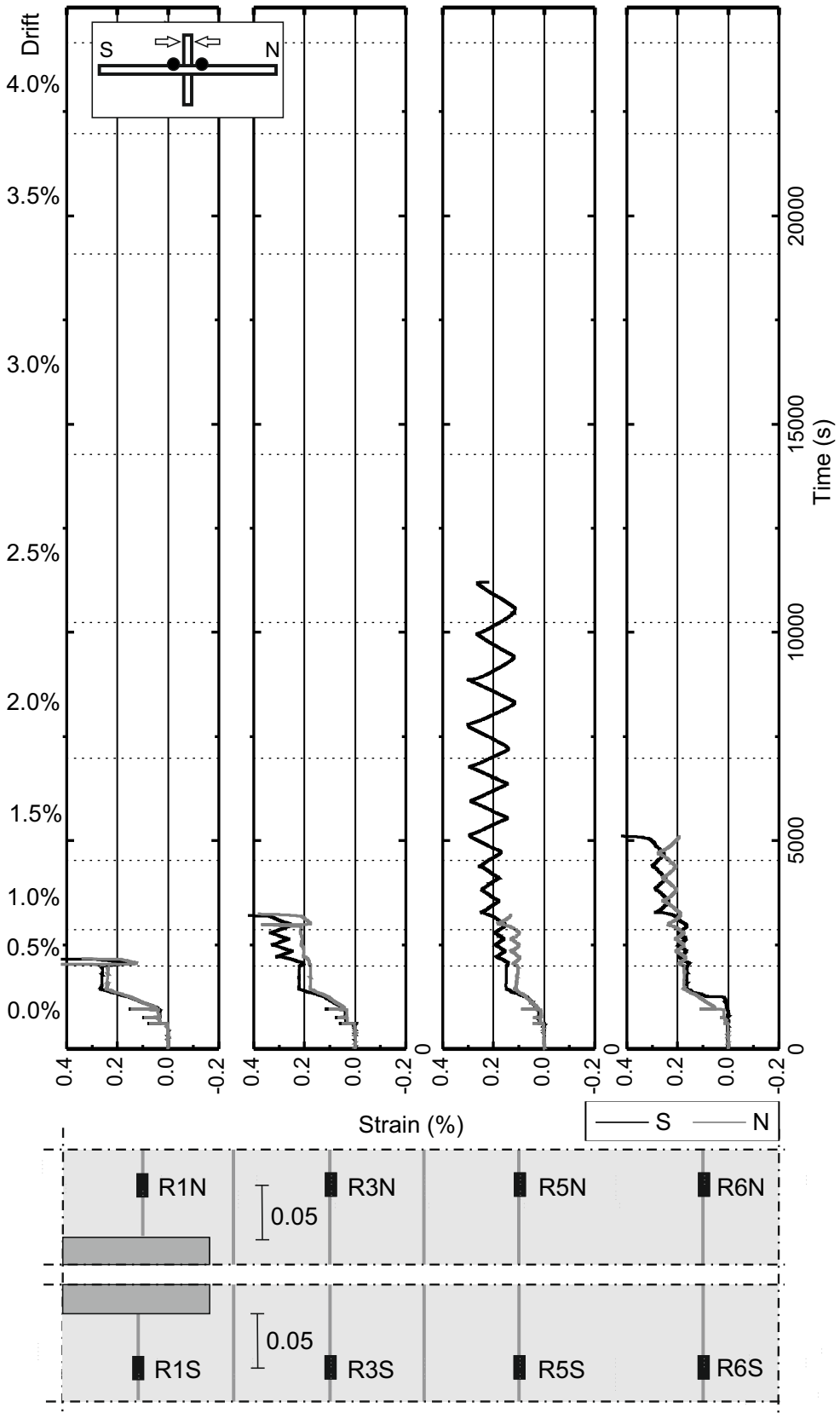


Figure B.5: Top reinforcement strains along the test, specimen C-SSR5c

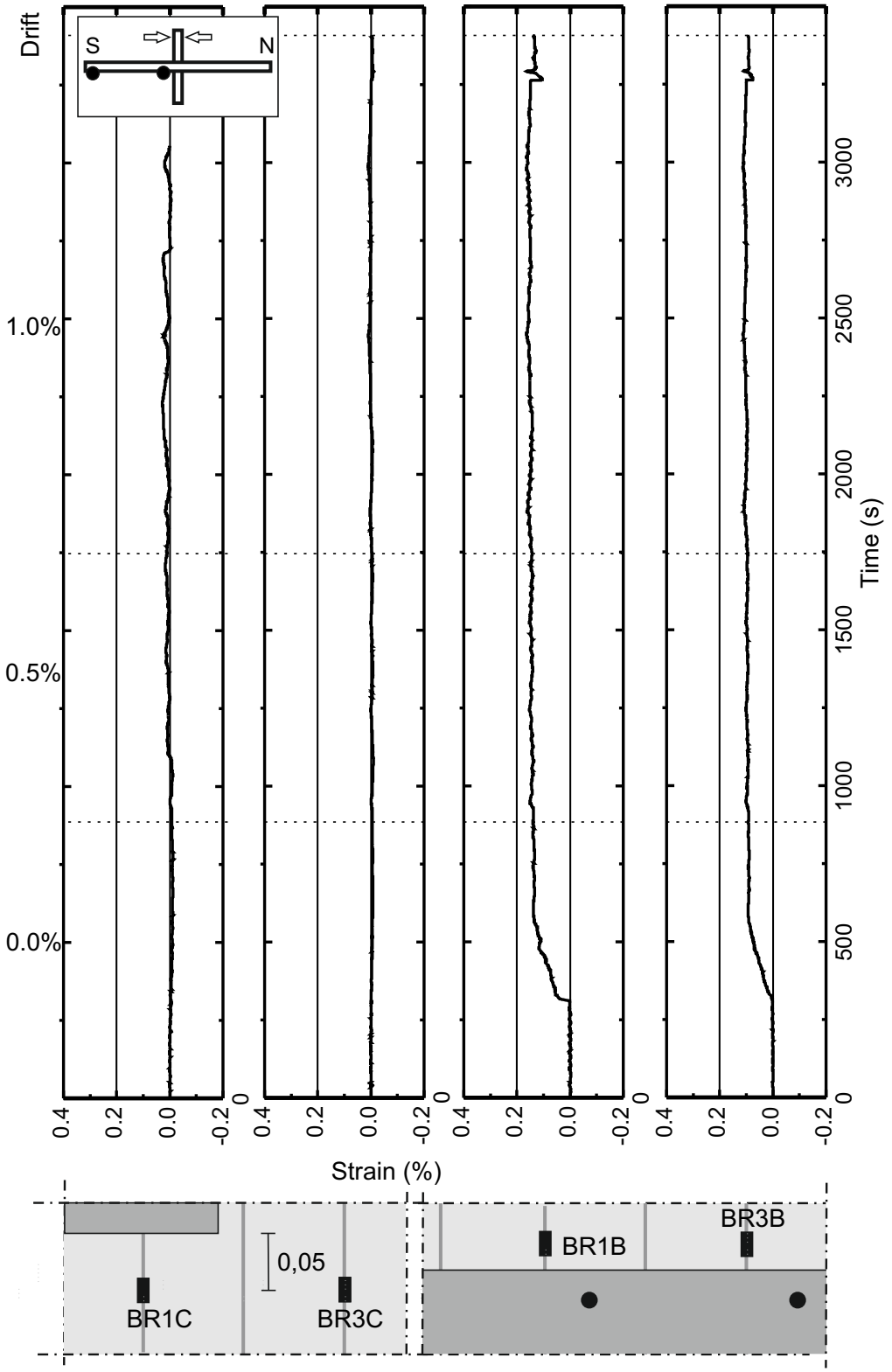


Figure B.6: Bottom reinforcement strains along the test, specimen C-Ref

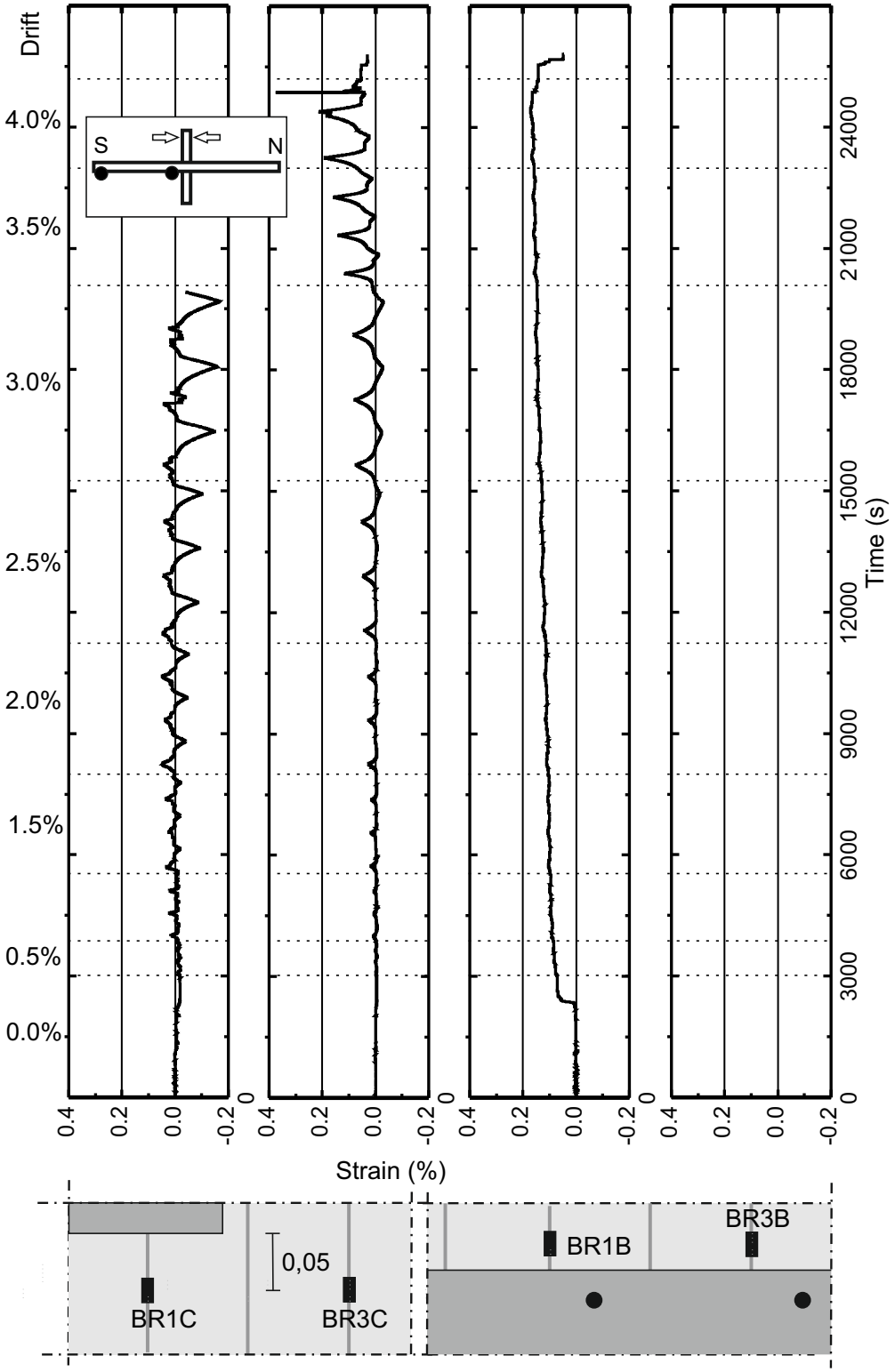


Figure B.7: Bottom reinforcement strains along the test, specimen C-SSR3

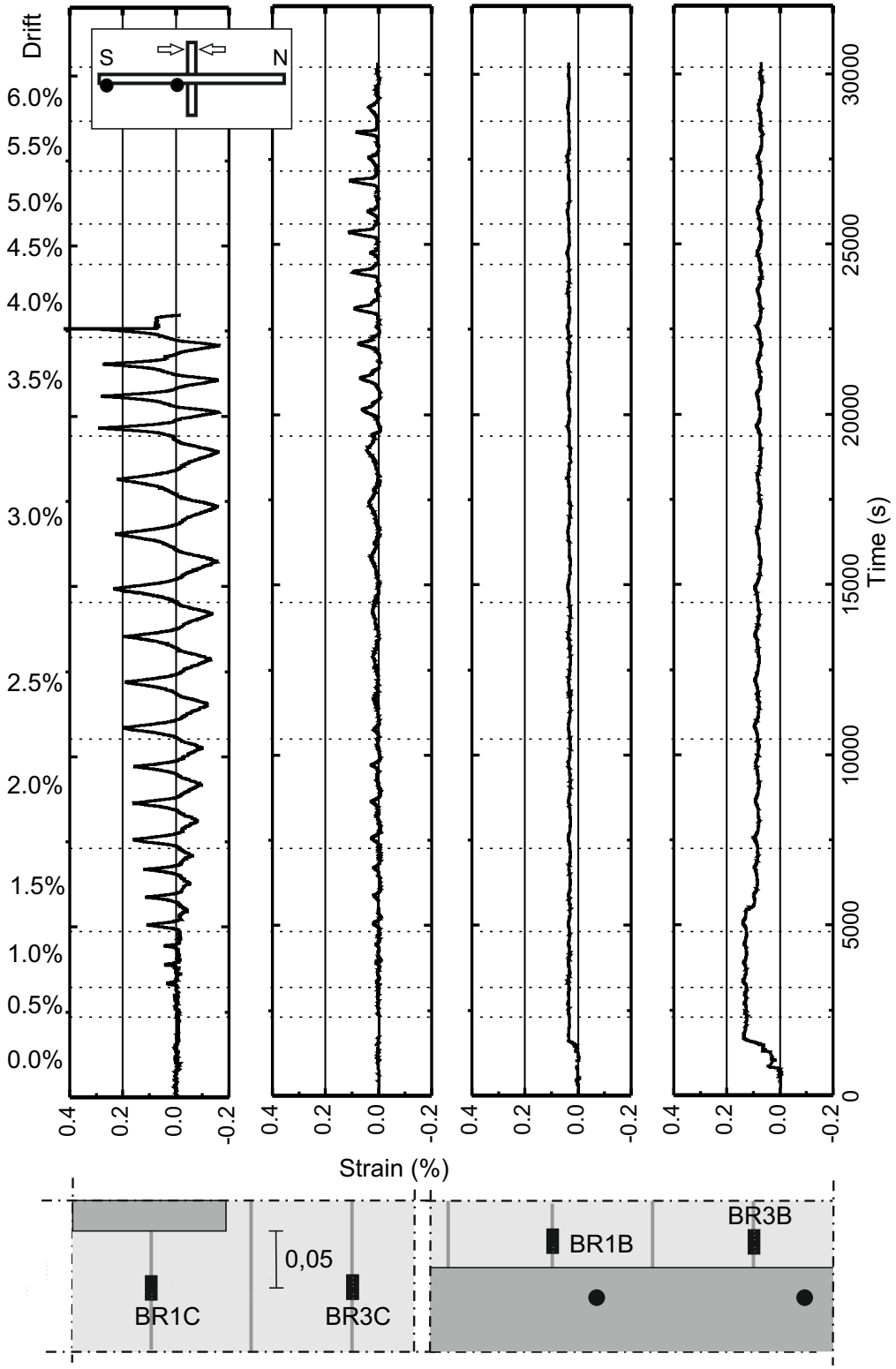


Figure B.8: Bottom reinforcement strains along the test, specimen C-SSR5a

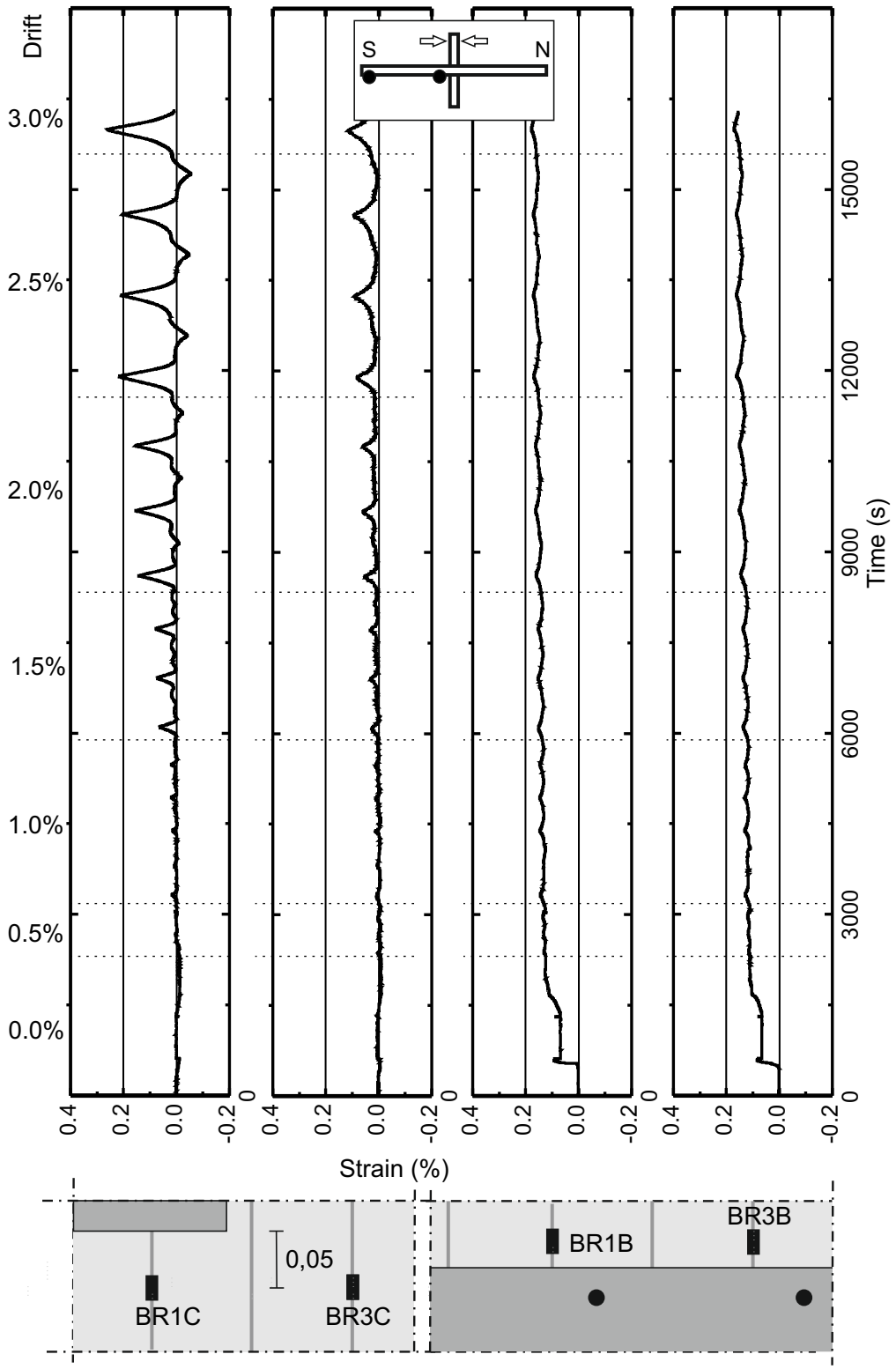


Figure B.9: Bottom reinforcement strains along the test, specimen C-SSR5b, Phase I

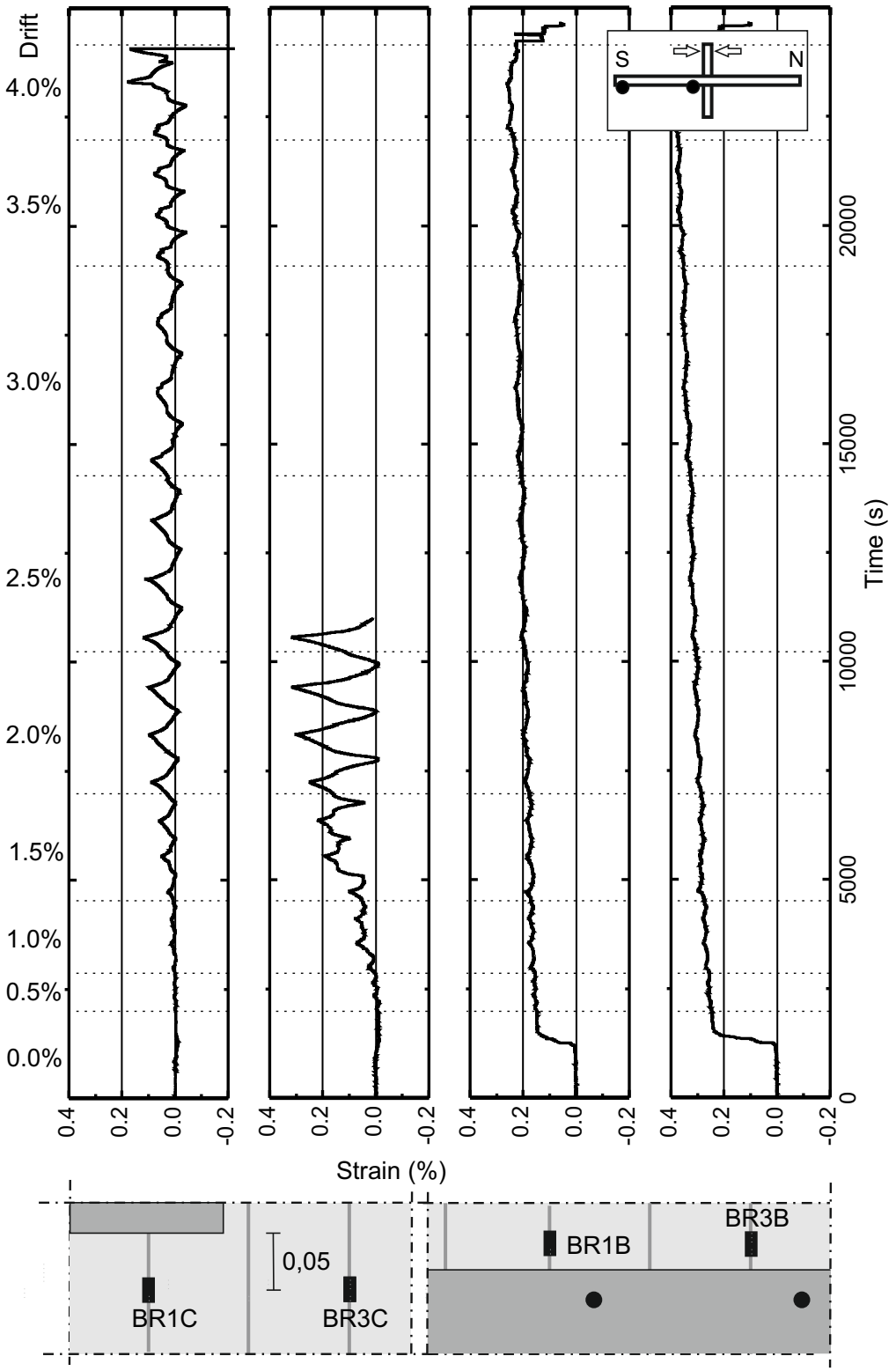


Figure B.10: Bottom reinforcement strains along the test, specimen C-SSR5c

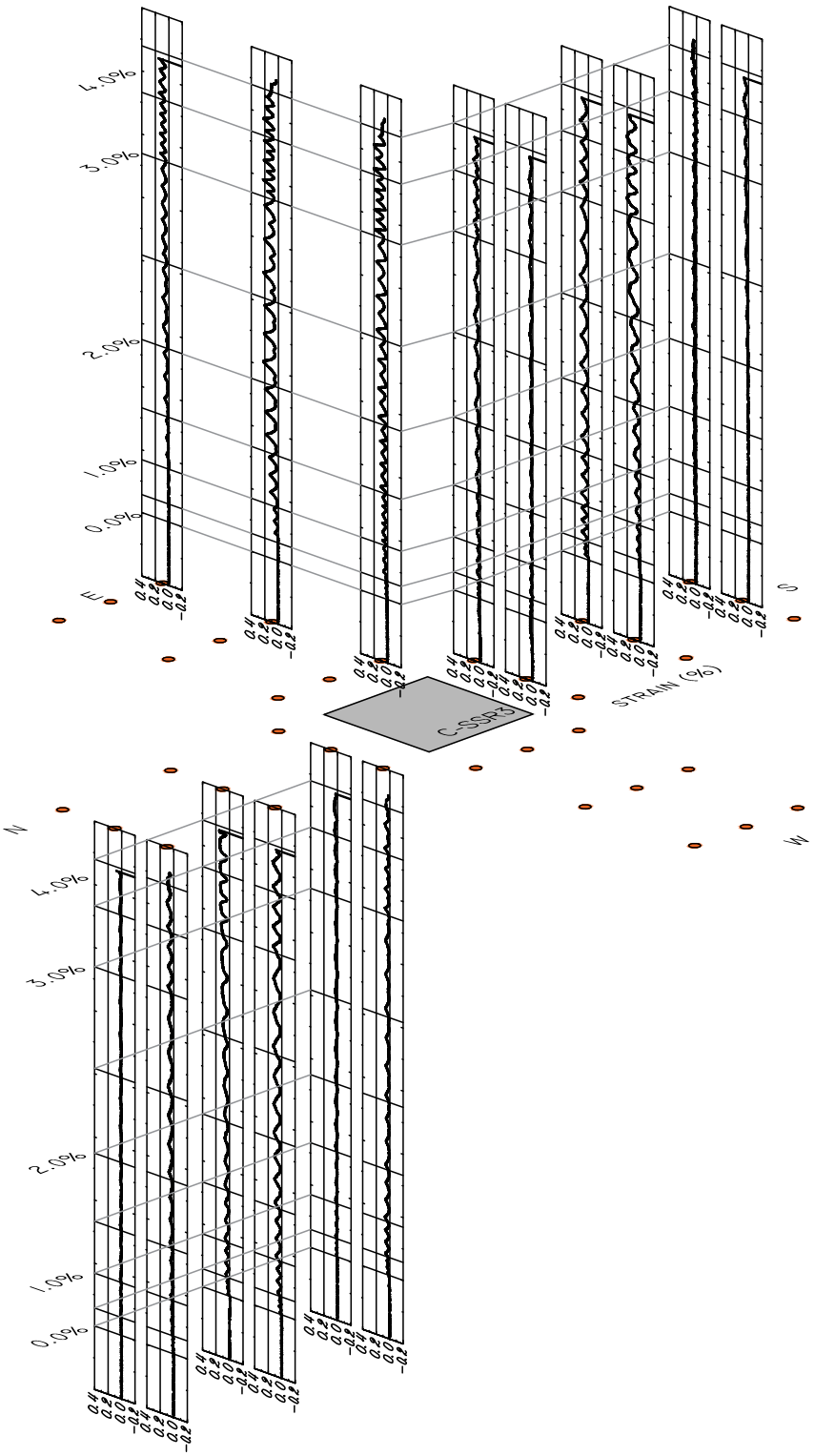


Figure B.11: Strains in studs, specimen C-SSR3

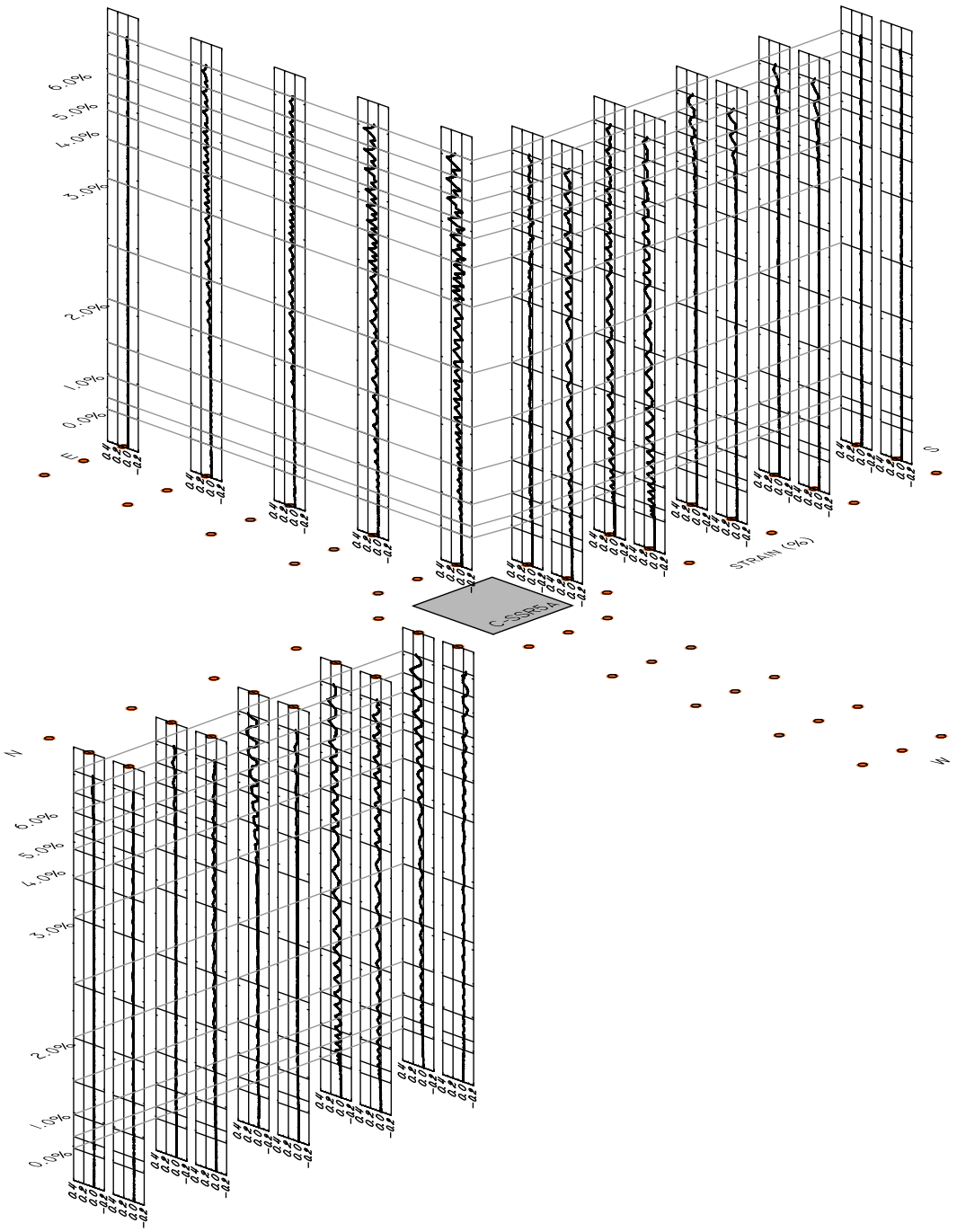


Figure B.12: Strains in studs, specimen C-SSR5a

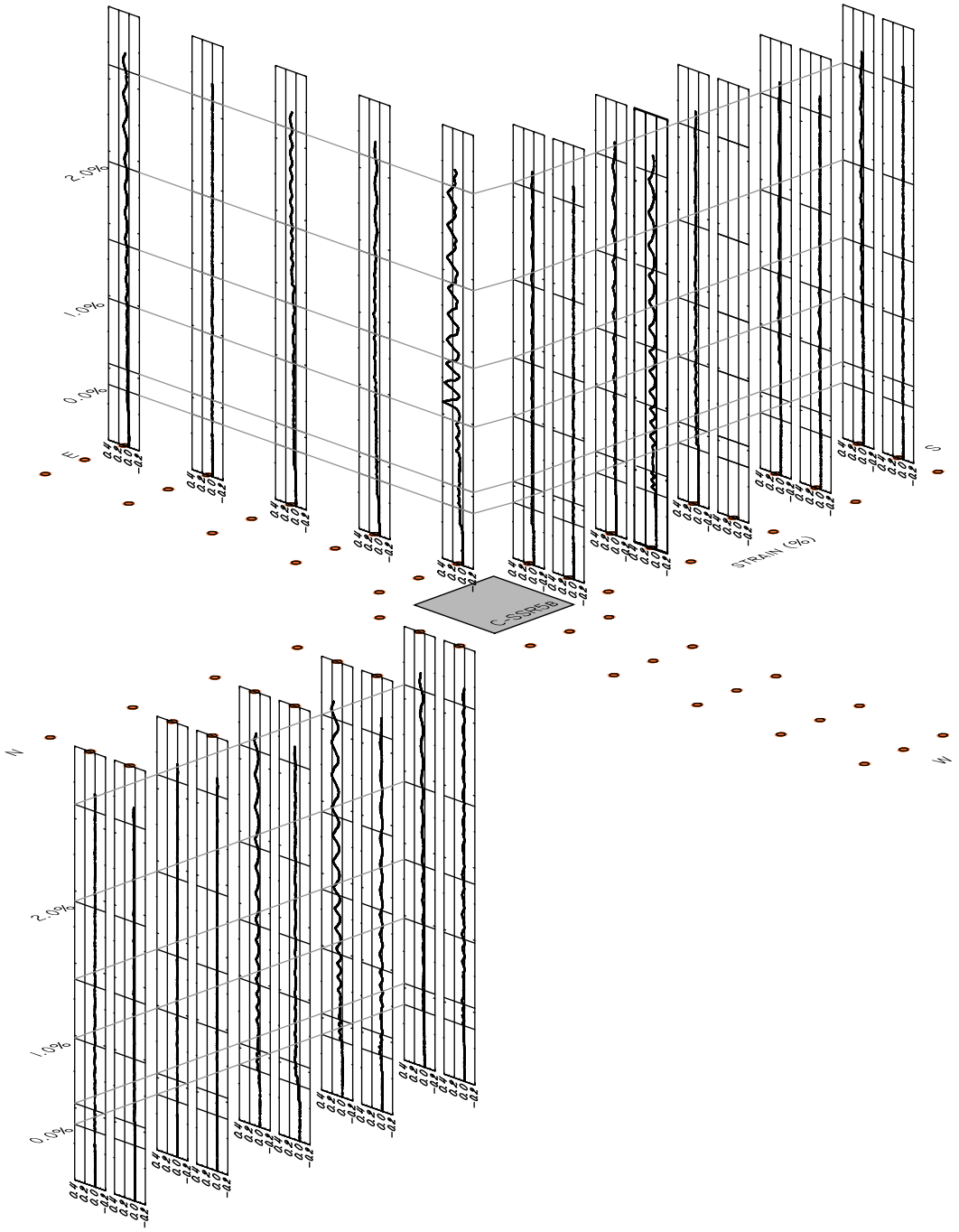


Figure B.13: Strains in studs, specimen C-SSR5b

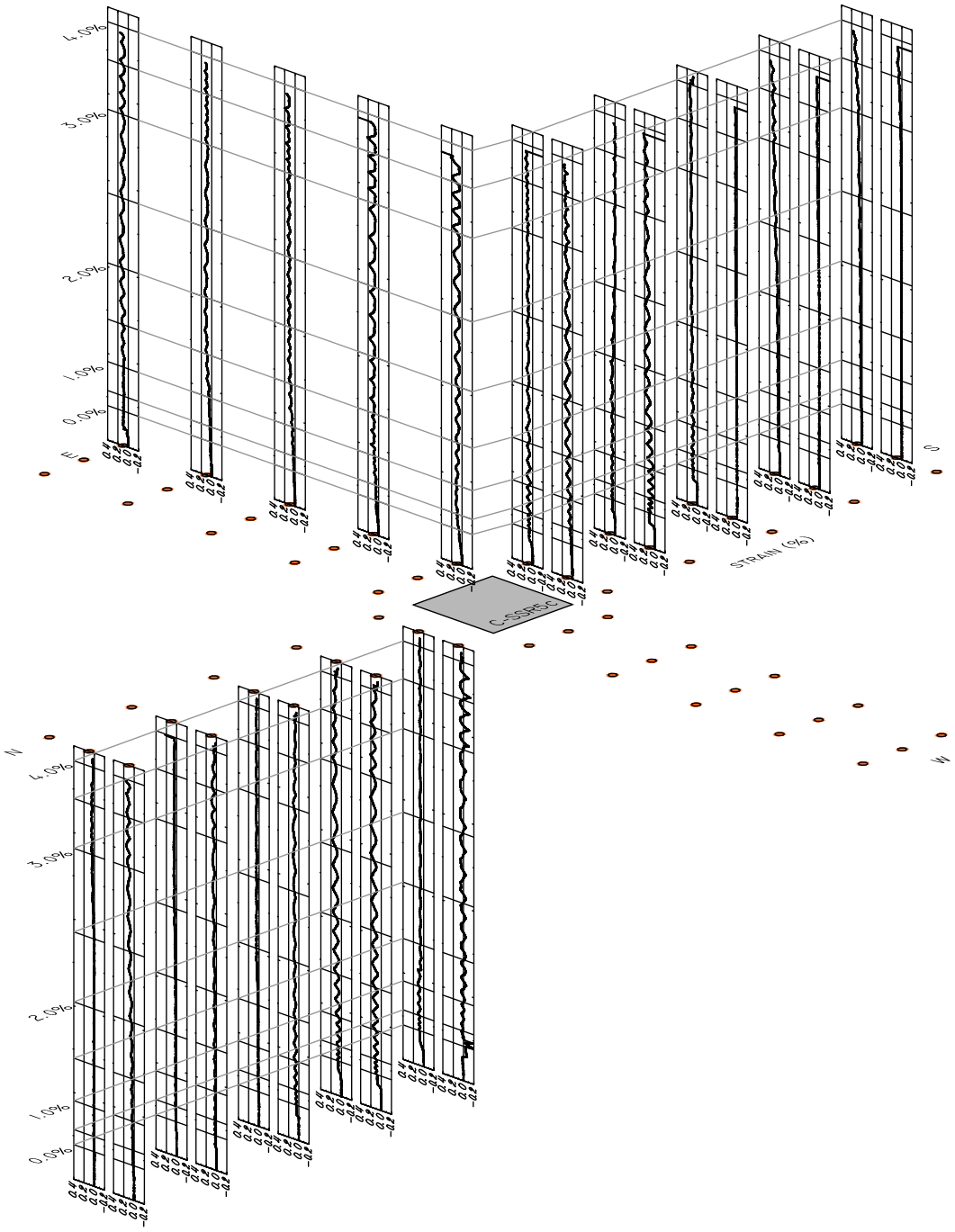


Figure B.14: Strains in studs, specimen C-SSR5c

# Appendix C

# Ground motion records

This appendix contains three tables, one for each set of ground motion records used in Chapter 6 for the seismic fragility analysis of flat slab frames. The information displayed in these tables is obtained from the PEER NGA-West2 database (*PEER NGA-West2 Ground Motion Database*; Ancheta et al. 2013).

The first column of each table contains the earthquake name, as displayed in the PEER NGA-West2 database. The second column contains the year of the seismic event. The third column contains the station from which the record was obtained. Note that some of the ground motion records correspond to the same seismic event recorded in different stations. The last two column contain the magnitude and the shear wave velocity averaged over the top 30 m of soil, $v_{s30}$.

Table C.1: Ground motion characteristics for Set I of unscaled records (target spectrum with $a_{gR}$ = 0.10 g)

| Earthquake name | Year | Station name | Magnitude | $v_{s30}$ |
|---|---|---|---|---|
| "Tabas_ Iran" | 1978 | "Boshrooyeh" | 7.35 | 324.6 |
| "Imperial Valley-06" | 1979 | "El Centro Array #12" | 6.53 | 196.9 |
| "Imperial Valley-06" | 1979 | "El Centro Array #13" | 6.53 | 249.9 |
| "Imperial Valley-06" | 1979 | "Niland Fire Station" | 6.53 | 212 |
| "Imperial Valley-06" | 1979 | "Parachute Test Site" | 6.53 | 348.7 |
| "Taiwan SMART1(45)" | 1986 | "SMART1 O06" | 7.30 | 293.5 |
| "Loma Prieta" | 1989 | "Bear Valley #12_ Williams Ranch" | 6.93 | 331.2 |
| "Loma Prieta" | 1989 | "Fremont - Emerson Court" | 6.93 | 284.8 |
| "Loma Prieta" | 1989 | "Halls Valley" | 6.93 | 281.6 |
| "Cape Mendocino" | 1992 | "Eureka - Myrtle West" | 7.01 | 337.5 |
| "Northridge-01" | 1994 | "Compton - Castlegate St" | 6.69 | 266.9 |
| "Northridge-01" | 1994 | "El Monte - Fairview Av" | 6.69 | 290.6 |
| "Northridge-01" | 1994 | "Garden Grove - Santa Rita" | 6.69 | 301.1 |
| "Northridge-01" | 1994 | "LA - E Vernon Ave" | 6.69 | 283.1 |
| "Northridge-01" | 1994 | "LA - Pico Sentous" | 6.69 | 304.7 |
| "Northridge-01" | 1994 | "LA - S. Vermont Ave" | 6.69 | 301.9 |
| "Northridge-01" | 1994 | "LA - W 15th St" | 6.69 | 329.5 |
| "Northridge-01" | 1994 | "Lakewood - Del Amo Blvd" | 6.69 | 267.4 |
| "Northridge-01" | 1994 | "Lawndale - Osage Ave" | 6.69 | 311.9 |
| "Northridge-01" | 1994 | "Manhattan Beach - Manhattan" | 6.69 | 351.6 |
| "Northridge-01" | 1994 | "Playa Del Rey - Saran" | 6.69 | 345.7 |
| "Gulf of Aqaba" | 1995 | "Eilat" | 7.20 | 354.9 |
| "Manjil_ Iran" | 1990 | "Rudsar" | 7.37 | 242.1 |
| "Hector Mine" | 1999 | "Baker Fire Station" | 7.13 | 324.6 |
| "Chuetsu-oki_ Japan" | 2007 | "NGN001" | 6.80 | 303.7 |
| "Chuetsu-oki_ Japan" | 2007 | "NIG022" | 6.80 | 193.2 |
| "Iwate_ Japan" | 2008 | "Oomagari Hanazono-cho_ Daisen" | 6.90 | 262.3 |
| "Iwate_ Japan" | 2008 | "Takanashi Daisen" | 6.90 | 217.1 |
| "Darfield_ New Zealand" | 2010 | "RKAC" | 7.00 | 295.7 |
| "Darfield_ New Zealand" | 2010 | "SBRC" | 7.00 | 263.2 |

Table C.2: Ground motion characteristics for Set II of unscaled records (target spectrum with $a_{gR}$ = 0.20 g)

| Earthquake name | Year | Station name | Magnitude | $v_{s30}$ |
|---|---|---|---|---|
| "Northern Calif-03" | 1954 | "Ferndale City Hall" | 6.50 | 219.3 |
| "Taiwan SMART1(45)" | 1986 | "SMART1 M07" | 7.30 | 327.6 |
| "Superstition Hills-02" | 1987 | "Westmorland Fire Sta" | 6.54 | 193.7 |
| "Loma Prieta" | 1989 | "Agnews State Hospital" | 6.93 | 239.7 |
| "Loma Prieta" | 1989 | "Emeryville; Pacific Park #2 Free Field" | 6.93 | 198.7 |
| "Loma Prieta" | 1989 | "Hollister - South Pine" | 6.93 | 282.1 |
| "Loma Prieta" | 1989 | "Hollister City Hall" | 6.93 | 198.8 |
| "Loma Prieta" | 1989 | "Palo Alto - 1900 Embarc." | 6.93 | 209.9 |
| "Loma Prieta" | 1989 | "Sunnyvale - Colton Ave." | 6.93 | 267.7 |
| "Landers" | 1992 | "Yermo Fire Station" | 7.28 | 353.6 |
| "Northridge-01" | 1994 | "LA - Baldwin Hills" | 6.69 | 297.1 |
| "Northridge-01" | 1994 | "Moorpark - Fire Sta" | 6.69 | 341.6 |
| "Kobe Japan" | 1995 | "Amagasaki" | 6.90 | 256.0 |
| "Chuetsu-oki Japan" | 2007 | "Kubikiku Hyakken Joetsu City" | 6.80 | 342.7 |
| "Chuetsu-oki Japan" | 2007 | "Joetsu City" | 6.80 | 294.7 |
| "Chuetsu-oki Japan" | 2007 | "Sanjo Shinbori" | 6.80 | 278.1 |
| "Chuetsu-oki Japan" | 2007 | "Nakanoshima Nagaoka" | 6.80 | 319.0 |
| "Chuetsu-oki Japan" | 2007 | "Shiura Nagaoka" | 6.80 | 336.9 |
| "Chuetsu-oki Japan" | 2007 | "Yan Sakuramachi City watershed" | 6.80 | 265.8 |
| "Iwate Japan" | 2008 | "AKTH19" | 6.90 | 288.0 |
| "Iwate Japan" | 2008 | "Nakashinden Town" | 6.90 | 276.3 |
| "El Mayor-Cucapah Mexico" | 2010 | "El Centro Array #10" | 7.20 | 202.9 |
| "Darfield New Zealand" | 2010 | "Christchurch Botanical Gardens" | 7.00 | 187.0 |
| "Darfield New Zealand" | 2010 | "Christchurch Cashmere High School" | 7.00 | 204.0 |
| "Darfield New Zealand" | 2010 | "Kaiapoi North School " | 7.00 | 255.0 |
| "Darfield New Zealand" | 2010 | "NNBS North New Brighton School " | 7.00 | 211.0 |
| "Darfield New Zealand" | 2010 | "Pages Road Pumping Station" | 7.00 | 206.0 |
| "Darfield New Zealand" | 2010 | "Riccarton High School " | 7.00 | 293.0 |
| "Darfield New Zealand" | 2010 | "Shirley Library" | 7.00 | 207.0 |
| "El Mayor-Cucapah Mexico" | 2010 | "Westside Elementary School" | 7.20 | 242.0 |

Table C.3: Ground motion characteristics for Set III of unscaled records (target spectrum with $a_{gR}$ = 0.30 g)

| Earthquake name | Year | Station name | Magnitude | $v_{s30}$ |
|---|---|---|---|---|
| "Superstition Hills-02" | 1987 | "Westmorland Fire Sta" | 6.54 | 193.7 |
| "Loma Prieta" | 1989 | "Emeryville; Pacific Park #2 Free Field" | 6.93 | 198.7 |
| "Loma Prieta" | 1989 | "Hollister - South Pine" | 6.93 | 282.1 |
| "Loma Prieta" | 1989 | "Hollister City Hall" | 6.93 | 198.8 |
| "Loma Prieta" | 1989 | "Palo Alto - 1900 Embarc." | 6.93 | 209.9 |
| "Loma Prieta" | 1989 | "Sunnyvale - Colton Ave." | 6.93 | 267.7 |
| "Landers" | 1992 | "Yermo Fire Station" | 7.28 | 353.6 |
| "Northridge-01" | 1994 | "LA - Baldwin Hills" | 6.69 | 297.1 |
| "Kobe Japan" | 1995 | "Amagasaki" | 6.90 | 256.0 |
| "Chuetsu-oki Japan" | 2007 | "Kubikiku Hyakken Joetsu City" | 6.80 | 342.7 |
| "Chuetsu-oki Japan" | 2007 | "Joetsu City" | 6.80 | 294.7 |
| "Chuetsu-oki Japan" | 2007 | "Sanjo Shinbori" | 6.80 | 278.1 |
| "Chuetsu-oki Japan" | 2007 | "Nakanoshima Nagaoka" | 6.80 | 319.0 |
| "Chuetsu-oki Japan" | 2007 | "Yan Sakuramachi City watershed" | 6.80 | 265.8 |
| "Iwate Japan" | 2008 | "AKTH19" | 6.90 | 288.0 |
| "Iwate Japan" | 2008 | "Nakashinden Town" | 6.90 | 276.3 |
| "Iwate Japan" | 2008 | "Iwadeyama" | 6.90 | 345.6 |
| "El Mayor-Cucapah Mexico" | 2010 | "RIITO" | 7.20 | 242.1 |
| "El Mayor-Cucapah Mexico" | 2010 | "El Centro - Meloland Geot. Array" | 7.20 | 264.6 |
| "El Mayor-Cucapah Mexico" | 2010 | "El Centro - Imperial Ross" | 7.20 | 229.3 |
| "El Mayor-Cucapah Mexico" | 2010 | "El Centro Array #10" | 7.20 | 202.9 |
| "El Mayor-Cucapah Mexico" | 2010 | "El Centro Array #11" | 7.20 | 196.3 |
| "Darfield New Zealand" | 2010 | "Christchurch Cathedral College" | 7.00 | 198.0 |
| "Darfield New Zealand" | 2010 | "Christchurch Cashmere High School" | 7.00 | 204.0 |
| "Darfield New Zealand" | 2010 | "DFHS" | 7.00 | 344.0 |
| "Darfield New Zealand" | 2010 | "Kaiapoi North School " | 7.00 | 255.0 |
| "Darfield New Zealand" | 2010 | "NNBS North New Brighton School " | 7.00 | 211.0 |
| "Darfield New Zealand" | 2010 | "Pages Road Pumping Station" | 7.00 | 206.0 |
| "Darfield New Zealand" | 2010 | "Riccarton High School " | 7.00 | 293.0 |
| "El Mayor-Cucapah Mexico" | 2010 | "Westside Elementary School" | 7.20 | 242.0 |